NUMERICAL AND EXPERIMENTAL INVESTIGATION OF TWO-PHASE FLOW DISTRIBUTION THROUGH MULTIPLE OUTLETS FROM A HORIZONTAL DRUM

A THESIS SUBMITTED TO
THE GRADUATE SCHOOL OF NATURAL AND APPLIED SCIENCES
OF
MIDDLE EAST TECHNICAL UNIVERSITY

BY

ENİS PEZEK

IN PARTIAL FULFILLMENT OF THE REQUIREMENTS

FOR

THE DEGREE OF DOCTOR OF PHILOSOPHY

IN

MECHANICAL ENGINEERING

MARCH 2006

Approval of the Graduate School of Natural and Applied Sciences.

<div align="right">
Prof. Dr. Canan ÖZGEN
Director
</div>

I certify that this thesis satisfies all the requirements as a thesis for the degree of Doctor of Philosophy.

<div align="right">
Prof. Dr. S. Kemal İDER
Head of Department
</div>

This is to certify that we have read this thesis and that in our opinion it is fully adequate, in scope and quality, as a thesis for the degree of Doctor of Philosophy.

<div align="right">
Prof. Dr. A. Orhan YEŞİN
Supervisor
</div>

Examining Committee Members

Prof.Dr. M. Haluk AKSEL   (METU, ME) _____

Prof.Dr. A. Orhan YEŞİN   (METU, ME) _____

Prof.Dr. Ö. Ercan ATAER (GAZI Unv., ME) _____

Asst.Prof.Dr. İlker TARI   (METU, ME) _____

Assoc.Prof.Dr. C. Niyazi SÖKMEN (HU, NE) _____

I hereby declare that all information in this document has been obtained and presented in accordance with academic rules and ethical conduct. I also declare that, as required by these rules and conduct, I have fully cited and referenced all material and results that are not original to this work.

Name, Last Name : Enis Pezek

Signature   :

ABSTRACT

NUMERICAL AND EXPERIMENTAL INVESTIGATION OF
TWO-PHASE FLOW DISTRIBUTION THROUGH MULTIPLE
OUTLETS FROM A HORIZONTAL DRUM

Pezek, Enis

Ph.D., Department of Mechanical Engineering

Supervisor: Prof. Dr. A. Orhan Yeşin

March 2006, 187 pages

In CANDU reactors, under normal operating conditions, the inlet headers collect and distribute single-phase liquid flow (heavy water) to the fuel cooling channels via the feeders. However, under some postulated loss of coolant accidents, the inlet headers may receive two-phase fluid (steam/water) and the fluid forms a stratified region inside the header. To predict the thermal-hydraulic behaviour of headers for the reactor safety analysis, the two-phase flow distribution within the headers and through the feeders must be modelled. In order to analyse the two-phase flow behaviour of a scaled CANDU inlet header; a transparent and instrumented version of a header with 5 feeders was previously built in the Mechanical Engineering Department of Middle East Technical University (METU-Two Phase Flow Test Facility / METU-TPFTF).

The aim of this study is to investigate two-phase flow distribution through

multiple outlets from such a horizontal drum both numerically and experimentally.

For this purpose, three-dimensional incompressible finite difference equations in cylindrical coordinates were derived by using two-fluid model to simulate adiabatic two-phase flow (air/water) in the header numerically.

The discretized equations were then programmed into a computer code which was developed specifically for modelling the header type geometry. A method based on the principles of Implicit Multi Field (IMF) technique has been utilised to solve those equations. The solution algorithm was tested by using some numerical benchmark problems.

A number of experimental tests covering single and two-phase flow distribution through outlet pairs from the header were performed. Void fractions and flow rates obtained from these tests are in good agreement with the code results. The code also predicts the void fraction and pressure distribution in the header satisfactorily.

Keywords: two-fluid model, CANDU inlet header, two-phase flow, implicit multifield technique, METU-Two Phase Flow Test Facility

ÖZ

YATAY BİR SİLİNDİRİN ÇOKLU ÇIKIŞ AĞIZLARINDAN OLAN
İKİ-FAZLI AKIŞ DAĞILIMININ SAYISAL VE DENEYSEL OLARAK
İNCELENMESİ

Pezek, Enis

Doktora, Makina Mühendisliği Bölümü

Tez Yöneticisi: Prof. Dr. A. Orhan Yeşin

Mart 2006, 187 sayfa

CANDU reaktörlerinde, normal işletme koşullarında, soğutucu dağıtma hazneleri (inlet header) tek-fazlı akışı (ağır su) toplamakta ve yakıt soğutma kanallarına kendisine bağlı besleme boruları (feeder) aracılığıyla dağıtmaktadır. Fakat, olabileceği öngörülen bazı soğutucu kaybı kazalarında, bu hazneler iki-fazlı (buhar/su) akışa maruz kalabilir ve akışkan, haznelerin içinde ayrık akış bölgesi oluşturabilir. Reaktör güvenlik analizleri için soğutucu dağıtma haznelerinin ısılhidrolik davranışını tespit etmek amacıyla, soğutucu dağıtma haznesi ve besleme borularındaki iki-fazlı akış dağılımının modellenmesi gerekmektedir. Ölçeklendirilmiş bir CANDU soğutucu dağıtma haznesinin iki-fazlı akış altındaki davranışını incelemek için saydam ve ölçüm cihazlarıyla donatılmış bir benzeri, bağlı 5 besleme borusuyla birlikte, daha önce Ortadoğu Teknik Üniversitesi Makina Mühendisliği Bölümü'nde (METU-İki Fazlı Akış Test Düzeneği/METU-TPFTF) tesis edilmişti.

Bu çalışmanın amacı böyle bir yatay silindirin çoklu çıkış ağızlarından olan iki-fazlı akış dağılımını sayısal ve deneysel olarak incelemektir.

Bu amaçla, dağıtma haznesinde, iki-fazlı akışın (hava/su) modellenmesi için iki-akışkan modeli kullanılarak, üç-boyutlu silindirik koordinatlarda sıkıştırılamaz fazlar için sonlu farklar denklemleri türetilmiştir.

Kesikli hale getirilen denklemler daha sonra programlanarak haznelerin kendine has geometrisi için bu çalışmada özel olarak geliştirilmiş bir bilgisayar programında çözülmektedir. Bu denklemleri çözmek için Örtük Çoklu Alan (IMF) tekniğinin prensiplerinden yararlanan bir çözüm yöntemi oluşturulmuştur. Bu çözüm yöntemi bazı sayısal doğrulama problemleriyle test edilmiştir.

Dağıtma haznesi bileşeninin farklı kombinasyonlarda çiftler halinde açılan çıkış ağızlarından olan tek-fazlı(su) ve iki-fazlı (hava/su) akış dağılımını tespit etmek amacıyla birtakım deneysel testler gerçekleştirilmiştir. Bu testlerden elde edilen boşluk oranları ve akış hızları bilgisayar programı tarafından ortaya konulan sonuçlarla uyum halindedir. Program, hazne içindeki boşluk oranı ve basınç dağılımını memnun edici surette hesaplamaktadır.

Anahtar Kelimeler: İki-akışkan modeli, soğutucu dağıtma haznesi, iki-fazlı akış, Örtük Çoklu Alan Tekniği, METU-İki Fazlı Akış Test Düzeneği.

To My Wife

ACKNOWLEDGMENTS

and encouragement.

Lastly, but most important of all, I owe my deepest gratitude to my wife, Tuba, for the great strength, support and encouragement she gave me during my Ph.D studies and for always standing by me. Her endless love, understanding attitude and everlasting optimism towards my long working hours have been essential for the completion of this thesis. There are not enough words to describe all the thanks you deserve. This thesis is dedicated to you. "I Love You!"

TABLE OF CONTENTS

LIST OF TABLES

LIST OF FIGURES

LIST OF SYMBOLS

C_D drag coefficient

D   discrepancy in continuity equation

d   bubble diameter

g   gravitational acceleration

K   interfacial momentum transfer function

P   pressure, Pa

q   phase selection index

Re   reynolds number

r   radial distance, m

t   time, s

$\vec{u}$ velocity vector

U   velocity in radial direction, m/s

V   velocity in axial direction, m/s

W   velocity in azimuthal direction, m/s

z   axial distance, m

Greek Symbols

Γ condensation or evaporation rate, kg/m^3s

ϵ	the convergence criterion
θ	volume fraction
θ^*	switch void fraction
λ	second coefficient of viscosity, kg/ms
μ	first coefficient of viscosity, kg/ms
ρ	microscopic density, kg/m^3
$\acute{\rho}$	macroscopic density, mass per unit of mixture volume, kg/m^3
τ	viscous stress tensor, N/m^2
ϕ	angle
ω	relaxation parameter

Subscripts

c	condensation
e	evaporation
g	gas phase
i	cell index for radial direction
in	inflow boundary condition
j	cell index for axial direction
k	cell index for azimuthal direction
l	liquid phase
out	outflow boundary condition
qi	index for interface interactions
r	radial direction
z	axial direction

ϕ azimuthal direction

Superscripts

n   current value

n+1   new value after time step advancement

——   intermediate time level value

CHAPTER 1

INTRODUCTION

Flow of two different fluids occurs in a wide range of modern engineering processes, such as condensation of steam in power plants, two-phase flow in jets and fluidized beds, boiling flow in heat exchangers, air-water flow in a cooling tower. The study of two-phase flows is necessary to evaluate and to optimize the performances of these kind of processes. The understanding and accurate modelling of two-phase flow phenomena is also very important for design studies and safety analysis of nuclear reactors.

Another field of study in two-phase research is drums, headers, which distribute or collect a fluid to or from small multiple branch pipes and are commonly used in boilers, in heat exchangers and also in heat transport systems of nuclear reactors (e.g. CANDU, VVER).

In addition to experimental investigations, the numerical simulation is also an important method of study for such processes. In order to simulate a two-phase flow numerically, a number of sets of differential equations governing the motion of each phase including velocities, temperatures, masses, densities etc, at each location in the two-phase domain are required. Solving these equations for the simulation of two-phase flow characteritics are rather complicated [70].

1

This dissertation describes the numerical modelling of two-phase flow distribution through multiple outlets of a horizontal drum (a scaled model of a CANDU reactor inlet header). It contains details about coding of the numerical model and validation studies of this code with some selected benchmark problems. Finally, code verification with the experiments conducted in METU Two Phase Flow Test Facility (METU-TPFTF) are also presented.

In this first chapter, an introduction is made to CANDU Heat Transport System and to its important components, "inlet headers". This introduction emphasises the importance of flow characteristics of those headers and motivation behind this thesis. A literature survey made on numerical modelling of two-phase will follow them.

1.1 Background

This work was part of a project funded by the Atomic Energy of Canada Limited (AECL), Middle East Technical University (METU) and Turkish Atomic Energy Authority (TAEK) to investigate the two-phase flow behaviour of a scaled CANDU reactor header similar to that used in RD-14M Test Facility. One of the objective of this project is to understand two-phase flow phenomena occuring under different flow conditions and to provide experimental data to validate for safety analysis.

Some basic information about CANDU Heat Transport System and about design and flow characteristics of inlet headers will be given in the following sections.

1.1.1 CANDU Heat Transport System

CANDU reactor is fuelled with natural uranium. The reactor consists of a large horizontal cylindrical tank, named calandria, which contains the D_2O moderator at low pressure. This tank is penetrated by 380 channels which contain the fuel. Each six meter long fuel channel contains 12 fuel bundles.
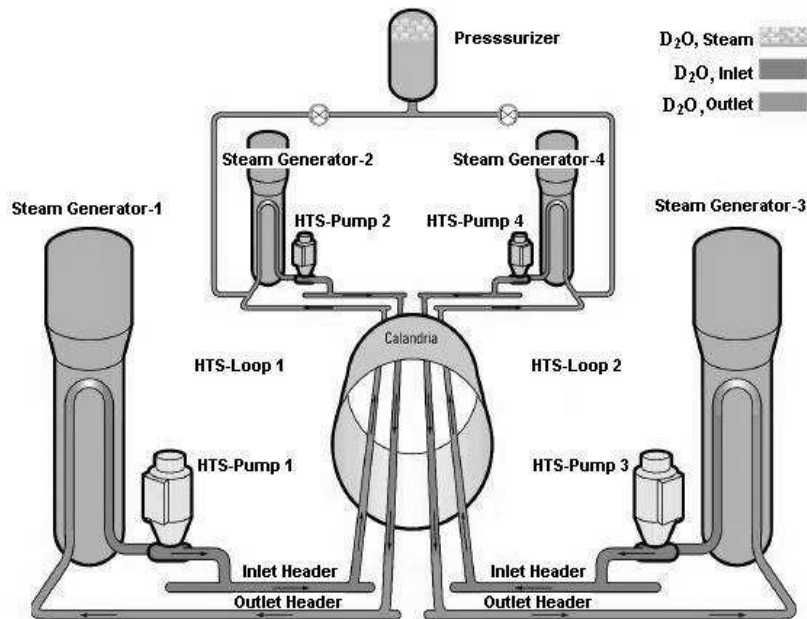
Figure 1.1: CANDU HTS

Two parallel Heat Transport System (HTS) coolant loops are provided in a CANDU-6 reactor. The heat from half of the fuel channels in the core is removed by each loop. The HTS circulates pressurized D_2O coolant (at a pressure of about 10 MPa) through the fuel channels to remove the heat produced by the nuclear fission in the fuel. The coolant passes from the reactor to a header and then to a steam generator where steam is produced. The coolant then returns to the reactor, passing in the opposite direction through an adjacent fuel channel, where it is heated again before flowing to the second steam generator (Figure 1.1).

Each HTS loop has a "figure of 8" configuration and has one "inlet" and one "outlet" header at each end of the reactor core. Coolant is fed to each of the fuel channels through individual "feeder" pipes from the inlet headers and is returned from each channel through outlet headers as shown in Figure 1.2.
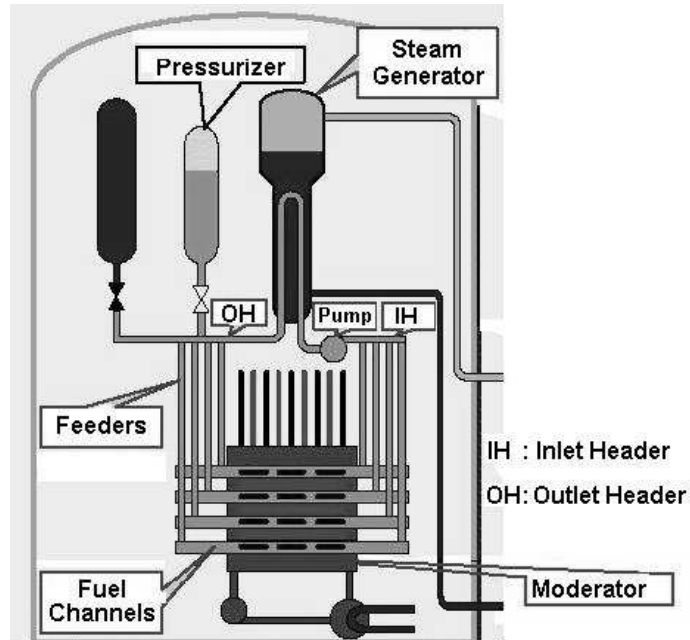
Figure 1.2: Inlet and Outlet Headers with Feeders

1.1.2 Inlet Header Design and Flow Characteristics

Typically, an inlet header of a CANDU-6 reactor consists of a large horizontal pipe (approximately 6-m long and 0.356 to 0.406 m. i.d.) closed on both ends. The flow enters from a number openings at the top of this pipe and exits through banks of feeders at various axial locations and angles along the header. These "inlet" feeders bring the coolant from the header to the fuel channels (see Figure 1.2). Each feeder bank consists of five 50.8 mm i.d. tubes attached to the header at angles $0^o, 45^o, 90^o, 145^o, 180^o$ measured from a horizontal line [45].

Under normal operating conditions, inlet headers distribute single-phase liquid flow to the heated channels via the feeders. Under some postulated

4

loss of coolant accidents, electrical power to the pumps are lost and pumps run down. Consequently, the flow in the fuel channels decreases. After the pumps have run down completely, decay heat is removed from the reactor core by single or two-phase natural circulation of the primary coolant to the steam generators. This flow is possible because the steam generators are located above the core. The flow is induced by the difference in the density of the hot and cold coolant in the vertical sections of the piping on the inlet and outlet sides of the core. As the primary flow decreases, the inlet headers receive a two-phase fluid which forms a stratified region inside the header [45]. How the phases are distributed within the headers can effect the thermalhydraulic behaviour of the header and other components like the channels and the steam generators during two-phase flow conditions [105]. When the two-phases in a header are stratified, cooling of a fuel channel may be influenced by the elevation of its feeder connection on the header. Some feeders may receive water while some of them may receive steam. Therefore, special models/tools must be developed to treat this problem.

1.2 Motivation

Since almost all feeder pairs in a CANDU primary heat transport loop (see Figure 1.2) differ, feeder geometry and elevation effects must be addressed in test facilities in order to extrapolate the experimental results to a full scale CANDU reactor.

One of the test facility investigates header behaviour is RD-14M located at Atomic Energy of Canada Limited (AECL)'s Whiteshell Laboratories (Manitoba, Canada). RD-14M is a multiple heated channel, full elevation, scaled test facility possessing the key components of a CANDU Primary Heat Transport System. It is arranged standart CANDU two-pass "figure-of-eight" configuration.

Experiments have been conducted in this facility to determine the phase

5

distribution within the header and the flow and phase distribution in each feeders [105]. However, RD-14M headers was not well instrumented and tests in RD-14M have provided limited data to determine the header behaviour [57]. Test data obtained from RD-14M indicated that the void distribution inside the header is extremely complex [57] and flow and void through feeders at the same cross section and elevation significantly differed. Therefore, the phase and flow distributions within the headers and the feeders must be better understood to improve the understanding of the two-phase flow [105, 125].

To provide experimental data to improve understanding of header/feeder behaviour, a transparent RD-14M header was installed with full instrumentation and with connected feeders as a test facility at the The Department of Mechanical Engineering of the METU [67, 52]. Details about this facility can be found in Chapter 6.

Developing a numerical analysis tool to simulate experimental findings is also an important part of two-phase studies. Although, the one-dimensional numerical models are generally practical and widely used in describing two-phase flow systems, few of the papers in the literature dealt directly with three-dimensional modelling of two-phase flow. However, there is a need for accurate multi-dimensional prediction capability for optimising the design of components, for evaluating their performances, and for improving understanding of complex two-phase flow phenomena inside them [126]. This is also the case for describing flow dynamics of a drum having header-type geometry used in the present study.

Existing several multi-purpose computational fluid dynamics (CFD) programs could be used to model and to simulate the header type geometries, however, no computational model is available which deals specifically with the headers.

Therefore, in this study, a three dimensional computer code is developed to obtain numerical solutions of two-phase flow through the horizontal drum

(header) having multiple outlets. The study also covers the verification of the code with the data obtained from the tests conducted in the METU TPFTF by using air-water flow.

1.3 Literature Survey

The history of computational efforts for modeling of two-phase flow phenomena will be reviewed in this section.

1.3.1 Numerical Models of Two-phase Flows

In the literature, formulations of the equations governing the flow of a two-phase mixture may generally be categorised under two fundamentally different groups as [37, 90, 13]:

1. One-fluid models (interface tracking methods) and

2. Two-fluid models.

In the first group, there exist methods that track the motion of the interface between the two phases specifically. Since they solve one set of momentum equations for all fluids, this type of methods are called as "one-fluid" models.

The most widely used one-fluid method is known as "Volume Of Fluid Method (VOF) developed by Hirt and Nichols [49]. In VOF method, tracking of interface(s) between phases is accomplished by solution of a volume fraction continuity equation for each phase. This method is considered to be appropriate for motion of large bubbles in a liquid and for steady or transient tracking of any liquid-gas interface, but is considered to be inappropriate for flows involving small bubbles. Therefore, VOF is more suitable for flow where immiscible fluids have a clearly defined interface [74].

There are other one-fluid methods; "Front Tracking Method" introduced by Unverdi and Tryggvason [129] and "The Level Set Method" introduced

by Osher and Sethian [101] whose solution algorithms are so similar to that of Volume of Fluid Method.

In 1965, Harlow and Welch developed the "Marker and Cell (MAC)" method for incompressible multiphase flows [44]. MAC was one of the first interface tracking methods. This method with its successors has subsequently been improved [5, 37, 68]. SOLA-VOF method [95] can be given as an example of a MAC successor which coupled the SOLA (SOLution Algorithm) methodology with a volume tracking method for fluid interfaces [68].

However, one-fluid methods have limited applicabilities. They are still under development and their advantages have to be further assessed. These are ideal models for separated flows or free surfaces, because in most of the two-phase cases flows are too mixed, e.g. bubbly flows, and the number of interfaces is too large to track for that interface tracking methods to be suitable [11]. To model this type of flows, it is clear that another strategy is needed [65, 11, 37]. It is widely accepted in the literature that "Two-Fluid Model" is more appropriate for modeling gas-liquid or liquid-liquid flows and is generally employed when the exact position of the interface is not followed specifically.

In this second group, averaged behaviors of both phases are treated by continuum approximation. Sometimes, "two-fluid model" is called as the "interpenetrating-continua approach" or "Eulerian-Eulerian approach" since each phase is seen from an Eulerian point of view.

Two-fluid is one of the most successful model. Ishii [58] established the mathematical foundation of this model. This formulation is supported by an extensive literature found in the area of multi-phase flows and is widely used in the simulation of two-phase flows.

In this study, two-fluid model is considered to be better suited for the purposes and it is chosen for modelling the header in the METU-TPFTF.

Harlow and Amsden [43] developed the Implicit Continuous-fluid Eulerian (ICE) method to solve multidimensional flows. With Semi-Implicit Method

for Pressure-Linked Equations method (SIMPLE), developed by Patankar and Spalding [106], ICE method established a basis for early two-fluid flow codes [92]. After extention of SIMPLE algorithm to two-phase flow by Spalding it has been called as IPSA (InterPhase-Slip Algorithm) [30].

However, detailed numerical modeling of multiphase flows especially for reactor safety analysis began in 1974 with the development of the KACHINA code by Harlow and Amsden [3]. KACHINA was the first code to provide stable numerical solutions for multidimensional two-phase flow [2].

In 1977, Rivard and Torrey developed a code named K-FIX [110] for three-dimensional flow of two compressible phases. This code is based on the Implicit MultiField (IMF) method developed by Harlow and Amsden [41] for KACHINA [3].

Examples of early two-fluid solution schemes are variants of these IMF Method and the InterPhase Slip Algorithm (IPSA). Several commercial CFD codes uses such semi-implicit methods.

Some selected important studies in two-phase modelling which were utilised in the present study can be given as follows;

In 1997, Enwald and Peirano developed the finite difference GEMINI code [23] which uses the IMF numerical algorithm [3]. Same year, Peirano modified GEMINI to take gas and particle turbulence into account [23].

In 1999, Uchiyama [127] proposed an upstream finite element method for gas-liquid two-phase flow, based on an incompressible two-fluid model. He used Petrov-Galerkin method for two-dimensional geometry in his study. He applied this method to the computation of air-water two-phase flows around a rectangular cylinder.

Latsa et al. [76] used two-phase flow model for the simulation of one or two-dimensional batch sedimentation processes in vertical or inclined settling tanks by solving the continuity and momentum equations for the pure-clear liquid and the sludge phases. They used IPSA algorithm by using TFLOW-2D code to solve the conservation equations in staggered grid.

In 2001, Pain et al. [104] attempted to model gas-solid particle fluidized beds using the two-fluid solution method, assuming both gas and solid phases are incompressible. A transient mixed finite element formulation was used to discretize the equations.

Snider [117] presented a three-dimensional, incompressible, multiphase particle-in-cell (PIC) method for dense particle flows. He used a numerical technique which solves the governing equations of the liquid phase using a continuum model and those of the particle phase using a Lagrangian model. In this model, particles were implicitly coupled to the liquid phase, and the liquid momentum and pressure equations are implicitly solved. He also tested his algorithm with four different types of the problem.

Uchiyama [128] proposed a two-fluid model for solving incompressible gas-liquid two-phase flow including moving boundaries based on ALE finite element form. Solution algorithm was parallel to a fractional step method. Galerkin method was employed for the formulation. He applied this method to calculate the flow around a circular cylinder, which is forced to oscillate in a quiescent air-water two-phase mixture.

Friberg [30] constructed a three-dimensional mathematical model in cylindrical dimensions to use in simulations of large-scale, impeller stirred bioreactors. In order to evaluate this model, he made simulations for a bubble column, a single phase impeller stirred vessel and a two-phase impeller stirred. These results are then compared with experimental data from literature. He used IPSA algorithm to solve finite volume representations of the governing equations.

In 2003, Andrianov [6] investigated several systems of two-phase flow equations analytically and numerically. He used a combination of Godunov and Roe schemes by using the approach of Saurel and Abgrall [113]. He worked on several benchmark studies by using those schemes.

Gallouet et al. [31] studied on numerical modeling of two-phase flows by using two-fluid model with two-pressure approach. However they used

Godunov and Rusanov schemes as finite volume methods.

Development of multiphase computational techniques and the studies for the application of these techniques to practical problems is still an ongoing effort. Also, many number of computing tools have been developed to solve two-phase problems. Some of them are described in the following section.

1.3.2 Two-Fluid Computer Codes

In 1980s and 1990s, thermalhydraulics two-fluid system codes such as RE-LAP5, TRAC-PF1, CATHARE, ATHLET, CATHENA(AECL) were developed for nuclear reactor analysis during a simulated accident [2, 97]. Extensive validation and development carried out over the last 25 years have made these codes reliable tools for safety analysis in both operating and accidental conditions [126]. Generally, various thermal-hydraulic components of a nuclear reactor are modelled as one-dimensional components by these codes.

Among them, the RELAP5 (one-dimensional) and RELAP5-3D (three-dimensional version of RELAP5) [55] codes employ a transient, two-fluid model for flow of a two-phase vapor/gas-liquid mixture. The system model is solved numerically using a semi-implicit finite-difference technique [54].

CATHENA was developed by AECL for the safety and licencing analysis of postulated accident conditions in CANDU reactors and for the designs of future CANDU reactors. It has been also used in the design and analysis of the multiple experimental (Multipurpose Applied Physics Lattice Experiment-MAPLE) class of reactors and in the analysis of thermalhydraulic test facilities (e.g. RD-14M) conducted by AECL [40].

CATHARE uses a fully implicit formulation [120] and solves by a Newton-Raphson iterative method in one-dimensional geometry. As in CATHENA, CATHARE uses donor formulations for the mass and energy flux terms to enhance stability and is based on a staggered difference mesh.

Recently, Stadtke et al. [121] have undertaken an EU shared-cost action

11

"ASTAR Project". They have been developing characteristic-based upwind differencing numerical methods and their application to transient two-phase flow using a single-pressure two-fluid model.

Nuclear Reactor Division of CEA developed TRIO-U Code [69] which is 3-dimensional thermal-hydraulic tool to simulate two-phase flow based on finite volume formulation.

CFX, FLUENT and PHOENICS codes can also be given as examples to other commercial multiphase codes.

1.4   Dissertation Outline

In Chapter 1, the background and motivation of the present work is given. Also a relevant literature survey on numerical models of two-phase flows is presented.

The general two-fluid model differential equations that form the basis for the hydrodynamic model of the header and assumptions are presented in Chapter 2.

The development of a convenient form of the differential equations that is used as the basis for the numerical solution scheme is presented in Chapter 3. The semi-implicit finite difference equations, together with a discussion of the solution procedure are also given in Chapter 3.

Chapter 4 gives an overview of the structure and important features of the computer code that was developed to solve the two-fluid model of the header.

Chapter 5 provides the definition of the three benchmark problems selected to validate the solution algorithm. The results of the computer code's simulation is given.

Chapter 6 gives detailed information about the experimental facility employing a scaled RD-14M inlet header with attached feeders established in METU-TPFTF.

Comparison of the experimental results with the calculated results is given in Chapter 7.

Chapter 8 presents the conclusions of the thesis study and gives the recommendations for the future works.

CHAPTER 2

THREE DIMENSIONAL TWO-FLUID MODEL

In this chapter, general forms of three-dimensional conservation equations of the two-fluid model in cylindrical coordinates with corresponding closure and constitutive relations are presented.

2.1 Introduction

Two-fluid model treats each "phase" as a separate "continuum". Separate treatment of the two phases and detailed considerations of phase interactions allow the two-fluid model describe the two-phase flow system more accurately among available models.

This approach can be applied to liquid, gas and solid phases. Each point in the flow domain is occupied simultaneously in variable proportions by both phases. Separate sets of partial differential equations expressing the mass, momentum and energy conservation equations are described for each phase. Since each fluid is treated separately, the two-fluid model handles multiple velocities due to the existence of the relative motion of one phase with respect to the other in the same spatial location at the same time.

14

Two-fluid model relies on averaging procedure of the single-phase equations. In the literature, there are several types of averaging. These are time averaging [58, 73], volume averaging [73]. Therefore, two-fluid model can provide information only on the average flow behaviour [82]. It is simply assumed that the phases are dispersed enough over a control volume that assuming average properties would be accurate. Thus the method used in this study assumes volume averaged values. However, all the averaging procedures yields averaged equations which formally have the same structure. Therefore, conservation equations used in the computational fluid dynamics literature is more or less the same, regardless of what averaging technique is used [30].

Averaging leads to the appearance of a new variable, "volume fraction", θ_q, defined as the proportion of volume occupied at each point by a given phase of q, to characterise each phase [82, 35].

Since the phases are separated by interfaces, the averaging also results in additional terms which couple the transport of mass, momentum and energy across the interface [59]. Because, information at the interface separating the two phases is lost during such averaging processes [120].

As a starting point of the present work, the "traditional" forms of the conservation equations describing the two-phase flow will be given in the following section.

2.2   General Two-Fluid Model

The two-fluid system is presented here in its most general form. The general objective of the two-fluid system is to determine unknown velocities, volume fractions and temperatures of each phase as well as the pressure. A set of partial differential equations can be written which represent the conservation of mass, momentum, and energy for each phase. The equations are coupled through the terms expressing the interfacial transfer of mass, momentum and

energy.

First of all, continuity equation for each phase q (q=l or g representing liquid and gas phases respectively) can be written as [60, 59, 121, 78],

$$\frac{\partial(\theta_q \rho_q)}{\partial t} + \nabla \cdot (\theta_q \rho_q \vec{u_q}) = \Gamma_q \qquad (2.1)$$

where ρ_q, θ_q and $\vec{u_q}$ are the density, volume fraction and velocity of phase q respectively, while Γ_q is the volumetric mass transfer rate due to phase change (condensation,evaporation) of phase q. Here, unlike single phase flow, two-phase continuity equations have this source term, Γ_q, that accounts for interphase mass transfer due to phase change.

Summation over both phases leads to the overall continuity equation:

$$\sum_{q=1}^{2} \left(\frac{\partial(\theta_q \rho_q)}{\partial t} + \nabla \cdot (\theta_q \rho_q \vec{u_q}) \right) = 0 \qquad (2.2)$$

The right hand side of the above equation is equal to zero signifying that there is no net creation or destruction of mass. Therefore, the gas generation term is the negative of the liquid generation, that is, $\Gamma_g = -\Gamma_l$, [83, 54, 121].

Momentum equation for phase q can be written as [110, 78, 23, 34]:

$$\frac{\partial}{\partial t}(\theta_q \rho_q \vec{u_q}) + [\nabla \cdot (\theta_q \rho_q \vec{u_q} \vec{u_q})] = \nabla \cdot (\theta_q \tau_q) + \theta_q \rho_q \vec{g} - (\theta_q \nabla P_q)$$
$$+ M_{qi} + \Gamma_q \vec{u_{qi}} \qquad (2.3)$$

where i represents the value at the interface.

The first term (transient term) on the left in the above equation represents the net rate of momentum increase in the volume, while the second term (convection term) on the left represents the net rate of convection of momentum into the volume. The first term (viscous stress term) on the right

represents the transport of momentum from the viscosity, while the second term (gravity term) represents body force acting on the volume. Third term (pressure gradient term) on the right represents the pressure force acting on the volume. Fourth term (drag term) represents the momentum transfer between the two phases [123, 116]. The last term, $\Gamma_q \vec{u}_{qi}$, represents the momentum gained or lost between the phases due to interfacial mass transfer.

Energy equation for phase q can be written in simplified form by Ishii and Mishima [60] as;

$$
\begin{aligned}
\frac{\partial}{\partial t}(\theta_q \rho_q H_q) + [\nabla \cdot (\theta_q \rho_q H_q \vec{u}_q)] &= -\nabla \cdot \theta_q(q_q + q_q{}^T) + \theta_q \frac{D_q}{Dt} P_q \\
&+ H_{qi}\Gamma_q + q''{}_{qi}/L_s + \Phi_q
\end{aligned} \tag{2.4}
$$

Here $H_q, q_q, q_q{}^T, H_{qi}, q''{}_{qi}, \Phi_q, L_s$ are the specific enthalpy of phase q, laminar heat flux, turbulent heat flux, the specific enthalpy of phase q evaluated at the interface, the interfacial heat flux, dissipation and the lenght scale at the interface, respectively [60, 82]. Left hand side represents the convective terms and the first term on the right hand side is the rates of heat diffusion, second term is the rate of work of compression, and the last term is the rate of viscous dissipation.

2.3 Modeling Assumptions

In their most general forms, as shown in Equations 2.1, 2.3 and 2.4, the conservation equations apply to a wide variety of fluid flow and heat transfer situations. However, these equations could be reduced to several forms of simpler models as can be found in the literature by making certain assumptions to limit them to the problem of particular interest.

In this section, such kind of modelling assumptions are discussed, and then the final set of governing equations with all assumptions applied is given.

Considering a viscous flow occupying a domain, two-phase flows are described by some variables, i.e., void fraction θ, pressure P, liquid and gas phase velocities $\vec{u_l}$ and $\vec{u_g}$. To simulate the horizontal drum in the experimental facility used for the present study, following assumptions are made due to system properties and limitations;

- The flow is modeled as three-dimensional unsteady flow.

- Both phases are treated as Newtonian fluids.

- Viscosity of each phase is assumed to be constant at average temperature of $22\,°C$.

- The velocities of the phases are not equal.

Also,

- The header wall is adiabatic.

- The system is isothermal, therefore phases are at thermal equilibrium.

Therefore, the flow is taken as incompressible, that is, the density of each phase (air, water) assumed to be constant [39, 72, 71]. Also,

- Since there is no change of phase (evaporation or condensation) in the system, the mass transfer between liquid and gas phases does not exist. Therefore, interfacial mass transfer term, $\Gamma_q(\Gamma_g$ and $\Gamma_l)$ in Equations 2.1, 2.3 and 2.4 is taken as zero.

- The phasic pressures are assumed all equal ("single pressure approximation"). This assumption is a common modeling basis because of the local equilibrium between the two fields [3, 42, 70].

Considering the incompressibility, the phasic continuity equation 2.1 reduces to conservation of volume [16, 131, 117, 119];

$$\frac{\partial(\theta_q)}{\partial t} + \nabla \cdot (\theta_q \vec{u}_q) = 0 \tag{2.5}$$

With applying these assumptions, incompressibility (ρ_q=constant) and single pressure field for both phases ($P_q = P$), momentum equation 2.3 reduces to [16, 131, 117, 119],

$$\frac{\partial}{\partial t}(\theta_q \vec{u}_q) + [\nabla \cdot (\theta_q \vec{u}_q \vec{u}_q)] = \frac{\nabla \cdot (\theta_q \tau_q)}{\rho_q} + \theta_q \vec{g} - \frac{(\theta_q \nabla P)}{\rho_q} + \frac{M_{qi}}{\rho_q} \tag{2.6}$$

However, due to isothermal and adiabatic flow assumptions, it is not needed to consider the energy equation 2.4 in solving the system of equations in this study [84, 32, 84].

2.4 Three-Dimensional Conservation Equations

The equations expressing the balance of mass and momentum required for the description of the two-phase flow in the header are presented in this section for three-dimensional cylindrical coordinates appropriate to the geometric properties of the header.

The dependent variables to be computed are the velocity and the volume fractions of each phase and the pressure. The independent variables are time(t) and distance (r, ϕ, z for cylindrical geometry).

Since, the velocity vector is $\vec{u} = U\vec{i} + V\vec{j} + W\vec{k}$ where $\vec{i}, \vec{j}$ and $\vec{k}$ are unit vectors and U, V and W are the velocity components in r, z and ϕ directions, respectively, one can have three momentum equations for each phase (totally six equations) and two continuity equations. An equation for the gas and liquid volumetric fractions ($\theta_g + \theta_l = 1$) are needed to represent the adiabatic two-phase (air/water) flow concerned in this study.

The governing equations in their explicit forms are as follows:

2.4.1 Conservation Of Mass

Continuity equation for the gas phase is [111, 10, 23],

$$\frac{\partial \theta_g}{\partial t} + \nabla \cdot (\theta_g \vec{u}_g) = 0 \qquad (2.7)$$

and that for the liquid phase is [111, 10, 23],

$$\frac{\partial \theta_l}{\partial t} + \nabla \cdot (\theta_l \vec{u}_l) = 0 \qquad (2.8)$$

Here, the volume fractions (θ_g, θ_l) are defined as the fraction of a control volume occupied by a given phase.

2.4.2 Conservation Of Momentum

The time-dependent, three dimensional phasic (q=g,l) momentum equations are given as follows [111, 10, 23],

in r-direction;

$$\begin{aligned}
\frac{\partial}{\partial t}(\theta_g U_g) &= -[\nabla \cdot (\theta_g \vec{u}_g U_g)] + \frac{1}{\rho_g}\nabla \cdot (\theta_g \tau_g) + \theta_g \vec{g}_r - \frac{1}{\rho_g}(\theta_g \nabla P) \\
&\quad + \frac{K}{\rho_g}(U_l - U_g) \qquad (2.9)
\end{aligned}$$

$$\begin{aligned}
\frac{\partial}{\partial t}(\theta_l U_l) &= -[\nabla \cdot (\theta_l \vec{u}_l U_l)] + \frac{1}{\rho_l}\nabla \cdot (\theta_l \tau_l) + \theta_l \vec{g}_r - \frac{1}{\rho_l}(\theta_l \nabla P) \\
&\quad + \frac{K}{\rho_l}(U_g - U_l) \qquad (2.10)
\end{aligned}$$

in z-direction;

$$\begin{aligned}
\frac{\partial}{\partial t}(\theta_g V_g) &= -[\nabla \cdot (\theta_g \vec{u}_g V_g)] + \frac{1}{\rho_g}\nabla \cdot (\theta_g \tau_g) + \theta_g \vec{g}_z - \frac{1}{\rho_g}(\theta_g \nabla P) \\
&\quad + \frac{K}{\rho_g}(V_l - V_g) \qquad (2.11)
\end{aligned}$$

$$\begin{aligned}
\frac{\partial}{\partial t}(\theta_l V_l) &= -[\nabla \cdot (\theta_l \vec{u}_l V_l)] + \frac{1}{\rho_l}\nabla \cdot (\theta_l \tau_l) + \theta_l \vec{g}_z - \frac{1}{\rho_l}(\theta_l \nabla P) \\
&\quad + \frac{K}{\rho_l}(V_g - V_l) \qquad (2.12)
\end{aligned}$$

while in ϕ direction;

$$\frac{\partial}{\partial t}(\theta_g W_g) = -[\nabla \cdot (\theta_g \vec{u}_g W_g)] + \frac{1}{\rho_g}\nabla \cdot (\theta_g \tau_g) + \theta_g \vec{g}_\phi - \frac{1}{\rho_g}(\theta_g \nabla P)$$
$$+\frac{K}{\rho_g}(W_l - W_g) \tag{2.13}$$

$$\frac{\partial}{\partial t}(\theta_l W_l) = -[\nabla \cdot (\theta_l \vec{u}_l W_l)] + \frac{1}{\rho_l}\nabla \cdot (\theta_l \tau_l) + \theta_l \vec{g}_\phi - \frac{1}{\rho_l}(\theta_l \nabla P)$$
$$+\frac{K}{\rho_l}(W_g - W_l) \tag{2.14}$$

Last terms in the above equations represent the interfacial force (M_{qi}) exerted by the other phase on the one under consideration. It is modelled by use of a drag function (K) multiplying the relative phase velocity $(\vec{u}_g - \vec{u}_l)$ for liquid phase equations and $(\vec{u}_l - \vec{u}_g)$ for gas phase equations [38].

For a Newtonian fluid, viscous stress tensors has the following form;

$$\tau_{qrr} = \mu_q\left\{2\frac{\partial U_q}{\partial r} - \frac{2}{3}(\frac{1}{r}\frac{\partial rU_q}{\partial r} + \frac{1}{r}\frac{\partial W_q}{\partial \phi} + \frac{\partial V_q}{\partial z})\right\} \tag{2.15}$$

$$\tau_{qr\phi} = \mu_q\left\{r\frac{\partial}{\partial r}(\frac{W_q}{r}) + \frac{1}{r}\frac{\partial U_q}{\partial \phi}\right\} \tag{2.16}$$

$$\tau_{q\phi\phi} = \mu_q\left\{2(\frac{1}{r}\frac{\partial W_q}{\partial \phi} + \frac{U_q}{r}) - \frac{2}{3}\{\frac{1}{r}\frac{\partial(rU_q)}{\partial r} + \frac{1}{r}\frac{\partial W_q}{\partial \phi} + \frac{\partial V_q}{\partial z}\}\right\} \tag{2.17}$$

$$\tau_{q\phi z} = \mu_q\left\{\frac{1}{r}\frac{\partial V_q}{\partial \phi} + \frac{\partial W_q}{\partial z}\right\} \tag{2.18}$$

$$(\tau_{qzz}) = \mu_q\left\{2(\frac{\partial V_q}{\partial z}) - \frac{2}{3}\{\frac{1}{r}\frac{\partial(rU_q)}{\partial r} + \frac{1}{r}\frac{\partial W_q}{\partial \phi} + \frac{V_q}{\partial z}\}\right\} \tag{2.19}$$

$$(\tau_{qrz}) = \mu_q\left\{\frac{\partial U_q}{\partial z} + \frac{\partial V_q}{\partial r}\right\} \tag{2.20}$$

21

here μ_q is the fluid dynamic viscosities [9].

The resulting equations (equations 2.7 through 2.14) are not closed. There are 9 unknown variables which are $P, \theta_g, \theta_l, U_g, U_l, V_g, V_l, W_g, W_l$ while having 8 equations. Since such a system contains more unknowns than equations, some additional relations must be specified.

In the following section, the closure and constitutive relations that are necessary to form a closed set of equations are discussed.

2.4.3   Closure Relations

For incompressible multi-phase flow, the closure relation include the geometric conservation equation which means that the volume fractions must sum up to unity [91]. Dinh et al. [19] and Oliveira and Issa [99] define this equation as the "compatibility equation".

$$\sum_{n=1}^{N} \theta_n = 1 \tag{2.21}$$

where N is the total number of phases. Since in the present case, there are two phases (gas and liquid) altogether following equation

$$\theta_g + \theta_l = 1 \tag{2.22}$$

must be satisfied.

With the assumption of incompressibility, the equations of state are also trivially reduced into constant values of phase densities ρ_g and ρ_l [19, 96].

2.4.4   Constitutive Relations

Although two-fluid model does not treat interface, the effects of interface behaviour on the flow are taken into account by emprical relations. Completion

22

of the analysis requires "constitutive" relations that describe these interactions. However, as pointed out by many authors [60, 120, 11], the weakest link in the multifluid model formulation is the constitutive equations which are deduced from experiments. The number of these constitutive relationships is really large and complex.

Constitutive relations generally include the state-of-the-art physical models for the flow regime modelling, interfacial energy and mass transfer, interfacial forces, wall momentum exchange, wall heat transfer and thermodynamic and transport properties of the fluids [115].

Although the exact expressions for the transfer terms are usually uncertain and still questions of debate, for the two-fluid model to be reliable, the interfacial interaction terms must be accurate [59, 94]. It is generally agreed that much more detailed experimental information are necessary to develop models and reliable relations [13, 60, 6].

In this work, is is considered only the interfacial momentum transfer by including the drag force terms, K, in the momentum equations which arise because of the relative motion between the phases [39]. Several models have been developed for the interfacial momentum transfer terms. In general, the drag function K depends on the flow regime, void fraction, gas and liquid densities, Reynolds number and phase velocities. The following form which is commonly used in the literature to model the interphase drag force acting on phase α due to phase β is inserted into the momentum equations instead of M_{qi} notation.

$$M_{qi} = K_{\alpha\beta}(U_\beta - U_\alpha) \qquad (2.23)$$

As a summary, a two-fluid model consists of conservation equations, closure and constitutive relations. Naturally, initial and boundary conditions are also needed to solve them.

CHAPTER 3

NUMERICAL SOLUTION OF TWO-FLUID MODEL

In order to solve the governing nonlinear equations described in Chapter 2, the finite difference method is used in this study. As a solution algorithm Implicit MultiField (IMF) which is classified as a point relaxation technique by Rivard and Torrey [110] and Broadus et al. [10], is selected to solve the resulting finite difference equations.

In this chapter, finite difference form of the governing equations and their numerical solution technique are presented which are based on the work of Rivard and Torrey [110].

3.1   Numerical Algorithm

The two-fluid equations are discretised by finite difference technique and are solved by using the principles of IMF (Implicit Multifield) algorithm as applied in the K-FIX code [110]. IMF method, which is an extention of the Implicit Continuous-fluid Eulerian (ICE) technique developed for single-phase flows [110, 2, 16], was developed by Harlow and Amsden [41], and was implemented in the K-FIX code [110]. Rivard and Torrey later extended this

method to perform three dimensional calculations [112].

IMF method is based on the finite difference approximations to the mass, momentum and energy equations. However, due to the restrictive assumptions made in this study, 2-continuity (2.7 and 2.8)and 6-momentum equations (2.9 through 2.14) are to be solved along with the required constitutive relations in space and time for 3-dimensional cylindrical coordinates.

The main features of IMF Method can be summarised as follows:

- It is a semi-implicit finite difference method based on a staggered grid. That is, scalar variables such as volume fractions and pressure are cell-centered quantities, whereas velocities are cell-edge quantities located on the sides of the cells.

- Implicitness is used for the velocity in the mass convection terms, for the pressure gradient and interface mass and momentum exchange terms.

- Convective terms are discretised by a donor-cell differencing(first-order upwind scheme).

Several codes based on this method have been developed for different investigations. Among them, KACHINA [3] was the first one which has a solution capability in axisymmetric two-dimensional geometry. Later on, K-FIX was developed by Rivard and Torrey [110]. It is a three-dimensional code capable of simulating in cartezian, cylindrical and spherical geometries and treats mass, momentum and energy exchange terms between two-phases in fully implicit way.

Amsden and Harlow developed a two-dimensional K-TIF code [4] for numerical solution of the transient dynamics of steam and water in a pressurized water reactor downcomer.

BEACON/MOD3 code was also developed by Broadus et al. [10] whose solution algorithm is about the same as that of K-FIX. It is a contain-

ment analysis code used to predict environmental conditions under short-term transients within Pressurised Water Reactor (PWR) dry containment systems. However, it can simulate transient, one or two-dimensional, two-phase(gas-liquid) flow.

In 2002, FLUFIX/MOD2 code was developed by using IMF technique settled in K-FIX code. This code solves the conservation equations in two-dimensional cartesian and axisymmetric cylindrical coordinates for isothermal fluid-solids hydrodynamics and finds an application area in simulations of fluidized bed combustors [84].

MFIX code by Syamlal et al. [122, 124] was also developed based on the same technique implemented in the K-FIX code, however to describe chemical reactions and heat transfer in dense or dilute fluid-solids flows in three dimensional cartesian or cylindrical geometries and used in simulations of energy conversion and chemical systems.

Gomez et al. [36] used MULTIFIX code which is defined as an extention of the K-FIX code. They used MULTIFIX in simulating gas-solid two-phase flow in the riser of the circulating fluidized beds.

There are also some works in the literature which uses IMF technique and/or K-FIX code as a numerical solution algorithm in their studies as follows;

Lee [78] developed a stable semi-implicit numerical scheme for solving nonequilibrium two-phase flow problems. Lee used IMF technique to solve governing two-dimensional two-fluid equations in cylindrical coordinates. He simulated two-phase jet impinged on vertical plate in his work.

Lee and Shah [81] developed a computer program TWOP to obtain numcerical solutions of three-dimensional, transient two-phase flow system by employing IMF technique and applied it to high pressure jet impingement and separation of steam and water problems.

Huilin et al. [53] used K-FIX code in simulating bubble behaviour in a two-dimensional bubbling fluidized bed by implementing the granular kinetic

theory and the granular equations into this code.

Davidson [16] analysed isothermal two-phase flow resulting from bottom gas injection into an axisymmetric liquid bath by using K-FIX code after adapting it to include some extra equations (e.g. virtual mass, particle lift). The predicted steady void fraction and gas velocity distributions were compared with the experimental results. He assumed both phases are incompressible and no phase change occurance.

Lee and Lyczkowski [80] studied 5 different two-phase flow equation sets which are all solved by using the same finite differencing technique (IMF), numerical scheme, and computer code structure. It was realized that almost the same results could be obtained from all these models. They also presented more stable numerical scheme to solve those equation sets in their paper.

Hong et al. [50] solved the problem of inclined jet penetration lenght in a gas-solid fluidized bed by using IMF method and compared the numerical results with experimental data.

3.2   Finite Difference Formulation

In this section, Equations 2.7 through 2.14 will be written in finite difference forms in three-dimensional (3-D) cylindrical geometry for the quantities for their numerical solution at time $t = (n+1)\delta t$. There are eight (two mass, six momentum) differential equations and one closure relation (Equation 2.22) for the nine dependent variables; the volume fractions, θ_g, θ_l; the pressure, P; the gas velocity components U_g, V_g, W_g and the liquid velocity components U_l, V_l, W_l in the r, z and ϕ directions, respectively. The details about discretization strategy can be found in the following sections.

3.2.1 Control Volume Discretization Method in Cylindrical Coordinates

Conservation equations have been discretized for a staggered grid, widely used in two-fluid codes, as in the K-FIX scheme by using control volume approach in which mass and momentum being conserved over finite volumes.
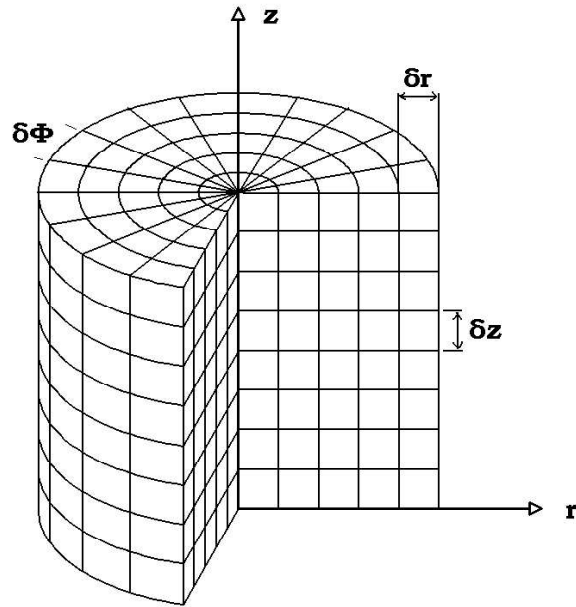
Figure 3.1: Control Volume Discretization

The geometric region of interest is divided into many finite-sized and space fixed (Eulerian mesh) zones in r,z and ϕ directions as shown in Figure 3.1.

Figure 3.2 shows a typical computational unit cell and the relative spatial locations of the variables that appear in the finite difference equations with the cell indices. Computational cells are distinguished along the r-axis by subscript i, along the z-axis by subscript j, and along the ϕ-axis by subscript k. Cell centers are labeled with the indices (i,j,k) while the cell-edge location

28

indices are represented by half integers (i.e. $i + \frac{1}{2}, j + \frac{1}{2}, k + \frac{1}{2}$).
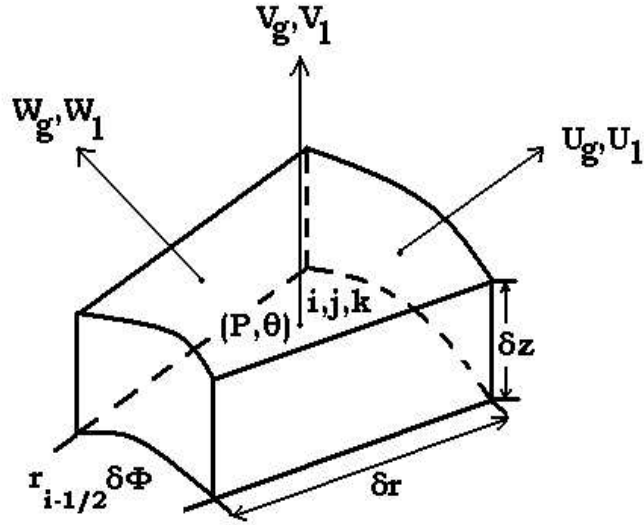
Figure 3.2: Unit Cell Representation in Cylindrical Coordinates

For a given cell, having central coordinates of $(_{i,j,k})$, the vector quantities (velocity components, U_q, V_q, W_q in r, z and ϕ directions respectively) for each phase (q=g,l) are defined at the midpoints of cell faces normal to them, whereas the scalar variables (volume fraction, θ_q, and pressure, P) are defined in the cell center as indicated in Figure 3.2 [42, 10, 110].

This means that the equations for scalar variables (pressure, void fraction) are going to be solved at the cell centers, while the momentum equations for the phasic velocity components are going to be solved at the cell boundaries.

3.2.1.1 Discrete Forms of Continuity Equations

If the basic continuity equations (Equations 2.7 and 2.8) are expanded in three-dimensional cylindrical geometry,

$$\frac{\partial \theta_g}{\partial t} + \frac{1}{r}\frac{\partial}{\partial r}(\theta_g U_g r) + \frac{\partial}{\partial z}(\theta_g V_g) + \frac{1}{r}\frac{\partial}{\partial \phi}(\theta_g W_g) = 0 \qquad (3.1)$$

$$\frac{\partial \theta_l}{\partial t} + \frac{1}{r}\frac{\partial}{\partial r}(\theta_l U_l r) + \frac{\partial}{\partial z}(\theta_l V_l) + \frac{1}{r}\frac{\partial}{\partial \phi}(\theta_l W_l) = 0 \qquad (3.2)$$

are obtained for both phases. They are differenced fully implicitly as follows [4, 110, 32];

$$
\begin{aligned}
(\theta_g)_{i,j,k}^{n+1} &= (\theta_g)_{i,j,k}^{n} + \delta t \left\{ \frac{-<\theta_g{}^{n+1}U_g{}^{n+1}r>_{i,j,k}}{r_i \delta r} - \frac{<\theta_g{}^{n+1}V_g{}^{n+1}>_{i,j,k}}{\delta z} \right. \\
&\left. - \frac{<\theta_g{}^{n+1}W_g{}^{n+1}>_{i,j,k}}{r_i \delta \phi} \right\}
\end{aligned}
\qquad (3.3)
$$

$$
\begin{aligned}
(\theta_l)_{i,j,k}^{n+1} &= (\theta_l)_{i,j,k}^{n} + \delta t \left\{ \frac{-<\theta_l{}^{n+1}U_l{}^{n+1}r>_{i,j,k}}{r_i \delta r} - \frac{<\theta_l{}^{n+1}V_l{}^{n+1}>_{i,j,k}}{\delta z} \right. \\
&\left. - \frac{<\theta_l{}^{n+1}W_l{}^{n+1}>_{i,j,k}}{r_i \delta \phi} \right\}
\end{aligned}
\qquad (3.4)
$$

Here, δt denotes the time step. The superscripts "n" and "n+1" represent the values at the respective time levels t and $t + \delta t$. The cell centers are labeled with the indices (i,j,k).

In the IMF method, convective terms (flux quantities) denoted symbolically by angular brackets $< \theta \vec{u} >$ in the gas continuity equation (Equation 3.3), are expanded by using upwinding (donor-cell differencing) scheme, i.e. the gradients are calculated using upstream values [110, 3, 32]. For instance;

$$
\begin{aligned}
<\theta_g U_g r>_{i,j,k} &= U_{g\,i+\frac{1}{2},j,k} r_{i+\frac{1}{2}} \begin{cases} \theta_{g\,i,j,k} & \text{if } U_{g\,i+\frac{1}{2},j,k} \geq 0 \\ \theta_{g\,i+1,j,k} & \text{if } U_{g\,i+\frac{1}{2},j,k} < 0 \end{cases} \\
&- U_{g\,i-\frac{1}{2},j,k} r_{i-\frac{1}{2}} \begin{cases} \theta_{g\,i-1,j,k} & \text{if } U_{g\,i-\frac{1}{2},j,k} \geq 0 \\ \theta_{g\,i,j,k} & \text{if } U_{g\,i-\frac{1}{2},j,k} < 0 \end{cases}
\end{aligned}
\qquad (3.5)
$$

$$< \theta_g V_g >_{i,j,k} \;\; = \;\; V_{g\,i,j+\frac{1}{2},k} \begin{cases} \theta_{g\,i,j,k} & \text{if} \;\; V_{g\,i,j+\frac{1}{2},k} \geq 0 \\ \theta_{g\,i,j+1,k} & \text{if} \;\; V_{g\,i,j+\frac{1}{2},k} < 0 \end{cases}$$

$$-V_{g\,i,j-\frac{1}{2},k} \begin{cases} \theta_{g\,i,j-1,k} & \text{if} \;\; V_{g\,i,j-\frac{1}{2},k} \geq 0 \\ \theta_{g\,i,j,k} & \text{if} \;\; V_{g\,i,j-\frac{1}{2},k} < 0 \end{cases} \qquad (3.6)$$

$$< \theta_g W_g >_{i,j,k} \;\; = \;\; W_{g\,i,j,k+\frac{1}{2}} \begin{cases} \theta_{g\,i,j,k} & \text{if} \;\; W_{g\,i,j,k+\frac{1}{2}} \geq 0 \\ \theta_{g\,i,j,k+1} & \text{if} \;\; W_{g\,i,j,k+\frac{1}{2}} < 0 \end{cases}$$

$$-W_{g\,i,j,k-\frac{1}{2}} \begin{cases} \theta_{g\,i,j,k-1} & \text{if} \;\; W_{g\,i,j,k-\frac{1}{2}} \geq 0 \\ \theta_{g\,i,j,k} & \text{if} \;\; W_{g\,i,j,k-\frac{1}{2}} < 0 \end{cases} \qquad (3.7)$$

The upwind scheme applied to liquid phase continuity equation (Equation 3.4) is defined similarly and is presented in Appendix A.1.

3.2.1.2 Discrete Forms of Momentum Equations

The momentum equations are differenced over a staggered mesh of computational cells semi-implicitly as suggested in K-FIX code [110].

Writing the gas phase momentum equations (2.9, 2.11 and 2.13) in a more open form gives;

$$\frac{\partial(\theta_g U_g)}{\partial t} \;\; = \;\; -\nabla \cdot (\theta_g \vec{u}_g U_g) + \frac{1}{\rho_g}\left(\frac{1}{r}\frac{\partial}{\partial r}(\theta_g r \tau_{g\,rr}) + \frac{1}{r}\frac{\partial}{\partial \phi}(\theta_g \tau_{g\,r\phi}) - \frac{\tau_{g\,\phi\phi}}{r} \right.$$
$$\left. +\frac{\partial}{\partial z}(\theta_g \tau_{g\,rz}) \right) + \theta_g \vec{g}_r - \frac{\theta_g}{\rho_g}\frac{\partial P}{\partial r} + \frac{K}{\rho_g}(U_l - U_g) \qquad (3.8)$$

$$\frac{\partial(\theta_g V_g)}{\partial t} \;\; = \;\; -\nabla \cdot (\theta_g \vec{u}_g V_g) + \frac{1}{\rho_g}\left(\frac{1}{r}\frac{\partial}{\partial r}(\theta_g r \tau_{g\,rz}) + \frac{1}{r}\frac{\partial}{\partial \phi}(\theta_g \tau_{g\,\phi z}) \right.$$
$$\left. +\frac{\partial}{\partial z}(\theta_g \tau_{g\,zz}) \right) + \theta_g \vec{g}_z - \frac{\theta_g}{\rho_g}\frac{\partial P}{\partial z} + \frac{K}{\rho_g}(V_l - V_g) \qquad (3.9)$$

$$\frac{\partial(\theta_g W_g)}{\partial t} = -\nabla \cdot (\theta_g \vec{u}_g W_g) + \frac{1}{\rho_g}\left(\frac{1}{r^2}\frac{\partial}{\partial r}(\theta_g r^2 \tau_{gr\phi}) + \frac{1}{r}\frac{\partial}{\partial \phi}(\theta_g \tau_{g\phi\phi})\right.$$

$$\left. +\frac{\partial}{\partial z}(\theta_g \tau_{g\phi z})\right) + \theta_g \vec{g}_\phi - \frac{1}{r}\frac{\theta_g}{\rho_g}\frac{\partial P}{\partial \phi} + \frac{K}{\rho_g}(W_l - W_g) \quad (3.10)$$

These equations (3.8, 3.9 and 3.10) after a time discretization according to the IMF method, can be expressed semi-implicitly as follows [4, 32, 110, 42],

$$(\theta_g U_g)^{n+1}_{i+\frac{1}{2},j,k} = \overline{(\theta_g U_g)}^{n}_{i+\frac{1}{2},j,k} + \delta t\left\{ -\frac{\theta_{g}{}^{n+1}_{i+\frac{1}{2},j,k}(P^{n+1}_{i+1,j,k} - P^{n+1}_{i,j,k})}{\rho_g \delta r}\right.$$

$$\left. +\frac{K^n_{i+\frac{1}{2},j,k}(U_{l}{}^{n+1}_{i+\frac{1}{2},j,k} - U_{g}{}^{n+1}_{i+\frac{1}{2},j,k})}{\rho_g}\right\} \quad (3.11)$$

$$(\theta_g V_g)^{n+1}_{i,j+\frac{1}{2},k} = \overline{(\theta_g V_g)}^{n}_{i,j+\frac{1}{2},k} + \delta t\left\{ -\frac{\theta_{g}{}^{n+1}_{i,j+\frac{1}{2},k}(P^{n+1}_{i,j+1,k} - P^{n+1}_{i,j,k})}{\rho_g \delta z}\right.$$

$$\left. +\frac{K^n_{i,j+\frac{1}{2},k}(V_{l}{}^{n+1}_{i,j+\frac{1}{2},k} - V_{g}{}^{n+1}_{i,j+\frac{1}{2},k})}{\rho_g}\right\} \quad (3.12)$$

$$(\theta_g W_g)^{n+1}_{i,j,k+\frac{1}{2}} = \overline{(\theta_g W_g)}^{n}_{i,j,k+\frac{1}{2}} + \delta t\left\{ -\frac{\theta_{g}{}^{n+1}_{i,j,k+\frac{1}{2}}(P^{n+1}_{i,j,k+1} - P^{n+1}_{i,j,k})}{\rho_g r_i \delta \phi}\right.$$

$$\left. +\frac{K^n_{i,j,k+\frac{1}{2}}(W_{l}{}^{n+1}_{i,j,k+\frac{1}{2}} - W_{g}{}^{n+1}_{i,j,k+\frac{1}{2}})}{\rho_g}\right\} \quad (3.13)$$

Writing similar equations for the liquid phase results;

$$\frac{\partial(\theta_l U_l)}{\partial t} = -\nabla \cdot (\theta_l \vec{u}_l U_l) + \frac{1}{\rho_l}\left(\frac{1}{r}\frac{\partial}{\partial r}(\theta_l r \tau_{lrr}) + \frac{1}{r}\frac{\partial}{\partial \phi}(\theta_l \tau_{lr\phi}) - \frac{\theta_l \tau_{l\phi\phi}}{r}\right.$$

$$\left. +\frac{\partial}{\partial z}(\theta_l \tau_{lrz})\right) + \theta_l \vec{g}_r - \frac{\theta_l}{\rho_l}\frac{\partial P}{\partial r} + \frac{K}{\rho_l}(U_g - U_l) \quad (3.14)$$

32

$$\frac{\partial(\theta_l V_l)}{\partial t} = -\nabla \cdot (\theta_l \vec{u}_l V_l) + \frac{1}{\rho_l}\left(\frac{1}{r}\frac{\partial}{\partial r}(\theta_l r \tau_{lrz}) - \frac{1}{r}\frac{\partial}{\partial \phi}(\theta_l \tau_{l\phi z})\right.$$

$$\left. -\frac{\partial}{\partial z}(\theta_l \tau_{lzz})\right) + \theta_l \vec{g}_z - \frac{\theta_l}{\rho_l}\frac{\partial P}{\partial z} + \frac{K}{\rho_l}(V_g - V_l) \qquad (3.15)$$

$$\frac{\partial(\theta_l W_l)}{\partial t} = -\nabla \cdot (\theta_l \vec{u}_l W_l) + \frac{1}{\rho_l}\left(\frac{1}{r^2}\frac{\partial}{\partial r}(\theta_l r^2 \tau_{lr\phi}) + \frac{1}{r}\frac{\partial}{\partial \phi}(\theta_l \tau_{l\phi\phi})\right.$$

$$\left. +\frac{\partial}{\partial z}(\theta_l \tau_{l\phi z})\right) + \theta_l \vec{g}_\phi - \frac{1}{r}\frac{\theta_l}{\rho_l}\frac{\partial P}{\partial \phi} + \frac{K}{\rho_l}(W_g - W_l) \qquad (3.16)$$

discretising those liquid phase equations similarly gives the following equations [4, 42, 110];

$$(\theta_l U_l)^{n+1}_{i+\frac{1}{2},j,k} = \overline{(\theta_l U_l)}^{n}_{i+\frac{1}{2},j,k} + \delta t\left\{ -\frac{\theta_{l\,i+\frac{1}{2},j,k}^{n+1}(P^{n+1}_{i+1,j,k} - P^{n+1}_{i,j,k})}{\rho_l \delta r} \right.$$

$$\left. +\frac{K^{n}_{i+\frac{1}{2},j,k}(U_{g\,i+\frac{1}{2},j,k}^{n+1} - U_{l\,i+\frac{1}{2},j,k}^{n+1})}{\rho_l}\right\} \qquad (3.17)$$

$$(\theta_l V_l)^{n+1}_{i,j+\frac{1}{2},k} = \overline{(\theta_l V_l)}^{n}_{i,j+\frac{1}{2},k} + \delta t\left\{ -\frac{\theta_{l\,i,j+\frac{1}{2},k}^{n+1}(P^{n+1}_{i,j+1,k} - P^{n+1}_{i,j,k})}{\rho_l \delta z} \right.$$

$$\left. +\frac{K^{n}_{i,j+\frac{1}{2},k}(V_{g\,i,j+\frac{1}{2},k}^{n+1} - V_{l\,i,j+\frac{1}{2},k}^{n+1})}{\rho_l}\right\} \qquad (3.18)$$

$$(\theta_l W_l)^{n+1}_{i,j,k+\frac{1}{2}} = \overline{(\theta_l W_l)}^{n}_{i,j,k+\frac{1}{2}} + \delta t\left\{ -\frac{\theta_{l\,i,j,k+\frac{1}{2}}^{n+1}(P^{n+1}_{i,j,k+1} - P^{n+1}_{i,j,k})}{\rho_l r_i \delta \phi} \right.$$

$$\left. +\frac{K^{n}_{i,j,k+\frac{1}{2}}(W_{g\,i,j,k+\frac{1}{2}}^{n+1} - W_{l\,i,j,k+\frac{1}{2}}^{n+1})}{\rho_l}\right\} \qquad (3.19)$$

As can be easily seen in the momentum equations above that pressure gradient term and the interface momentum exchange (drag terms) are implicitly discretized [114, 32, 36, 124]. Also note that interfacial drag force

terms are linearly implicit in the velocities which provides a coupling between the phases [32, 23].

Here, the terms that do not directly proportional to the velocity difference between the two phases or to the pressure gradient are grouped into one explicit term denoted by a superscript overline [38, 42]. That approach provides a faster computation [114]. These overlined quantities account for the effects of momentum convection, gravity and viscous stress through the following relations [4, 10, 32, 42, 110];

$$
\begin{aligned}
\overline{(\theta_g U_g)}_{i+\frac{1}{2},j,k} = (\theta_g U_g)^n_{i+\frac{1}{2},j,k} + \delta t \Bigg\{ & -\frac{< \theta_g^n U_g^n U_g^n r >_{i+\frac{1}{2},j,k}}{r_{i+\frac{1}{2}} \delta r} \\
& -\frac{< \theta_g^n U_g^n V_g^n >_{i+\frac{1}{2},j,k}}{\delta z} - \frac{< \theta_g^n U_g^n W_g^n >_{i+\frac{1}{2},j,k}}{r_{i+\frac{1}{2}} \delta \phi} \\
& +\frac{[\theta_g^n (W_g^n)^2]_{i+\frac{1}{2},j,k}}{r_{i+\frac{1}{2}}} + \frac{[r_{i+1} \theta_{g\,i+1,j,k}^n \tau_{grr\,i+1,j,k}^n - r_i \theta_{g\,i,j,k}^n \tau_{grr\,i,j,k}^n]}{\rho_g r_{i+\frac{1}{2}} \delta r} \\
& +\frac{[\theta_{g\,i+\frac{1}{2},j,k+\frac{1}{2}}^n \tau_{gr\phi\,i+\frac{1}{2},j,k+\frac{1}{2}}^n - \theta_{g\,i+\frac{1}{2},j,k-\frac{1}{2}}^n \tau_{gr\phi\,i+\frac{1}{2},j,k-\frac{1}{2}}^n]}{\rho_g r_{i+\frac{1}{2}} \delta \phi} \\
& +\frac{[\theta_{g\,i+\frac{1}{2},j+\frac{1}{2},k}^n \tau_{grz\,i+\frac{1}{2},j+\frac{1}{2},k}^n - \theta_{g\,i+\frac{1}{2},j-\frac{1}{2},k}^n \tau_{grz\,i+\frac{1}{2},j-\frac{1}{2},k}^n]}{\rho_g \delta z} \\
& -\frac{[\theta_{g\,i+\frac{1}{2},j,k}^n \tau_{g\phi\phi\,i+\frac{1}{2},j,k}^n]}{\rho_g r_{i+\frac{1}{2}}} + \theta_{g\,i+\frac{1}{2},j,k}^n \vec{g}_r \Bigg\}
\end{aligned}
\tag{3.20}
$$

$$
\begin{aligned}
\overline{(\theta_g V_g)}_{i,j+\frac{1}{2},k} = (\theta_g V_g)^n_{i,j+\frac{1}{2},k} + \delta t \Bigg\{ & -\frac{< \theta_g^n V_g^{\,n} U_g^{\,n} r >_{i,j+\frac{1}{2},k}}{r_i \delta r} \\
& -\frac{< \theta_g^n V_g^{\,n} V_g^{\,n} >_{i,j+\frac{1}{2},k}}{\delta z} - \frac{< \theta_g^n V_g^{\,n} W_g^{\,n} >_{i,j+\frac{1}{2},k}}{r_i \delta \phi} \\
& +\frac{[r_{i+\frac{1}{2}} \theta_{g\,i+\frac{1}{2},j+\frac{1}{2},k}^n \tau_{grz\,i+\frac{1}{2},j+\frac{1}{2},k}^n - r_{i-\frac{1}{2}} \theta_{g\,i-\frac{1}{2},j+\frac{1}{2},k}^n \tau_{grz\,i-\frac{1}{2},j+\frac{1}{2},k}^n]}{\rho_g r_i \delta r} \\
& +\frac{[\theta_{g\,i,j+\frac{1}{2},k+\frac{1}{2}}^n \tau_{g\phi z\,i,j+\frac{1}{2},k+\frac{1}{2}}^n - \theta_{g\,i,j+\frac{1}{2},k-\frac{1}{2}}^n \tau_{g\phi z\,i,j+\frac{1}{2},k-\frac{1}{2}}^n]}{\rho_g r_i \delta \phi} \\
& +\frac{[\theta_{g\,i,j+1,k}^n \tau_{gzz\,i,j+1,k}^n - \theta_{g\,i,j,k}^n \tau_{gzz\,i,j,k}^n]}{\rho_g \delta z} + \theta_{g\,i,j+\frac{1}{2},k}^n \vec{g}_z \Bigg\}
\end{aligned}
\tag{3.21}
$$

$$\overline{(\theta_g W_g)}_{i,j,k+\frac{1}{2}} = (\theta_g W_g)^n_{i,j,k+\frac{1}{2}} + \delta t \Bigg\{ -\frac{<\theta_g^n W_g^n U_g^n r>_{i,j,k+\frac{1}{2}}}{r_i \delta r}$$

$$-\frac{<\theta_g^n W_g^n V_g^n>_{i,j,k+\frac{1}{2}}}{\delta z} - \frac{<\theta_g^n W_g^n W_g^n>_{i,j,k+\frac{1}{2}}}{r_i \delta \phi} - \frac{[\theta_g^{\,n} U_g^{\,n} W_g^{\,n}]_{i,j,k+\frac{1}{2}}}{r_i}$$

$$+\frac{[(r^2)^n_{i+\frac{1}{2}}\theta_{g_{i+\frac{1}{2},j,k+\frac{1}{2}}}^n \tau_{gr\phi_{i+\frac{1}{2},j,k+\frac{1}{2}}}^n - (r^2)^n_{i-\frac{1}{2}}\theta_{g_{i-\frac{1}{2},j,k+\frac{1}{2}}}^n \tau_{gr\phi_{i-\frac{1}{2},j,k+\frac{1}{2}}}^n]}{\rho_g r_i^2}$$

$$+\frac{[\theta_{g_{i,j,k+1}}^{\,n}\tau_{g\phi\phi_{i,j,k+1}}^n - \theta_{g_{i,j,k}}^{\,n}\tau_{g\phi\phi_{i,j,k}}^n]}{\rho_g r_i \delta \phi}$$

$$+\frac{[\theta_{g_{i,j+\frac{1}{2},k+\frac{1}{2}}}^{\,n}\tau_{gz\phi_{i,j+\frac{1}{2},k+\frac{1}{2}}}^n - \theta_{g_{i,j-\frac{1}{2},k+\frac{1}{2}}}^{\,n}\tau_{gz\phi_{i,j-\frac{1}{2},k+\frac{1}{2}}}^n]}{\rho_g \delta z}$$

$$+\theta_{g_{i,j,k+\frac{1}{2}}}^{\,n}\vec{g}_\phi \Bigg\} \tag{3.22}$$

$$\overline{(\theta_l U_l)}_{i+\frac{1}{2},j,k} = (\theta_l U_l)^n_{i+\frac{1}{2},j,k} + \delta t \Bigg\{ -\frac{<\theta_l^n U_l^n U_l^n r>_{i+\frac{1}{2},j,k}}{r_{i+\frac{1}{2}} \delta r}$$

$$-\frac{<\theta_l^n U_l^n V_l^n>_{i+\frac{1}{2},j,k}}{\delta z} - \frac{<\theta_l^n U_l^n W_l^n>_{i+\frac{1}{2},j,k}}{r_{i+\frac{1}{2}} \delta \phi}$$

$$+\frac{[\theta_l^n (W_l^n)^2]_{i+\frac{1}{2},j,k}}{r_{i+\frac{1}{2}}} + \frac{[r_{i+1}\theta_{l_{i+1,j,k}}^n \tau_{lrr_{i+1,j,k}}^n - r_i \theta_{l_{i,j,k}}^n \tau_{lrr_{i,j,k}}^n]}{\rho_l r_{i+\frac{1}{2}} \delta r}$$

$$+\frac{[\theta_{l_{i+\frac{1}{2},j,k+\frac{1}{2}}}^n \tau_{lr\phi_{i+\frac{1}{2},j,k+\frac{1}{2}}}^n - \theta_{l_{i+\frac{1}{2},j,k-\frac{1}{2}}}^n \tau_{lr\phi_{i+\frac{1}{2},j,k-\frac{1}{2}}}^n]}{\rho_l r_{i+\frac{1}{2}} \delta \phi}$$

$$+\frac{[\theta_{l_{i+\frac{1}{2},j+\frac{1}{2},k}}^n \tau_{lrz_{i+\frac{1}{2},j+\frac{1}{2},k}}^n - \theta_{l_{i+\frac{1}{2},j-\frac{1}{2},k}}^n \tau_{lrz_{i+\frac{1}{2},j-\frac{1}{2},k}}^n]}{\rho_l \delta z}$$

$$-\frac{[\theta_{l_{i+\frac{1}{2},j,k}}^n \tau_{l\phi\phi_{i+\frac{1}{2},j,k}}^n]}{\rho_l r_{i+\frac{1}{2}}} + \theta_{l_{i+\frac{1}{2},j,k}}^n \vec{g}_r \Bigg\} \tag{3.23}$$

$$\overline{(\theta_l V_l)}_{i,j+\frac{1}{2},k} = (\theta_l V_l)^n_{i,j+\frac{1}{2},k} + \delta t \Bigg\{ -\frac{<\theta_l^n V_l^n U_l^n r>_{i,j+\frac{1}{2},k}}{r_i \delta r}$$

$$-\frac{<\theta_l^n V_l^n V_l^n>_{i,j+\frac{1}{2},k}}{\delta z} - \frac{<\theta_l^n V_l^n W_l^n>_{i,j+\frac{1}{2},k}}{r_i \delta \phi}$$

$$+\frac{[r_{i+\frac{1}{2}}\theta_{l_{i+\frac{1}{2},j+\frac{1}{2},k}}^n \tau_{lrz_{i+\frac{1}{2},j+\frac{1}{2},k}}^n - r_{i-\frac{1}{2}}\theta_{l_{i-\frac{1}{2},j+\frac{1}{2},k}}^n \tau_{lrz_{i-\frac{1}{2},j+\frac{1}{2},k}}^n]}{\rho_l r_i \delta r}$$

$$+\frac{[\theta_{l_{i,j+\frac{1}{2},k+\frac{1}{2}}}^n \tau_{l\phi z_{i,j+\frac{1}{2},k+\frac{1}{2}}}^n - \theta_{l_{i,j+\frac{1}{2},k-\frac{1}{2}}}^n \tau_{l\phi z_{i,j+\frac{1}{2},k-\frac{1}{2}}}^n]}{\rho_l r_i \delta \phi}$$

$$+\frac{[\theta_{l\,i,j+1,k}^{n}\tau lzz_{i,j+1,k}^{n} - \theta_{l\,i,j,k}^{n}\tau lzz_{i,j,k}^{n}]}{\rho_l \delta z} + \theta_{l\,i,j+\frac{1}{2},k}^{n}\vec{g}_z \Bigg\} \tag{3.24}$$

$$\overline{(\theta_l W_l)}_{i,j,k+\frac{1}{2}} = (\theta_l W_l)_{i,j,k+\frac{1}{2}}^{n} + \delta t \Bigg\{ -\frac{< \theta_l^n W_l^n U_l^n r >_{i,j,k+\frac{1}{2}}}{r_i \delta r}$$

$$-\frac{< \theta_l^n W_l^n V_l^n >_{i,j,k+\frac{1}{2}}}{\delta z} - \frac{< \theta_l^n W_l^n W_l^n >_{i,j,k+\frac{1}{2}}}{r_i \delta \phi} - \frac{[\theta_l^n U_l^n W_l^n]_{i,j,k+\frac{1}{2}}}{r_i}$$

$$+\frac{[(r^2)_{i+\frac{1}{2}}^n \theta_{l\,i+\frac{1}{2},j,k+\frac{1}{2}}^n \tau lr\phi_{i+\frac{1}{2},j,k+\frac{1}{2}}^n - (r^2)_{i-\frac{1}{2}}^n \theta_{l\,i-\frac{1}{2},j,k+\frac{1}{2}}^n \tau lr\phi_{i-\frac{1}{2},j,k+\frac{1}{2}}^n]}{\rho_l r_i^2}$$

$$+\frac{[\theta_{l\,i,j,k+1}^n \tau l\phi\phi_{i,j,k+1}^n - \theta_{l\,i,j,k}^n \tau l\phi\phi_{i,j,k}^n]}{\rho_l r_i \delta \phi}$$

$$+\frac{[\theta_{l\,i,j+\frac{1}{2},k+\frac{1}{2}}^n \tau lz\phi_{i,j+\frac{1}{2},k+\frac{1}{2}}^n - \theta_{l\,i,j-\frac{1}{2},k+\frac{1}{2}}^n \tau lz\phi_{i,j-\frac{1}{2},k+\frac{1}{2}}^n]}{\rho_l \delta z}$$

$$+\theta_{l\,i,j,k+\frac{1}{2}}^n \vec{g}_\phi \Bigg\} \tag{3.25}$$

Each of the convective terms represented by brackets "$<>$", in the equations 3.20 through 3.25 are expanded in finite difference form by using the donor-cell treatment [110, 23, 38] as performed in Section 3.2.1.1. However, the discrete forms of the convection terms are more complicated than those obtained in discretizing of the continuity equations. For example, they contain two velocities (e.g. $U_{g\,i,j,k}, U_{g\,i+1,j,k}$) defined on two different grids. Therefore, in order to give an idea about the procedure for evaluating these terms, only the terms found in the radial component of the gas momentum equation (3.11) are presented below [110, 23, 88];

$$< \theta_g U_g U_g r >_{i+\frac{1}{2},j,k} = U_{g\,i+1,j,k} r_{i+1} \begin{cases} (\theta_g U_g)_{i+\frac{1}{2},j,k} & \text{if } U_{g\,i+1,j,k} \geq 0 \\ (\theta_g U_g)_{i+\frac{3}{2},j,k} & \text{if } U_{g\,i+1,j,k} < 0 \end{cases}$$

$$-U_{g\,i,j,k} r_i \begin{cases} (\theta_g U_g)_{i-\frac{1}{2},j,k} & \text{if } U_{g\,i,j,k} \geq 0 \\ (\theta_g U_g)_{i+\frac{1}{2},j,k} & \text{if } U_{g\,i,j,k} < 0 \end{cases} \tag{3.26}$$

$$< \theta_g U_g V_g >_{i+\frac{1}{2},j,k} = V_{g\,i+\frac{1}{2},j+\frac{1}{2},k} \begin{cases} (\theta_g U_g)_{i+\frac{1}{2},j,k} & \text{if } V_{g\,i+\frac{1}{2},j+\frac{1}{2},k} \geq 0 \\ (\theta_g U_g)_{i+\frac{1}{2},j+1,k} & \text{if } V_{g\,i+\frac{1}{2},j+\frac{1}{2},k} < 0 \end{cases}$$

$$-V_{g\,i+\frac{1}{2},j-\frac{1}{2},k}\begin{cases}(\theta_g U_g)_{i+\frac{1}{2},j-1,k} & \text{if} \quad V_{g\,i+\frac{1}{2},j-\frac{1}{2},k} \geq 0 \\ (\theta_g U_g)_{i+\frac{1}{2},j,k} & \text{if} \quad V_{g\,i+\frac{1}{2},j-\frac{1}{2},k} < 0\end{cases} \qquad (3.27)$$

$$<\theta_g U_g W_g>_{i+\frac{1}{2},j,k} \; = \; W_{g\,i+\frac{1}{2},j,k+\frac{1}{2}}\begin{cases}(\theta_g U_g)_{i+\frac{1}{2},j,k} & \text{if} \quad W_{g\,i+\frac{1}{2},j,k+\frac{1}{2}} \geq 0 \\ (\theta_g U_g)_{i+\frac{1}{2},j,k+1} & \text{if} \quad W_{g\,i+\frac{1}{2},j,k+\frac{1}{2}} < 0\end{cases}$$

$$-W_{g\,i+\frac{1}{2},j,k-\frac{1}{2}}\begin{cases}(\theta_g U_g)_{i+\frac{1}{2},j,k-1} & \text{if} \quad W_{g\,i+\frac{1}{2},j,k-\frac{1}{2}} \geq 0 \\ (\theta_g U_g)_{i+\frac{1}{2},j,k} & \text{if} \quad W_{g\,i+\frac{1}{2},j,k-\frac{1}{2}} < 0\end{cases} \qquad (3.28)$$

Taking equation 3.26 into consideration, if the flow is positive in a cell of (i,j,k) or (i,j+1,k), the velocity at the nearest point (at the left boundary of the cell) should be used. If the flow is negative, the velocity at the nearest point (at the right boundary of the cell) should be used.

The upwind scheme applied to the convection quantities of gas momentum equations (3.17, 3.12) for the other directions (z, ϕ) can be found in Appendix A.2.1 and A.2.2. Similar equations (3.18, 3.13 and 3.19) for the liquid phase in all directions can also be found in Appendix A.2.3, A.2.4 and A.2.5.

The viscous stress components appeared in equations 2.15 through 2.20, denoted as τ_q, are calculated at the time level (n) [10, 110, 23, 66]. Here, some discretised viscous terms are given as an example below;

$$\begin{aligned}(\tau_{qrr})_{i+1,j,k}^n \; = \; & \mu_q\Bigg\{2\Big(\frac{U_{q\,i+\frac{3}{2},j,k}^n - U_{q\,i+\frac{1}{2},j,k}^n}{\delta r}\Big) - \frac{2}{3}\Big(\frac{U_{q\,i+\frac{3}{2},j,k}^n r_{i+\frac{3}{2}} - U_{q\,i+\frac{1}{2},j,k}^n r_{i+\frac{1}{2}}}{r_{i+1}\delta r} \\ & + \; \frac{V_{q\,i+1,j+\frac{1}{2},k}^n - V_{q\,i+1,j-\frac{1}{2},k}^n}{\delta z} + \frac{W_{q\,i+1,j,k+\frac{1}{2}}^n - W_{q\,i+1,j,k-\frac{1}{2}}^n}{r_{i+1}\delta\phi}\Big)\Bigg\}\end{aligned} \quad (3.29)$$

$$\begin{aligned}(\tau_{qr\phi})_{i+\frac{1}{2},j,k+\frac{1}{2}}^n \; = \; & \mu_q\Bigg\{\frac{U_{q\,i+\frac{1}{2},j,k+1}^n - U_{q\,i+\frac{1}{2},j,k}^n}{r_{i+\frac{1}{2}}\delta\phi} \\ & + \frac{r_{i+\frac{1}{2}}\Big(\frac{W_{q\,i+1,j,k+\frac{1}{2}}^n}{r_{i+1}} - \frac{W_{q\,i,j,k+\frac{1}{2}}^n}{r_i}\Big)}{\delta r}\Bigg\}\end{aligned} \qquad (3.30)$$

$$
\left(\tau_{qrz}\right)_{i+\frac{1}{2},j+\frac{1}{2},k}^{n} \;=\; \mu_q\Bigg\{ \frac{V_{qi+1,j+\frac{1}{2},k}^{n} - V_{qi,j+\frac{1}{2},k}^{n}}{\delta r}
$$

$$
+ \frac{U_{qi+\frac{1}{2},j+1,k}^{n} - U_{qi+\frac{1}{2},j,k}^{n}}{\delta z} \Bigg\} \tag{3.31}
$$

$$
\left(\tau_{q\phi\phi}\right)_{i+\frac{1}{2},j,k}^{n} \;=\; \mu_q\Bigg\{ 2\Big(\frac{U_{qi+\frac{1}{2},j,k}^{n}}{r_{i+\frac{1}{2}}} + \frac{W_{qi+\frac{1}{2},j,k+\frac{1}{2}}^{n} - W_{qi+\frac{1}{2},j,k-\frac{1}{2}}^{n}}{r_{i+\frac{1}{2}}\delta\phi} \Big)
$$

$$
- \frac{2}{3}\Big(\frac{r_{i+1}U_{qi+1,j,k}^{n} - r_i U_{qi,j,k}^{n}}{r_{i+\frac{1}{2}}\delta r} + \frac{V_{qi+\frac{1}{2},j+\frac{1}{2},k}^{n} - V_{qi+\frac{1}{2},j-\frac{1}{2},k}^{n}}{\delta z}
$$

$$
+ \frac{W_{qi+\frac{1}{2},j,k+\frac{1}{2}}^{n} - W_{qi+\frac{1}{2},j,k-\frac{1}{2}}^{n}}{r_{i+\frac{1}{2}}\delta\phi} \Big) \Bigg\} \tag{3.32}
$$

$$
\left(\tau_{q\phi z}\right)_{i,j+\frac{1}{2},k+\frac{1}{2}}^{n} \;=\; \mu_q\Bigg\{ \frac{(V_{qi,j+\frac{1}{2},k+1}^{n} - V_{qi,j+\frac{1}{2},k}^{n}}{r_i\delta\phi}
$$

$$
+ \frac{W_{qi,j+1,k+\frac{1}{2}}^{n} - W_{qi,j,k+\frac{1}{2}}^{n}}{\delta z} \Bigg\} \tag{3.33}
$$

$$
\left(\tau_{qzz}\right)_{i,j+1,k}^{n} \;=\; \mu_q\Bigg\{ 2\Big(\frac{V_{qi,j+\frac{3}{2},k}^{n} - V_{qi,j+\frac{1}{2},k}^{n}}{\delta z} \Big)
$$

$$
- \frac{2}{3}\Big(\frac{r_{i+\frac{1}{2}}U_{qi+\frac{1}{2},j+1,k}^{n} - r_{i-\frac{1}{2}}U_{qi-\frac{1}{2},j+1,k}^{n}}{r_i\delta r} + \frac{V_{qi,j+\frac{3}{2},k}^{n} - V_{qi,j+\frac{1}{2},k}^{n}}{\delta z}
$$

$$
+ \frac{W_{qi,j+1,k+\frac{1}{2}}^{n} - W_{qi,j+1,k-\frac{1}{2}}^{n}}{r_i\delta\phi} \Big) \Bigg\} \tag{3.34}
$$

All the remaining viscous terms referenced in r,z and ϕ momentum equations for each phase are calculated similarly and can be found in Appendix A.3.

Although continuity equations does not involve such terms, some quantities in the discretized momentum equations described so far are used on grid points where they are not directly computed. Linear interpolations are performed in evaluating such kind of terms at these points [23, 110]. For example, value of θ_g at the cell face, $(i + \frac{1}{2}, j, k)$, is determined as;

38

$$\theta_{g_{i+\frac{1}{2},j,k}} = (\theta_{g_{i,j,k}} + \theta_{g_{i+1,j,k}})/2 \qquad (3.35)$$

Similarly, some velocities not positioned normal to the cell edges are obtained by simple averaging of the two adjacent quantities [10, 23, 5], e.g.;

$$U_{g_{i+1,j,k}} = (U_{g_{i+\frac{3}{2},j,k}} + U_{g_{i+\frac{1}{2},j,k}})/2 \qquad (3.36)$$

$$V_{g_{i+\frac{1}{2},j+\frac{1}{2},k}} = (V_{g_{i,j+\frac{1}{2},k}} + V_{g_{i+1,j+\frac{1}{2},k}})/2 \qquad (3.37)$$

$$W_{g_{i+\frac{1}{2},j,k+\frac{1}{2}}} = (W_{g_{i,j,k+\frac{1}{2}}} + W_{g_{i+1,j,k+\frac{1}{2}}})/2 \qquad (3.38)$$

3.3 Interfacial Momentum Transfer Term

General two-fluid model defined in Chapter 2 has the capacity to predict phasic interactions such as interfacial mass, momentum and energy transfer, which is not possible with more simplified mixture models [59]. Therefore, one of the most important work in deriving the two-phase flow equations is the modeling of these interfacial effects which provide coupling between the equations.

As it was mentioned before, only the exchange of the momentum due to drag force between both phases were considered in this study. This exchange arises because the two phases do not travel at the same velocity [83].

A number of correlations have been proposed to formulate the drag terms in the literature, but it seems that none of them has been recognised as a standart formulation. In this study, two different formulation of K function are used.

3.3.1 Lee and Shah's Formulation

It is a simple equation given by Lee and Shah [81]. It defines K function as;

$$K = C \cdot f(\theta_g) \tag{3.39}$$

where C is some coefficient, and

$$f(\theta_g) = \begin{cases} 1 + 10^{2000(0.01 - \theta_g)} & \text{when} \quad \theta_g \leq 0.01 \\ 1 & \text{when} \quad 0.01 < \theta < 0.99 \\ 1 + 10^{2000(\theta_g - 0.99)} & \text{when} \quad \theta_g \geq 0.99 \end{cases}$$

Lee and Shah [81] gave some values of $10^3, 10^4$ and 10^5 $kg/m^3 s$ in their simulations for the problem of separation of steam and water. However they appointed the values of 2.0x10^8, 2.0x10^{10} and 2.0x10^{12} $kg/m^3 s$ to K in simulating high pressure jet impingement problem. Lee [78] used K values of 2.2x10^6, 2.0x10^7 and 2.2x10^8 $kg/m^3 s$ in his study on two-phase jet impinged on vertical plate.

3.3.2   Schiller-Naumann Formulation

It is more elaborate form of K and is known as "Schiller-Naumann Drag Model". It is one of the most common formulations used in the literature. The drag force, M_{qi}, in the momentum equation 2.3 is defined as [7, 41, 107];

$$M_{qi} = \frac{3}{4} \frac{C_D}{d} \theta_g \rho_l (\vec{u_g} - \vec{u_l}) \mid \vec{u_g} - \vec{u_l} \mid \tag{3.40}$$

therefore, K function becomes,

$$K = \frac{3}{4} \frac{C_D}{d} \theta_g \rho_l \mid \vec{u_g} - \vec{u_l} \mid \tag{3.41}$$

Equation 3.41 models the viscous and pressure forces acting on spherical bubbles of diameter d in the direction of the relative velocity $\vec{u_g} - \vec{u_l}$ between

the liquid and gas phase and includes a drag coefficient C_D that is based on the Reynolds number as follows [77, 50, 53, 99]:

$$C_D = \begin{cases} \frac{24}{Re}(1 + 0.15 Re^{0.687}) & \text{if} \quad Re < 1000 \\ 0.44 & \text{if} \quad Re \geq 1000 \end{cases} \quad \text{where} \quad Re = \frac{|u_d - u_c| * d}{\nu_c}$$

where subscript c represents continuous phase, while subscript d is for dispersed phase. Here, the coefficient of drag is determined using relations developed by Ishii and Zuber [61] for dispersed two-phase flows based on the Reynolds number.

3.4 Initial and Boundary Conditions

In order to completely specify the two-fluid model numerically, the conservation equations and the closure relations already defined, should be supplemented by appropriate initial and boundary conditions expressing the particular situation to be investigated as in the following sections:

3.4.1 Initial Conditions

To start the solution of the finite difference equations in time domain, initial conditions should be specified for each cell. Uniform initial conditions for velocities are defined by specifying values for $U_g = U_l, V_g = V_l, W_g = W_l$.

However, in order to avoid numerical solution problems, all variables are given a small positive/negative value are given to all variables (especially to void fraction values) initially in the whole computational domain as recommended by Friberg [30] who used 0.01 for void fraction in his study. For pressure, hydrostatic pressure distribution can be defined as an initial condition where it is needed.

3.4.2 Boundary Conditions

A solution of the equations also requires accurate specification of conditions at the boundaries of the domain. The boundary condition specifications utilized in this work are described in this section.

There are many references to the boundaries of computational domain in finite difference equations. Therefore, proper boundary conditions for the variables around the computing mesh have been numerically defined.

Boundary conditions are more easily implemented if the computing mesh shown in Figure 3.3 in fixed angular direction, is surrounded by a belt of fictitious cells represented by dashed lines lying outside the boundries. This is called as "ghost (or dummy) cell" approach [110, 3, 123]. Cells in this fictitious area are called boundary cells and the use of such approach simplifies the definition of boundary conditions especially those relating to velocities [5].
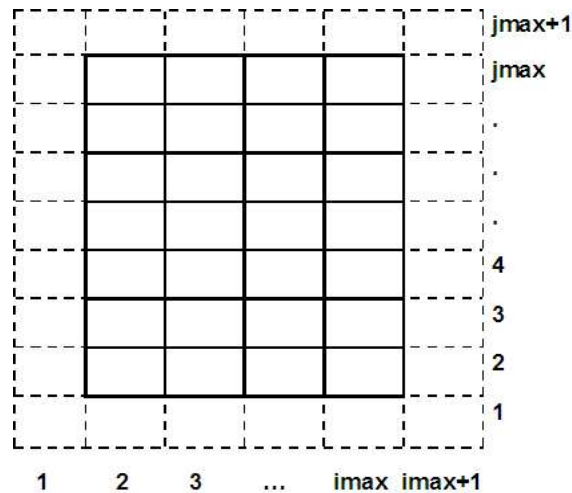
Figure 3.3: Ghost Cell Definitions in r and z Directions

Since the first order upwind schemes are used in finite differencing, only one row of ghost cells is enough to be used along each boundaries of the computational domain [23]. Therefore, boundary conditions are applied by

setting the values in these single rows of ghost cells.

3.4.3 Slip Boundary Conditions

Slip boundary conditions are often employed in hydrodynamic simulations at solid internal/external impermeable boundaries. The main idea behind using slip boundary conditions is that the normal velocities are set to zero while the tangential velocity components is specified either as a no-slip or as a free-slip condition as explained below.

3.4.3.1 Free-Slip Boundary Conditions

A free-slip boundary represents an axial centerline or a plane of symmetry at which it can be assumed that there is a mirror image of the fluid flow on the opposite side of the plane [3, 110, 5]

As an example to show how to treat these type of boundary conditions, the fluid velocity component in the r-direction at the left boundary of the unit cell shown in Figure 3.2 is given as an example.

The normal velocity component of each phases vanishes at the left boundary of the cell according to free-slip boundary condition definition meaning that velocity normal to the wall is set to zero [5, 16];

- $U_{q_{i-\frac{1}{2},j,k}} = 0$

While the free-slip condition states for the other directions [5];

- $V_{q_{i-1,j+\frac{1}{2},k}} = V_{q_{i,j+\frac{1}{2},k}}$

- $W_{q_{i-1,j,k+\frac{1}{2}}} = W_{q_{i,j,k+\frac{1}{2}}}$

so that the gradient of the tangential velocity component at the wall is zero namely Neumann type condition [16, 110].

The cell-centered variables, θ_q and P, are treated the same as in above equations written for V and W, meaning that there is no gradient across the boundary [3, 16];

- $\theta_{i-1,j,k} = \theta_{i,j,k}$

- $P_{i-1,j,k} = P_{i,j,k}$

3.4.3.2 No-Slip Boundary Conditions

"No-slip" is the most common type of wall boundary condition implementation. Amsden and Harlow [5] defines a no-slip boundary as a viscous boundary that exerts a drag upon the fluid. This is accomplished by forcing the tangential velocity to go to zero at the wall.

Now suppose that, the right wall of the same unit cell is a no-slip boundary. Normal velocity at the wall must be zero [5], e.g.,

- $U_{i+\frac{1}{2},j,k} = 0$

so that no through flow at the right face of the cell occur. For the other velocity components, no slip boundary conditions specifies zero velocity along the wall and by using linear interpolation;

- $V_{i+1,j+\frac{1}{2},k} = -V_{i,j+\frac{1}{2},k}$

- $W_{i+1,j,k+\frac{1}{2}} = -W_{i,j,k+\frac{1}{2}}$

are obtained (Dirichlet type condition).

The variables θ and P are treated similarly as it is done for a free-slip boundary.

- $\theta_{i+1,j,k} = \theta_{i,j,k}$

- $P_{i+1,j,k} = P_{i,j,k}$

3.4.4 Flow Boundary Conditions

Two types of flow boundary condition are defined in this study. One type is for inlet and the other type for outlets of the domain. Each will be considered in turn.

3.4.4.1 Constant Pressure Boundary Condition

Boundaries that have flow leaving the grid domain are known as outflow boundaries. One of the most commonly used condition for the outflow boundary is specified "constant pressure" condition at the outlets [123, 71]. Gavage et al. [33] states that especially for a subsonic outflow, prescribing the pressure, works perfectly well.

As its name implies, constant pressure boundary condition states that the pressure on the boundary, considering top face of the unit cell, is fixed at a specified value throughout the computations;

- $P_{i,j+1,k} = P_{i,j,k} = P_{out}$

A zero gradient condition (Neumann type) is applied to the velocities by extrapolating the velocity components of U_q, V_q, W_q from the interior cells [53, 1, 66, 5];

- $U_{i+\frac{1}{2},j+1,k} = U_{i+\frac{1}{2},j,k}$

- $V_{i,j+\frac{3}{2},k} = V_{i,j+\frac{1}{2},k}$

- $W_{i,j+1,k+\frac{1}{2}} = W_{i,j,k+\frac{1}{2}}$

Volume fractions are also considered in the same logic as,

- $\theta_{q_{i,j+1,k}} = \theta_{q_{i,j,k}}$

3.4.4.2 Inflow Boundary Conditions

An inflow boundary is described as a boundary which allows fluid to move into the domain at a prescribed inlet velocity distribution, $\vec{u_q}$, as well as at a prescribed value of θ_q's [71]. If the bottom face of the unit cell is considered as inflow boundary;

- $U_{i+\frac{1}{2},j-1,k} = U_{in}$

- $V_{i,j-\frac{1}{2},k} = V_{in}$

- $W_{i,j-1,k+\frac{1}{2}} = W_{in}$

- $\theta_{q_{i,j-1,k}} = \theta_{q_{in}}$

where subscript "in" refers to specified inlet value. However, the pressure at the inlet is unknown and a boundary value is extrapolated from the interior of the flow domain;

- $P_{i,j-1,k} = P_{i,j,k}$

In contrast to constant pressure boundary condition, outflow of the fluid is not permitted in inflow boundary condition.

3.4.5 Periodic Boundary Condition

Since cylindrical coordinates is used in the discretization, a periodic condition appears in the angular direction of ϕ. Such a condition must be set to provide a coupling between the variables at the first and last cells exist in the angular sweep.

Periodic boundary condition states for velocity components, volume fractions and pressure, in the aft and fore cells respectively;

- $U_{q_{i+\frac{1}{2},j,2}} = U_{q_{i+\frac{1}{2},j,kmax+1}}$, $U_{q_{i+\frac{1}{2},j,kmax}} = U_{q_{i+\frac{1}{2},j,1}}$

- $V_{q_{i,j+\frac{1}{2},2}} = V_{q_{i,j+\frac{1}{2},kmax+1}}$, $V_{q_{i,j+\frac{1}{2},kmax}} = V_{q_{i,j+\frac{1}{2},1}}$

- $W_{q_{i,j,\frac{1}{2}}} = W_{q_{i,j,kmax+\frac{1}{2}}}$, $W_{q_{i,j,kmax+\frac{3}{2}}} = W_{q_{i,j,\frac{5}{2}}}$

- $\theta_{q_{i,j,2}} = \theta_{q_{i,j,kmax+1}}$, $\theta_{q_{i,j,kmax}} = \theta_{q_{i,j,1}}$

- $P_{i,j,2} = P_{i,j,kmax+1}$, $P_{i,j,kmax} = P_{i,j,1}$

3.5 Solution Procedure

Before starting to construct a computer program (code) which will help to solve those finite difference equations, a solution algorithm as shown in Figure 3.4 is to be outlined according to the technique similar to that proposed by Harlow and Amsden [41] in IMF method and as it is applied in K-FIX code [110]. The resulting finite difference equations are semi-implicit and are solved by an implicit point relaxation technique [110, 16] as outlined in this section.

The iteration procedure [80, 81] is described simply below in the same order as the computation is performed. As can be seen in Figure 3.4, after setting the initial velocities and void fraction,

1. the pressure distribution at time $t + \Delta t$ is guessed,

2. the momentum equations will be solved to compute initial estimation of the three velocity components of each of the two phases, for a guessed pressure distribution,

3. phasic volume fraction, θ_q is estimated from the continuity equation of liquid (gas),

4. then it is checked if gas(liquid) continuity equation is satisfied with this estimation. If satisfied, a new timestep is chosen and steps 1 to 4 are repeated. If the equation is not satisfied, the pressure is corrected iteratively by using an equation derived from the gas(liquid) continuity equation. Velocities are updated and steps 3 to 4 are repeated. This iteration procedure is continued until the mass residuals are less than the specified convergence criterion, ϵ, in all the computational cells simultaneously .

To be a more specific, the details of this iterative procedure are given below [110, 10, 36];

47
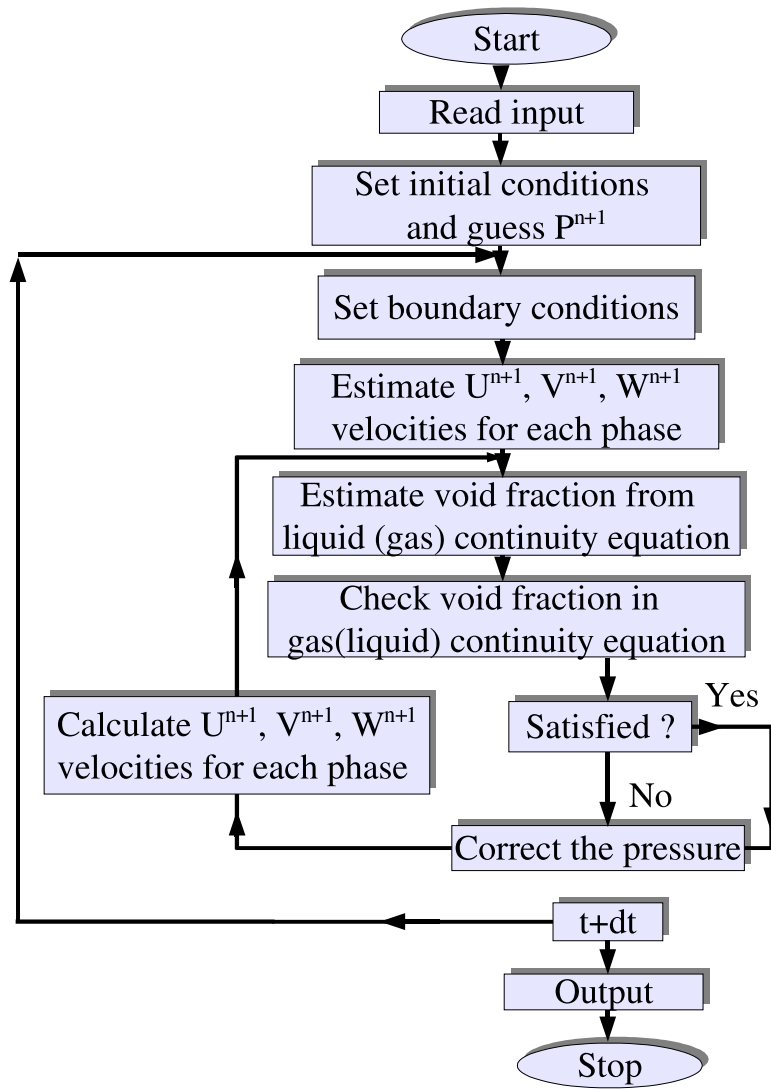
Figure 3.4: Solution Algorithm

a.The overlined (explicit) quantities are calculated using equations 3.20 through 3.25.

b.The drag coefficients are calculated explicitly.

c.New time level (n+1) velocities are estimated by using following equations. These velocities which are derived algebraically from equations 3.11 through 3.13 and from equations 3.17 through 3.19 on the right, top and aft boundaries are calculated for both phases as [4, 110, 42, 10, 32];

$$
\begin{aligned}
U_{g_{i+\frac{1}{2},j,k}}^{n+1} = & \left\{ \left(\rho_g \overline{(\theta_g U_g)}_{i+\frac{1}{2},j,k} - \frac{\delta t}{\delta r} \theta_{g_{i+\frac{1}{2},j,k}}^{n+1} (P_{i+1,j,k}^{n+1} - P_{i,j,k}^{n+1}) \right) \right. \\
& \left(\rho_l \theta_{l_{i+\frac{1}{2},j,k}}^{n+1} + \delta t K_{i+\frac{1}{2},j,k}^{n} \right) + \delta t K_{i+\frac{1}{2},j,k}^{n} \left(\rho_l \overline{(\theta_l U_l)}_{i+\frac{1}{2},j,k} \right. \\
& \left. \left. - \frac{\delta t}{\delta r} \theta_{l_{i+\frac{1}{2},j,k}}^{n+1} (P_{i+1,j,k}^{n+1} - P_{i,j,k}^{n+1}) \right) \right\} \\
& \bigg/ \left(\rho_g \theta_{g_{i+\frac{1}{2},j,k}}^{n+1} \left\{ \rho_l \theta_{l_{i+\frac{1}{2},j,k}}^{n+1} + \delta t K_{i+\frac{1}{2},j,k}^{n} \right\} + \delta t \rho_l \theta_{l_{i+\frac{1}{2},j,k}}^{n+1} K_{i+\frac{1}{2},j,k}^{n} \right) \quad (3.42)
\end{aligned}
$$

$$
\begin{aligned}
V_{g_{i,j+\frac{1}{2},k}}^{n+1} = & \left\{ \left(\rho_g \overline{(\theta_g V_g)}_{i,j+\frac{1}{2},k} - \frac{\delta t}{\delta z} \theta_{g_{i,j+\frac{1}{2},k}}^{n+1} (P_{i,j+1,k}^{n+1} - P_{i,j,k}^{n+1}) \right) \right. \\
& \left(\rho_l \theta_{l_{i,j+\frac{1}{2},k}}^{n+1} + \delta t K_{i,j+\frac{1}{2},k}^{n} \right) + \delta t K_{i,j+\frac{1}{2},k}^{n} \left(\rho_l \overline{(\theta_l V_l)}_{i,j+\frac{1}{2},k} \right. \\
& \left. \left. - \frac{\delta t}{\delta z} \theta_{l_{i,j+\frac{1}{2},k}}^{n+1} (P_{i,j+1,k}^{n+1} - P_{i,j,k}^{n+1}) \right) \right\} \\
& \bigg/ \left(\rho_g \theta_{g_{i,j+\frac{1}{2},k}}^{n+1} \left\{ \rho_l \theta_{l_{i,j+\frac{1}{2},k}}^{n+1} + \delta t K_{i,j+\frac{1}{2},k}^{n} \right\} + \delta t \rho_l \theta_{l_{i,j+\frac{1}{2},k}}^{n+1} K_{i,j+\frac{1}{2},k}^{n} \right) \quad (3.43)
\end{aligned}
$$

$$
\begin{aligned}
W_{g_{i,j,k+\frac{1}{2}}}^{n+1} = & \left\{ \left(\rho_g \overline{(\theta_g W_g)}_{i,j,k+\frac{1}{2}} - \frac{\delta t}{r_i \delta \phi} \theta_{g_{i,j,k+\frac{1}{2}}}^{n+1} (P_{i,j,k+1}^{n+1} - P_{i,j,k}^{n+1}) \right) \right. \\
& \left(\rho_l \theta_{l_{i,j,k+\frac{1}{2}}}^{n+1} + \delta t K_{i,j,k+\frac{1}{2}}^{n} \right) + \delta t K_{i,j,k+\frac{1}{2}}^{n} \left(\rho_l \overline{(\theta_l W_l)}_{i,j,k+\frac{1}{2}} \right. \\
& \left. \left. - \frac{\delta t}{r_i \delta \phi} \theta_{l_{i,j,k+\frac{1}{2}}}^{n+1} (P_{i,j,k+1}^{n+1} - P_{i,j,k}^{n+1}) \right) \right\} \\
& \bigg/ \left(\rho_g \theta_{g_{i,j,k+\frac{1}{2}}}^{n+1} \left\{ \rho_l \theta_{l_{i,j,k+\frac{1}{2}}}^{n+1} + \delta t K_{i,j,k+\frac{1}{2}}^{n} \right\} + \delta t \rho_l \theta_{l_{i,j,k+\frac{1}{2}}}^{n+1} K_{i,j,k+\frac{1}{2}}^{n} \right) \quad (3.44)
\end{aligned}
$$

$$U_{l_{i+\frac{1}{2},j,k}}^{n+1} = \left\{ \left(\rho_l \overline{(\theta_l U_l)}_{i+\frac{1}{2},j,k} - \frac{\delta t}{\delta r} \theta_{l_{i+\frac{1}{2},j,k}}^{n+1} (P_{i+1,j,k}^{n+1} - P_{i,j,k}^{n+1}) \right) \right.$$

$$\left(\rho_g \theta_{g_{i+\frac{1}{2},j,k}}^{n+1} + \delta t K_{i+\frac{1}{2},j,k}^n \right) + \delta t K_{i+\frac{1}{2},j,k}^n \left(\rho_g \overline{(\theta_g U_g)}_{i+\frac{1}{2},j,k} \right.$$

$$\left. \left. - \frac{\delta t}{\delta r} \theta_{g_{i+\frac{1}{2},j,k}}^{n+1} (P_{i+1,j,k}^{n+1} - P_{i,j,k}^{n+1}) \right) \right\}$$

$$\left/ \left(\rho_g \theta_{g_{i+\frac{1}{2},j,k}}^{n+1} \left\{ \rho_l \theta_{l_{i+\frac{1}{2},j,k}}^{n+1} + \delta t K_{i+\frac{1}{2},j,k}^n \right\} + \delta t \rho_l \theta_{l_{i+\frac{1}{2},j,k}}^{n+1} K_{i+\frac{1}{2},j,k}^n \right) \right. \quad (3.45)$$

$$V_{l_{i,j+\frac{1}{2},k}}^{n+1} = \left\{ \left(\rho_l \overline{(\theta_l V_l)}_{i,j+\frac{1}{2},k} - \frac{\delta t}{\delta z} \theta_{l_{i,j+\frac{1}{2},k}}^{n+1} (P_{i,j+1,k}^{n+1} - P_{i,j,k}^{n+1}) \right) \right.$$

$$\left(\rho_g \theta_{g_{i,j+\frac{1}{2},k}}^{n+1} + \delta t K_{i,j+\frac{1}{2},k}^n \right) + \delta t K_{i,j+\frac{1}{2},k}^n \left(\rho_g \overline{(\theta_g V_g)}_{i,j+\frac{1}{2},k} \right.$$

$$\left. \left. - \frac{\delta t}{\delta z} \theta_{g_{i,j+\frac{1}{2},k}}^{n+1} (P_{i,j+1,k}^{n+1} - P_{i,j,k}^{n+1}) \right) \right\}$$

$$\left/ \left(\rho_g \theta_{g_{i,j+\frac{1}{2},k}}^{n+1} \left\{ \rho_l \theta_{l_{i,j+\frac{1}{2},k}}^{n+1} + \delta t K_{i,j+\frac{1}{2},k}^n \right\} + \delta t \rho_l \theta_{l_{i,j+\frac{1}{2},k}}^{n+1} K_{i,j+\frac{1}{2},k}^n \right) \right. \quad (3.46)$$

$$W_{l_{i,j,k+\frac{1}{2}}}^{n+1} = \left\{ \left(\rho_l \overline{(\theta_l W_l)}_{i,j,k+\frac{1}{2}} - \frac{\delta t}{r_i \delta \phi} \theta_{l_{i,j,k+\frac{1}{2}}}^{n+1} (P_{i,j,k+1}^{n+1} - P_{i,j,k}^{n+1}) \right) \right.$$

$$\left(\rho_g \theta_{g_{i,j,k+\frac{1}{2}}}^{n+1} + \delta t K_{i,j,k+\frac{1}{2}}^n \right) + \delta t K_{i,j,k+\frac{1}{2}}^n \left(\rho_g \overline{(\theta_g W_g)}_{i,j,k+\frac{1}{2}} \right.$$

$$\left. \left. - \frac{\delta t}{r_i \delta \phi} \theta_{g_{i,j,k+\frac{1}{2}}}^{n+1} (P_{i,j,k+1}^{n+1} - P_{i,j,k}^{n+1}) \right) \right\}$$

$$\left/ \left(\rho_g \theta_{g_{i,j,k+\frac{1}{2}}}^{n+1} \left\{ \rho_l \theta_{l_{i,j,k+\frac{1}{2}}}^{n+1} + \delta t K_{i,j,k+\frac{1}{2}}^n \right\} + \delta t \rho_l \theta_{l_{i,j,k+\frac{1}{2}}}^{n+1} K_{i,j,k+\frac{1}{2}}^n \right) \right. \quad (3.47)$$

d. A new variable, $\beta_{i,j,k}$, is calculated from the following equation [42];

$$\beta_{i,j,k} = \left[\frac{\partial (Di, j, k)}{\partial P_{i,j,k}} \right]^{-1} \quad (3.48)$$

in which the partial derivatives are calculated by means of the following equations:

50

in case of $\quad \theta_{g_{i,j,k}} < \theta^*_{i,j,k}$,

$$
\begin{aligned}
\left(\frac{\partial D_l}{\partial P}\right)^{n+1}_{i,j,k} = {} & \frac{\delta t^2}{\rho_l r_i \delta r^2}\left[r_{i+\frac{1}{2}}\theta^{n+1}_{l_{i+\frac{1}{2},j,k}} + r_{i-\frac{1}{2}}\theta^{n+1}_{l_{i-\frac{1}{2},j,k}}\right] \\
& + \frac{\delta t^2}{r_i \delta r \rho_l}\left[r_{i+\frac{1}{2}}K^n_{i+\frac{1}{2},j,k}\frac{\partial[U_g-U_l]^{n+1}_{i+\frac{1}{2},j,k}}{\partial P^{n+1}_{i,j,k}} - r_{i-\frac{1}{2}}K^n_{i-\frac{1}{2},j,k}\frac{\partial[U_g-U_l]^{n+1}_{i-\frac{1}{2},j,k}}{\partial P^{n+1}_{i,j,k}}\right] \\
& + \frac{\delta t^2}{\delta z^2 \rho_l}\left[\theta^{n+1}_{l_{i,j+\frac{1}{2},k}} + \theta^{n+1}_{l_{i,j-\frac{1}{2},k}}\right] \\
& + \frac{\delta t^2}{\delta z \rho_l}\left[K^n_{i,j+\frac{1}{2},k}\frac{\partial[V_g-V_l]^{n+1}_{i,j+\frac{1}{2},k}}{\partial P^{n+1}_{i,j,k}} - K^n_{i,j-\frac{1}{2},k}\frac{\partial[V_g-V_l]^{n+1}_{i,j-\frac{1}{2},k}}{\partial P^{n+1}_{i,j,k}}\right] \\
& + \frac{\delta t^2}{\rho_l r_i{}^2(\delta\phi)^2}\left[\theta^{n+1}_{l_{i,j,k+\frac{1}{2}}} + \theta^{n+1}_{l_{i,j,k-\frac{1}{2}}}\right] \\
& + \frac{\delta t^2}{r_i \delta\phi \rho_l}\left[K^n_{i,j,k+\frac{1}{2}}\frac{\partial[W_g-W_l]^{n+1}_{i,j,k+\frac{1}{2}}}{\partial P^{n+1}_{i,j,k}} - K^n_{i,j,k-\frac{1}{2}}\frac{\partial[W_g-W_l]^{n+1}_{i,j,k-\frac{1}{2}}}{\partial P^{n+1}_{i,j,k}}\right] \quad (3.49)
\end{aligned}
$$

where

$$
\frac{\partial[U_g-U_l]^{n+1}_{i+\frac{1}{2},j,k}}{\partial P^{n+1}_{i,j,k}} = \frac{\frac{\delta t}{\delta r}(\theta_g\theta_l)^{n+1}_{i+\frac{1}{2},j,k}(\rho_l-\rho_g)}{(\theta_g{}^{n+1}\rho_g(\theta_l{}^{n+1}\rho_l + K^n\delta t) + \theta_l{}^{n+1}\rho_l K^n\delta t)_{i+\frac{1}{2},j,k}} \quad (3.50)
$$

$$
\frac{\partial[U_g-U_l]^{n+1}_{i-\frac{1}{2},j,k}}{\partial P^{n+1}_{i,j,k}} = \frac{\frac{\delta t}{\delta r}(\theta_g\theta_l)^{n+1}_{i-\frac{1}{2},j,k}(\rho_g-\rho_l)}{(\theta_g{}^{n+1}\rho_g(\theta_l{}^{n+1}\rho_l + K^n\delta t) + \theta_l{}^{n+1}\rho_l K^n\delta t)_{i-\frac{1}{2},j,k}} \quad (3.51)
$$

$$
\frac{\partial[V_g-V_l]^{n+1}_{i,j+\frac{1}{2},k}}{\partial P^{n+1}_{i,j,k}} = \frac{\frac{\delta t}{\delta z}(\theta_g\theta_l)^{n+1}_{i,j+\frac{1}{2},k}(\rho_l-\rho_g)}{(\theta_g{}^{n+1}\rho_g(\theta_l{}^{n+1}\rho_l + K^n\delta t) + \theta_l{}^{n+1}\rho_l K^n\delta t)_{i,j+\frac{1}{2},k}} \quad (3.52)
$$

$$
\frac{\partial[V_g-V_l]^{n+1}_{i,j-\frac{1}{2},k}}{\partial P^{n+1}_{i,j,k}} = \frac{\frac{\delta t}{\delta z}(\theta_g\theta_l)^{n+1}_{i,j-\frac{1}{2},k}(\rho_g-\rho_l)}{(\theta_g{}^{n+1}\rho_g(\theta_l{}^{n+1}\rho_l + K^n\delta t) + \theta_l{}^{n+1}\rho_l K^n\delta t)_{i,j-\frac{1}{2},k}} \quad (3.53)
$$

$$
\frac{\partial[W_g-W_l]^{n+1}_{i,j,k+\frac{1}{2}}}{\partial P^{n+1}_{i,j,k}} = \frac{\frac{\delta t}{r_i\delta\phi}(\theta_g\theta_l)^{n+1}_{i,j,k+\frac{1}{2}}(\rho_l-\rho_g)}{(\theta_g{}^{n+1}\rho_g(\theta_l{}^{n+1}\rho_l + K^n\delta t) + \theta_l{}^{n+1}\rho_l K^n\delta t)_{i,j,k+\frac{1}{2}}} \quad (3.54)
$$

51

$$\frac{\partial[W_g - W_l]^{n+1}_{i,j,k-\frac{1}{2}}}{\partial P^{n+1}_{i,j,k}} = \frac{\frac{\delta t}{r_i\delta\phi}(\theta_g\theta_l)^{n+1}_{i,j,k-\frac{1}{2}}(\rho_g - \rho_l)}{(\theta_g^{n+1}\rho_g(\theta_l^{n+1}\rho_l + K^n\delta t) + \theta_l^{n+1}\rho_l K^n\delta t)_{i,j,k-\frac{1}{2}}} \quad (3.55)$$

while similarly for $\quad \theta_{g_{i,j,k}} \geq \theta^*_{i,j,k},$

$$\left(\frac{\partial D_g}{\partial P}\right)^{n+1}_{i,j,k} = \frac{\delta t^2}{\rho_g r_i\delta r^2}\left[r_{i+\frac{1}{2}}\theta_{g_{i+\frac{1}{2},j,k}}^{n+1} + r_{i-\frac{1}{2}}\theta_{g_{i-\frac{1}{2},j,k}}^{n+1}\right]$$

$$+ \frac{\delta t^2}{r_i\delta r\rho_g}\left[r_{i+\frac{1}{2}}K^n_{i+\frac{1}{2},j,k}\frac{\partial[U_l - U_g]^{n+1}_{i+\frac{1}{2},j,k}}{\partial P^{n+1}_{i,j,k}} - r_{i-\frac{1}{2}}K^n_{i-\frac{1}{2},j,k}\frac{\partial[U_l - U_g]^{n+1}_{i-\frac{1}{2},j,k}}{\partial P^{n+1}_{i,j,k}}\right]$$

$$+ \frac{\delta t^2}{\delta z^2\rho_g}\left[\theta_{g_{i,j+\frac{1}{2},k}}^{n+1} + \theta_{g_{i,j-\frac{1}{2},k}}^{n+1}\right]$$

$$+ \frac{\delta t^2}{\delta z\rho_g}\left[K^n_{i,j+\frac{1}{2},k}\frac{\partial[V_l - V_g]^{n+1}_{i,j+\frac{1}{2},k}}{\partial P^{n+1}_{i,j,k}} - K^n_{i,j-\frac{1}{2},k}\frac{\partial[V_l - V_g]^{n+1}_{i,j-\frac{1}{2},k}}{\partial P^{n+1}_{i,j,k}}\right]$$

$$+ \frac{\delta t^2}{\rho_g r_i^2(\delta\phi)^2}\left[\theta_{g_{i,j,k+\frac{1}{2}}}^{n+1} + \theta_{g_{i,j,k-\frac{1}{2}}}^{n+1}\right]$$

$$+ \frac{\delta t^2}{r_i\delta\phi\rho_g}\left[K^n_{i,j,k+\frac{1}{2}}\frac{\partial[W_l - W_g]^{n+1}_{i,j,k+\frac{1}{2}}}{\partial P^{n+1}_{i,j,k}} - K^n_{i,j,k-\frac{1}{2}}\frac{\partial[W_l - W_g]^{n+1}_{i,j,k-\frac{1}{2}}}{\partial P^{n+1}_{i,j,k}}\right] \quad (3.56)$$

where

$$\frac{\partial[U_l - U_g]^{n+1}_{i+\frac{1}{2},j,k}}{\partial P^{n+1}_{i,j,k}} = \frac{\frac{\delta t}{\delta r}(\theta_g\theta_l)^{n+1}_{i+\frac{1}{2},j,k}(\rho_g - \rho_l)}{(\theta_g^{n+1}\rho_g(\theta_l^{n+1}\rho_l + K^n\delta t) + \theta_l^{n+1}\rho_l K^n\delta t)_{i+\frac{1}{2},j,k}} \quad (3.57)$$

$$\frac{\partial[U_l - U_g]^{n+1}_{i-\frac{1}{2},j,k}}{\partial P^{n+1}_{i,j,k}} = \frac{\frac{\delta t}{\delta r}(\theta_g\theta_l)^{n+1}_{i-\frac{1}{2},j,k}(\rho_l - \rho_g)}{(\theta_g^{n+1}\rho_g(\theta_l^{n+1}\rho_l + K^n\delta t) + \theta_l^{n+1}\rho_l K^n\delta t)_{i-\frac{1}{2},j,k}} \quad (3.58)$$

$$\frac{\partial[V_l - V_g]^{n+1}_{i,j+\frac{1}{2},k}}{\partial P^{n+1}_{i,j,k}} = \frac{\frac{\delta t}{\delta z}(\theta_g\theta_l)^{n+1}_{i,j+\frac{1}{2},k}(\rho_g - \rho_l)}{(\theta_g^{n+1}\rho_g(\theta_l^{n+1}\rho_l + K^n\delta t) + \theta_l^{n+1}\rho_l K^n\delta t)_{i,j+\frac{1}{2},k}} \quad (3.59)$$

$$\frac{\partial[V_l - V_g]^{n+1}_{i,j-\frac{1}{2},k}}{\partial P^{n+1}_{i,j,k}} = \frac{\frac{\delta t}{\delta z}(\theta_g\theta_l)^{n+1}_{i,j-\frac{1}{2},k}(\rho_l - \rho_g)}{(\theta_g^{n+1}\rho_g(\theta_l^{n+1}\rho_l + K^n\delta t) + \theta_l^{n+1}\rho_l K^n\delta t)_{i,j-\frac{1}{2},k}} \quad (3.60)$$

$$\frac{\partial [W_l - W_g]^{n+1}_{i,j,k+\frac{1}{2}}}{\partial P^{n+1}_{i,j,k}} = \frac{\frac{\delta t}{r_i \delta \phi}(\theta_g \theta_l)^{n+1}_{i,j,k+\frac{1}{2}}(\rho_g - \rho_l)}{(\theta_g^{n+1}\rho_g(\theta_l^{n+1}\rho_l + K^n \delta t) + \theta_l^{n+1}\rho_l K^n \delta t)_{i,j,k+\frac{1}{2}}} \quad (3.61)$$

$$\frac{\partial [W_l - W_g]^{n+1}_{i,j,k-\frac{1}{2}}}{\partial P^{n+1}_{i,j,k}} = \frac{\frac{\delta t}{r_i \delta \phi}(\theta_g \theta_l)^{n+1}_{i,j,k-\frac{1}{2}}(\rho_l - \rho_g)}{(\theta_g^{n+1}\rho_g(\theta_l^{n+1}\rho_l + K^n \delta t) + \theta_l^{n+1}\rho_l K^n \delta t)_{i,j,k-\frac{1}{2}}} \quad (3.62)$$

Here, β represents the derivatives of the residue $D_{i,j,k}$ related to the pressure, and is analytically obtained from the fluid continuity and momentum equations [42, 36]. Rivard and Torrey [110] derived β for two-dimensional cylindrical coordinates by including drag function. Later, they added one term to this equation to include the third dimension, ϕ directional effect [112]. Lee and Lyczkowski [80] ignored the momentum exchange terms, $K(\vec{u_g} - \vec{u_l})$ and $K(\vec{u_l} - \vec{u_g})$ in the derivations of equations 3.49 and 3.56. They found that these formulations result in greater stability for pressure calculations for the problems that they had been investigated. Also, Lee and Shah [81] obtained β, but in cartesian three-dimensional equations by ignoring drag terms. Gomez et al. [36] found β for two-dimensional cylindrical coordinates by neglecting K term. Lee [78] gave the detailed derivation of these derivative terms in 2-D cylindrical coordinates of r and z.

By using Lee's approach, the derivaties of $\frac{\partial D_q}{\partial P^{n+1}}$ (for q=g,l) are rederived by including the drag terms (K's), for incompressible equations in three-dimensional cylindrical geometry by considering ϕ direction terms. Amsden and Harlow [3] found that calculation and storage of $\beta_{i,j,k}$ before entering into iteration step and holding them invariant throughout this stage makes help to enhance computer efficiency.

e.Pressure is adjusted iteratively in a cell in order to ensure mass conservation in the flow, that is to minimize the residual of the continuity equation below convergence criteria [42, 23, 24, 110] or until the number of iterations

exceed a predefined "inner iterations limit" defined for pressure convergence. The computations proceed until the entire computational domain is covered [32].

Gamwo et al. [32] and Syamlal [124] sets a value of 5 iterations for this inner iteration limit. Broadus et al. [10] recommends this number to be 5 or greater.

The residues are calculated from the following equations in a fully implicit way for different cases of the θ_g value as used in K-FIX [110]. Gamwo et al., Enwald and Peirano [24, 23] uses only D_g in the iteration steps. If $\theta < \theta^*$, D_l is calculated from the following equation [10, 4, 23];

$$
\begin{aligned}
(D_l)_{i,j,k}^{n+1} &= \left[(\theta_l)_{i,j,k}^{n+1} - (\theta_l)_{i,j,k}^{n}\right] + \frac{\delta t}{r_i \delta r}\left[(\theta_l U_l r)_{i+\frac{1}{2},j,k}^{n+1} - (\theta_l U_l r)_{i-\frac{1}{2},j,k}^{n+1}\right] \\
&+ \frac{\delta t}{\delta z}\left[(\theta_l V_l)_{i,j+\frac{1}{2},k}^{n+1} - (\theta_l V_l)_{i,j-\frac{1}{2},k}^{n+1}\right] \\
&+ \frac{\delta t}{r_i \delta \phi}\left[(\theta_l W_l)_{i,j,k+\frac{1}{2}}^{n+1} - (\theta_l W_l)_{i,j,k-\frac{1}{2}}^{n+1}\right]
\end{aligned}
\tag{3.63}
$$

or if $\theta > \theta^*$, D_g is discretised as in the liquid equation above [10, 36, 23],

$$
\begin{aligned}
(D_g)_{i,j,k}^{n+1} &= \left[(\theta_g)_{i,j,k}^{n+1} - (\theta_g)_{i,j,k}^{n}\right] + \frac{\delta t}{r_i \delta r}\left[(\theta_g U_g r)_{i+\frac{1}{2},j,k}^{n+1} - (\theta_g U_g r)_{i-\frac{1}{2},j,k}^{n+1}\right] \\
&+ \frac{\delta t}{\delta z}\left[(\theta_g V_g)_{i,j+\frac{1}{2},k}^{n+1} - (\theta_g V_g)_{i,j-\frac{1}{2},k}^{n+1}\right] \\
&+ \frac{\delta t}{r_i \delta \phi}\left[(\theta_g W_g)_{i,j,k+\frac{1}{2}}^{n+1} - (\theta_g W_g)_{i,j,k-\frac{1}{2}}^{n+1}\right]
\end{aligned}
\tag{3.64}
$$

At the end of such a computational sweep, if convergence was not obtained in any of the cells, the sweeps are repeated. If a pressure adjustment is necessary in any of the cells, the procedure is repeated until simultaneous convergence in all of the cells is obtained. The number of such sweeps are restricted by specifying maximum allowable number of iterations called as "outer iterations limit" defined for convergence during a time step [36]. If

this number is exceeded, iterative process terminates and current values of $P, \theta_q, U_q, V_q, W_q$ are considered to be satisfactory and the calculations proceed to the next time step, [124]. Amsden and Harlow reported that this number is set to 100 and the usual number of iterations per cycle seldom exceeded 10 in their calculations [3]. However, in [124] it is set to a value of 500, while Lee [78] used 100 steps.

The calculation sequence of the pressure iteration for a single cell involves the following steps:

e.1.If $\mid D_l \mid$ or $\mid D_g \mid > \epsilon$, the pressure, $P_{i,j,k}^{n+1}$, is adjusted. Initial pressure adjustments (corrections) are performed using Newton's point iteration method in each cells as [24, 23, 80, 110, 36];

$$P^{n+1} = P^n + \delta P_{i,j,k} \tag{3.65}$$

by defining $\delta P_{i,j,k}$ as,

$$\delta P_{i,j,k} = -w(\beta D)_{i,j,k} \tag{3.66}$$

gives, for $\theta_{g\,i,j,k} < \theta_{i,j,k}^*$,

$$P_{i,j,k}^{n+1} = P_{i,j,k}^n - w\frac{D_{l\,i,j,k}}{\left(\frac{\partial D_l}{\partial P}\right)_{i,j,k}^{n+1}} \tag{3.67}$$

and for $\theta_{g\,i,j,k} \geq \theta_{i,j,k}^*$,

$$P_{i,j,k}^{n+1} = P_{i,j,k}^n - w\frac{D_{g\,i,j,k}}{\left(\frac{\partial D_g}{\partial P}\right)_{i,j,k}^{n+1}} \tag{3.68}$$

meaning that the new pressure field becomes the sum of the old pressure field and the pressure correction.

Here, w is an over/under relaxation parameter of order unity [4]. Amsden and Harlow [3] stated that since a relaxation procedure based on Jacobi's method is used in this algorithm, the iteration will converge only if $0 < w \leq 1$. Lee and Lyczkowski [80] used w=0.95 in their calculations. A value of 1.0 is used in the present study as it was used by Rivard and Torrey in [110].

Newton's method is continued until $D_{i,j,k}$ changes sign, [110, 32, 36]. After $D_{i,j,k}$ changes sign, the next pressure correction is done by using a constrained two-sided secant method [80, 110]. This method is explained in detail in section 3.6.

e.2. By using equations 3.42 through 3.47 the new time velocities are calculated on the right, top and aft boundaries for both phases. The velocities on the left, bottom and fore boundaries are calculated similarly as described in step c and not mentioned here.

e.3. After that, new gas or liquid mass fluxes (convection terms) depending on whether $\theta < \theta^*$ or $\theta \geq \theta^*$ are determined. Then,

e.4. Case (i) if $\theta < \theta^*$: Equation 3.64 is solved for θ_g^{n+1} by putting $D_g = 0$. Then θ_l is calculated from $\theta_l = 1 - \theta_g$. If $D_l \leq \epsilon$, it is proceeded to the next cell, otherwise new liquid mass fluxes are computed using latest θ_l and velocities, and steps e.1 through e.3 are repeated.

Case (ii)if $\theta \geq \theta^*$: Equation 3.63 is solved for θ_l by putting $D_l = 0$. Then, $\theta_g$is calculated from $\theta_g = 1. - \theta_l$. If $D_g \leq \epsilon$, it is proceeded to the next cell, otherwise new gas mass fluxes are computed using latest θ_g and velocities, and steps e.1 through e.3 are repeated.

The pressure iteration is complete when the maximum value of $(D_g)_{i,j,k}$ or $(D_l)_{i,j,k}$, for all cell elements, is below a pre-defined value. When this condition is achieved, the pressure value is considered to be correct and complete solution to the continuity and the momentum equations has been obtained. This completes a computational cycle [10, 110].

3.5.1　Convergence Criteria

Iteration algorithm, which was mentioned in the previous section, also checks for the convergence criteria and determines how well continuity equations are satisfied [32]. The pressure is adjusted in the computing cells until $\mid D_l \mid$ or $\mid D_g \mid$ depending on θ^*, is less than a specified small quantity, ϵ_q, simultaneously in all cells. The value of the convergence criterion is defined similarly as in [110, 10] and taken as;

$$\epsilon_{q_{i,j,k}} = \begin{cases} \epsilon(\theta_l)_{i,j,k}^n & \text{for} \quad (\theta_g)_{i,j,k}^n < \theta^* \\ \epsilon(\theta_g)_{i,j,k}^n & \text{for} \quad (\theta_g)_{i,j,k}^n \geq \theta^* \end{cases}$$

Gamwo et al. [32] who uses same numerical algorithm assumed ϵ_g as $5 * 10^{-4}$. Broadus et al. [10] made a restriction that this value should be 10^{-5} or less in their code (Beacon).

Here θ^* called as "switch void fraction (SVF) parameter" is defined to determine whether to solve the liquid or gas mass continuity equation in the solution procedure. If the void fraction in a cell is smaller than SVF, the liquid continuity equation is solved, otherwise, the gas continuity equation is solved. Rivard and Torrey [110] states that the use of SVF ensures that D_l is computed in a pure liquid cell and D_g in a pure gas cell. Lee and Lyczkowski [80], Lee and Shah [81] used $\theta^* = 0.001$ in their calculations.

3.6　Secant Method for Pressure Adjustment

As mentioned in the previous sections, pressure-adjustment algorithm is based on the calculation of discrepancies in both gas (D_g) and liquid (D_l) continuity equations. When D_l or D_g fails to satisfy the convergence criteria in $cell_{i,j,k}$, the pressure in that cell is needed to be adjusted [110].

Pressure adjustments are done by using a constrained two-sided secant method which is a combination of the secant method and bisection method after $D_{i,j,k}$ changes sign in the iteration loop of the solution algorithm. The

principles of this method is described in detail by Rivard and Torrey in [110]
and rewritten here:
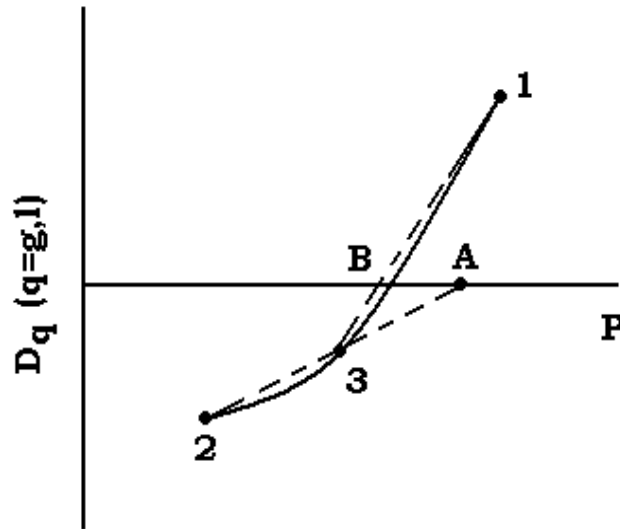
Figure 3.5: Pressure Adjustment Technique [110]

According to this method (see Figure 3.5), given the three points 1,2 and
3, of which 1 and 2 bracket the desired pressure 3 which lies between them,
the pressure P_A and P_B are determined by straight line extrapolation and
interpolation, respectively. The new estimate of the advanced time pressure
is then computed as $P_{i,j,k}^{n+1} = 0.5 * (P_A + P_B)$. If the pressure P_A should lie
outside the interval P_1 to P_3, it is given the value $0.5 * (P_1 + P_3)$. After $P_{i,j,k}^{n+1}$
is estimated, point 2 is discarded and points 1 and 3 are retained as improved
bounds for the next pressure estimate. This method requires knowledge of
two pressures that bracket the desired pressure [110].

3.7 Stability

The numerical difference equations are subject to numerical stability condi-
tions that a volume of fluid cannot move more than one control volume in

one time step that is assured by Courant-Friedrichs-Lewy (CFL) condition described as follows [30].

$$| U | \, \delta t < \delta x \qquad\qquad (3.69)$$

In other words, the amount of fluid which leaves a cell in one time step is no more than the amount of fluid that was originally in the cell.

CFL condition is described by a dimensionless number, $\frac{|u| * \Delta t_{CFL}}{\Delta z}$, Courant Number, and it determines maximum allowable time step for stability [14]. It is well known that the Courant number, should be less than one for accurate results. In FLOW-3D [48], it is stated that if Courant number is allowed to exceed this value, then the convective term will become unstable, i.e., the error will grow with successive iterations.

However, satisfaction of the CFL condition is a necessary condition for stability, but is not sufficient to guarantee stability. Therefore it is a common procedure to select the Courant number $\ll 1$ [21].

CHAPTER 4

COMPUTER CODE

In Chapters 2 and 3, a detailed discussion of the governing equations and a description of the numerical technique that will be used to simulate header component in METU-TPFTF were given.

In order to solve all those separate sets of conservation equations which describe three-dimensional two-phase gas/liquid flow, a two-fluid computer program(code) was developed. This code solves the governing equations in the same order as defined in Chapter 3. In this chapter, outlines of this code are given.

4.1 Programming Environment

The code is written in Fortran-77 language and is compiled by g77 compiler in LINUX environment. All calculations are performed with 3.0 GHz Pentium-IV processor.

4.2 Program Structure

In this section general structure of the code is described. Main program contains following subprograms which have special functions as tabulated in Table 4.1.

Table 4.1: Computer Code Subroutines and Their Functions

Subroutine	Function
BNDRY	applies boundary conditions
DRAG	computes the drag force term, K
DTCALC	computes maximum allowable timestep interval based on CFL condition
EXPLCT	calculates explicit terms in the gas and liquid phase momentum equations
FLAG	sets flags for the cells at which boundary conditions will be applied
GASD	calculates discrepancy in gas mass equation
IMPLCT	controls the iterations, checks for the convergence criteria and updates all variables
INITIAL	defines initial conditions of all variables
LIQD	calculates discrepancy in the liquid mass equation
MAIN	sequences execution of input data processing and transient computation
MFLUXG	calculates mass flux terms for the gas phase
MFLUXL	calculates mass flux terms for the liquid phase
NEWVELS	calculates advanced time velocity components and velocity estimates on the faces of the cells
NFLAG	defines the flags for neighbour cells of each cells
PINTP	calculates new time pressure level from three (P, D_q) points
PDERIV	computes discrepancy, $D_{q_{i,j,k}}$, derivatives with respect to pressure
PPSHR	calculates $\tau_{q_{\phi\phi}}$ terms
PRSHR	calculates $\tau_{q_{\phi r}}$ terms
PZSHR	calculates $\tau_{q_{\phi z}}$ terms
RRSHR	calculates $\tau_{q_{rr}}$ terms
RZSHR	calculates $\tau_{q_{rz}}$ terms
UGFLX	calculates gas phase momentum flux terms in r direction
ULFLX	calculates liquid phase momentum flux terms in r direction
VGFLX	calculates gas phase momentum flux terms in z direction
VLFLX	calculates liquid phase momentum flux terms in z direction
WGFLX	calculates gas phase momentum flux terms in ϕ direction
WLFLX	calculates liquid phase momentum flux terms in ϕ direction
ZZSHR	calculates $\tau_{q_{zz}}$ terms

The program calculation sequence starts with the MAIN program where the input data are read. MAIN program initializes system geometrical properties, physical properties of two phases and also settles 1 inlet and 5 outlet nozzles connected to the main body of the header. Then subroutine INITIAL sets the initial values of pressure, void fraction and velocities of each phases. The control then passes to subroutine FLAG. FLAG assigns values to the cells including ghost ones that is used to distinguish the various types of cells in the computing mesh. The flags of the each cells are designated according to the Table 4.2.

Table 4.2: Flag Definitions

FLAG	Cell Type
1	Fluid Cell
2	Free-Slip Boundary
3	No-slip Boundary
4	Inflow Boundary
5	Constant Pressure Boundary
6	Periodic Boundary

Except from the ghost cells which describe boundary conditions, all cells are assigned value of 1 to indicate being a "fluid cell". After that, subroutine NFLAG is called and flags of each 6 neighbour cells (top, right, bottom, left, aft and fore cells) are put into arrays for each computational cells.

Subroutine BNDRY, then checks for NFLAG arrays and sets the boundary conditions around the computational mesh perimeter. If BNDRY finds a boundary cell in any mesh sweep operation for $cell_{i,j,k}$ during the calculations, it sets boundary values for related variables for the fictitious cells around $cell_{i,j,k}$.

Table 4.3 summarizes available boundary types defined in the code by use of ghost cells surrounding the computational grid. For example, constant pressure outflow boundary can be prescribed along the top, right and

left boundaries, while inflow can be prescribed along the bottom and right boundaries. Due to three-dimensional computation, tens of different combinations specifying boundary cells have been defined in the code.

Table 4.3: Available Boundary Condition Flags for Cells

Cell Face	Flags				
	2	3	4	5	6
Top	-	√	-	√	-
Bottom	-	√	√	-	-
Right	-	√	√	√	-
Left	√	√	-	√	-
Aft	-	-	-	-	√
Fore	-	-	-	-	√

The momentum flux terms (convective terms) for the gas field are then evaluated in subroutine UGFLX, VGFLX, WGFLX, whereas those for the liquid field are evaluated in subroutines ULFLX, VLFLX and WLFLX. The viscous stress terms were calculated in 6 separate subroutines named ZZSHR, PZSHR, RZSHR, RRSHR, PRSHR, PPSHR.

EXPLCT puts all explicit terms came from the convection, gravity and viscous stress terms into a single term for all cells. The gas and liquid convection terms are then computed by using advanced time velocities obtained from flux routines, are calculated by calling MFLUXG and MFLUXL, respectively. In addition K^n is also computed by DRAG subroutine. PDERIV then calculates the values of $\frac{1}{\beta_{i,j,k}}$ that may be later used for pressure iterations.

Subroutine IMPLCT takes the control of the iterative part of the solution. When needed, the pressure is adjusted in IMPLCT by calling PINTP in the cells until D_g or D_l in equations 3.64 and 3.63 depending on whether $\theta \geq \theta^*$ or $\theta < \theta^*$, is less than a specified small quantity, $\epsilon_g or \epsilon_l$, simultaneously in all cells as the methodology applied in K-FIX and BEACON codes [110, 10]. It has also some calls to NEWVELS, MFLUXL, MFLUXG to calculate n+1

time level quantities for the velocity and volume fractions during iterations.

To have a physically realistic solution, the void fraction must be kept within the physical range of zero to one during the iterations. In IMPLCT, following procedure is installed as used in most of the two-fluid algorithms [8, 99].

$$\theta_g = MIN\Big[MAX(\theta_g, 0.0), 1.0\Big] \qquad (4.1)$$

Finally, subroutine DTCALC determines the time step size based on CFL criteria for the next time iteration which is described in the following section. At the end of the calculations, MAIN takes the control again and displays the time, time step size, and last iteration number on the output in order to control the program execution.

4.3   Time Step Control

In time step control algorithm a maximum δt is calculated to allow a good time convergence of the code predictions. Since the solution algorithm is semi-implicit, the Courant-Friedrichs-Lewy (CFL) limit check is done before a time advancement takes place [10]. This limit is evaluated by finding maximum velocities $(U_{max}, V_{max}, W_{max})$ which are the absolute maximum velocities in each volume of i,j,k in r,z and ϕ directions for each phase of q (e.g., $U_{max} = max(U_{g\,i+\frac{1}{2},j,k}, U_{l\,i+\frac{1}{2},j,k})$), respectively [10, 54, 62].

Then the code finds a Δt_{CFL} value among minimum of $\frac{\delta r}{U_{max}}, \frac{\delta z}{V_{max}}, \frac{r_i \delta \phi}{W_{max}}$ stating that;

$$\Delta t_{CFL} \leq min(\Delta z / \mid u \mid) \qquad (4.2)$$

Broadus et al. stated in [10] that to obtain best numerical results, timestep should be less than a tenth of Courant timestep or less.

In the code, first time step is specified by the user as Δt_{INP}. Time step control module DTCALC calculates the next time step value, Δt^{n+1}, by taking minimum of Δt_{INP} and Δt_{CFL} found from Equation 4.2. Computations continue until the time exceeds t_{STOP}.

4.4 Steady-State Convergence

Steady-state convergence of the transient solution can be characterized by a L_2 norm of error (root mean square error) defined as [97];

$$L_2 = \sqrt{\frac{\sum_{i,j,k} \mid \chi_q^{n+1} - \chi_q^n \mid^2}{N_{ijk}}} \tag{4.3}$$

where χ_q is the corresponding cell variable ($\vec{u_q}$, θ_q or P) at the $cell_{i,j,k}$. n and n+1 represents two preceeding time steps. N_{ijk} is a number of computational nodes used. After reaching the steady-state there is no need to continue further in computation. An algorithm which calculates such errors for each variable at each time step is placed into the code to observe whether the solution approaches to steady-state or not.

CHAPTER 5

NUMERICAL BENCHMARK STUDIES

5.1 Introduction

The numerical modelling described in the previous chapters will be applied to numerical experiments (numerical benchmark tests) to verify the relevance and the validity of the scheme. In this chapter, the results obtained from the benchmark tests of "Water Faucet Problem", "Pure Radial Symmetric Flow Problem" and "$R - \phi$ Symmetric Flow Problem" are reported, respectively.

5.2 Water Faucet Problem

Water Faucet Problem is actually a one-dimensional problem which simulates resolution of volume fraction waves. This test case was first introduced by Ransom [109] in 1987 and Ransom has proposed an approximate analytical solution to the problem.

This problem has previously been used by several authors [25, 14, 13, 102, 108, 34] for testing the ability of their proposed numerical schemes and has been established as a well-known standart numerical benchmark for the performance evaluation of numerical methods developed for the two-fluid model. So it was selected to test the present numerical solution method.

Objectives of this benchmark problem are defined by Ransom [109] and Nae et al. [93] as;

- Testing the interaction of the body force term with the temporal and convective acceleration terms in the momentum formulation.

- Testing the void fraction characteristic.

- Testing the stability and convergence.

- Testing the diffusive character of the numerical scheme since a discontinuity in the void fraction is formed and propogated through the solution domain.

- Testing the boundary conditions.

5.2.1 Definition of the Problem

In this problem, a water column surrounded by air, flows at a constant velocity of 10 m/s and a void fraction of 0.2 into the top of a vertical tube of 12 m lenght and 1 m in diameter [109, 65].

Top of the tube is close to the air flow while the tube is open to ambient pressure at the bottom. The system is isothermal and adiabatic [109].

A gravity field $g = 9.8m/s^2$ is applied upon the simulation start (t=0), resulting the water column to accelerate. The water column gets thinner due to acceleration. Several stages of the process are shown in Figure 5.1. This figure shows the propagation of the void profile down the tube until the wave has completely passed out of the tube and the steady-state profile remains.

The initial conditions of this problem are tabulated in Table 5.1, while boundary conditions are shown in Table 5.2 . Implied velocities are defined as inflow and constant pressure of $10^5 Pa$ is defined as outflow boundary conditions. At the outlet, the remaining variables $\vec{u_q}$'s and θ_q's at the boundaries are determined by simple extrapolation.
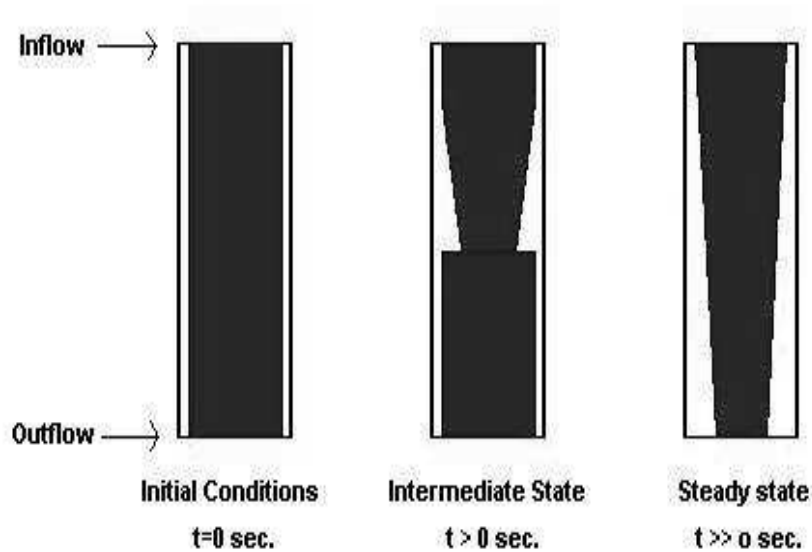
Figure 5.1: Water Faucet Problem: Schematic of Time Evolution of Liquid Column

Table 5.1: Initial Conditions of Water Faucet Problem

	liquid phase (water)	gas phase (air)
density	$1000 kg/m^3$	$1 kg/m^3$
pressure	10^5 Pa	10^5 Pa
velocity	10 m/s	0 m/s
volume fraction	0.8	0.2

Table 5.2: Boundary Conditions of Water Faucet Problem

		Water	Air
Inflow (top)	velocity	10 m/s	0 m/s
	volume fraction	0.8	0.2
Outflow (bottom)	pressure	10^5 Pa	10^5 Pa
	volume fraction	extrapolated	extrapolated

If pressure variation is ignored [13, 27], under the assumption that the liquid is incompressible , this problem has an approximate analytical solution for this problem was given by Ransom [109] for the liquid velocity and void fraction as:

$$
V(z,t) = \begin{cases} \sqrt{V_o^2 + 2gz} & for \;\; z < V_o t + gt^2/2 \\ V_o + gt & otherwise. \end{cases}
$$

$$
\theta_g(z,t) = \begin{cases} \theta_o(1 + 2gzV_o^{-2})^{-\frac{1}{2}} & for \;\; z < V_o t + gt^2/2 \\ \theta_o & otherwise. \end{cases}
$$

This analytical solution is used to test the code's predictions. For simplicity, interfacial drag force is neglected in this problem as suggested by Gallouet et al. [31] and suggested in Relap5/Mod3 [115].

5.2.2 Numerical Results

The code's predictions of the gas volume fraction, θ_g, and liquid velocity, V_l, are compared with the exact solutions obtained from the above equations. An increasing number of cells were used in five numerical tests with 40, 80, 160, 320 and 480 cells in the z direction. The calculation was carried out until a steady-state flow profile is obtained.

Figure 5.2 shows the numerical results by comparing the analytical solution of this problem for gas volume fraction at time=0.4 s while Figure 5.3 shows the liquid velocity at t=0.4 s. Both figures were obtained by using Courant number(CFL)=0.1. It is seen that especially at the cells near the inflow opening, consistent results with the analytical solutions are obtained. Near the discontinuity, a small undershot is observed which becomes more noticable when using finer grids above 320 cells. Such phenomenon is also reported by Paillere [102] and Karni et al. [65] in using finer grids.

Grid refinement resulted in good improvements on the void fraction and liquid velocity. However it seems that after 480 cells not much improvement
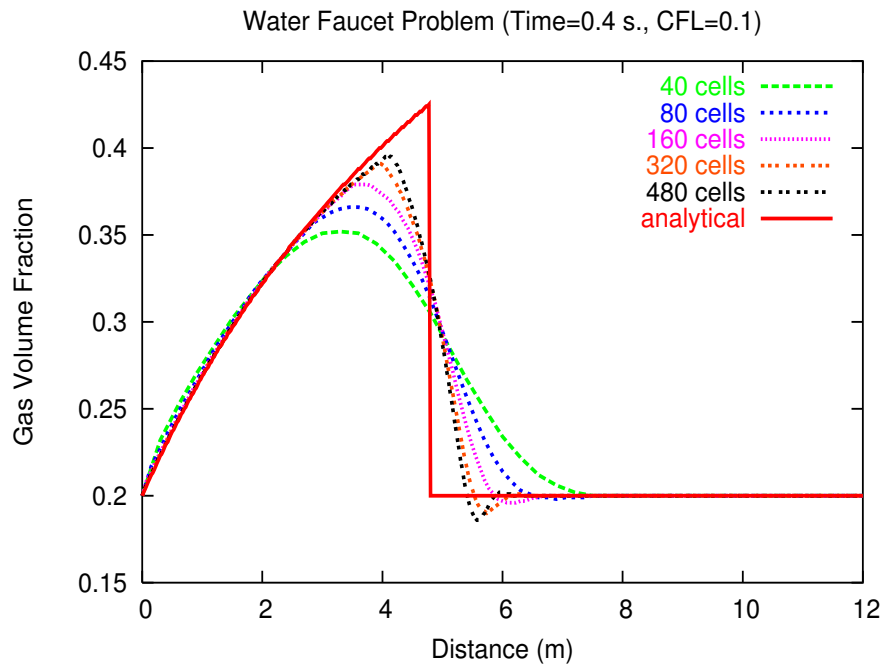
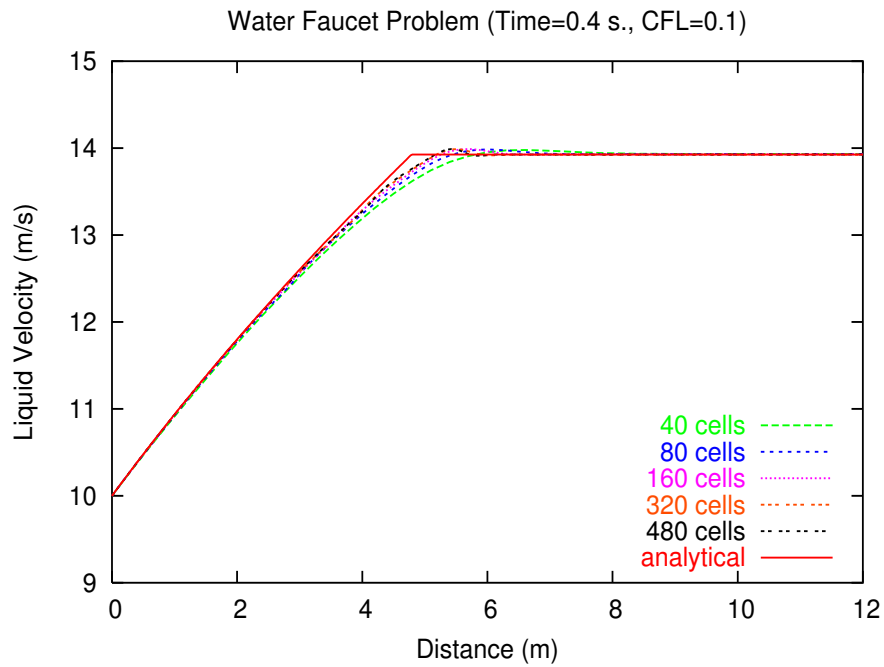Figure 5.2: Transient Void Fraction Profile for 40, 80, 160, 320, 480 Cells at t=0.4 sec.

Figure 5.3: Transient Liquid Velocity Profile for 40,80,160 and 320, 480 Cells at t=0.4 sec.

is expected and undershot near the discontinuity is expected to grow. Boundary conditions are working well and no instability oscillations were observed during numerical solution stage.

In order to test the effect of using smaller time steps, CFL number is reduced to 0.01 and tested for 40 through 480 cells. The results are more satisfactory than that of obtained for CFL=0.1 at t=0.4 s as can be seen in Figure 5.4 and Figure 5.5. Small undershots observed in Figure 5.2 in using finer grids are disappeared by reducing the time step. Figure 5.6 shows the void fraction evolution for 480 cells in z direction. Contact discontinuity is propogated along the tube and completely passed out of the tube as expected. Finally, the steady-state profile is attained. The code seems to simulate this behaviour reasonably good.
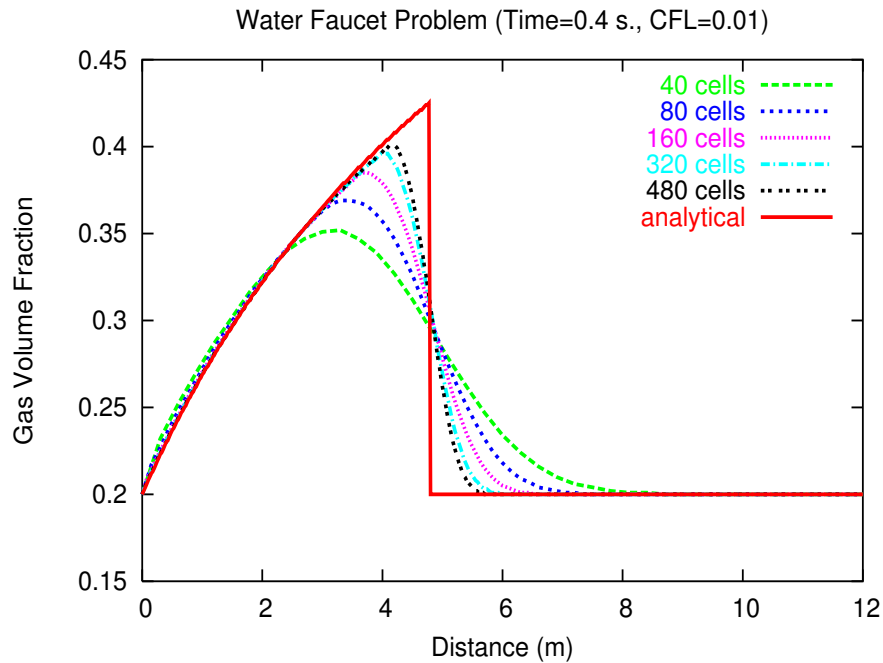

Figure 5.4: Transient Void Fraction Profile for 40, 80, 160, 320 and 480 Cells at t=0.4 sec.

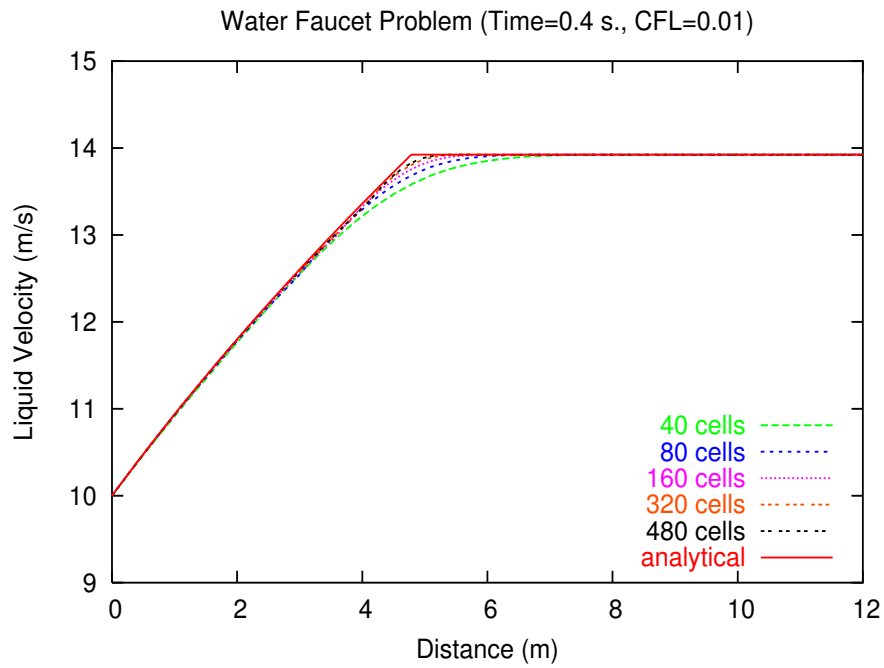Those results obtained in simulating water faucet benchmark problem are

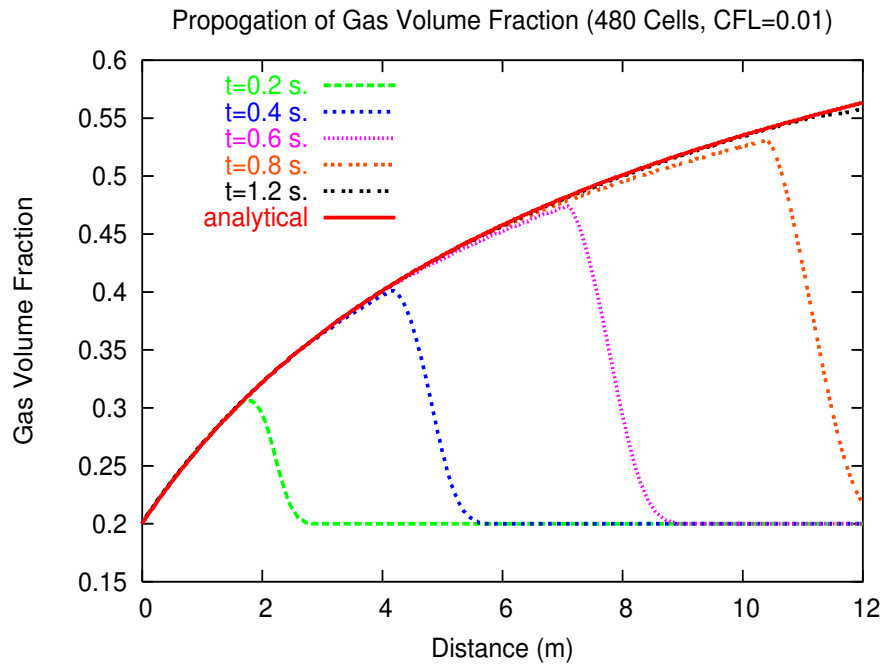Figure 5.5: Transient Liquid Velocity Profile for 40, 80, 160, 320 and 480 Cells at t=0.4 sec.

Figure 5.6: Void Fraction Propogation Along The Channel for 480 Cells

also in good agreement with so many works found in the literature presented below.

In 1997, Coquel et al. [13] used a constant ratio, $\delta t/\delta x = 5.0 * 10^{-4}$, in their simulations of faucet problem by using upwind scheme and Roe scheme. They used 12 through 200 cells. They showed that using finer grids resulted more closer results. However they observed some discrepancies near channel inlet.

In 1999, Paillere et al. [103] tested three schemes namely AUSM+, VFFC and Roe with this problem and found that results are virtually indistinguishable from one another.

In 2000, Paillere [102] obtained very close results with the analytical solution by using AUSM+ scheme. He presented the results for t=0.5 s. which show the behaviour of void fraction and liquid velocities for 20 to 1280 cells. Only in the case of 1280 cells case, a small overshoot and undershot has been observed before and after discontinuity respectively.

Ramos [108] studied water faucet problem and obtained results for t=0.5 s. by using 100 to 4500 points in one-dimensional grid. He showed that grid refinement has resulted more accurate results for void fraction and liquid velocity. He did not observe any over/undershoots near discontinuity.

In 2001, Ghidaglia et al. [35] and Kumbaro et al. [69] tested and gave the results for 192 cells (Figure 5.7) using central differenced finite volume discritization. They also showed that using fine grids resulted more closer results. However, they found that numerically unstable results obtained when so small δx is used.

In 2002, Cortes [14] used a finite volume explicit numerical method and density perturbation method to simulate two-phase multidimensional flow. He tested this model with faucet problem by using 120 and 480 cells and observed that results were in good agreement with the analytical solution especially in finer grids. He used constant CFL number having a value of 0.98.
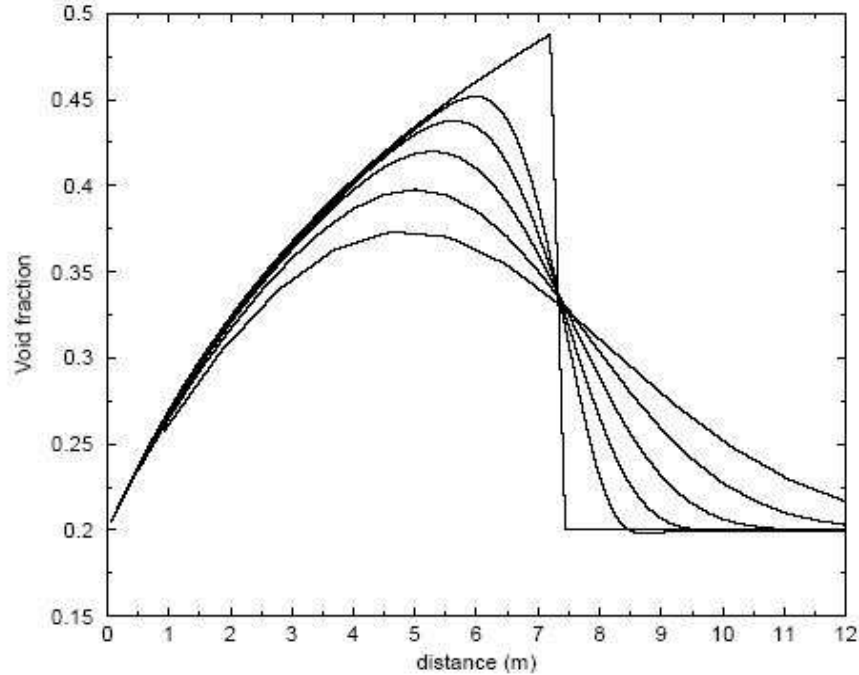
Figure 5.7: Void Fraction Profile at t=0.6 s., Ghidaglia et al. [35].

Nourgaliev et al. [97] introduced a new characteristic-based semi-implicit two-phase flow model and tested it with faucet problem by using two different liquid velocities (10 m/s and 15 m/s). They showed that higher-order schemes (ENO,WENO) are superior than the first-order accurate scheme in capturing discontinuity. The first-order scheme produced oscillatory solution with grid refinement.

Dinh et al. [19] gave the simulation results for faucet problem by using incompressible and isothermal two-fluid model for 100 nodes. With grid refinement (1000 nodes) the numerical solution sharpened and an overshoot became evident at a later time moment.

Evje and Flatten [25] presented the results of AUSMD, AUSMV and Roe schemes for void fraction and liquid velocity profile at t=0.6 s by refining mesh (using 24 through 1200 cells). They obtained more closer results by using ROE scheme.

74

In 2004, Karni et al. [65] tested their upwind schemes on the water faucet problem and found the results are in very good agreement with the exact solution. But in using finer grids, they saw over and undershootings (Figure 5.8) around the discontinuity line.
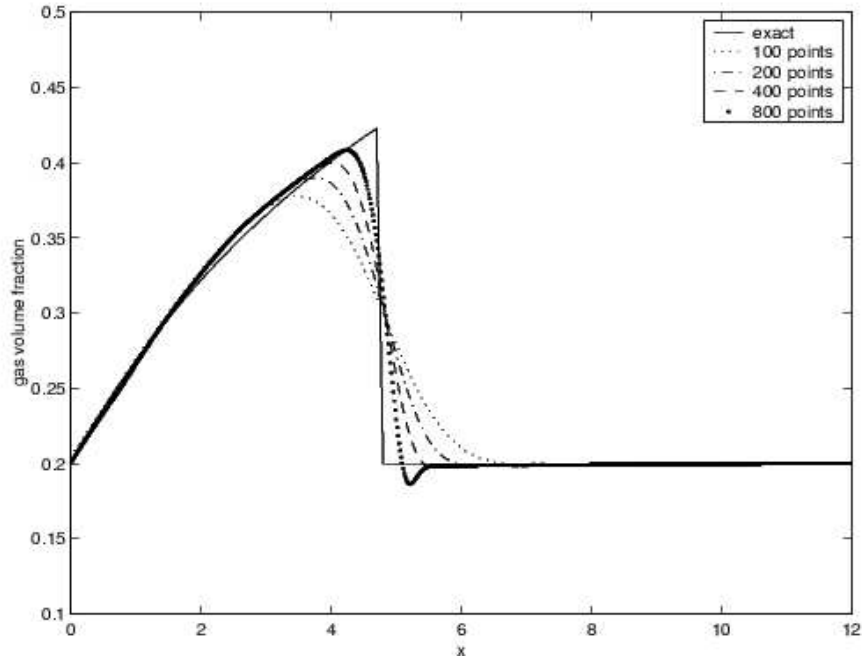

Figure 5.8: Void Fraction Profile at t=0.4 s., Karni et al. [65].

As a summary; the presented two-fluid model is tested with the water faucet benchmark problem and convergent and stable results are obtained with mesh refinement and decreasing of CFL number for overall transient behaviour. The numerical results are in good agreement with the analytical solution proposed by Ransom [109]. The results showed somehow deviations from the exact solutions especially near the discontinuity, but almost all studies in the literature shows more or less the same behaviour. Gravity effect, void propogation and diffusive character of the numerical scheme are observed in the present study. Also boundary conditions worked very well during the simulation.

5.3 Pure Radial Symmetric Flow Problem

Pure Radial Symmetric Problem has been used to test Relap5-Mod3 [56]. It is used to demonstrate that the equations in radial coordinates have been correctly coded and is used to validate numerical algorithm. This problem represents a hollow cylinder with a symmetric flow pattern (Figure5.9) in the radial direction in which the flow is assumed to be steady and incompressible. In order to simulate this problem, a one dimensional version of the code was generated by not making any change to the IMF numerical algorithm for gaining cpu time and for responding more faster to the problems that might occured during simulations.
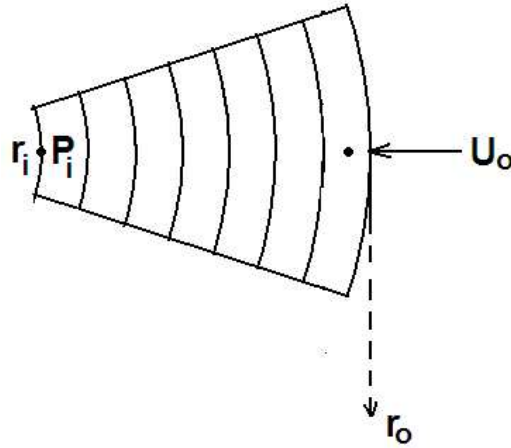

Figure 5.9: Pure Radial Symmetric Flow Problem Geometry

This problem has an analytical solution for velocity from the continuity equation and an analytical solution for pressure from the r-momentum equations. The analytical solutions can be written as;

$$U_l = U_o(r_o/r)$$ (5.1)

$$P = P_i - \frac{\rho_l(U_o r_o)^2(r_i{}^2 - r^2)}{2(r_i r)^2}$$ (5.2)

All azimuthal velocities are set to 0 m/s, pressure at the 1 m. radius position is 5x10^5 Pa, and radial velocity at the 7.5m radius position is 0.8667 m/s. (from outside to inside). Therefore, constant pressure boundary is defined for the left side (FLAG=5) of the innermost cells, while radial inflow boundary conditions are defined for the right side (FLAG=4) of the outermost cells.

Table 5.3: Two-Fluid Parameters Used to Simulate Single-Phase Flows

Assumptions	liquid density (kg/m^3)	gas density (kg/m^3)	void fraction
Set-1	1000.0	999.999	any
Set-2	1000.0	1.0	0.001

Since this problem is defined actually as a single-phase problem, the two-fluid model is used to simulate single-phase flow in two sets of assumption by using parameters shown in Table 5.3.

Both assumptions summarised in Table 5.3 are tested and gave very close results to each other, therefore here only the results obtained from Set-2 are presented.

5.3.1 Numerical Results

Figure 5.10 and 5.11 compares the numerical results with the analytical ones. Code results are in good agreement with the analytical solution. Radial velocity profile obtained by using 1040 cells in radial direction overlapped the exact solution curve.

Pressure adjustment algorithm worked very well and pressure profile obtained by using 520 and 1040 cells in radial direction is shown in Figure 5.11. As can be seen in this figure, using fine grids gave more satisfatory results.
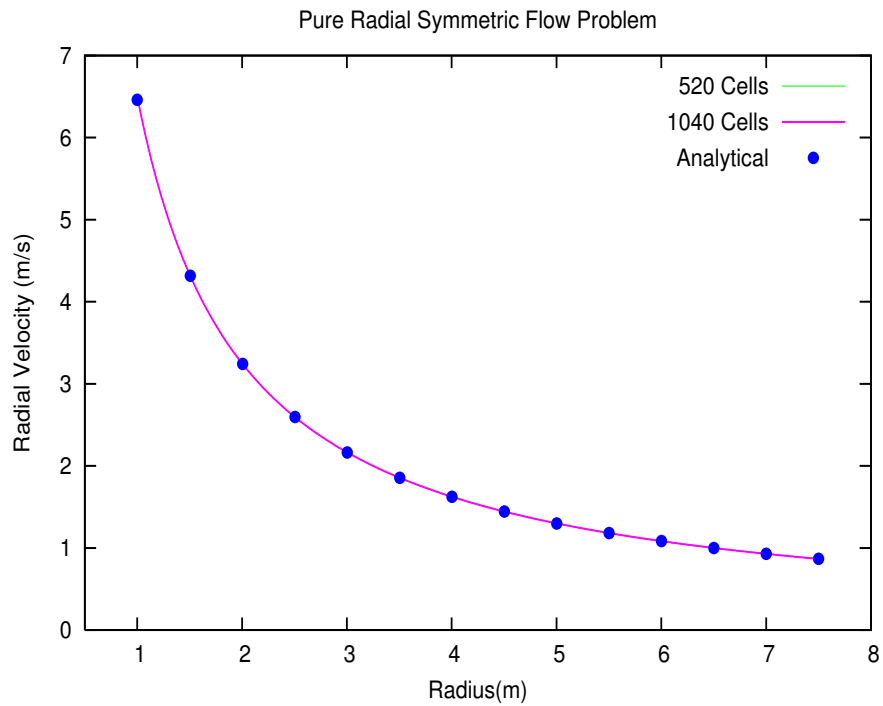
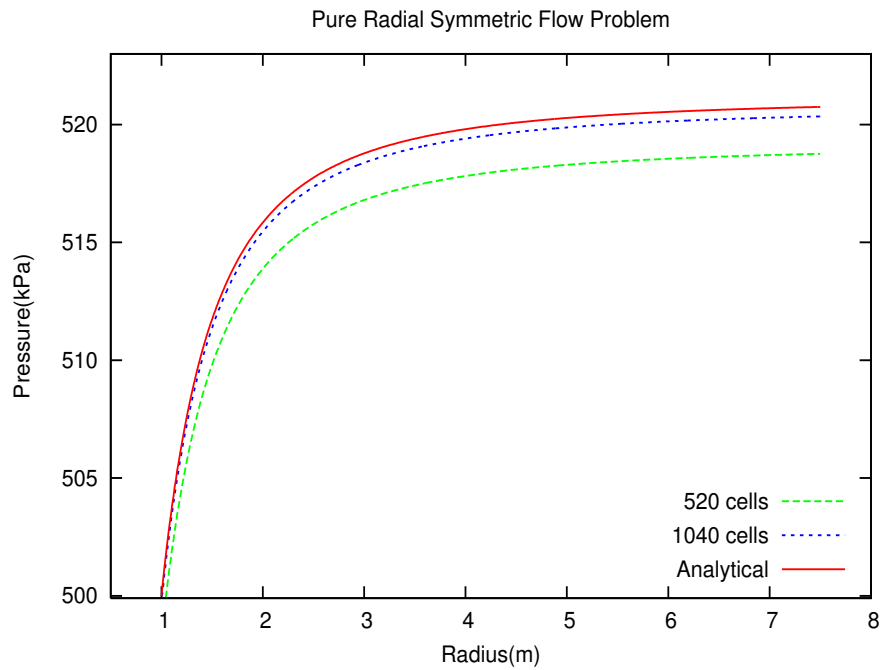Figure 5.10: Radial Liquid Velocity Profile (520, 1040 Cells in Radial Direction)

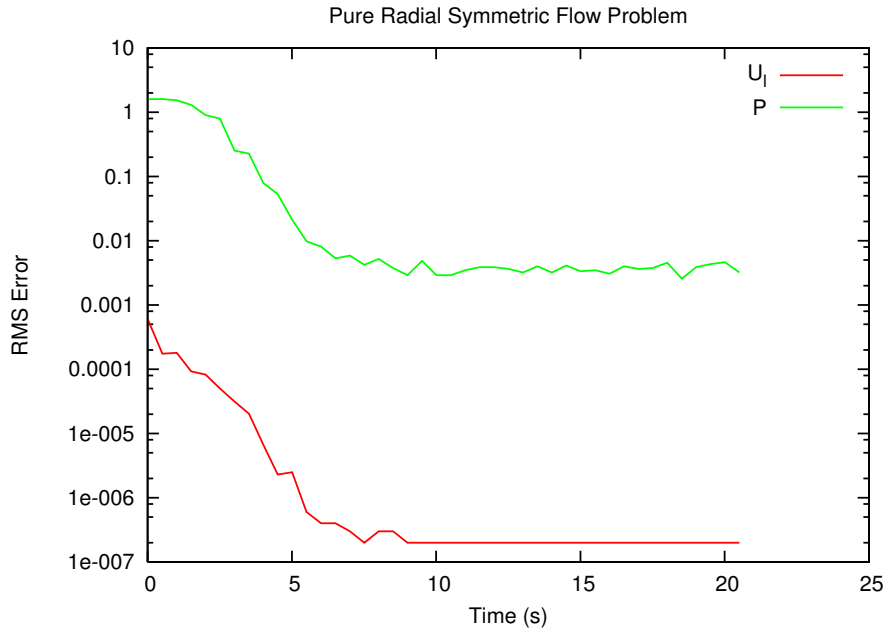Figure 5.11: Radial Pressure Profile (520, 1040 Cells in Radial Direction)

Figure 5.12: Convergence History (1040 Cells in Radial Direction)

Convergence history of the problem can be seen in Figure 5.12 for 1040 cells. In simulating this problem, the code is successively run from initial conditions through steady-state solution iteratively.

5.4 R-ϕ Symmetric Flow Problem

R-ϕ Symmetric Flow Problem has also been used to test Relap5-3D [56]. It is used to demonstrate that the equations in radial and azimuthal coordinates have been correctly coded cooperatively and it is used to test the numerical algorithm. This problem again represents a hollow cylinder with a symmetric flow pattern in both radial and azimuthal directions as shown in Figure 5.13. To simulate this problem, a two-dimensional version of the code was generated by not making any change to IMF numerical algorithm for the same reasons stated previously.
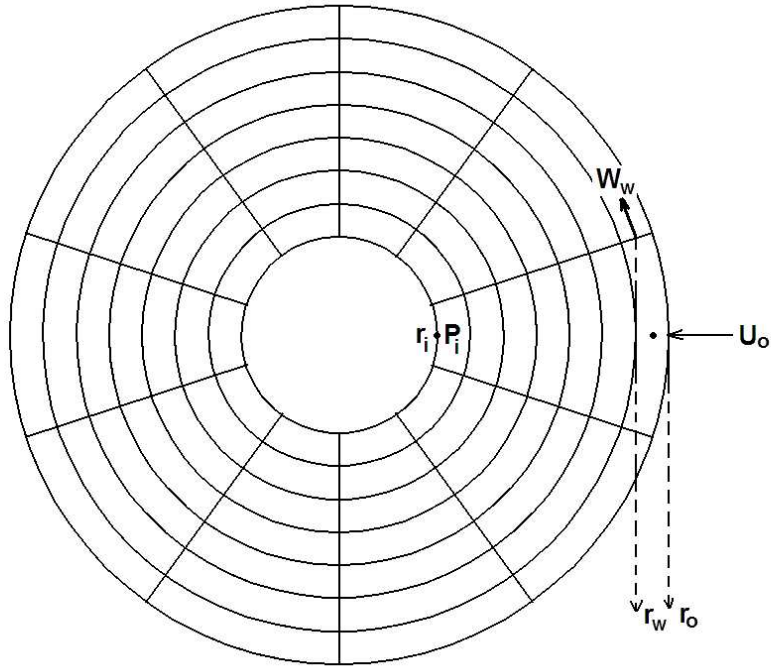
Figure 5.13: R-ϕ Symmetric Flow Problem Geometry

In this problem, the azimuthal velocity at the 6.5 m radius position is 1 m/s, while pressure at the 1 m. radius is set to $5\text{x}10^5$ Pa. Radial velocity is defined as 0.8667 m/s at the 7.5 m radius position from outside to inside. Parameters defined in Set-1 of Table 5.3 is used to simulate this problem. Constant pressure boundary is defined for the left side (FLAG=5) of the innermost cells, while radial inflow boundary conditions are defined for the right side (FLAG=4) of the outermost cells. Periodic boundary conditions (FLAG=6) are imposed to the cells found next to the start and finish lines of each angular sweep.

The analytical solutions can be written as;

$$U_l = U_o(r_o/r) \tag{5.3}$$

$$W_l = W_w(r_w/r) \tag{5.4}$$

$$P = P_i - \frac{\rho_l[(U_o r_o)^2 + (W_w r_w)^2](r_i{}^2 - r^2)}{2(r_i r)^2} \qquad (5.5)$$

5.4.1 Numerical Results

219 cells in r-direction and 55 cells in ϕ-direction are used to simulate this benchmark problem. Figure 5.14 compares the radial velocity profile obtained from code's simulation with the exact solution expressed by Equation 5.3. While Figure 5.15 gives the calculated azimuthal velocity profile in comparison with the analytical solution (Equation 5.4). Numerical results indicate that both velocity profiles are in good agreement with the analytical solution. Pressure profile (Figure 5.16) is also found to be very close to that of exact solution, Equation 5.5. Convergence of the variables to steady-state can be seen in Figure 5.17.

The code simulated this two-dimensional problem reasonably good. Periodic boundary condition implementation in angular direction is tested with this problem and worked very well in combination with the other type of boundary conditions. The numerical algorithm is successively tested in two dimensional, r and ϕ, geometry.

Considerable experience has been gained in the benchmark studies;

- to reduce the code running failures,

- to implement various, problem specific boundary conditions correctly,

- to test all momentum equations one by one,

- to validate pressure adjustment algorithm with continuity equations.
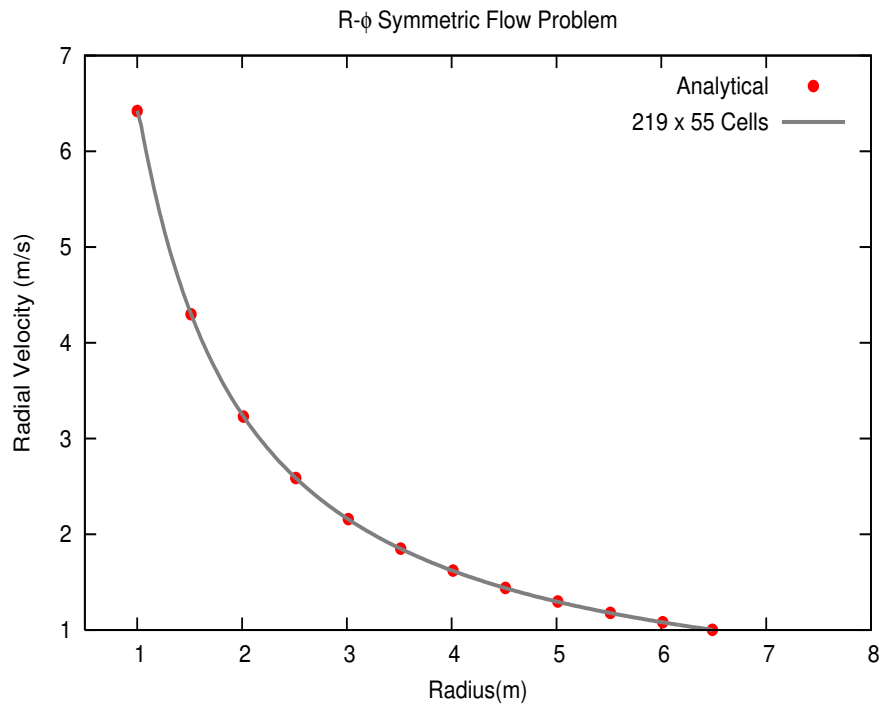
Figure 5.14: Radial Liquid Velocity Profile, 219 x 55 Cells
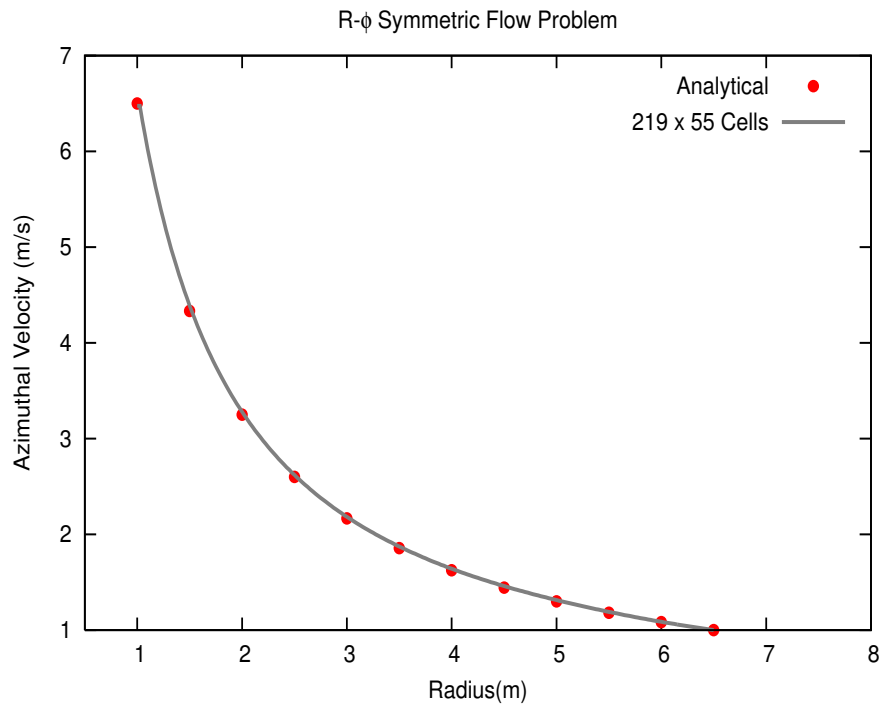
Figure 5.15: Azimuthal Liquid Velocity Profile, 219 x 55 Cells
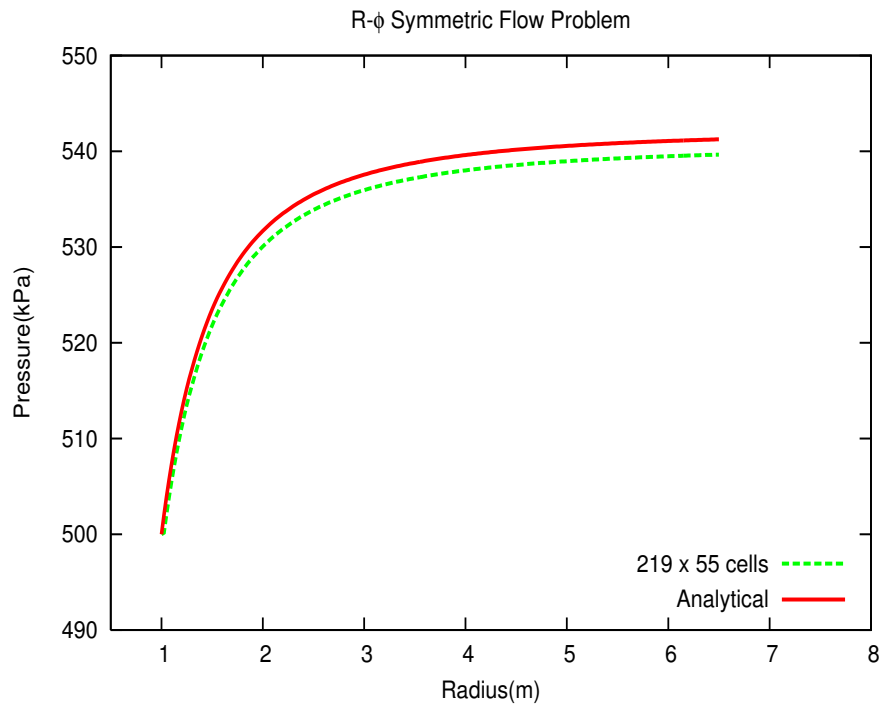
Figure 5.16: Radial Pressure Profile, 219 x 55 Cells
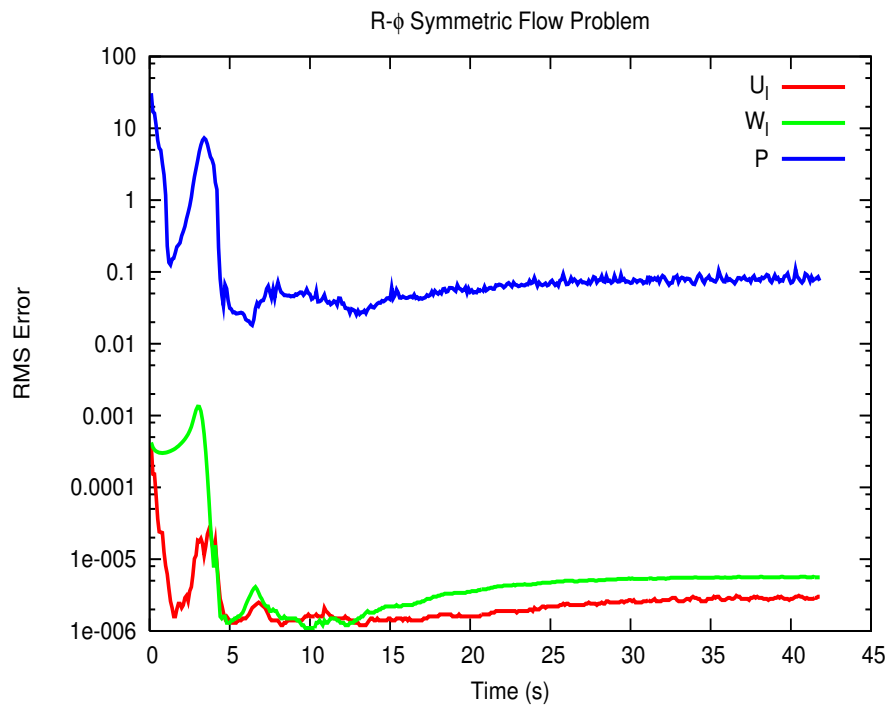
Figure 5.17: Steady-State Convergence History, 219 x 55 Cells

The two-fluid numerical algorithm also worked properly for simulating single-phase problems by using two-phase equations in one and two dimensions with the help of assumptions given in Table 5.3. The code's verification studies in three-dimensional geometry under single and two-phase conditions will be presented in Chapter 7.

CHAPTER 6

EXPERIMENTAL STUDIES

A number of tests have been done to predict two-phase flow distribution through the outlets of the header component in METU Two-Phase Flow Test Facility (METU TPFTP). The results obtained from these tests will provide a data set for validating the code's capability.

As mentioned in Chapter 1, knowledge of two-phase flow discharging through multiple branches is essential for the design and/or performance prediction of such header/feeder systems. However the studies reported on two-phase distribution in those systems are limited in number.

In 1997, Hassan et al. [45] presented experimental data for the mass flow rate and quality during single, dual and triple discharge from a stratified air-water region through small side branches (d=6.35 mm) installed on a semicircular wall. They conducted tests at two system pressures of 316 kPa and 517 kPa. They showed the effect of wall curvature on the mass flow rates of both phases and qualities. But they did not make an attempt to correlate those data.

An important contribution came from the studies of Parrott [105] in 1999. He conducted a series of tests on the RD-14M inlet header to determine the phase distribution within the header and flow and phase distribution in each

of the five feeders. They found asymmetric phase distribution in the header in both axial and latitudinal directions which causes uncover of feeder nozzles and void presence in the feeders. He also performed water only and steam only single-phase tests under different test conditions.

Ingham et al. [57] conducted single- and two-phase natural circulation experiments in the RD-14M facility and studied on the steam bubble entrainment and flashing mechanisms of void penetration of inflow headers.

In 1999, Osakabe et al. [100] studied on the flow distribution mechanism of the horizontal header for water with or without air and proposed a prediction method for water distribution behavior in horizontal header (40 mm x 40 mm in cross section) with four vertical branch pipes (10 mm i.d.) located at constant intervals (130mm). The prediction results agreed well with the experimental water distribution at a small amount of bubbles. They also concluded that the bubble contamination significantly affects the flow distribution in the header and if a uniform flow distribution to branch pipes is intended to achieve, it is recommended to avoid the contamination of bubbles in the header.

In 2000, Lee and Lee [79] investigated the two-phase flow behavior at the header-channel junctions simulating the corresponding parts of compact heat exchangers. The flow configuration in the square shaped header was upward co-current flow and the 6 number of rectangular parallel channels were connected to the header horizontally. The experiments were carried out for the annular flow regime at the header inlet. They analysed the effect of intrusion depth on flow distribution for this type of geometry.

In 2001, Maier et al. [86, 85] investigated the phenomenon of the onset of the liquid entrainment for the condition of the simultaneous discharge from a stratified air-water two-phase region through two horizontal branches mounted on a vertical wall theoretically and experimentally.

In 2002, Chandraker et al. [12] developed a mathematical model to evaluate the flow distribution in the feeders and the pressure distribution, however,

in the outlet header. They used continuity and momentum equations and also a discharge equation for the lateral flow through feeders to solve these distributions numerically by assuming incompressible flow in the header. The model has been validated with experimental data and they reported the flow distribution in the channels is dependent mainly on the header pressure distribution and the hydraulic resistances of the individual coolant channels and connected feeders.

In 2003, Teclemariam et al. [125] investigated two-phase (air-water) flow distribution in a scaled CANDU horizontal header (484.8 mm long, 38.1 mm i.d.) with two inlet turrets (36.2 mm i.d.) and six banks of five feeder pipes (6.4 mm i.d.) experimentally. They tested both one and two inlet turret injections in 16 tests. Outlet flow rates of air and water were measured in all of the feeders under the condition of equal pressure drop across all feeders. They concluded that the phase distribution in the header affected the gas and liquid flows in the feeders, and phase and flow distributions in the feeders were strongly affected by the inlet gas and liquid flow rates.

In 2004, Horiki et al. [51] studied on the flow distribution mechanism of a horizontal thin flow header with four vertical pipes to distribute feed water for a compact heat exchanger. They modified the prediction method of Osakabe et al. [100] with the simple iteration procedure for distribution behaviour to take account of the frictional pressure loss in the header. They presented the results of experimental study conducted with several kinds of thin rectangular and small square headers.

Most of these studies showed that two-phase flow distribution is uneven among the multiple outlet branches and there is a need to perform more studies for predicting two-phase flow distribution experimentally and especially numerically. The results were also seemed geometry specific and the effects of more parameters (distance between the branches, relative angular locations of the nozzles etc.) should be analysed [125, 86].

In the following sections, detailed information about experimental studies

performed on the METU-TPFTF is given.

6.1 Experimental Test Facility

Schematic diagram of the METU TPFTF used in the present study is shown
in Figures 6.1. The facility consists of a cylindrical header (19.4 cm i.d. and
1.1 m lenght) with 5 feeders which were made of transparent PVC and acrylic
for the observation purposes (see Figure 6.2). Each feeder connects to the
lower half of the header through nozzles at different elevations and different
angles. As shown in Table 6.1 there are two horizontal nozzles (2 and 6), two
nozzles (4 and 5) 36° down from horizontal, and one nozzle (nozzle-3) 72°
down from horizontal feeders. Also an injection nozzle (nozzle-1) is placed
on near one end of the header (See Figure 6.1). Air and distilled water is
used as the test fluids in this facility.

Table 6.1: Feeder Geometries

Nozzles	Inner Diameter (cm)	Connection Angle with Vertical Axis
Inlet	7.79	90°
Feeder-2	3.45	0°
Feeder-3	3.45	288°
Feeder-4	2.54	324°
Feeder-5	2.54	216°
Feeder-6	2.54	180°

The facility consists of a WILO-MHI 405 series water-circulating pump
which is connected to the bottom of a 100 liters of water-storage tank. Water
is drawn from this storage tank by means of the pump and introduced into
the water line. After pump, there is a by-pass line which is used to arrange
flow rate of water. The pipes in water supply line are made of plastic and
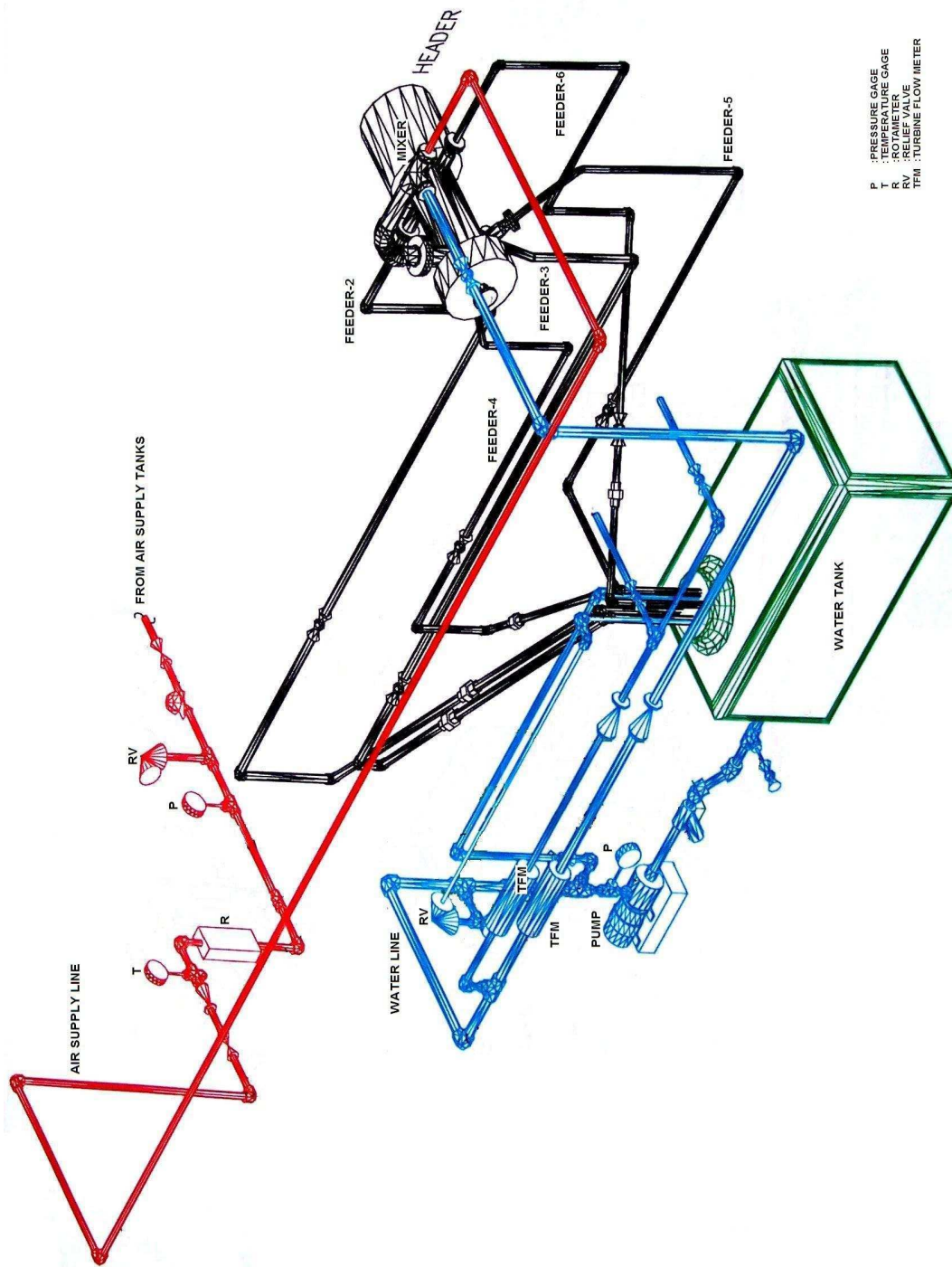have inlet diameters of 38 mm.

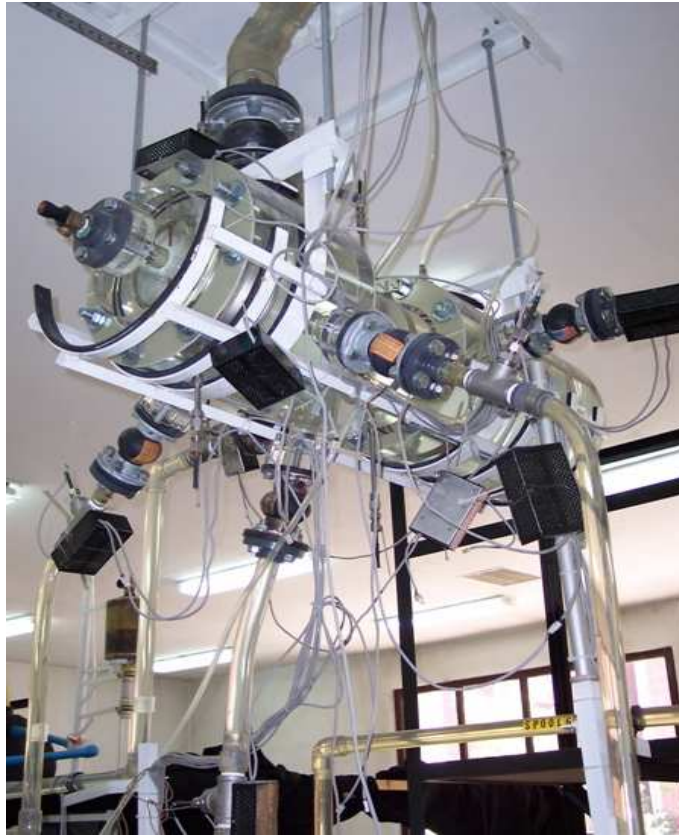Figure 6.1: METU Two-Phase Flow Test Facility

Figure 6.2: The Header, Mixing Section and The Feeders

On the other hand, there is also an air supply line which consists of 3 air storage tanks connected to a compressor. The compressed air is injected into the air supply line by means of a regulator valve (Figure 6.1). The pipes in air supply line are made of plastic and have inlet diameters of 25.4 mm.

In order to produce air-liquid mixed flow, a special mixer having small holes around its periphery was mounted just before the inlet nozzle of the header (Figure 6.1). Air comes from air supply line mixes with water flow in the mixer and the two-phase air/water mixture then flows downward through the header.

All feeders discharge into the water storage tank for recirculation of water. A globe valve is placed in each feeder to simulate the flow resistance of the channel and to obtain the required flow distribution in the feeders.

6.1.1 Instrumentation

METU-TPFTF has been supplied with instruments for measurement of test parameters. Table 6.2 shows the locations and properties of all the instruments of the test facility.

Table 6.2: The Instrumentation of the Test Facility

Instrumentation	Lines	Total Number	Accuracy / Measurement Range
Turbine Type Flowmeter	Water Line	1	± 1 % / 0.15-10 m/s
Differential Pressure Transmitters	All Feeders	5	± 0.15 % / 0-6.89 bars
Orificemeter	Air Line	1	± 0.15 % / 0-0.24 bars
Impedance Probes	All Feeders	5	± 6.1 % / 0-100 % void fraction
Rotameter	Air Line	1	± 2-6 % / 1.19-15.5 m^3/h
Pressure Transducers	Water Line	1	± 0.4 % / 0-6.89 bars
	Air Line	1	
	Mixing Line	1	

Air flow rate is measured by using orificemeter which consist of two elements: an orifice plate to cause a pressure drop and a differential pressure transmitter (OMEGA-PX771-100WDI) measuring pressure drop at downstream and upstream of the orifice which is a simple plate with a hole having 5.9 mm.

Water flow rate is measured by CHEMLINE PLASTIC's 2110TM model turbine flow meter. Volumetric flow rate values measured in air and water lines are used in the calculation of void fraction at the header inlet.

In order to calculate two-phase flow rate through each feeder, pressure drops across the globe valves treated as orifices in each feeder lines are mea-

sured by OMEGA-PX771-100DI type differential pressure transmitters.

Gage pressures are measured with OMEGA-PX605-100GI type pressure transducers at three points of the system, just before and after of the mixing section. There are also other conventional instruments including Bourdon pressure gages and temperature gages in both air and water lines of the system.

In the present work, the average void fraction in each of the feeders are measured with the impedance probes whose tips are placed at the centerlines of each feeder. Impedance probe measuring principle is based on the fact that a difference between excitation voltage and sensed voltage according to the electrical impedance (resistance and capacitance) occurs due to variation of void fraction around a sensor, as shown in Figure 6.3 [118, 52].
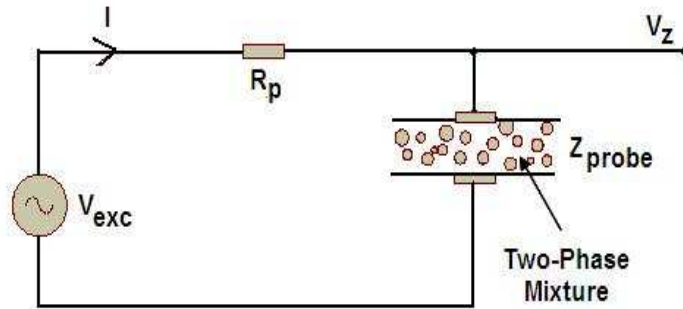

Figure 6.3: Impedance Probe Circuit

This voltage difference from the following equation can be interpreted as the void fraction [118, 52].

$$V_z = I \cdot Z_{probe} = \frac{V_{exc} \cdot \mid Z_{probe} \mid}{\mid Z_{probe} + R_P \mid} \qquad (6.1)$$

Hosanoglu [52] investigated sensitivity of the impedance probes by analyzing the effects of pre-resistance value, excitation frequency, flow regime, water temperature and found optimum values presented in Table 6.3 for those

probes. In the present study these parameters are used without change. Kaya [67] also used those probes in his study previously.

Table 6.3: Parameters Used In Each of Impedance Probes

Impedance Probe	Excitation Voltage	Excitation Frequency	Pre-determined Resistance
Feeder-2	3.54 V	500 Hz	409 kΩ
Feeder-3	3.54 V	500 Hz	371 kΩ
Feeder-4	3.54 V	500 Hz	238 kΩ
Feeder-5	3.54 V	500 Hz	238 kΩ
Feeder-6	3.54 V	500 Hz	287 kΩ

An AC excitation voltage source with variable frequency set (500Hz-20kHz) was used for these probes. Electronics for this sensor were based on power supply, signal generator, resistive divider and non-inverting amplifier, RMS to DC Converter and Bias Shift and Gain Blocks [52]. The outputs of impedance probes were set to 9 Volts and 0 Volts in the case of 0 and 100% void fraction, respectively. The sensor differs from those presented in the literature and the details about the principles and structures of the probes and their electronics can be found in [52].

Impedance probes are commonly employed for average void fraction determination in the literature. Many studies have been carried out on impedance probes to determine void fractions. Impedance probes were used by Fossa et al. [29], Lamarre and Melville [75], Devia and Fossa [18], Mi et al. [89] in their studies.

Mi et al. [89] supplied 100 kHz to the electrode of the impedance probes. Welter et al. [130] used impedance probes for measuring of the two-phase stratified liquid level in their study of liquid entrainment in a tee-junction with an upward-oriented vertical branch. They used 10 kHz signal and a voltage output from 2 to 9 V was obtained. Fieno et al. [26] used data

from impedance probe in their study to identify flow-regime by using neural networks.

As stated by several authors [75, 63, 118, 52], for frequency, $f \ll 1MHz$, the fluid becomes resistive (inverse of conductivity) and for $f \gg 1MHz$ it becomes capacitive meaning that excitation frequency determines the characteritics (conductance or capacitance) of a measured impedance. Therefore both type of probes could be used theoretically to measure void fraction.

Research using capacitance measurements include those by Jaworek et al. [63, 64] who used capacitance sensor operating at radio frequency of 80 MHz for void fraction measurements and also tested five different electrode configurations in their studies. Elkow and Rezkallah [22] used two different type of capacitance probes operating at 1 MHz excitation frequency to measure void fraction in gas-liquid flow.

With reference to the conductance measuring probes, Fossa [28] used conductance sensors by using 20 kHz of frequency for measuring void fraction in two-phase mixtures. Hibiki et al. [46, 47] used a multi-sensor conductivity probe to measure void fraction under the structure of a vertical downward bubbly flow. Ishii and Kim [59] used double-sensor conductivity probe in their study. Also, Dong et al. [20] used conductance probes in their studies. Song et al. [118] developed a conductance void meter with multi-channels to measure void fraction. They used 10 kHz as an excitation frequency.

All instruments of the facility are connected to the Data Acqusition System (DAS) which consists of 2 amplifier-multiplexer cards (OMEGA PCLD-789) and one Analog/Digital I/O Card (OMEGA PCL-812PG). The system is capable of reading 32 differential input channels. All instruments, except impedance probes, generate signals between 4-20 mA and then converted to 1-5 Volt signals and then fed into the DAS. Data Acquisition System consist of an Celeron-433 based computer with 768 MB RAM. A software (Advantech GENIE) was used to read, to display and to log the data coming from the instruments during test runs.

6.1.2 Calibration of Instrumentation

All differential pressure transmitters, pressure transducers, impedance probes, orificemeter and turbine-type flow meter exist in the facility were calibrated before testing began.

Orificemeter (an orifice plate with a differential pressure transmitter) was calibrated for different air flow rates from 1.2 m^3/h to 15.5 m^3/h by using OMEGA-FL-4611 type rotameter. While turbine flow-meter was calibrated by collecting and weighting water discharging from one of the feeders. Calibration procedure of orificemeter and turbine flow meter are described in detail by Kaya [67]. Three number of pressure transducers were also calibrated by using air line flow and pressure gages.

Impedance probes located on each feeders were calibrated in their original locations for different void fractions by adjusting flow rates of air and water. Void fractions below 12 % could not be obtained due to system limitations. Therefore the probes have been calibrated for void fractions between 12% and 40%. The homogeneous flow model assumption is used in this study in calibration procedures of differential pressure transmitters and impedance probes. Calibration procedure of the impedance probes was described in detail by Hosanoglu [52].

The function of θ_g-Voltage relation based on polynomial regression can be obtained from the calibration tests. If the form of the function is defined as;

$$\theta_g = a_4 x^4 + a_3 x^3 + a_2 x^2 + a_1 x + a_0 \qquad (6.2)$$

where x represents voltage signals from impedance probes, the calibration results gives the following regression constants for each feeders in Table 6.4. These functions can be used to estimate the void fraction of a two-phase flow.

Table 6.4: Constants of Polynomials For Calibration Curves of Impedance Probes

Impedance Probe	a_4	a_3	a_2	a_1	a_0	Void Fraction Range
Feeder-2	0.0	1.470	-1.750	1.030	0.105	0.0-0.39
Feeder-3	0.0	0.187	-0.553	0.625	0.007	0.0-0.39
Feeder-4	0.0	0.388	-0.956	0.849	-0.024	0.0-0.39
Feeder-5	-38.4	43.200	-16.800	3.230	-0.018	0.0-0.40
Feeder-6	0.0	5.999	-5.243	1.922	-0.011	0.0-0.47

After that, differential pressure transmitters on each feeder lines were calibrated by arranging each globe valves for different flow rates of air/water and void fraction values. Globe valve characteristics were also examined for small and large diameters and separate calibration curves were obtained for differential pressure transmitters in large and small diameter lines. However, it seemed difficult to develop such a regression function for determination of flow rates. In the following section, another methodology offered to correlate those varibles will be described.

6.1.3 Neural Network Representation of Calibration and Test Data

In this study, neural network approaches were used to determine intermediate values that will be obtained from instruments (especially from differential pressure transmitters) during test runs instead of finding emprical relations between void fraction, valve opening ratio and differential pressure signal with two-phase mass flow rate. The number of variables makes it difficult to describe this relation emprically.

In the literature, Oliveira and Sousa [98] formed a neural network system to correlate water mass flux term from pressures and flow rates of both air and water and also to correlate heat transfer coefficient from surface temperature and water mass flux. Malayeri et al. [87] correlated void fraction from

96

input data of volumetric flow ratio, density change and the Weber number by using neural network methodology and predicted void fraction with an overall average error of 3.6%.

The central idea behind neural network approach is that connections (weights and biases) between input and output elements can be adjusted so that a particular input leads to a specific target output. Thus, the neural network can be trained to do a particular job (in the present study, interpolation of calibration data) by adjusting the weight and bias parameters.

This is done in two main steps written below:

1. The training/learning phase, in which a set of known input-output patterns are presented to the network. The weights and biases are adjusted between the nodes until the desired output is provided by the system.

2. The test phase in which the trained network model is subjected to a set of new input patterns for which it was not trained before and whose outputs are known, but having the same format as the array used for the training . The performance of the network is also monitored in this phase [87].

Once the network is trained, data from test/calibration runs could be easily input to get approximate values of desired quantities (e.g. single-phase/two-phase flow rates). In the present case, about 85%-90% of calibration data were separated from the whole database for training the network and then rest of the data set (10%-15% of calibration data) were used to test the ability of the network to associate input-output pairs for which it has not been trained.

In this study, Neural Network Toolbox of MATLAB software [17] were used to perform neural network computations. Figure 6.4, generated by MATLAB shows the neural network system designed to calculate two-phase

flow rate from the inputs of void fraction, valve opening ratio and differential pressure signals. It includes two hidden-layers and one output layer since it was observed that multiple-layer networks were quite powerful rather than using single layer. A similar designation was also developed for determination of single-phase flow rate except having two-layers instead of three.

It is possible to utilize 16 learning algorithms in MATLAB. Many of them have been tried, however, Levenberg-Marquardt algorithm is found to be the most efficient among other learning algorithms and used for this study. Moreover, most commonly used transfer functions of tangent-sigmoid was used in hidden-layers and pure-linear function was used in output-layer for both single-phase and two-phase flow rate calculations as shown in Figure 6.4.
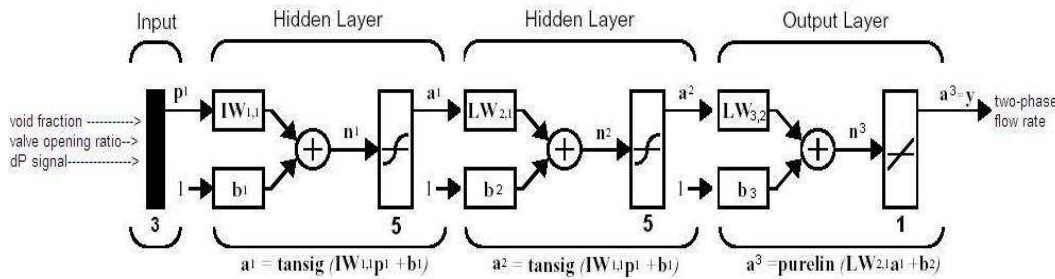

Figure 6.4: Neural Network Diagram for Two-Phase Data

All inputs and targets were scaled so that they always fall within a range of [-1,1] before introducing them into the network. This preprocessing made neural network training more efficient as recommended in [17].

Table 6.5 shows the test-phase (validation) results of such a neural system shown in Figure 6.4. First three columns shows the inputs of testing sets which are not used in training phase. Here, valve opening ratio represents the number of turn from the closed position divided by number of turn required to fully open the globe valves. For the valves located on the large diameter

feeders, turn number for fully opening is 3, while for small ones it is 4. Here feeder-3 was taken as a representative of large diameter feeders. For small diameter ones, different calibration data sets were collected from the Test Facility and were separated into two groups for training and testing phases.

Neural network estimated two-phase flow rate successively when compared with experimental (measured) target data. The maximum error observed as 6.31%. Inlet void fraction values above 0.28 and low flow rates showed a relatively high error which might be a result of insufficient data above this range.

Table 6.5: Neural Network Design for Determination of Two-Phase Flow Rate Through Feeder-3

Inputs			Output		
			Two-phase Mass Flow Rate (kg/s)		
Valve Opening Ratio	Void Fraction	dP Signal (Volt)	Measured	Neural Network Estimation	Error (%)
1.000	0.159	0.569	2.183	2.183	2.29
1.000	0.172	0.562	2.039	2.050	0.49
1.000	0.206	0.547	1.814	1.814	0.01
1.000	0.254	0.518	1.181	1.147	2.72
0.500	0.167	0.630	2.119	2.125	0.24
0.500	0.200	0.603	1.883	1.875	0.38
0.500	0.233	0.578	1.633	1.653	1.25
0.500	0.283	0.545	1.197	1.272	6.31
0.375	0.186	0.707	2.061	2.058	0.17
0.375	0.199	0.672	1.894	1.889	0.36
0.375	0.219	0.634	1.683	1.706	1.33
0.375	0.286	0.571	1.297	1.256	3.16
0.250	0.187	0.823	1.969	1.978	0.41
0.250	0.244	0.681	1.481	1.497	1.14
0.125	0.217	1.001	1.292	1.294	0.25
0.125	0.320	0.701	0.861	0.847	1.76

The network performance is controlled with a coefficient of determina-

tion, R^2, which shows the accuracy of the model. A perfect fit would result in R^2 value of 1, a very good fit near 1 and a poor fit near 0. In Figure 6.5 it can be seen that correlation coefficient (R-value) between the outputs and targets is very close to 1 representing how well the variaton in the output is explained by the targets.
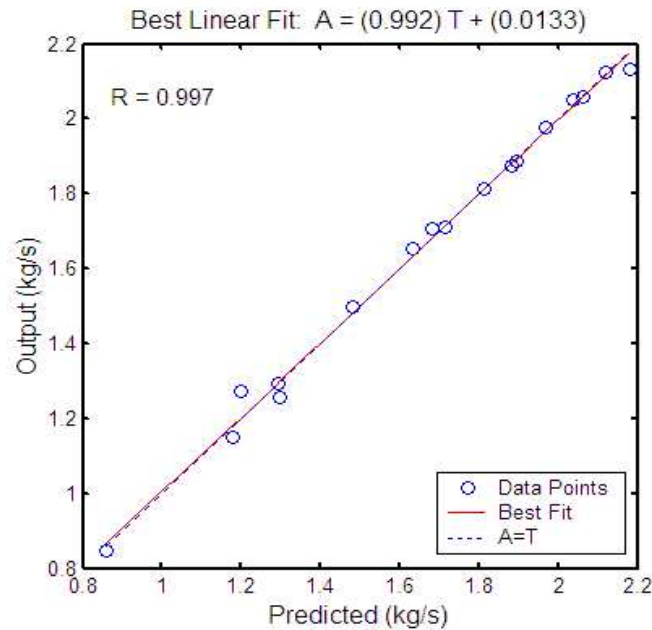

Figure 6.5: R^2 Value for Validation Data Set For Two-Phase Flow Calibration Test Through Feeder-3

Throughout this study several programs in MATLAB were also developed to perform the following neural network computations:

- Neural network training/learning

- Testing of a trained network

- Implementation to estimate single-phase/two-phase flow rates

100

6.2 Experimental Results

After getting a useful tool for relating the experimental data, a series of tests were performed. In principle, configurations having two feeders opened while the other feeders are closed by globe valves were studied (dual discharge tests). For this purpose, a number of single-phase and two-phase test with feeder-2,3,4 and feeder-5 under various paired combinations. These tests are used for validation of the code's results.

Working range of system parameters of the METU-TPFTF in these tests are summarized in Table 6.6.

<div align="center">

Table 6.6: Working Range of System Parameters

Water Pressure at Pump Outlet	0-2.6 bar
Air Pressure Before Orificemeter	0-2.6 bar
Minimum Void Fraction at the Inlet Nozzle	0.12
Air Flow Rate	1.2-15.5 m^3/h
Water Flow Rate	0.4-8.2 m^3/h
Water Temperature	18-24 C
Air Temperature	22-24 C

</div>

6.2.1 Single Phase and Two Phase Dual Discharge Tests

In the first tests, feeder-3 and feeder-5 which have different diameters connected to the header at different elevations and at different z-planes were selected. The results of the tests analysing the phase and flow distribution through both feeders are shown in Table 6.7.

In all single and two-phase tests, feeder-3 received more flow rate than feeder-5 as expected since the diameter of feeder-3 is larger than that of feeder-5. In all two-phase tests, no void is observed in feeder-3, therefore all void was observed in feeder-5 which seemed to divert more flow through feeder-3.

Table 6.7: Flow Distribution Through Feeder-3 and Feeder-5

Test No	Time Scan (s)	Inlet Flow Rate (kg/s)	Inlet Void Frac.	Void Fraction		Mass Flow Rate (kg/s)		Flow Split Ratio ($\dot{m}_3/\dot{m}_5$)
				F-3	F-5	F-3	F-5	
G000	30	2.211	0.000	0.000	0.000	1.329	0.950	1.40
G005	90	2.183	0.140	0.000	0.239	1.407	0.865	1.63
G006	90	2.169	0.179	0.000	0.330	1.468	0.786	1.87
G007	90	1.933	0.000	0.000	0.000	1.121	0.843	1.33
G008	90	1.892	0.158	0.000	0.260	1.235	0.778	1.59
G009	90	1.875	0.201	0.000	0.443	1.285	0.550	2.34
G001	30	1.664	0.000	0.000	0.000	0.916	0.725	1.26

Then the other larger diameter nozzle (feeder-2) is selected instead of feeder-3 and the results in Table 6.8 were obtained. Feeder-2 is at a higher level than feeders 3 and 5 and is far away from the inlet nozzle even beyond feeder-3 referring to Figure 7.1.

Table 6.8: Flow Distribution Through Feeder-2 and Feeder-5

Test No	Time Scan (s)	Inlet Flow Rate (kg/s)	Inlet Void Frac.	Void Fraction		Mass Flow Rate (kg/s)		Flow Split Ratio ($\dot{m}_2/\dot{m}_5$)
				F-2	F-5	F-2	F-5	
H002	90	2.211	0.0	0.0	0.0	1.283	0.933	1.38
H003	90	2.181	0.140	0.0	0.251	1.348	0.849	1.59
H004	90	2.169	0.179	0.0	0.379	1.448	0.695	2.08

As observed in previous tests, feeder-2 received more flow rate than feeder-5 for single and two-phase tests. For about the same inlet flow rate, again same flow split ratios are seen in both large and small diameter feeders. In the two-phase tests, no void is observed in feeder-2.

In order to investigate the effect of the symmetry, feeder-4 and feeder-5

were selected. Both feeders have same diameters and connected to the drum
at the same angle with vertical direction and at the same z-plane from the
inlet.

In all tests, it can be said that flow is splitted into two feeders approx-
imately equal in single-phase tests (J000,J007). However, in all two-phase
tests, more flow was observed in feeder-4 while more void was observed in
feeder-5.

Table 6.9: Flow Distribution Through Feeder-4 and Feeder-5

Test No	Time Scan (s)	Inlet Flow Rate (kg/s)	Inlet Void Frac.	Void Fraction		Mass Flow Rate (kg/s)		Flow Split Ratio
				F-4	F-5	F-4	F-5	$(\dot{m}_4/\dot{m}_5)$
J000	90	2.164	0.000	0.000	0.000	1.125	1.128	0.99
J002	90	2.106	0.191	0.143	0.234	1.078	1.044	1.03
J003	90	2.081	0.228	0.149	0.264	1.110	1.027	1.08
J004	90	2.075	0.254	0.145	0.305	1.120	0.993	1.13
J007	90	1.839	0.000	0.000	0.000	0.946	0.933	1.01
J008	90	1.781	0.166	0.137	0.227	0.930	0.892	1.04
J009	90	1.761	0.220	0.124	0.267	0.866	0.855	1.01
J010	90	1.744	0.253	0.170	0.351	0.975	0.798	1.22

After that, feeder-3 and feeder-4 were selected (Table 6.10). In every case,
feeder-3, received more flow rate than feeder-4. Voids go through feeder-4
which is closer to the inlet nozzle than feeder-3.

The mass balance between inlet and total outlet flow rates are tabulated
in Table 6.11. It is seen that the neural network simulation results are satis-
factory in mass balance for two-phase flow tests. Maximum errors are found
to be 7.2% and 10.1% in the last two tests, K003 and K006, respectively.
However, it seems meaningful since the void fractions in the feeder-3 deter-
mined from regression analysis as 0.052 and 0.032, respectively, are below
the measurable lower limit of void fraction, 0.12, in the facility.

Table 6.10: Flow Distribution Through Feeder-3 and Feeder-4

Test No	Time Scan (s)	Inlet Flow Rate (kg/s)	Inlet Void Frac.	Void Fraction		Mass Flow Rate (kg/s)		Flow Split Ratio $(\dot{m}_3/\dot{m}_4)$
				F-3	F-4	F-3	F-4	
K001	30	2.111	0.000	0.000	0.000	1.209	0.903	1.34
K002	30	2.078	0.146	0.000	0.151	1.307	0.879	1.49
K003	30	2.167	0.171	0.052	0.176	1.414	0.909	1.56
K005	90	1.797	0.000	0.000	0.000	0.974	0.760	1.28
K006	90	1.739	0.169	0.032	0.155	1.103	0.810	1.36

Table 6.11: Mass Balance

Test No	Inlet Mass Flow Rate(kg/s)	Total Outlet Mass Flow Rate(kg/s)	Difference
G000	2.211	2.279	+3.1 %
G005	2.183	2.272	+4.1 %
G006	2.169	2.254	+3.9 %
G007	1.933	1.964	+1.6 %
G008	1.892	2.013	+6.4 %
G009	1.875	1.835	-2.1 %
G001	1.664	1.641	-1.4 %
H002	2.211	2.216	+0.2 %
H003	2.181	2.197	+0.8 %
H004	2.169	2.143	-1.2 %
J000	2.164	2.253	+4.1 %
J002	2.106	2.122	+0.8 %
J003	2.081	2.138	+2.8 %
J004	2.075	2.113	+1.8 %
J007	1.839	1.879	+2.2 %
J008	1.781	1.822	+2.3 %
J009	1.761	1.721	-2.3 %
J010	1.744	1.772	+1.6 %
K001	2.111	2.112	0.0 %
K002	2.078	2.186	+5.2 %
K003	2.167	2.323	+7.2 %
K005	1.797	1.734	-3.5 %
K006	1.739	1.914	+10.1%

As a summary, following results were obtained for single-phase liquid tests;

- Neural network model supplied good data (maximum 4.1 % error was seen in mass balance, J000).

- In all 6 tests, large diameter feeders (2 and 3) received more flow rate (about 33-40 % higher for high flow cases) than small diameter ones (4 and 5).

- Decreasing flow rate leads to more homogeneous distribution between the selected feeders.

- Flow was equally shared by two small and symmetric diameter feeder-pairs (4 and 5)

while for two-phase air/water tests;

- Neural network model supplied good data (maximum 10.1 % error was seen in mass balances)

- In all tests done with feeders 3,4 and 5, air seemed to flow preferably through feeders closer to the inlet nozzle.

- Testing with equal diameter feeders (4 and 5) showed that more void was observed in feeder-5 (about two times more than that of feeder-4). Decreasing the inlet flow rate caused more voidage in feeder-5. This observation which is also reported by Parrott [105] in the tests performed in RD-14M Test Facility by using all five feeders might be due to the centrifugal force effect.

CHAPTER 7

NUMERICAL MODELLING OF HEADER

The code was modified for header's specific 3-dimensional geometry as shown in Figure 7.1. Radial outflow boundary conditions are defined for 5 feeder connections, while injection line (nozzle-1) is defined as radial inflow boundary condition. At the dead ends of the header, that is at z=0 and z=1.1 m, no-slip boundary conditions are defined. A switching algorithm is implemented into the code to open or to close selected feeder connections which makes it possible to simulate single, dual or if required multiple discharges from the header.

Since the header's geometry is horizontal, a non-symmetric flow is expected to occur around the centerline, $r \to 0$. In order to make a reasonable assumption at $r \to 0$, no-slip boundary condition is specified for the left side of the cells which are placed around the centerline meaning that a solid cylinder having a very small radius, e.g. 0.0001 m., is put along the centerline. Such an assumption is also needed to be made in order to overcome code running difficulties. The outer solid walls of the drum $r = 0.097m$ are also defined as no-slip boundaries as usual.
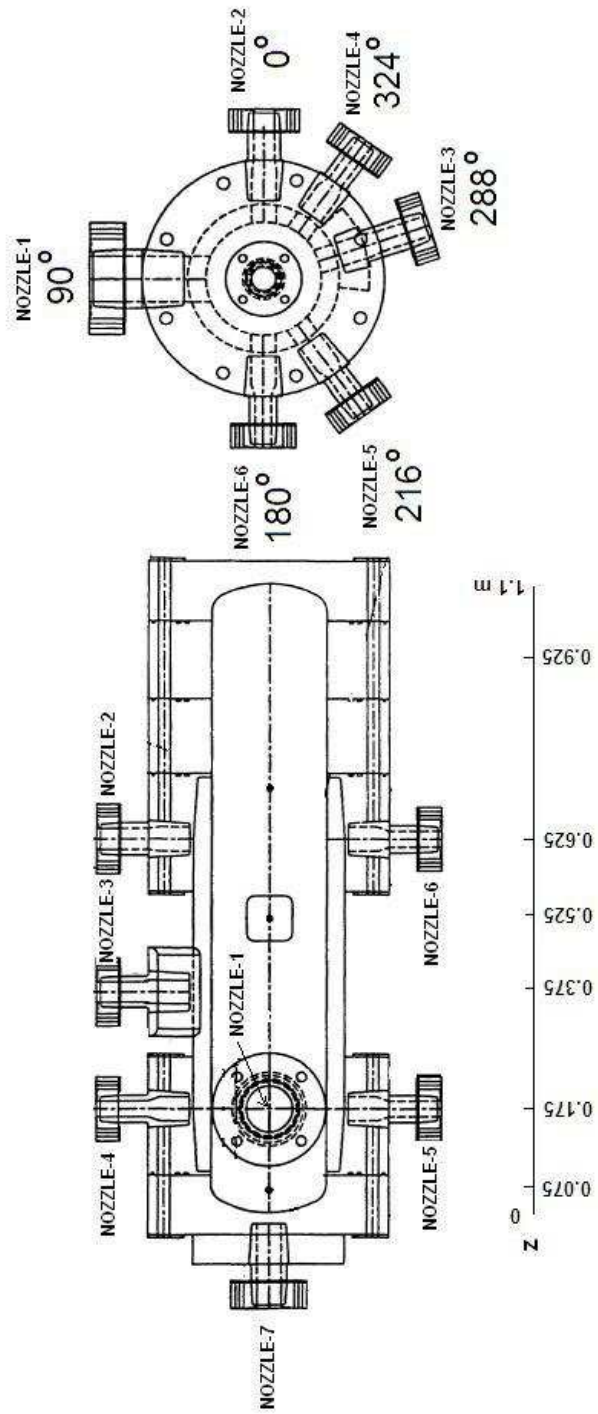
Figure 7.1: Header and Feeder Connections

For simplicity, the grid is formed by using 22 volumes in z-direction for 1.1 m lenght of the drum. In ϕ direction, the grid is divided into 10 volumes, 36° for each. There is not any restriction on the number of volumes defined in radial direction, however 10 is used at the present study. Therefore, totaly 2200 cells (10x10x22) are used to form the numerical modelling of header.

Some of the tests results which are used to verify the code's performance are presented in the following section.

7.1 Comparison with Experimental Data

As explained before, the code requires constant pressure condition for outflow boundaries placed at the nozzle connection points. However, METU-TPFTF has no pressure transducers mounted on the feeder lines. To overcome this difficulty, the following procedure is applied in order;

- A test matrix is formed by selecting one of the sequential single-phase and two-phase experimental tests given in Tables 6.7, 6.8, 6.9 and 6.10.

- Pressure measured at the mixing section, before inlet nozzle, is applied to one of the corresponding outlet nozzle as a constant pressure boundary condition.

- The pressure at the other outlet nozzle is adjusted until the code converges and finally matches with the measured single-phase flow split ratio (FSR) by a trial process.

- Then, the specified inlet void fraction and mass flow rate (measured experimentally) is forced to enter into the computational domain to start a two-phase flow transient (The predicted velocity and pressure distributions in the previous step is used as the initial conditions for the transient calculations)

- Finally, two-phase transient ends when mass residuals converges to a value below 10^{-3} kg/s. Predicted mass flow rates, void fractions and pressure are considered to be the final steady-state solution to the selected two-phase test.

This procedure seems to be appropriate, because it is also in agreement with the procedure applied when performing such tests. In all experiments performed, single-phase tests were performed at first and then air enters into the drum without changing upstream conditions (e.g. globe valve openings) of the corresponding nozzles.

In order to give an example;

- Test Matrix-G1 is formed with the data of Tests G000 (single-phase) and G005 (two-phase) in Table 6.7.

- The measured inlet nozzle pressure of 135 kPa is applied to nozzle-3.

- The pressure of the nozzle-5 is adjusted to achieve flow split ratio of 1.40 measured in Test-G000. At t=10 s, steady-state is reached, 134.75 kPa (250 Pa pressure difference with the nozzle-3) is found and is asigned as the present value to nozzle-5.

- Then, void fraction of 0.140 and mass flow rate of 2.183 kg/s is appointed as initial conditions to start the simulation of Test-G005 (Figure 7.2.

- After about 105 seconds, two-phase transient ends (Figure 7.3) and resulting mass flow rates, void fractions through the feeders and pressure and void distributions inside the drum is considered to be the final steady-state solution for the Test Matrix-G1.

Above procedure is applied to all other test matrices simulated in Section 7.1.2.
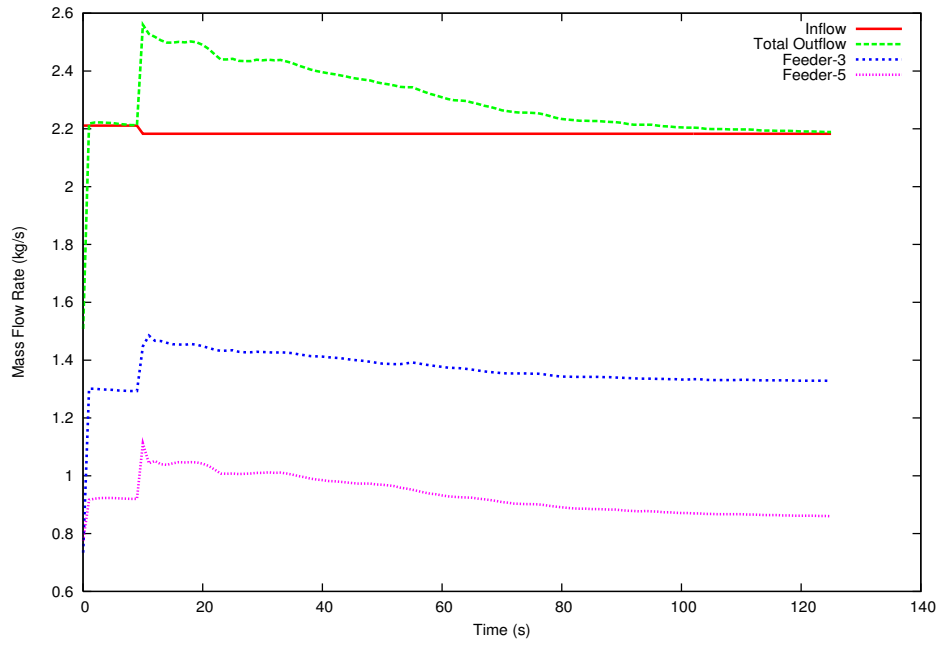
Figure 7.2: Mass Flow Rates, Test Matrix-G1
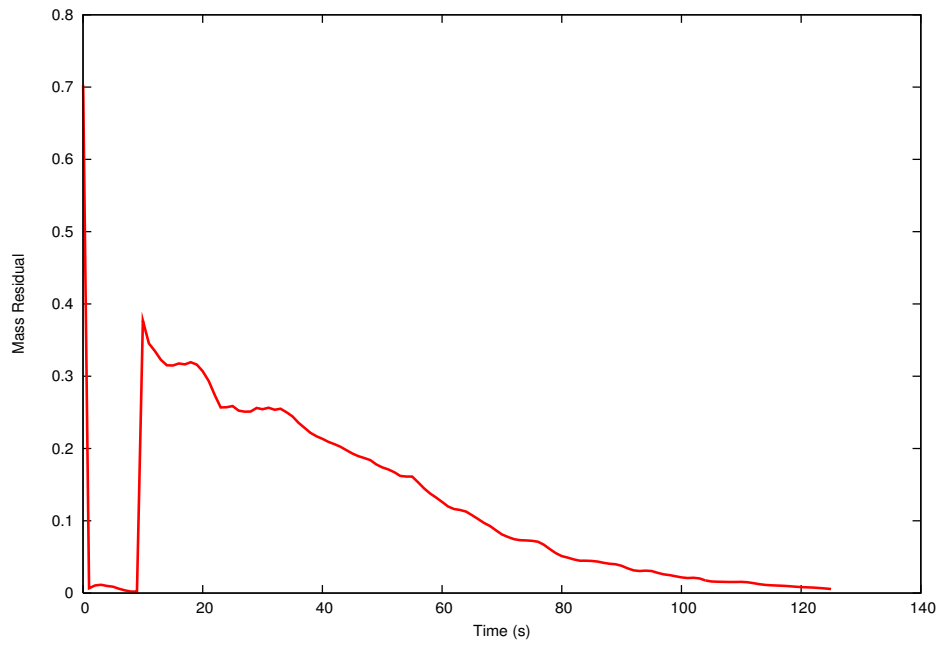
Figure 7.3: Mass Residual, Test Matrix-G1

110

7.1.1 Sensitivity Analysis for Drag Function

As stated in Chapter 2 the weakest point in the two-fluid model is the interfacial exchange terms, in the present study, it is the drag function, since it is based on emprical relations derived from the experiments. Therefore a convenient form of the drag function should be selected for the simulation of two-phase flow through the header.

In Section 3.3, two expressions are defined and coded, one Lee and Shah's formulation and the other Schiller and Naumann's formulation, and in this study, these two expressions were tested for Test-Matrix G1 before going into detailed investigation of two-phase flow simulations.

Use of Schiller and Naumann's formulation has encountered some code running problems and the code did not converge to any solution. In all tests performed, bubbly flow was not observed but stratified flow at various levels occured in the drum which is thought to be resulted from the buoyancy and slow air/water velocities. The formulation of Schiller and Naumann is applicable to bubbly flow which requires the droplet/bubble radius. Therfore, droplet/bubble radius could only be guessed which would introduce uncertanities in the model.

Lee and Shah's formulation was then tested with the same test matrix. Different values for C are applied to Equation 3.39 and steady-state results are shown in Figure 7.4 through 7.9 for different z-planes. As can be seen from these figures, value of K has an effect on the void distribution and pressure inside the header. The use of C=5x10^3 kg/m^3s increased the separation of both phases. Air moved to the upper part of the drum and a separated flow having water only and air only regions occured. Essentially no void is predicted through both nozzles(F-3 and F-5). These predictions are not fully supported by the experimental tests, especially near the inlet section. Flow split ratio increased to 1.518 in comparison with the experimental value of 1.627. The code does not seem to fully converge while using C=5x10^3 kg/m^3s

and lower values.

However, using greater value of C=5x10^4 kg/m^3s resulted more heterege-
nous flow inside and void is predicted in the nozzles 3 and 5 as it was observed
experimentally. Void fraction is calculated as 0.063 for nozzle-3 and 0.189 for
nozzle-5. In the experimental tests, all voids flew through nozzle-5 possibly
due to its location at the same z-plane with the inlet nozzle. More liquid flew
through nozzle-3 which has larger diameter. Flow split ratio is predicted as
1.548, where its experimental value is 1.627. No code running problems oc-
cured with Lee and Shah's formulation. All results are summarised in Table
7.1.

Table 7.1: Flow Distribution Through Feeder-3 and Feeder-5, Test Matrix
G1

TEST MATRIX G1								
	Single Phase (G000)							
	C	θ_{in}	$\dot{m}_{in}$ (kg/s)	θ_3	θ_5	$\dot{m}_3$ (kg/s)	$\dot{m}_5$ (kg/s)	FSR
Exper.		0.000	2.211	0.000	0.000	1.329	0.950	1.399
Numer.	5x10^3	0.001	2.211	0.000	0.000	1.293	0.920	1.405
Numer.	5x10^4	0.001	2.211	0.000	0.000	1.293	0.920	1.405
	Two Phase (G005)							
	C	θ_{in}	$\dot{m}_{in}$ (kg/s)	θ_3	θ_5	$\dot{m}_3$ (kg/s)	$\dot{m}_5$ (kg/s)	FSR
Exper.		0.140	2.183	0.000	0.239	1.407	0.865	1.627
Numer.	5x10^3	0.140	2.183	0.010	0.006	1.324	0.872	1.518
Numer.	5x10^4	0.140	2.183	0.063	0.189	1.327	0.857	1.548

In the literature, Lee and Shah [81] determined the effect of interfacial
drag on the high pressure jet impingement problem by using IMF model.
In this problem, they made a sensitivity study of variations of C by using
2.0x10^8, 2.0x10^{10} and 2.0x10^{12} kg/m^3s and reached a good agreement be-
tween the experimental data and calculated results with the value of 2.0x10^{12}
kg/m^3s.

Lee and Shah [81] also studied on the separation of steam and water problem by using same numerical model (IMF). They carried out numerical computation for $10^3, 10^4$ and 10^5 kg/m^3s and found out that the rate of separation increased with the decrease in the value of interfacial drag as it is observed in the current study.

As Lee [78] stated, it is found that convergence is sensitive to the interfacial drag term K. Lee made a conclusion that by doing sensitivity study, the lower bound values of drag function was approximately equal to 10^3 kg/m^3s. When using value of K lower than this limits, he did not obtain a stable solution. He concluded that a stable solution could only be obtained for certain ranges of K. Present study showed very similar findings with those of Lee [78] such that below $5x10^3$ it is getting harder for the code to converge to a steady-state profile.

Therefore simulations described in the following sections were performed with Lee and Shah's formulation with a value of $5x10^4$ kg/m^3s for C. In the following sections, the code's results are compared with the experimental test data presented in Chapter 6 in order.
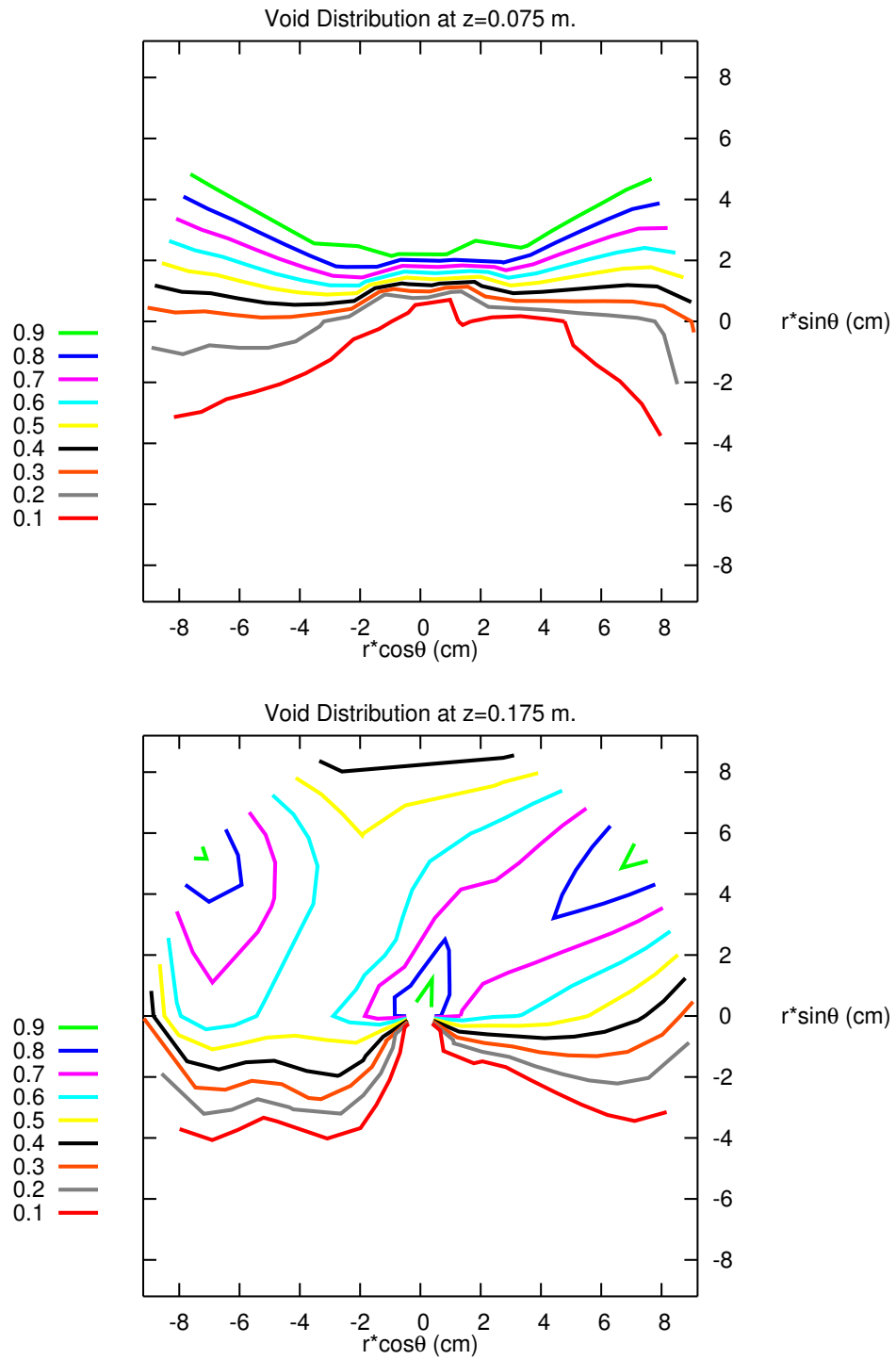
Figure 7.4: Void Distribution-I, Test Matrix-G1, K=5.0x10^3 kg/m^3s
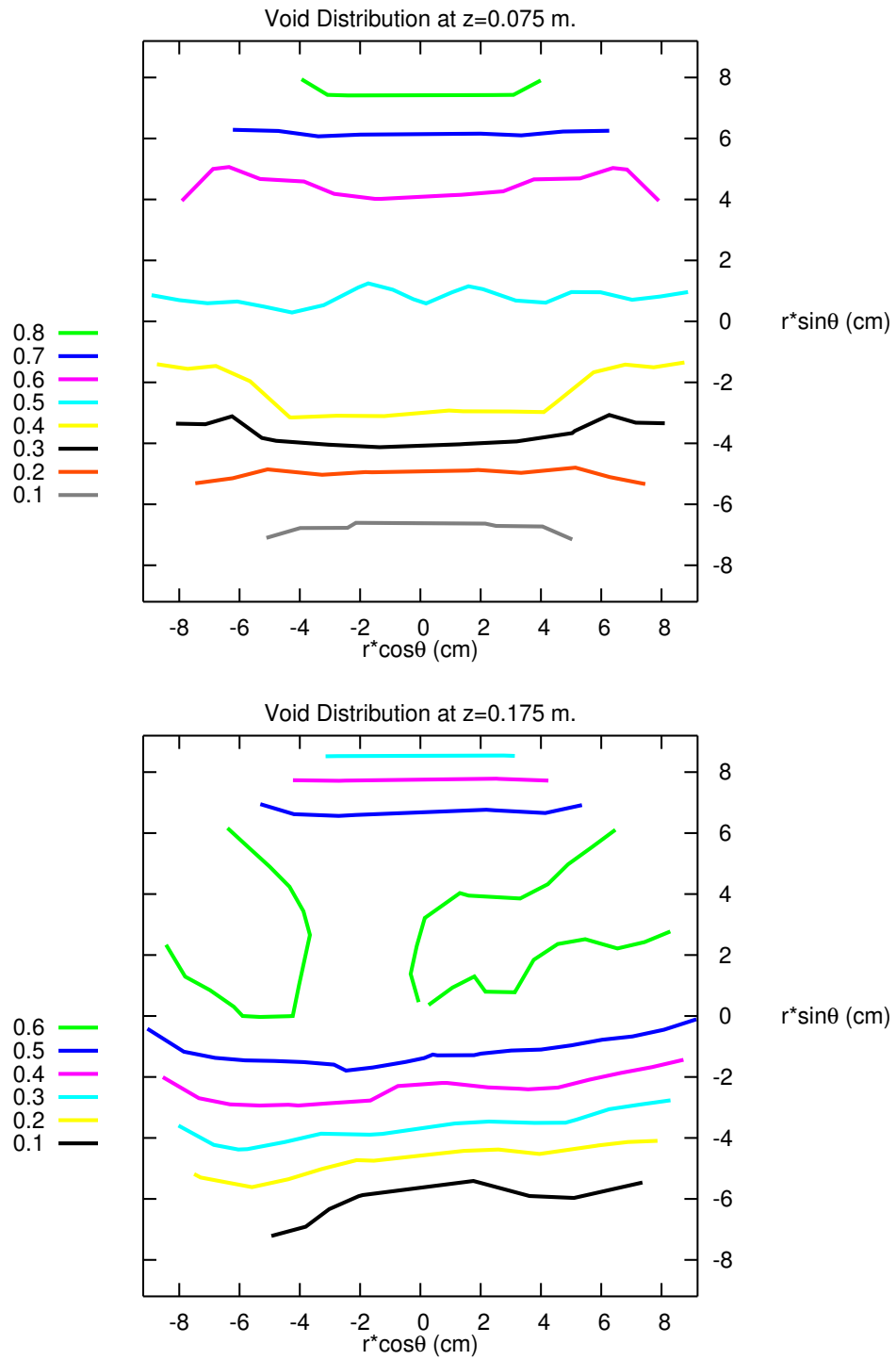
Figure 7.5: Void Distribution-I, Test Matrix-G1, K=5.0x10^4 kg/m^3s
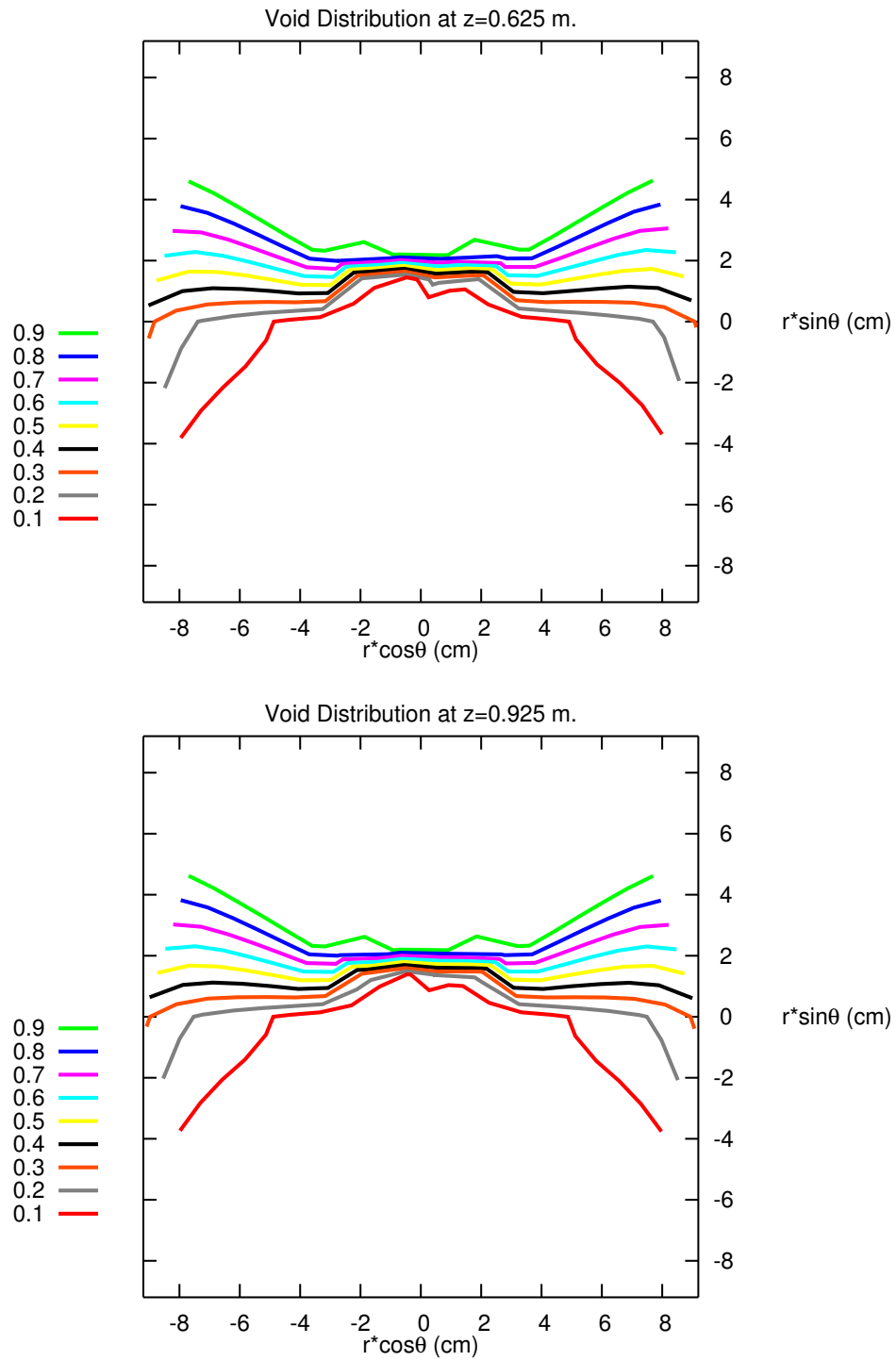
Figure 7.6: Void Distribution-II, Test Matrix-G1, K=5.0x10^3 kg/m^3s
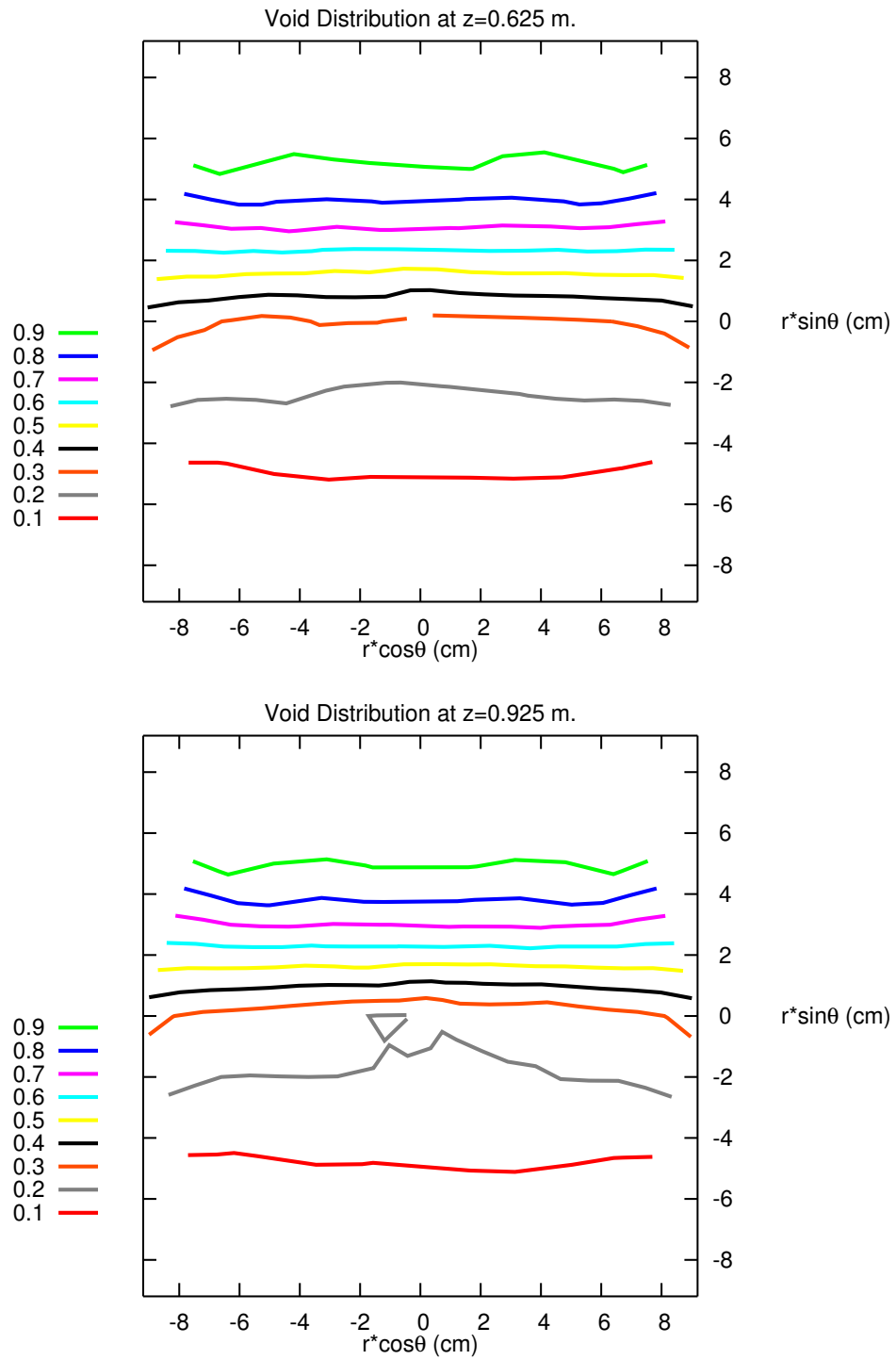
Figure 7.7: Void Distribution-II, Test Matrix-G1, K=5.0x10^4 kg/m^3s
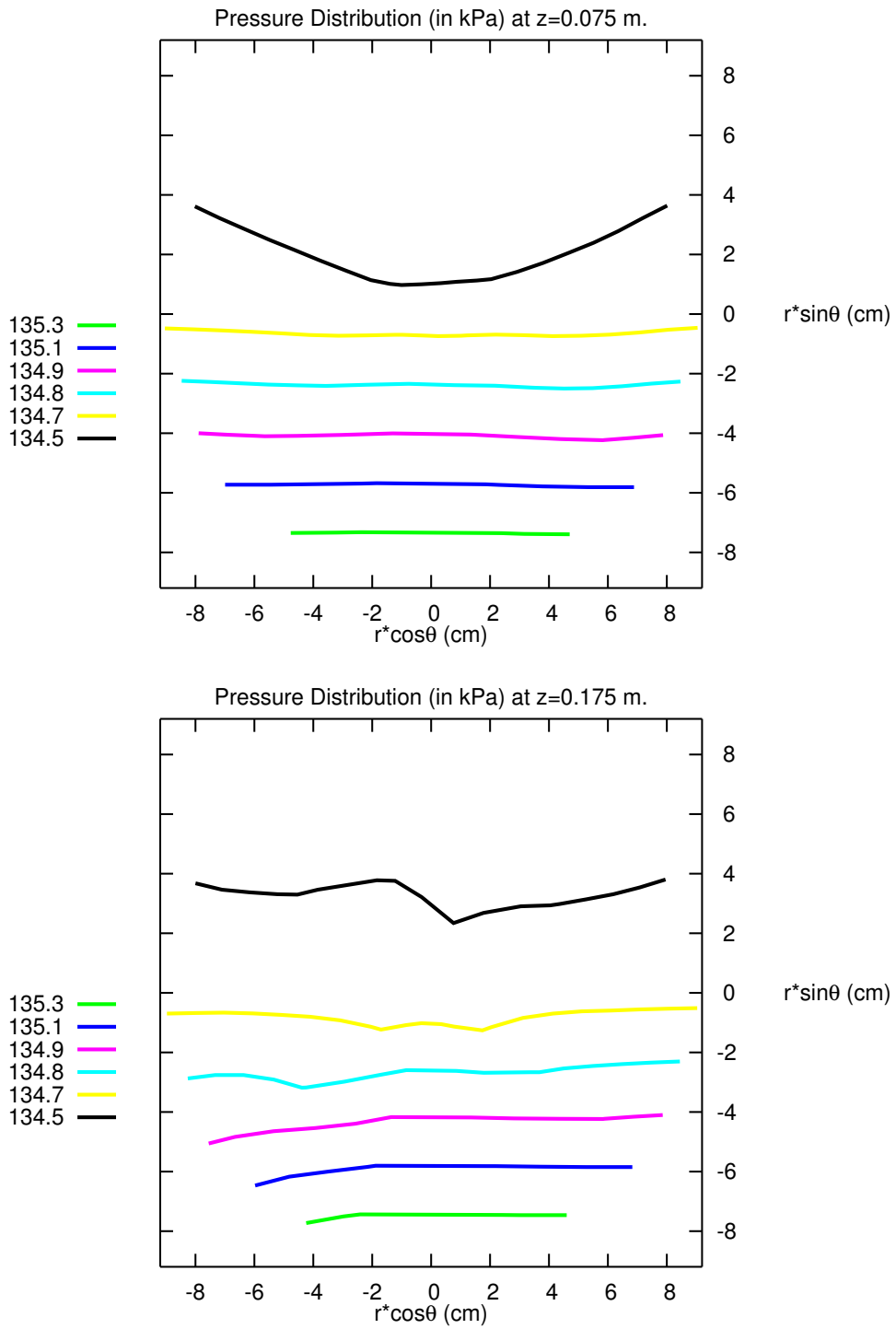
Figure 7.8: Pressure Distribution-I, Test Matrix-G1, K=5.0x10^3 kg/m^3s

118
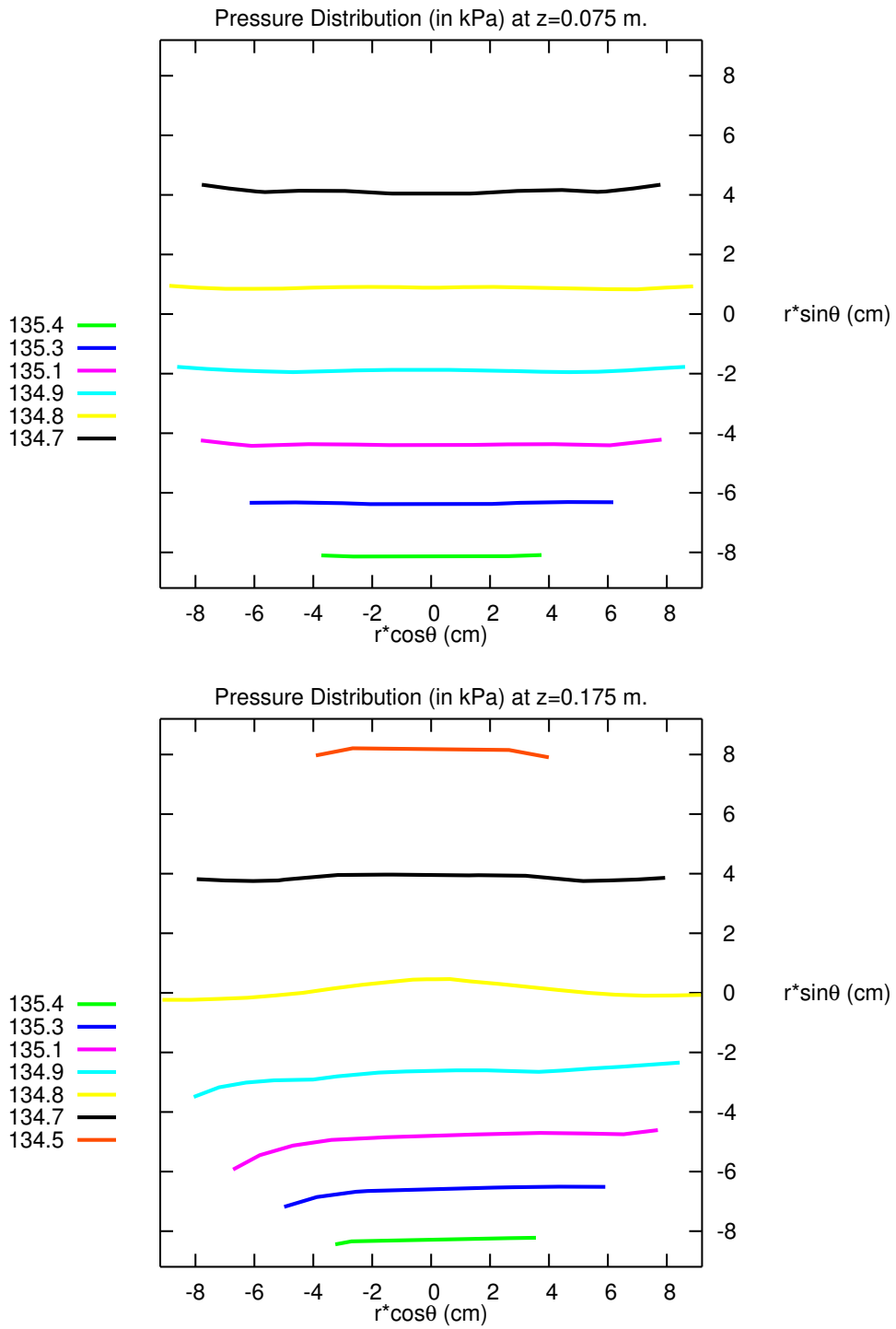
Figure 7.9: Pressure Distribution-I, Test Matrix-G1, K=5.0x10^4 kg/m^3s

7.1.2 Simulation Results

7.1.2.1 Test Matrix-G2 (G000, G006)

After selection of C=5x10^4, a new test matrix (G2) is formed for further investigation of the two-phase flow through Feeders 3 and 5. Tests numbered G000 and G006 are chosen. Transient is started at t=5 s. from the single-phase converged solution (Test-G000) by imposing void fraction of 0.179 and mass flow rate of 2.169 kg/s to the inflow boundary conditions. Figure 7.11 shows the mass flow rates of two-phase flow at the inlet and at two outlets (F-3, F-5). Total outflow represents the sum of the flow rates through corresponding nozzles. Figure 7.12 reflects the convergence history for the mass residual. It approaches to zero (steady-state) after about 90 seconds of the transient. This figure gives an idea about the convergence on satisfaction of mass conservation.

Table 7.2: Flow Distribution Through Feeder-3 and Feeder-5, Test Matrix G2

TEST MATRIX G2							
	Single Phase (G000)						
	θ_{in}	$\dot{m}_{in}$ (kg/s)	θ_3	θ_5	$\dot{m}_3$ (kg/s)	$\dot{m}_5$ (kg/s)	FSR
Experimental	0.000	2.211	0.000	0.000	1.329	0.950	1.399
Numerical	0.001	2.211	0.000	0.000	1.293	0.920	1.405
	Two Phase (G006)						
	θ_{in}	$\dot{m}_{in}$ (kg/s)	θ_3	θ_5	$\dot{m}_3$ (kg/s)	$\dot{m}_5$ (kg/s)	FSR
Experimental	0.179	2.169	0.000	0.330	1.468	0.786	1.868
Numerical	0.179	2.169	0.070	0.241	1.329	0.840	1.582

Figure 7.10 gives the convergence history of L_2 norm of the corresponding variables. As shown in Table 7.2, the void fraction is calculated as 0.070 for nozzle-3 and 0.241 for nozzle-5. More voids preferably flow through nozzle-5, however void fraction into nozzle-3 has not been changed significantly (0.070) compared with the perivous G1 test result (0.063) under the same

initial conditions. However flow split ratio is increased to 1.582. Nozzle-3 does not receive more liquid flow. Numerical solution shows the same trend increasing with the experimental results.

The void distribution at z=0.075 m. and at z=0.175 m. where the inlet nozzle and feeder-5 are located are presented in Figure 7.13. As observed in all of the tests, such a chaotic behaviour is seen in the numerical solutions for void fractions at both locations. The void distribution at z=0.075 m. seem to be effected largely from the inlet and outlet (feeder-5) sections which are in the vicinity. Such a behaviour are not observed for the far away points beyond z=0.375 m. as shown in Figures 7.15 and 7.17 in which almost the same void and pressure distributions are predicted. Void fraction graphics also give an idea that a certain level of water occurs below an air region which is in agreement with the experimental observations. This is also reflected by pressure distribution graphics as shown in Figures 7.14, 7.16 and 7.18 for six different locations. Pressure increases while moving to the bottom part of the drum due to presence of higher liquid fraction. As in the previous test (Matrix-G1), existance of feeder-3 at z=0.375 m. (See Figures 7.15, 7.16) causes a distortion in both void and pressure distributions.
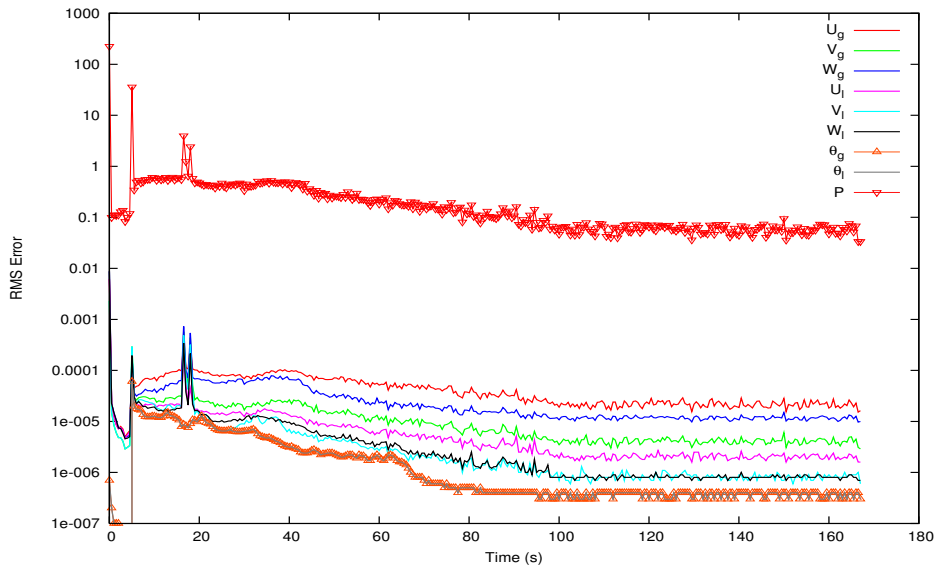
Figure 7.10: Root-Mean-Square Error, Test Matrix-G2
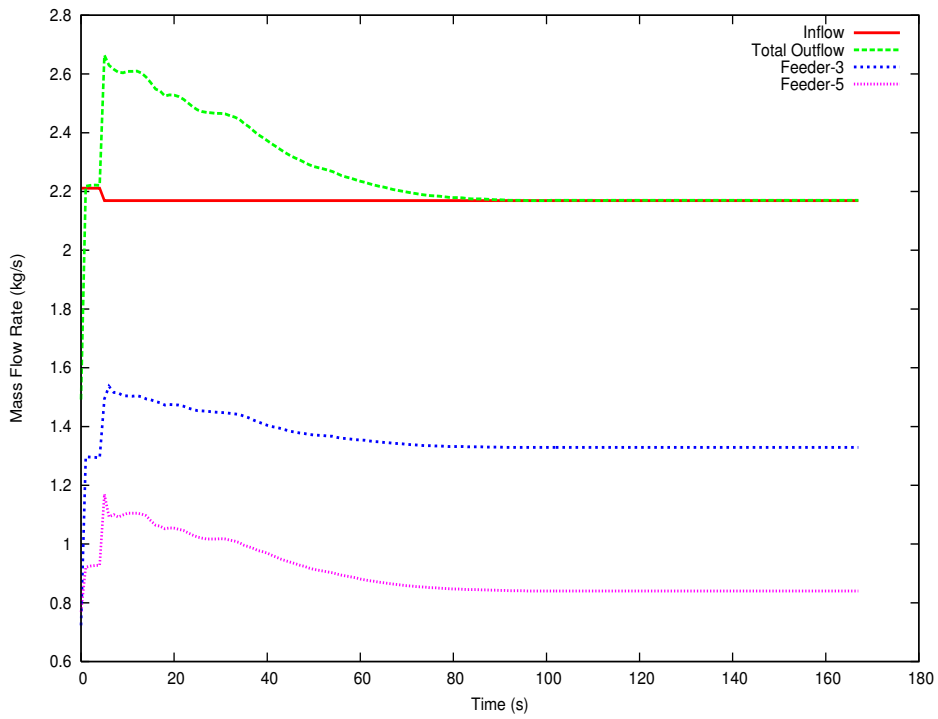
Figure 7.11: Mass Flow Rates, Test Matrix-G2
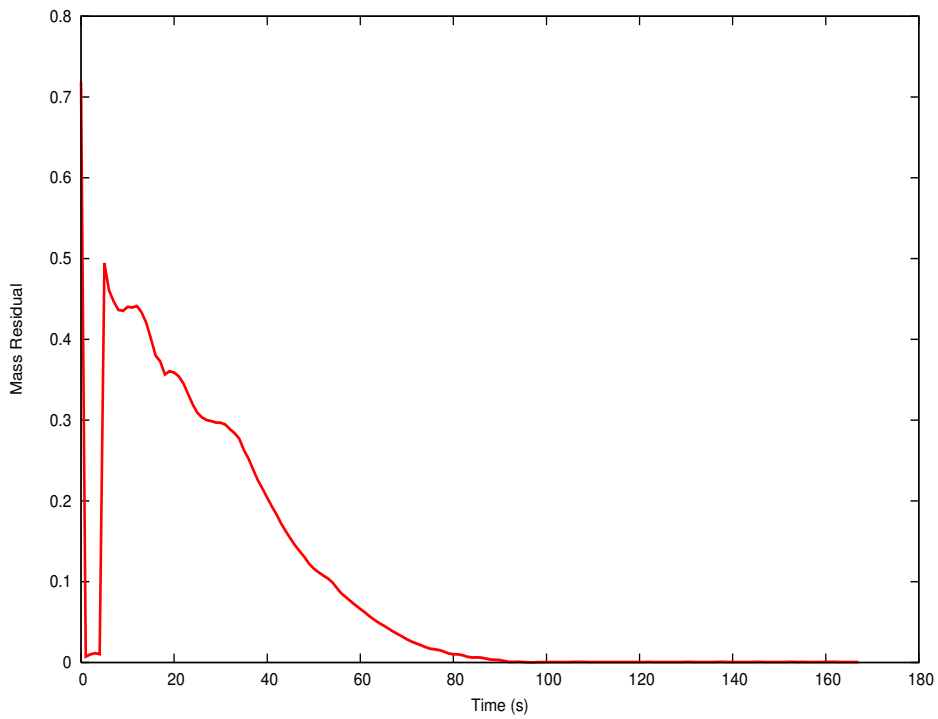
Figure 7.12: Mass Residual, Test Matrix-G2

122
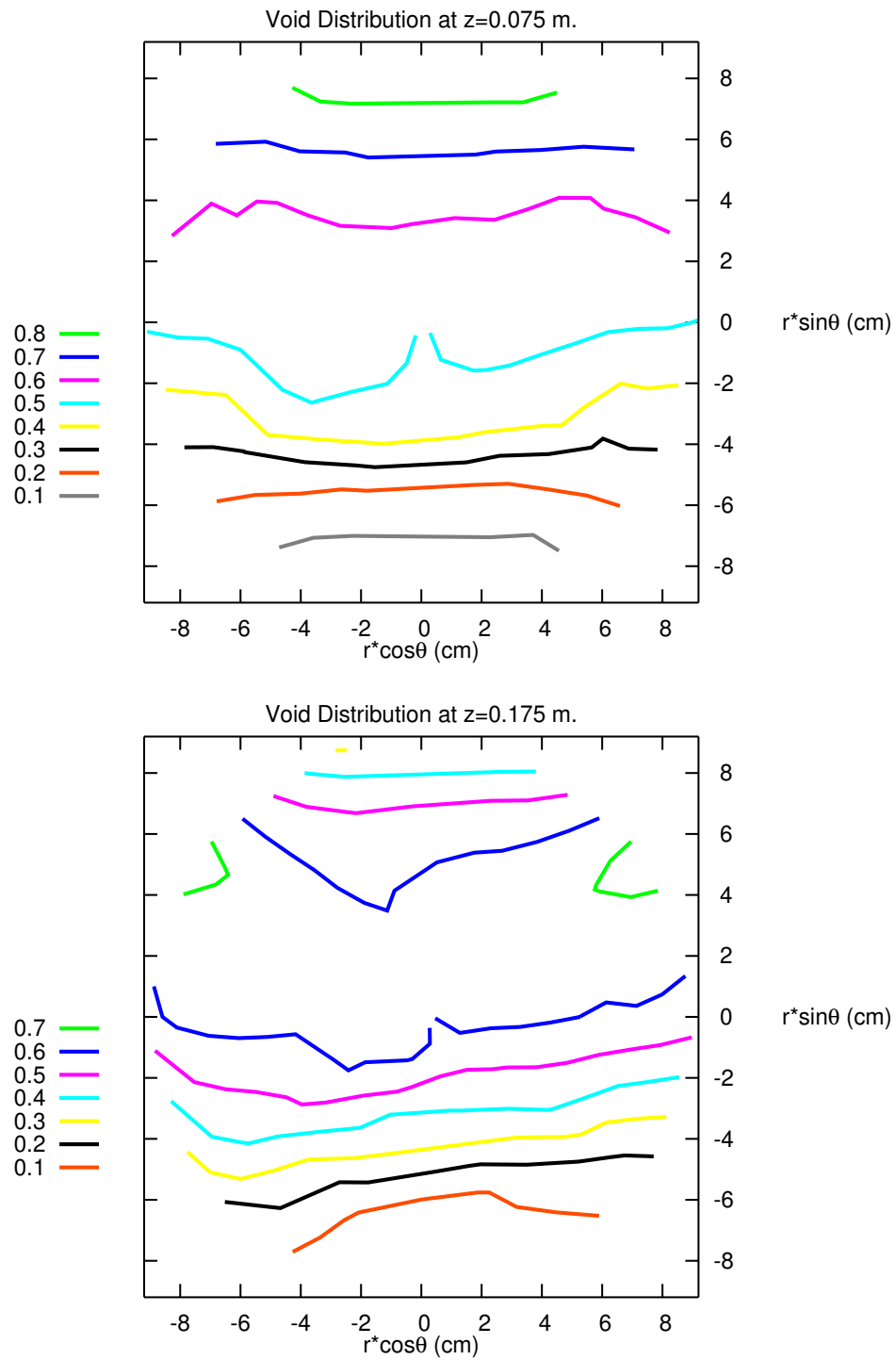
Figure 7.13: Void Distribution-I, Test Matrix-G2
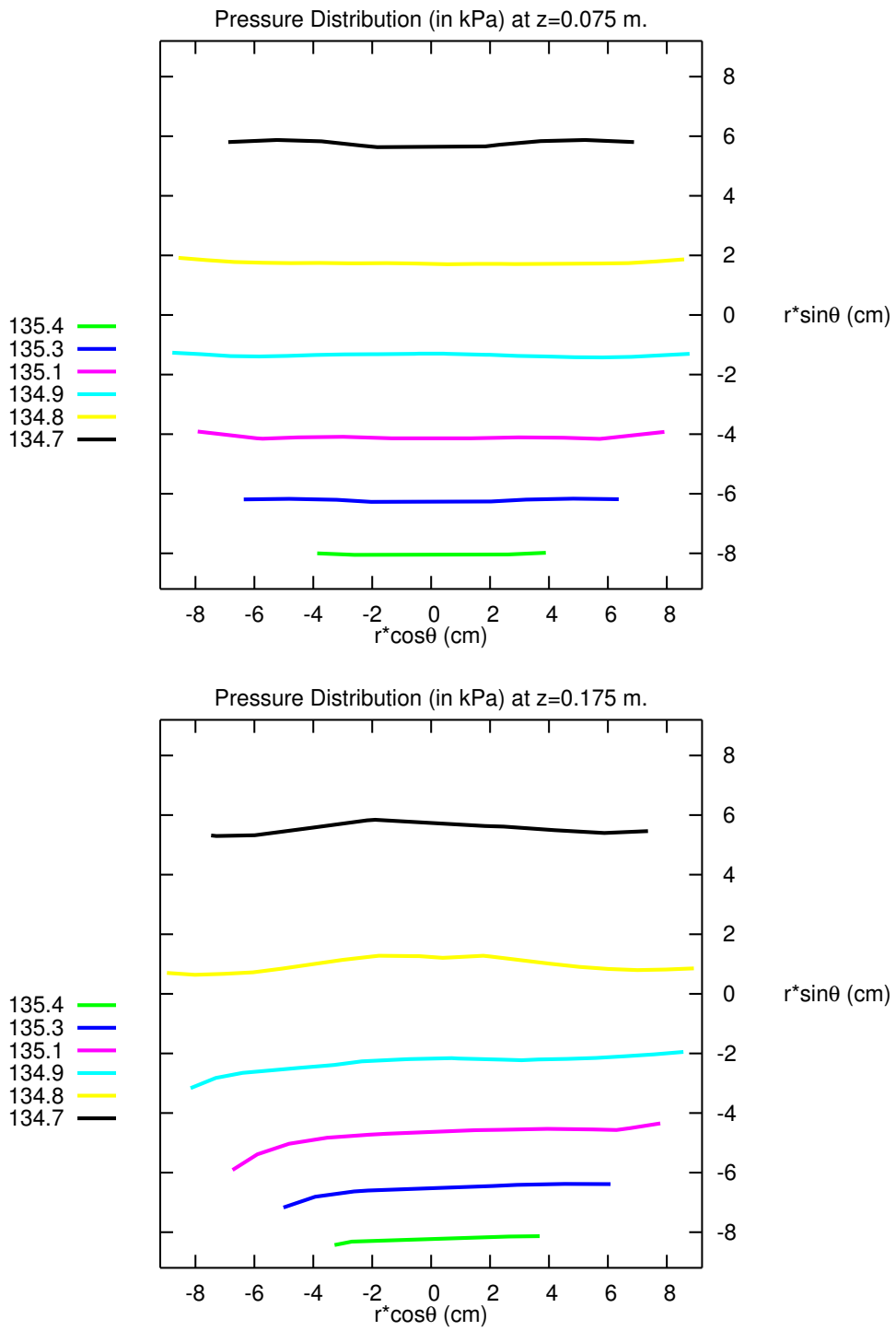
Figure 7.14: Pressure Distribution-I, Test Matrix-G2
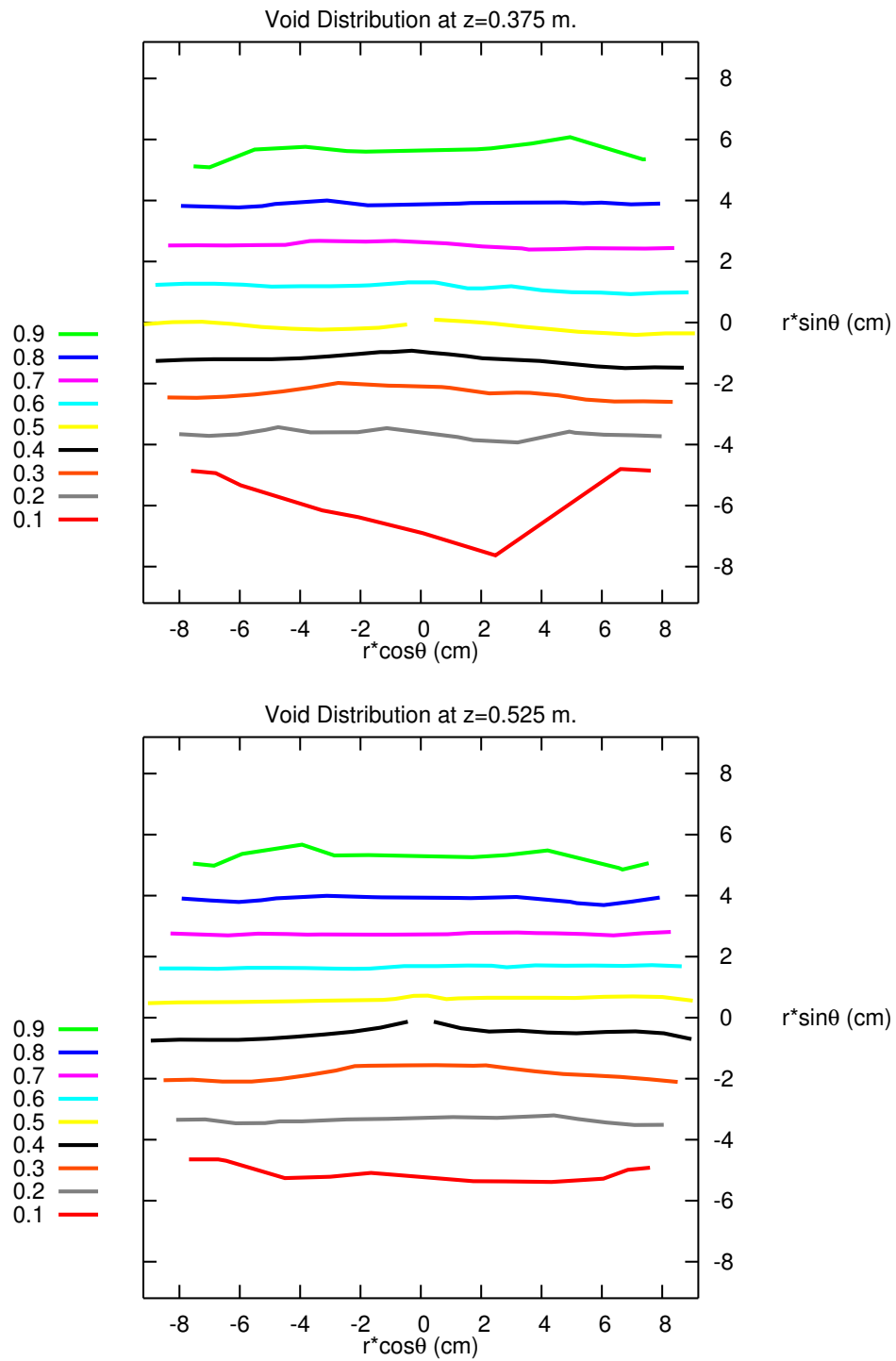
Figure 7.15: Void Distribution-II, Test Matrix-G2
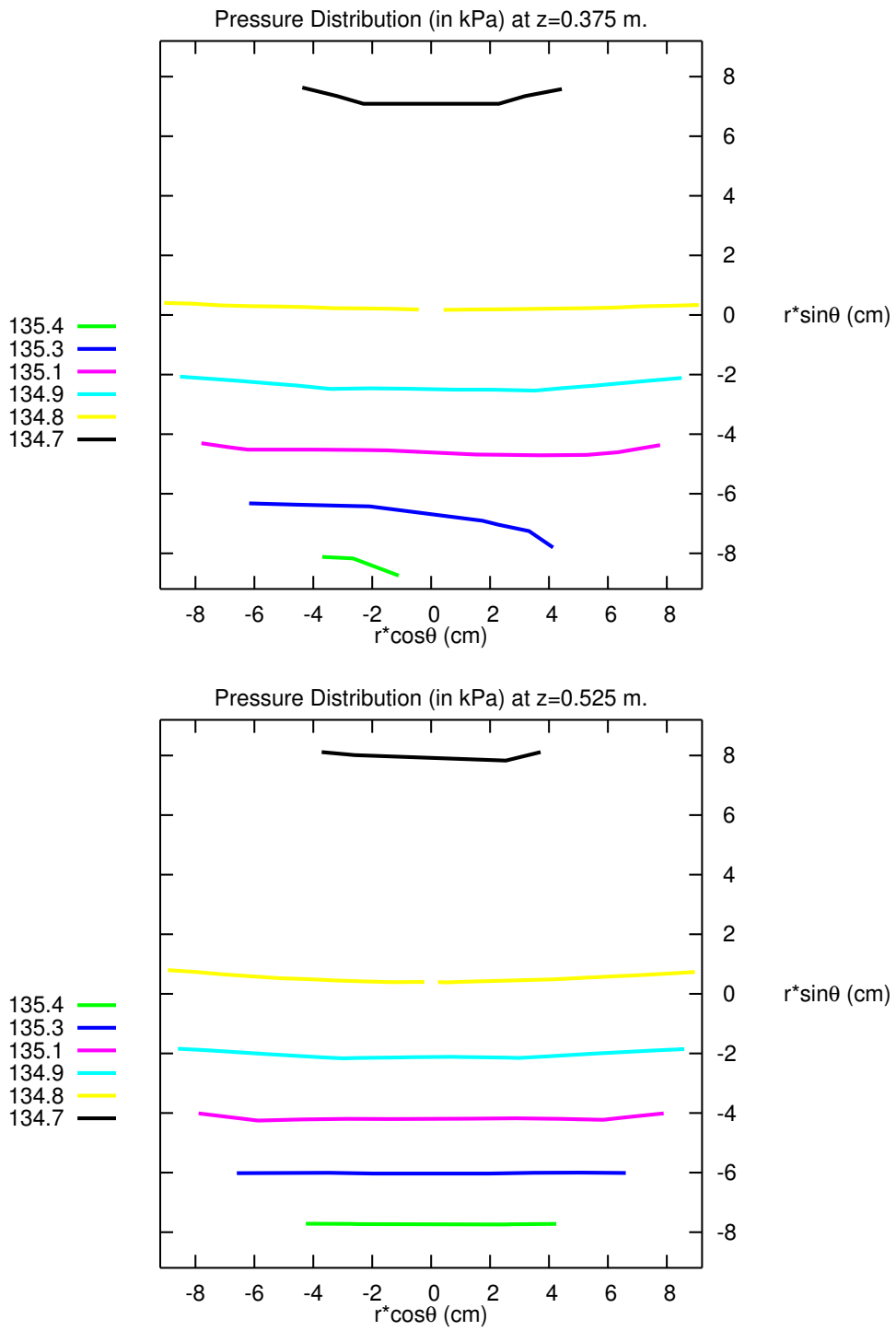
Figure 7.16: Pressure Distribution-II, Test Matrix-G2
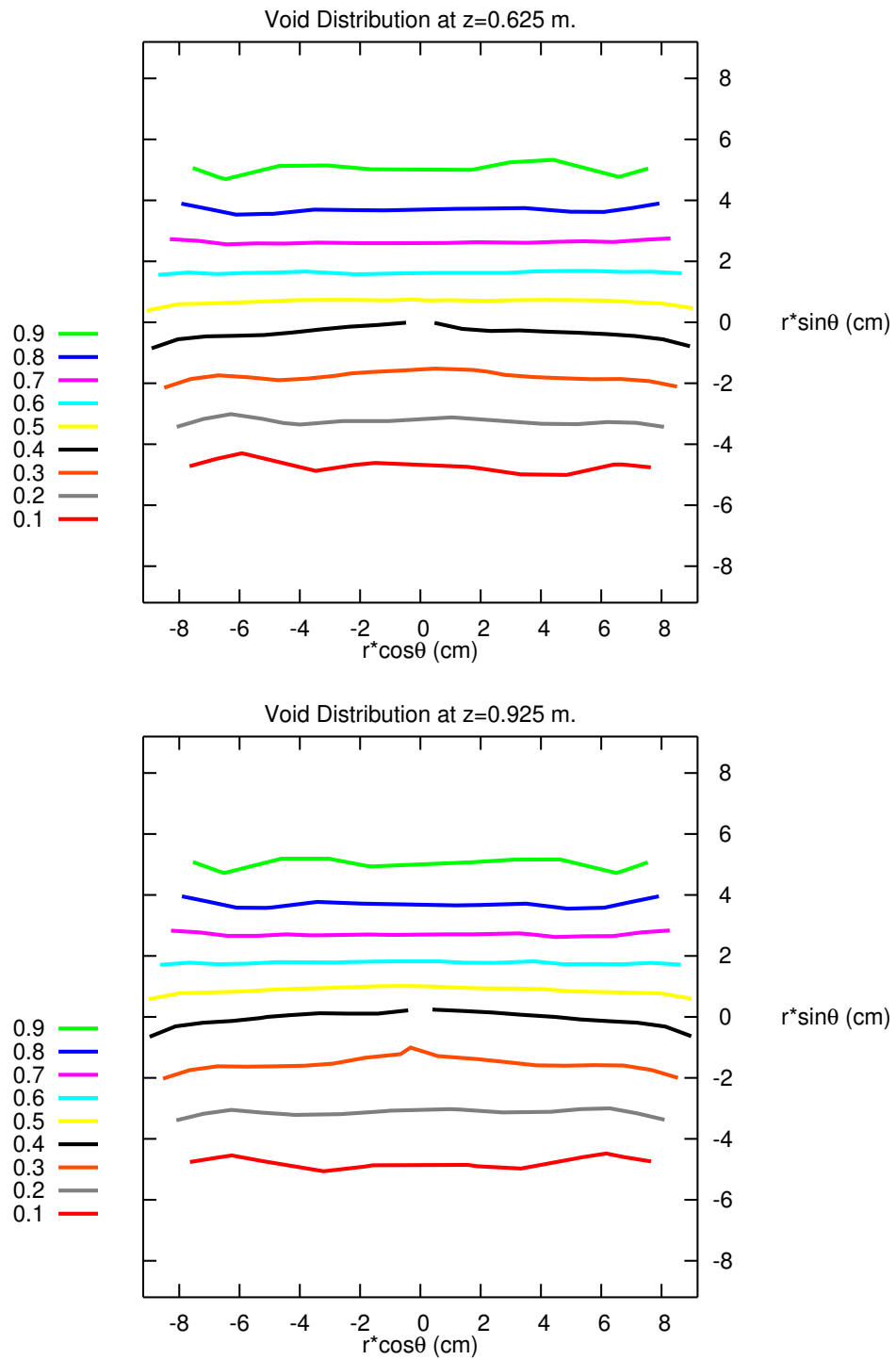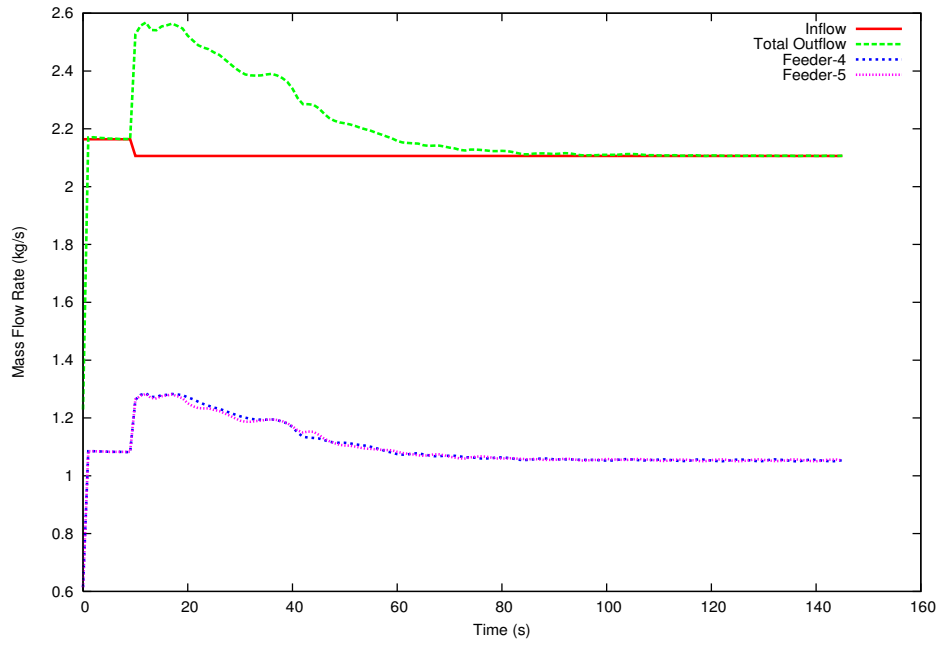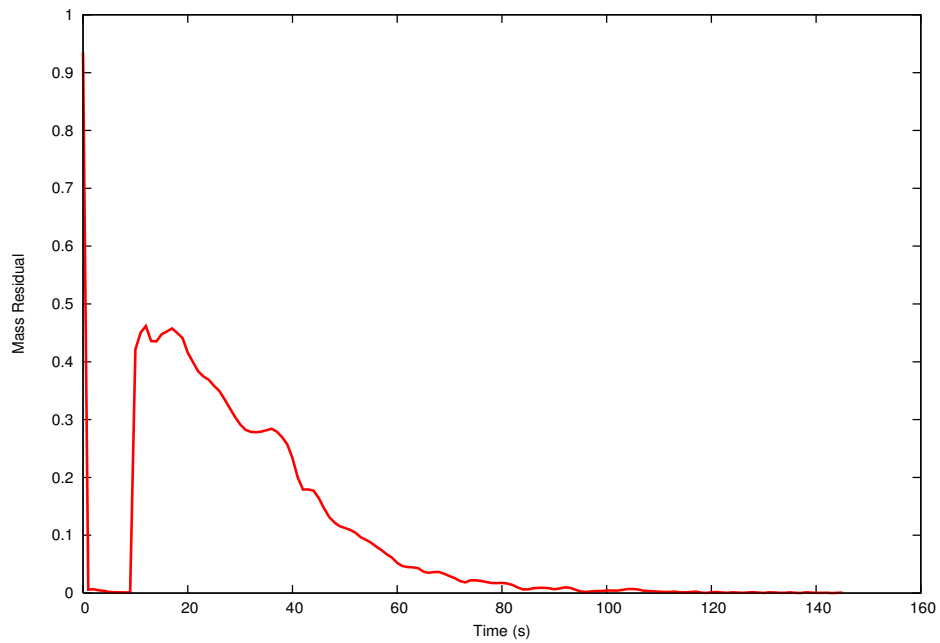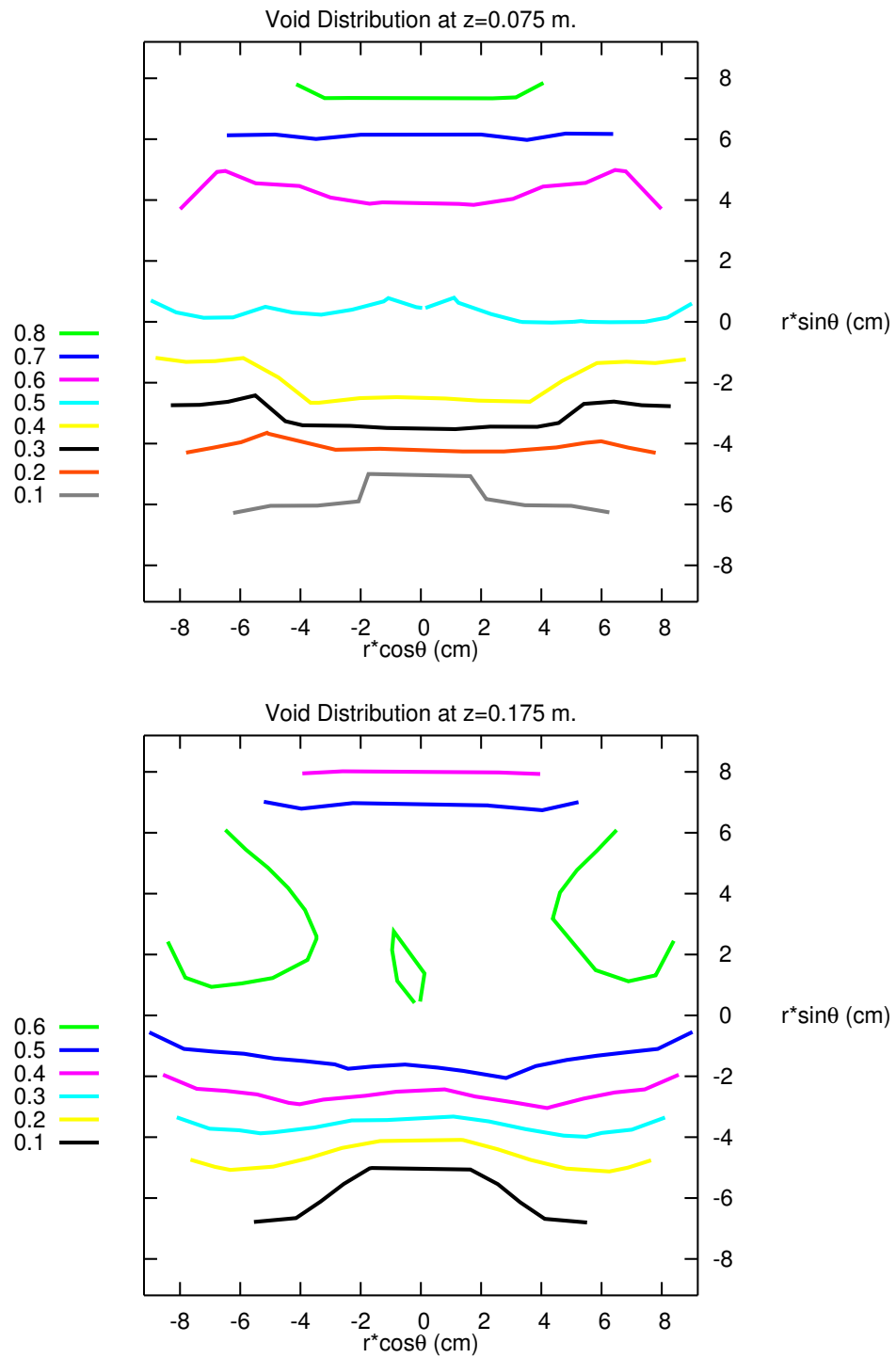
Figure 7.17: Void Distribution-III, Test Matrix-G2
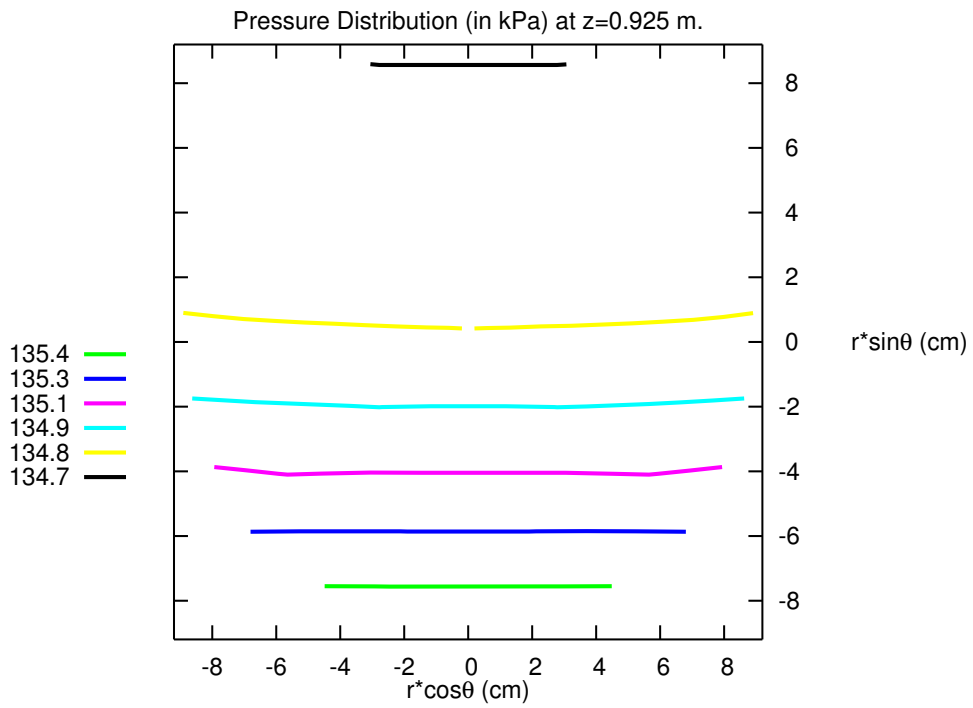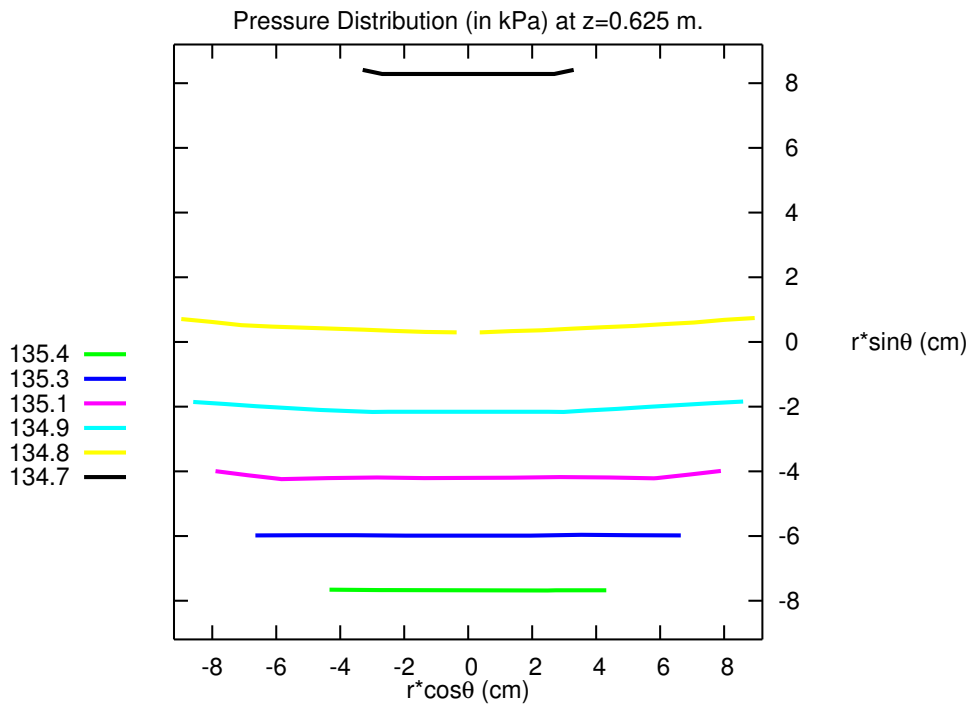
Figure 7.18: Pressure Distribution-III, Test Matrix-G2

128

7.1.2.2 Test Matrix-J1 (J000, J002)

In this section, two-phase flow through Feeders 4 and 5 is investigated. Tests numbered J000 and J002 combined to form Test Matrix-J1. After obtaining the single-phase converged solution (Test-J000) for inlet mass flow rate of 2.164 kg/s, transient is started at t=10 s. by imposing void fraction of 0.191 and mass flow rate of 2.106 kg/s to the inflow boundary conditions. Figure 7.19 shows the mass flow rates of two-phase flow at the inlet and the two outlets and total outflow, sum of the flow rates through corresponding nozzles. The convergence history for the mass residual is reflected by Figure 7.20. It approaches to zero after about 110 seconds of the transient meaning that total outflow is matched with the inflow in this simulation beyond 100 seconds from the initiation of air injection into the domain.

As shown in Table 7.3, void fraction is calculated as 0.154 for nozzle-4 and 0.152 for nozzle-5. While the symmetric prediction is similar for mass flow rates. Flow is equally distributed to both nozzles (1.054 vs. 1.053 kg/s). These results deviated from the experimental observations, in void fractions, since more void fraction was observed in feeder-5 than feeder-4 actually. However it can be concluded that the numerical simulation results seems reasonable. Since both nozzles are placed at the same elevations and the flow areas of both of the feeders are the same, the code showed symmetrical behaviour in the solution for both nozzles (flow split ratio is found to be 1.001). Such a behaviour is understandable, because of the definitions of boundary conditions. Inflow and outflow boundary conditions are defined by only radial direction velocities. Such a definition forces the solution to a fully symmetric one around the vertical axis. This Symmetry is preserved also for the two-phase flow test (J002), which actually gives an idea that numerical algorithm and the computer code works reasonably well in 3-dimensional geometry without distorting any variable's behaviour and without causing nonsymmetric solutions in the whole domain.

Table 7.3: Flow Distribution Through Feeder-4 and Feeder-5, Test Matrix J1

TEST MATRIX J1							
	Single Phase (J000)						
	θ_{in}	$\dot{m}_{in}$ (kg/s)	θ_4	θ_5	$\dot{m}_4$ (kg/s)	$\dot{m}_5$ (kg/s)	FSR
Experimental	0.000	2.164	0.000	0.000	1.125	1.128	0.997
Numerical	0.001	2.164	0.000	0.000	1.084	1.085	0.999
	Two Phase (J002)						
	θ_{in}	$\dot{m}_{in}$ (kg/s)	θ_4	θ_5	$\dot{m}_4$ (kg/s)	$\dot{m}_5$ (kg/s)	FSR
Experimental	0.191	2.106	0.143	0.234	1.078	1.044	1.033
Numerical	0.191	2.106	0.154	0.152	1.054	1.053	1.001

The void distribution is presented in Figure 7.21 for the points at z=0.075 m and at z=0.175 m planes on which inlet nozzle and feeder 4 and 5 are located. Different formations with respect to the other sections of the header (e.g. Figures 7.23 and 7.25) occur at both locations. Pressure distributions are shown in Figures 7.22, 7.24 and 7.26 for six different locations. Beyond z=0.375 m, almost the same void and pressure distributions are predicted. Void fraction and pressure graphics also give an idea that a certain level of water occurs below an air region as observed in the tests performed. Expected symmetric solution can be easily seen in all pressure graphics, increasing downwards. They also reflect the locations of nozzles 4 and 5 which distorts the pressure profile at their own locations at z=0.175 m (Figure 7.22).

Figure 7.19: Mass Flow Rates, Test Matrix-J1

Figure 7.20: Mass Residual, Test Matrix-J1

131

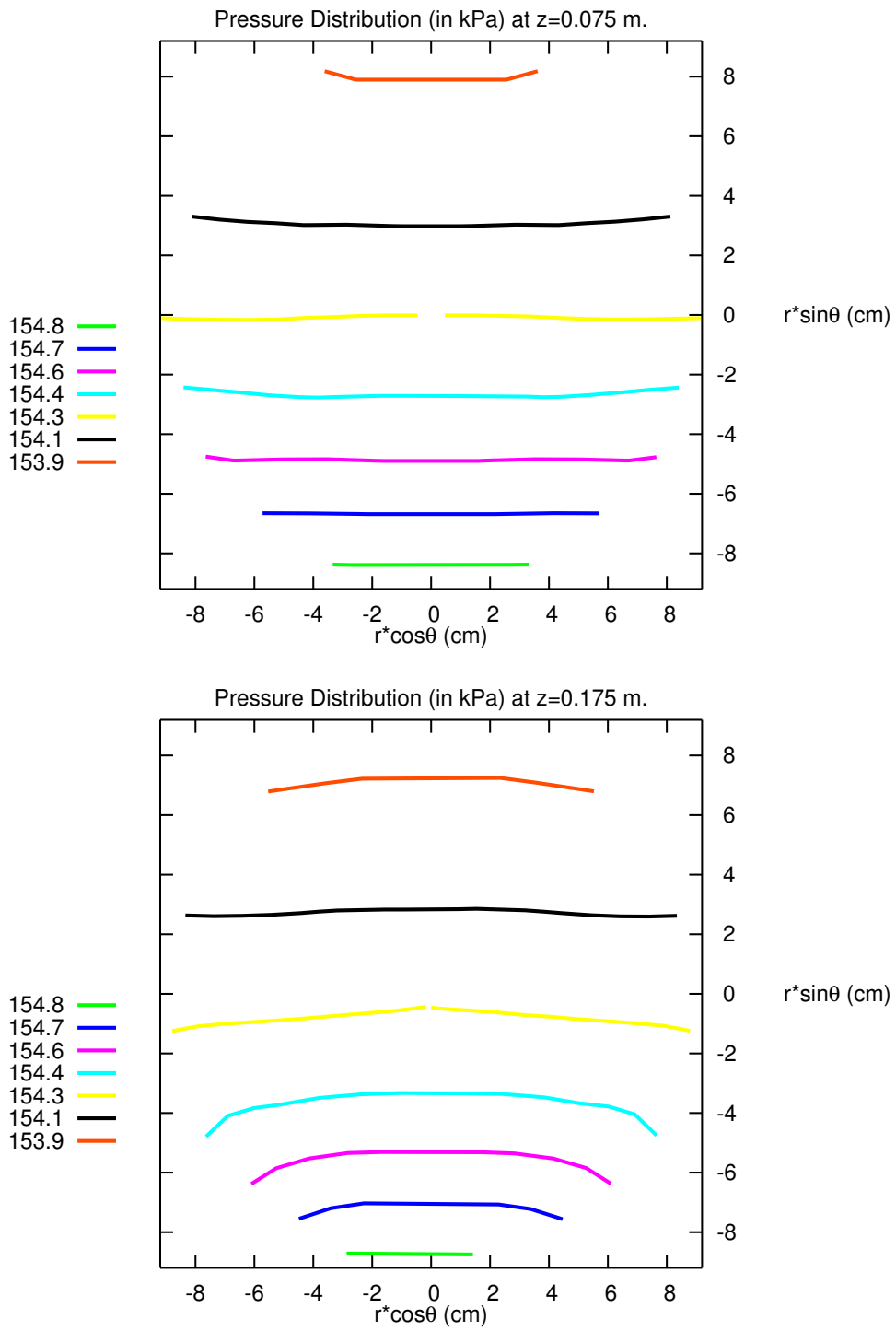Figure 7.21: Void Distribution-I, Test Matrix-J1

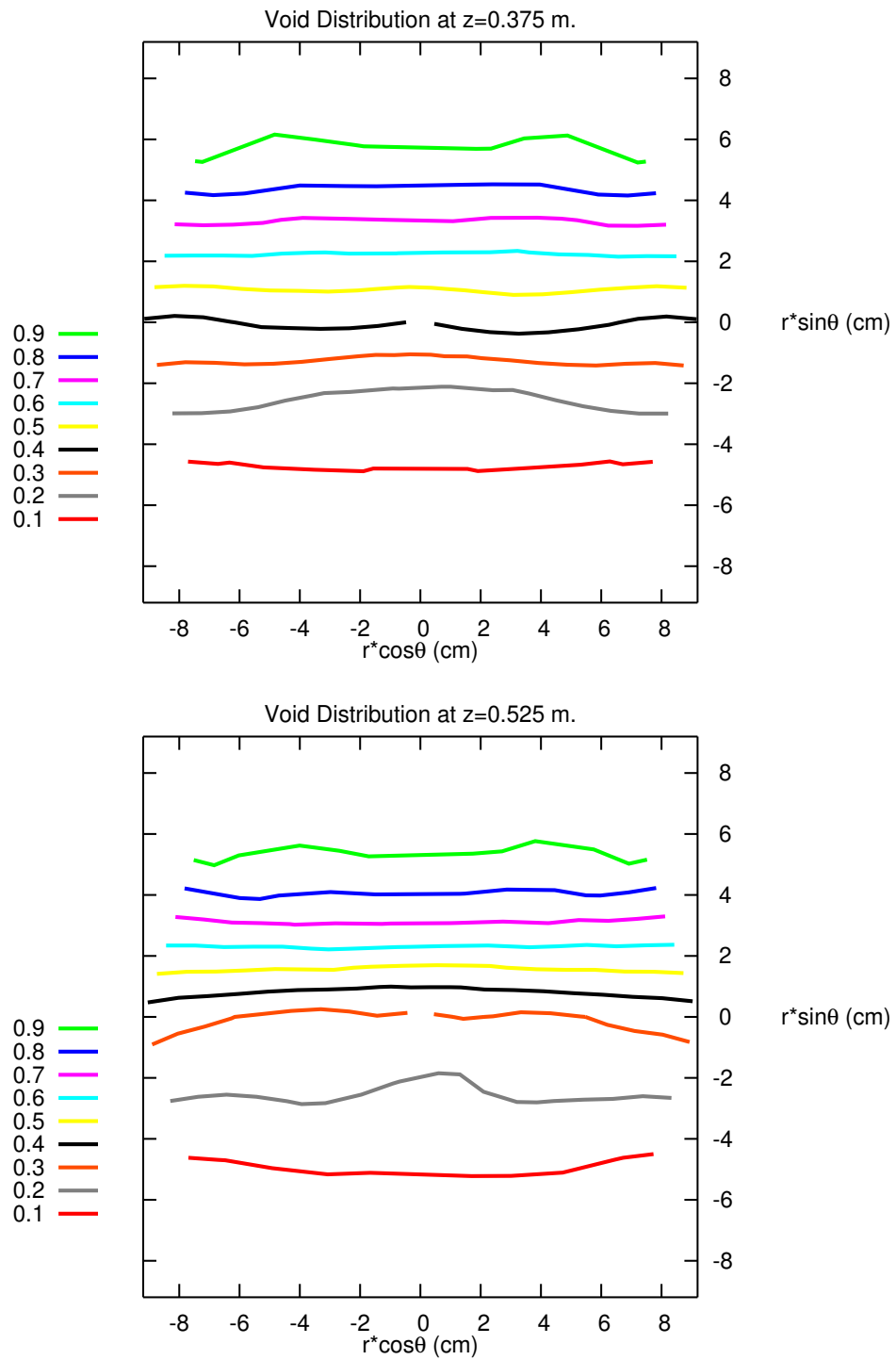Figure 7.22: Pressure Distribution-I, Test Matrix-J1
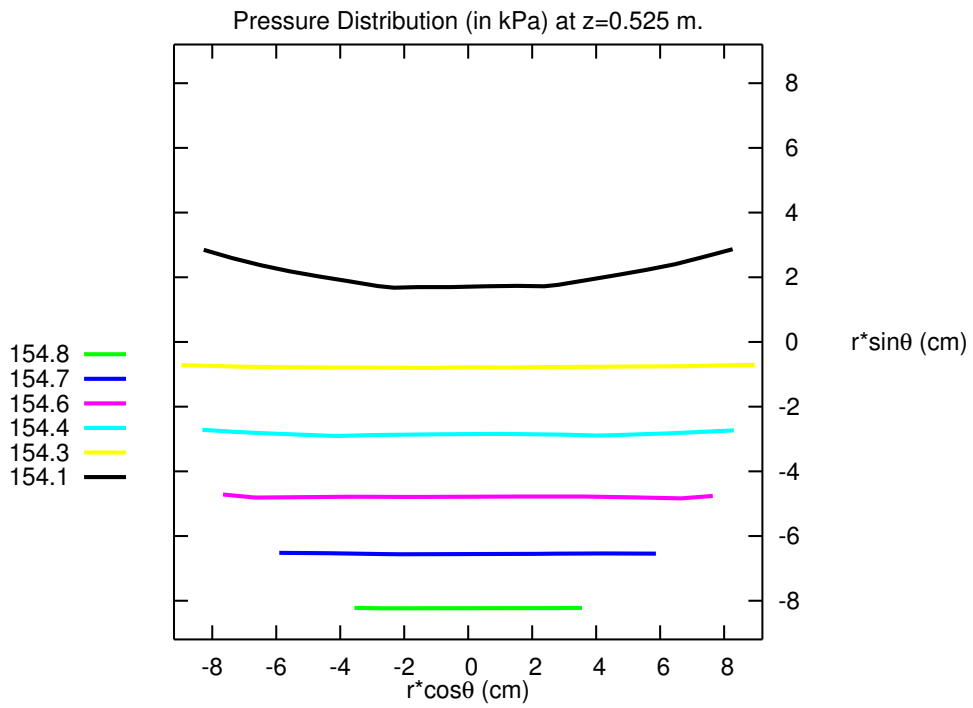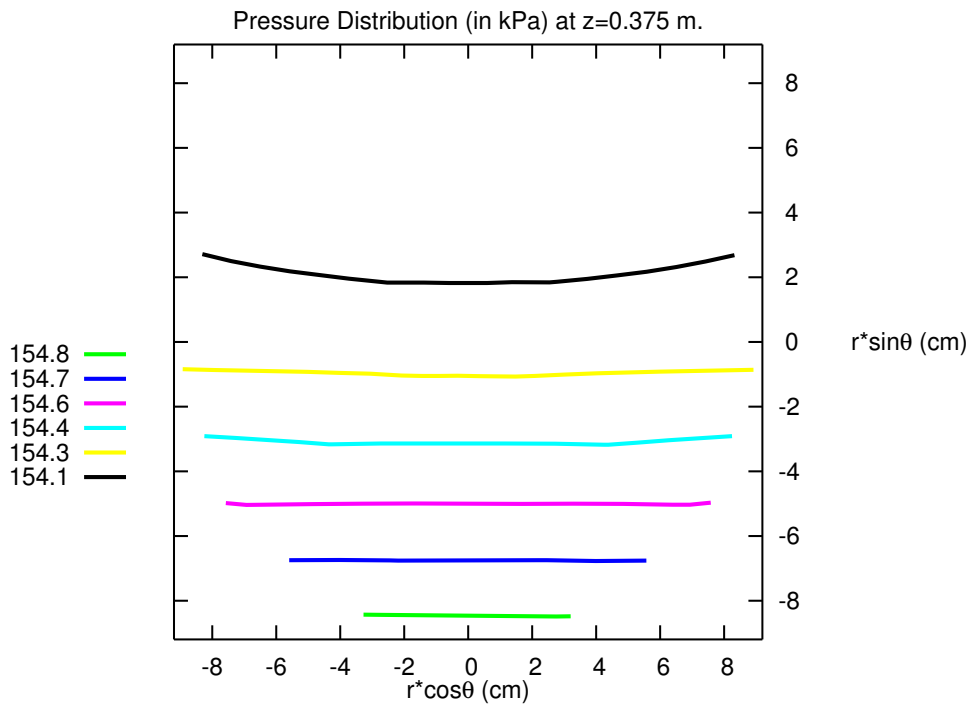
Figure 7.23: Void Distribution-II, Test Matrix-J1

Figure 7.24: Pressure Distribution-II, Test Matrix-J1

Void Distribution at z=0.625 m.

Void Distribution at z=0.925 m.
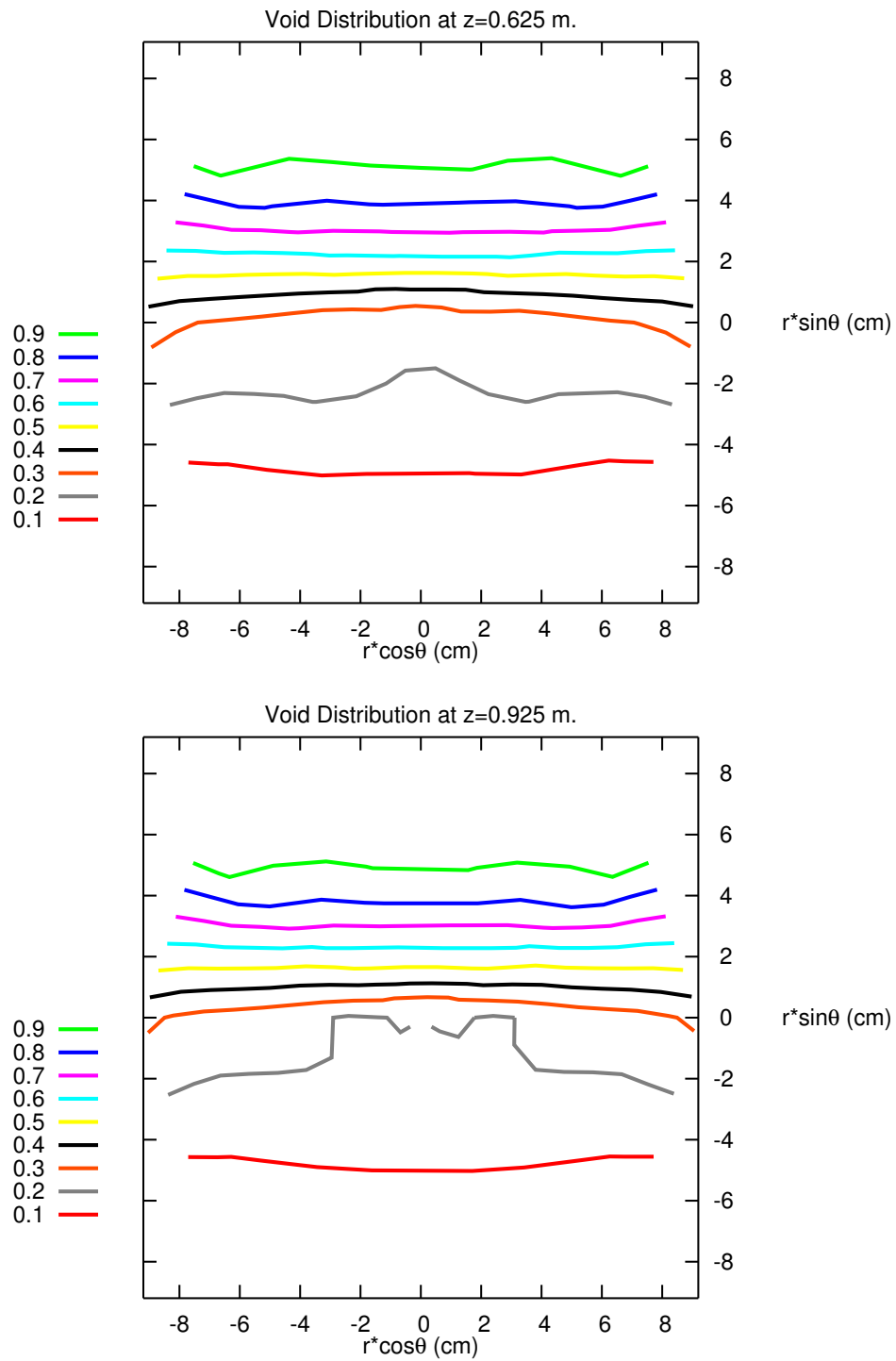
Figure 7.25: Void Distribution-III, Test Matrix-J1

136
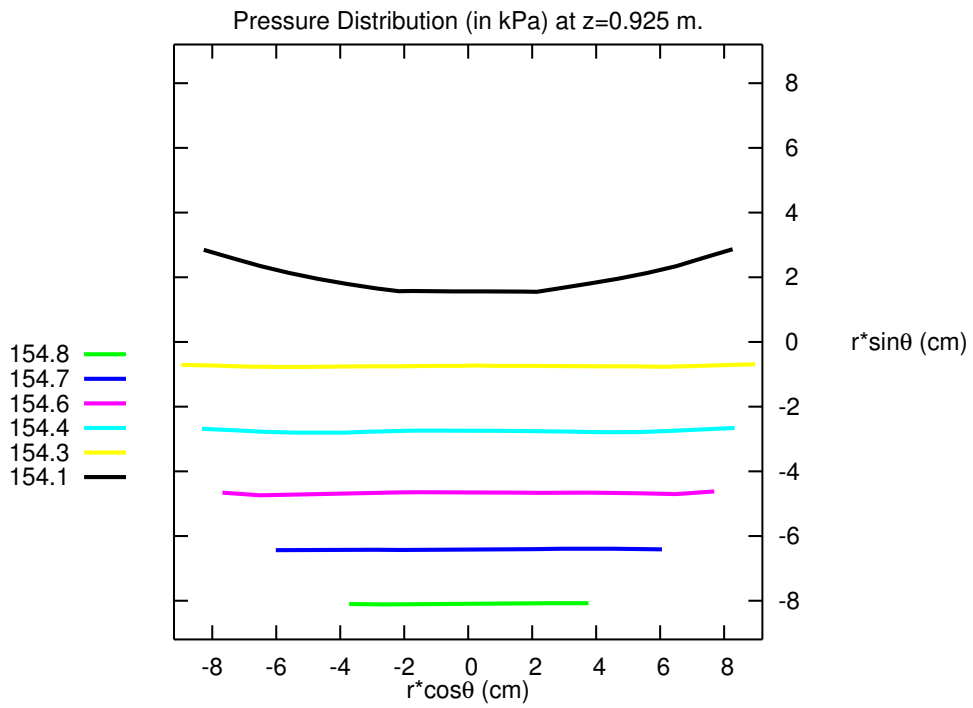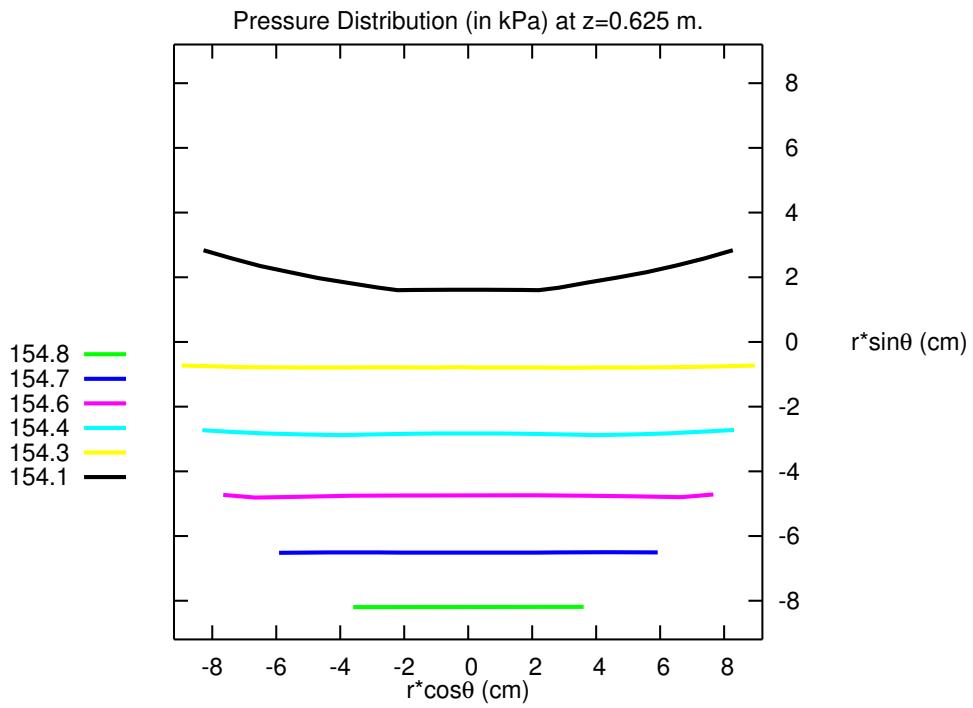
Figure 7.26: Pressure Distribution-III, Test Matrix-J1

7.1.2.3 Test Matrix-J2 (J000, J004)

Two-phase flow through Feeders 4 and 5 is further investigated in this section, with almost the same inlet mass flow rate but higher inlet void fraction. Test Matrix-J2 is formed by using Test-J000 and Test-J004. Initial conditions are obtained by converging the single-phase solution (Test-J004) for inlet mass flow rate of 2.164 kg/s at t=10 s. Then, two-phase fluid having void fraction of 0.254 and mass flow rate of 2.075 kg/s are forced to enter into the computational domain of header.

Convergence history of the variables can be seen in Figure 7.27. Mass flow rates of the two-phase flow at the inlet and at the two outlets (F-4, F-5) and total outflow are shown in Figure 7.28. The mass residual goes to zero at about 70 seconds after injection of two-phase mixture.
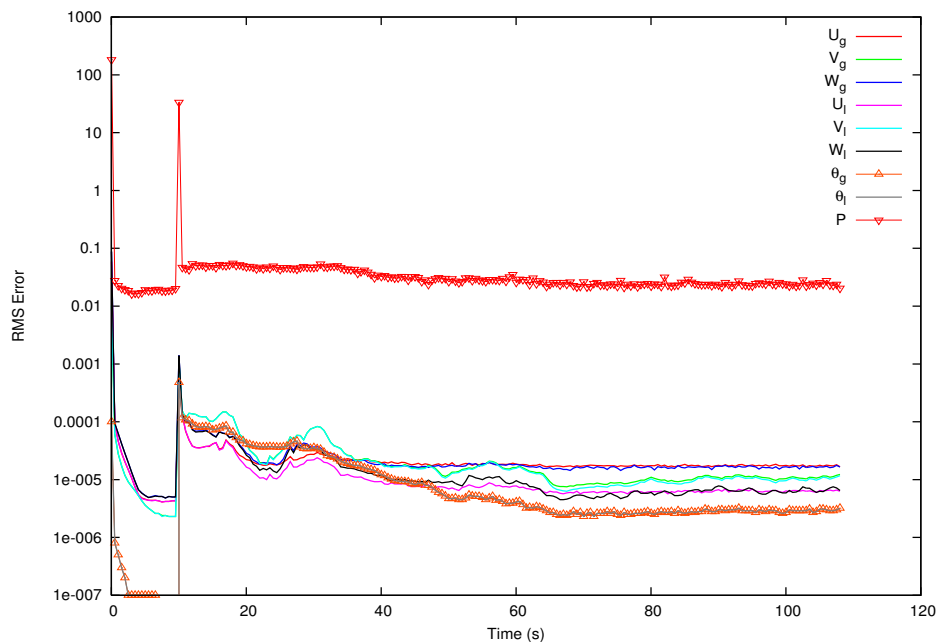

Figure 7.27: Root-Mean-Square Error, Transient Test-J2

As shown in Table 7.4, void fraction is calculated as 0.194 for nozzle-4 and 0.199 for nozzle-5, which are higher than those found in Test Matrix-J1

(0.154 and 0.152 respectively) as expected. Symmetric prediction is conserved again for mass flow rates. Flow is distributed to both nozzles almost equally (1.042 vs. 1.036 kg/s) while test results were 1.120 vs. 0.993 kg/s respectively. Applying more void fraction at the inlet did not make any effect on the flow rates and on the outlet void fractions. This prediction is not fully compliant with the experimental results that showed more voids to go to feeder-5 by increasing the inlet void fraction. Flow split ratio is predicted to be around 1.

Table 7.4: Flow Distribution Through Feeder-4 and Feeder-5,Test Matrix J2

TEST MATRIX J2							
	Single Phase (J000)						
	θ_{in}	$\dot{m}_{in}$ (kg/s)	θ_4	θ_5	$\dot{m}_4$ (kg/s)	$\dot{m}_5$ (kg/s)	FSR
Experimental	0.000	2.164	0.000	0.000	1.125	1.128	0.997
Numerical	0.001	2.164	0.000	0.000	1.084	1.085	0.999
	Two Phase (J004)						
	θ_{in}	$\dot{m}_{in}$ (kg/s)	θ_4	θ_5	$\dot{m}_4$ (kg/s)	$\dot{m}_5$ (kg/s)	FSR
Experimental	0.254	2.075	0.145	0.305	1.120	0.993	1.128
Numerical	0.254	2.075	0.194	0.199	1.042	1.036	1.006

Introduction of more voids into the domain resulted the void distribution profile as presented by Figure 7.30 for the points at z=0.075 m. and at z=0.175 m. planes. Contours showed similar complex behaviour at these planes. The other sections of the header beyond z=0.375 m. (Figures 7.32 and 7.34) have similar formations. Pressure distribution contours are shown in Figures 7.31, 7.33 and 7.35. Almost constant lines can be seen especially at the bottom region, proving the existance of the more liquid and less air. The effect of nozzles 4 and 5 locations can be seen in Figure 7.31 where their existance distorts the pressure profile to the right-downward and to the left-downward directions respectively.
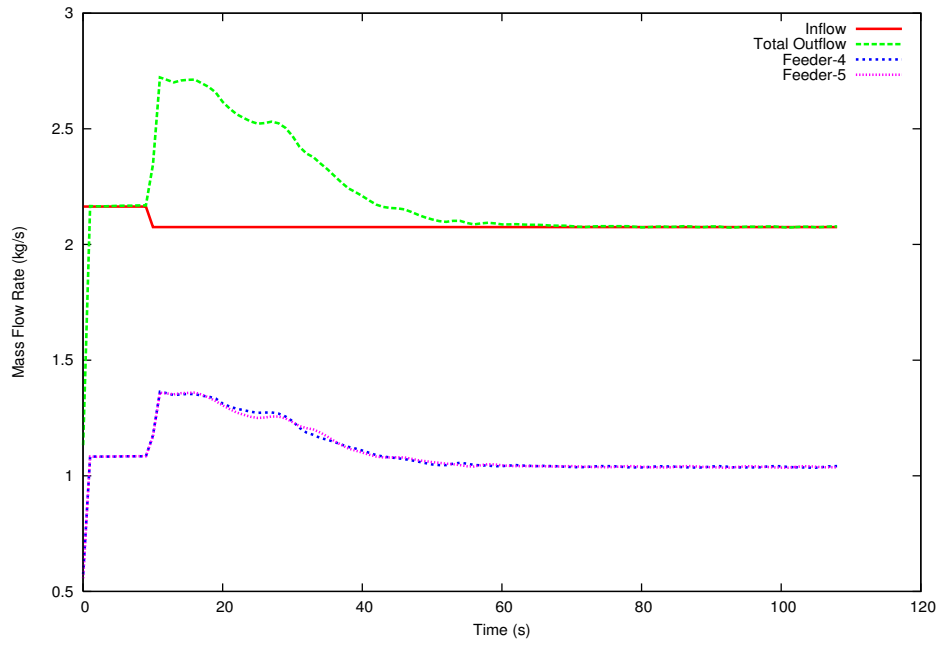
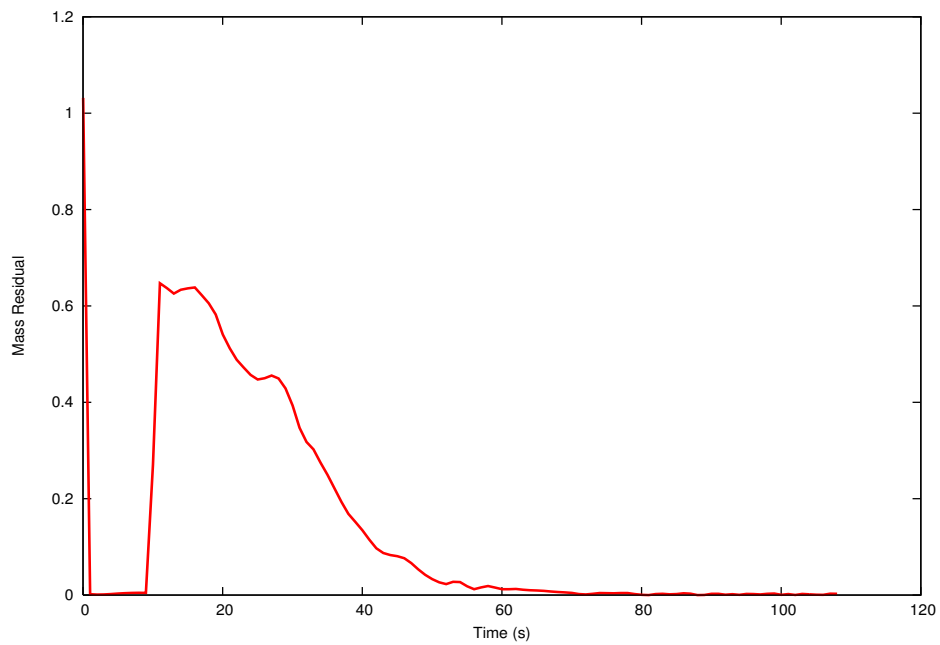Figure 7.28: Mass Flow Rates, Test Matrix-J2

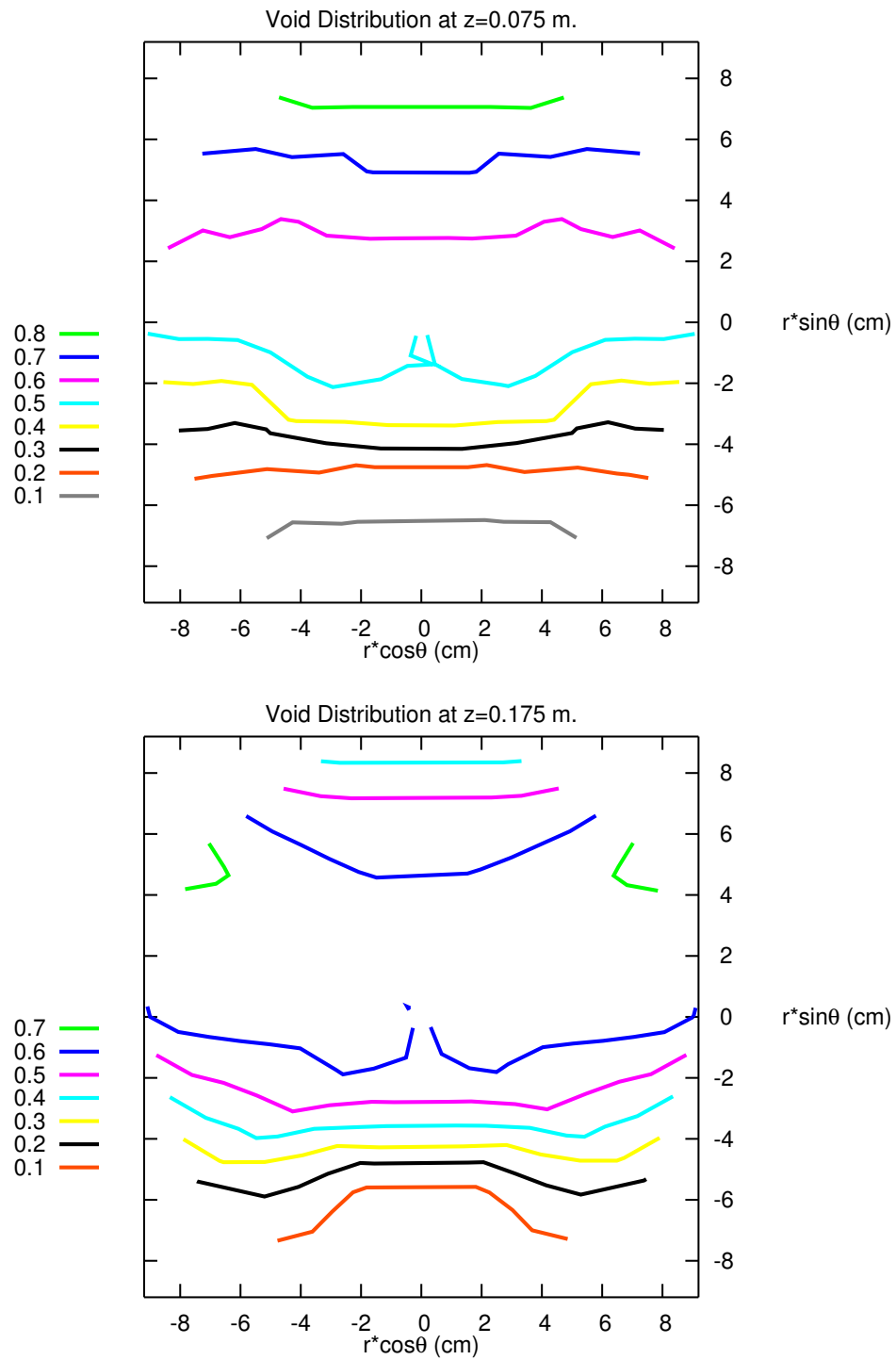Figure 7.29: Mass Residual, Test Matrix-J2
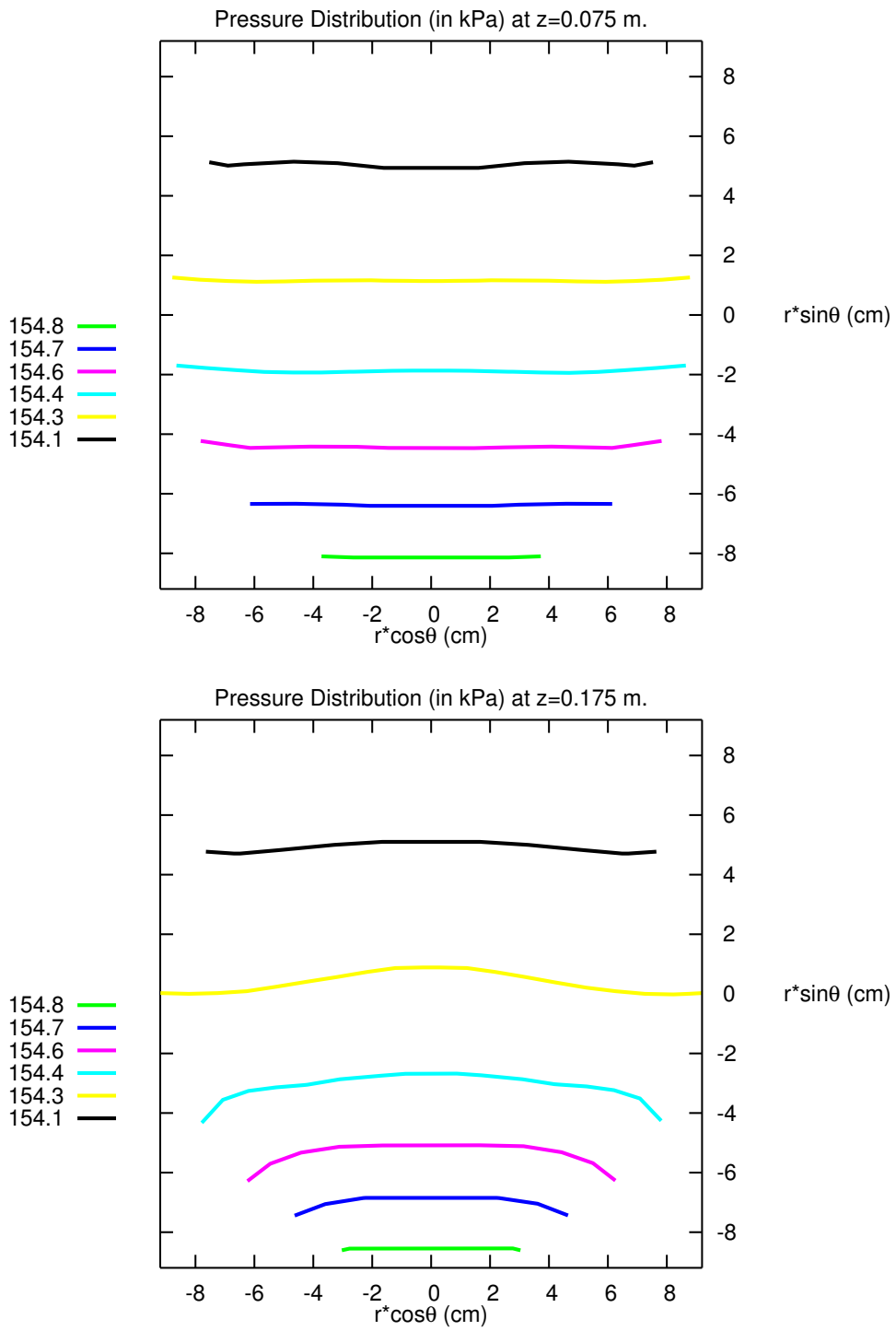
140

Figure 7.30: Void Distribution-I, Test Matrix-J2

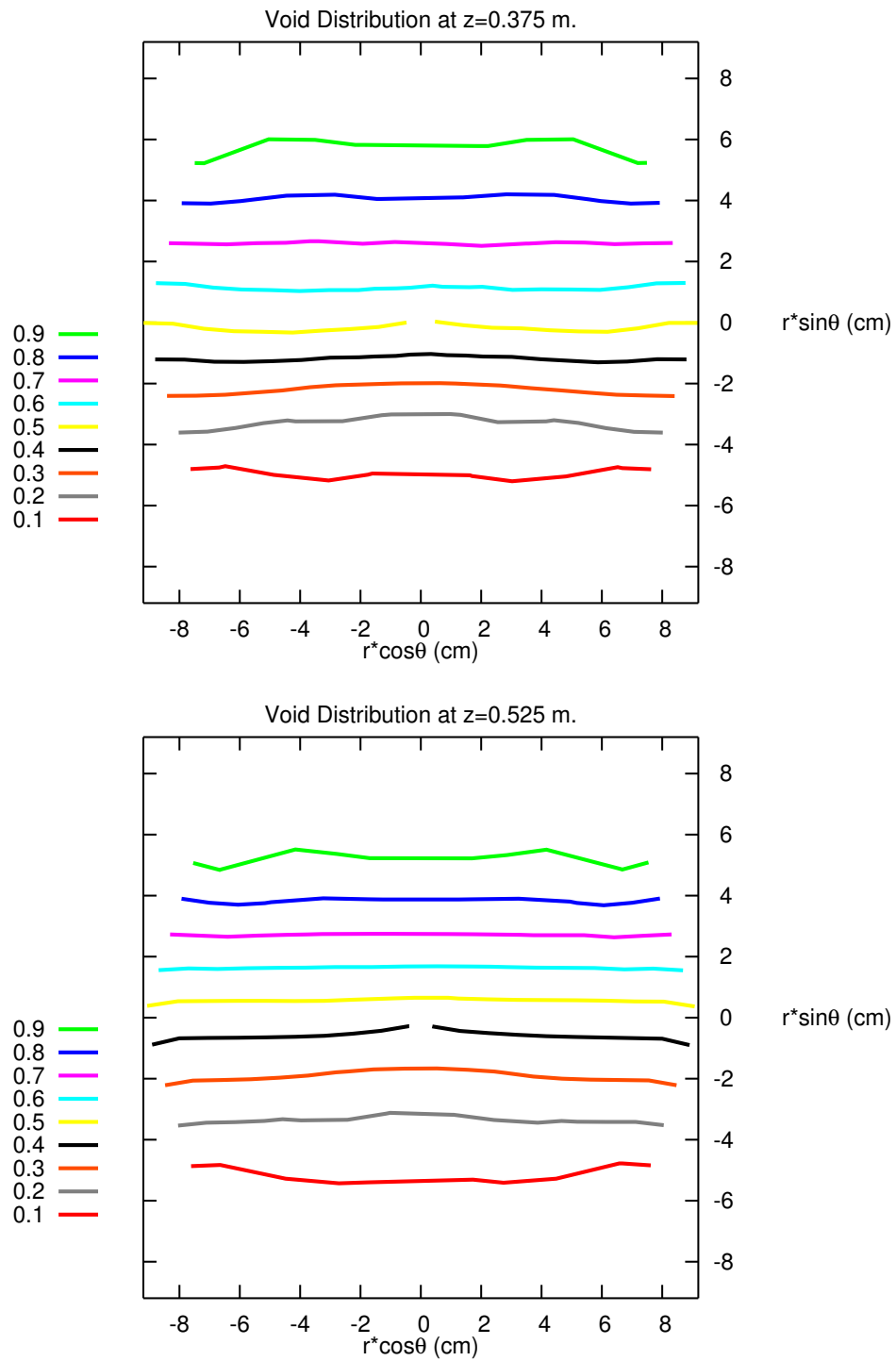Figure 7.31: Pressure Distribution-I, Test Matrix-J2
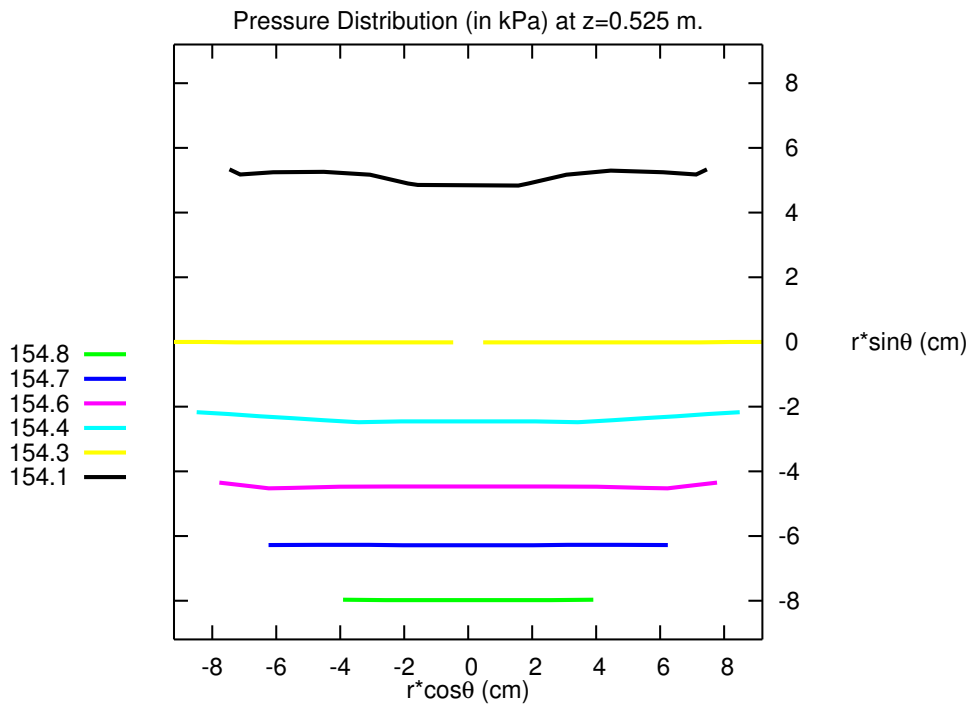
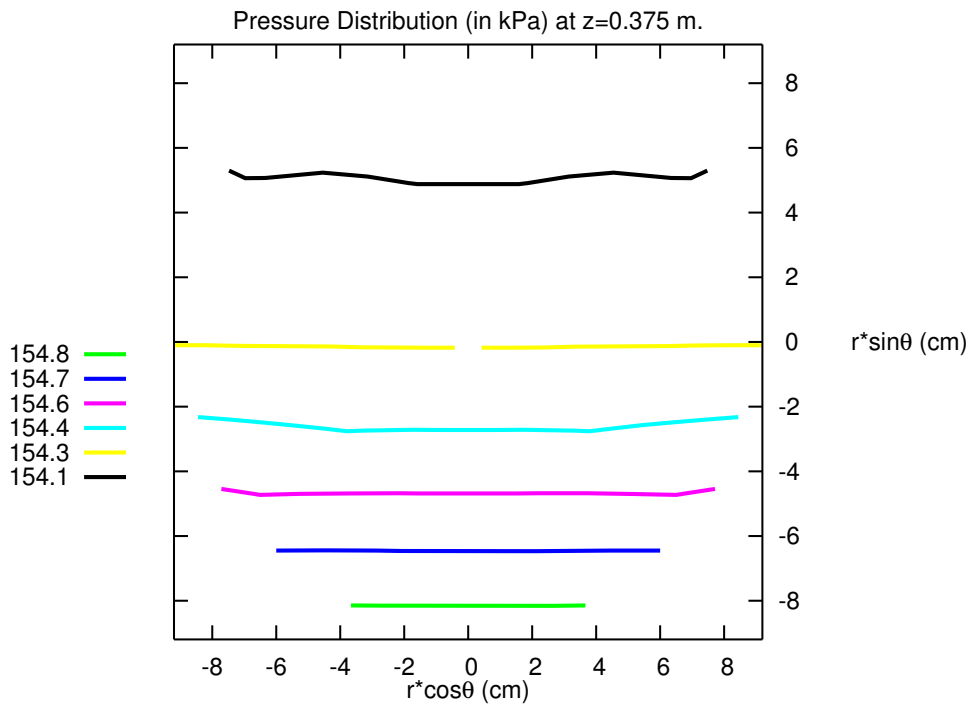Figure 7.32: Void Distribution-II, Test Matrix-J2

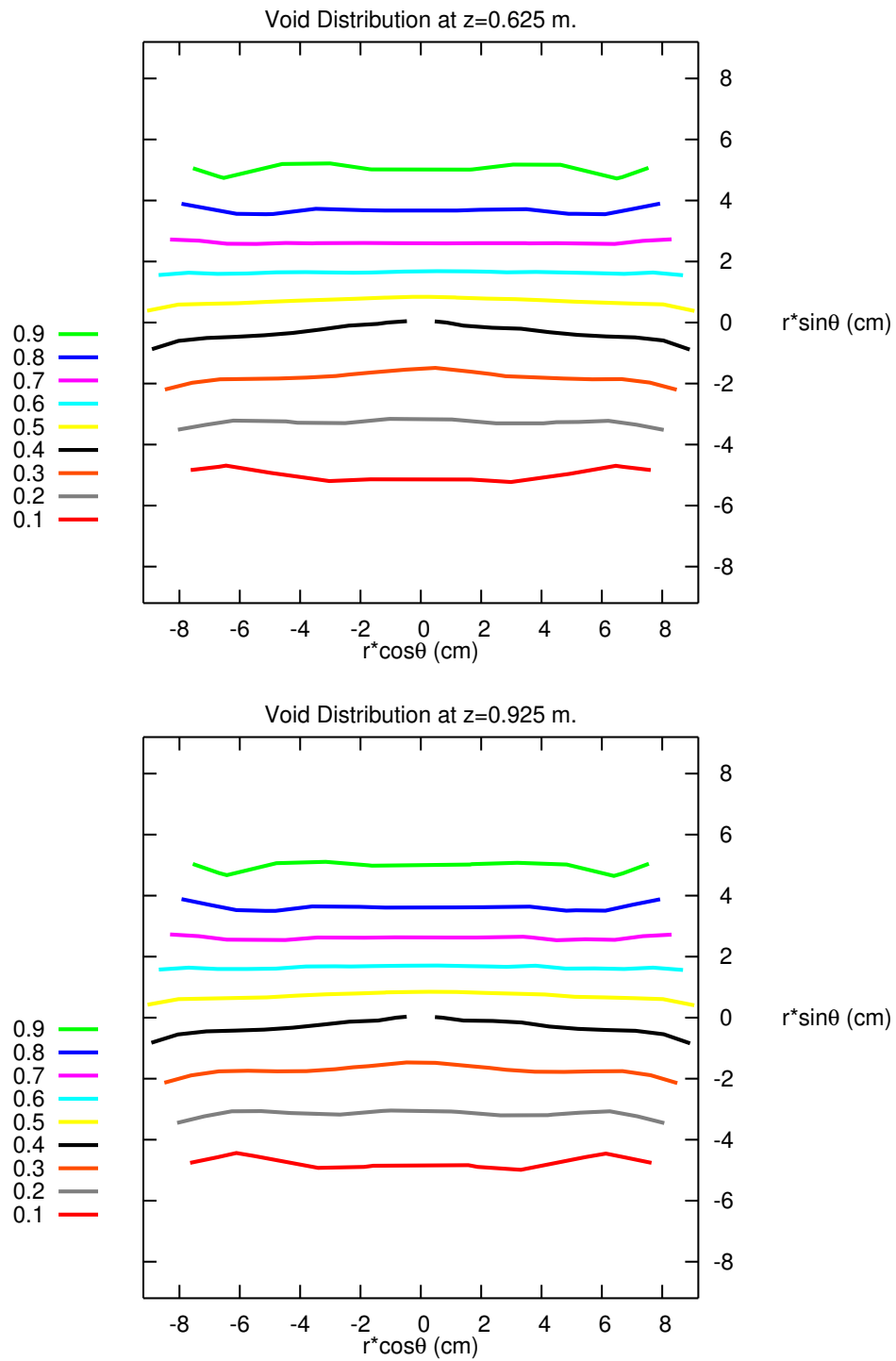Figure 7.33: Pressure Distribution-II, Test Matrix-J2

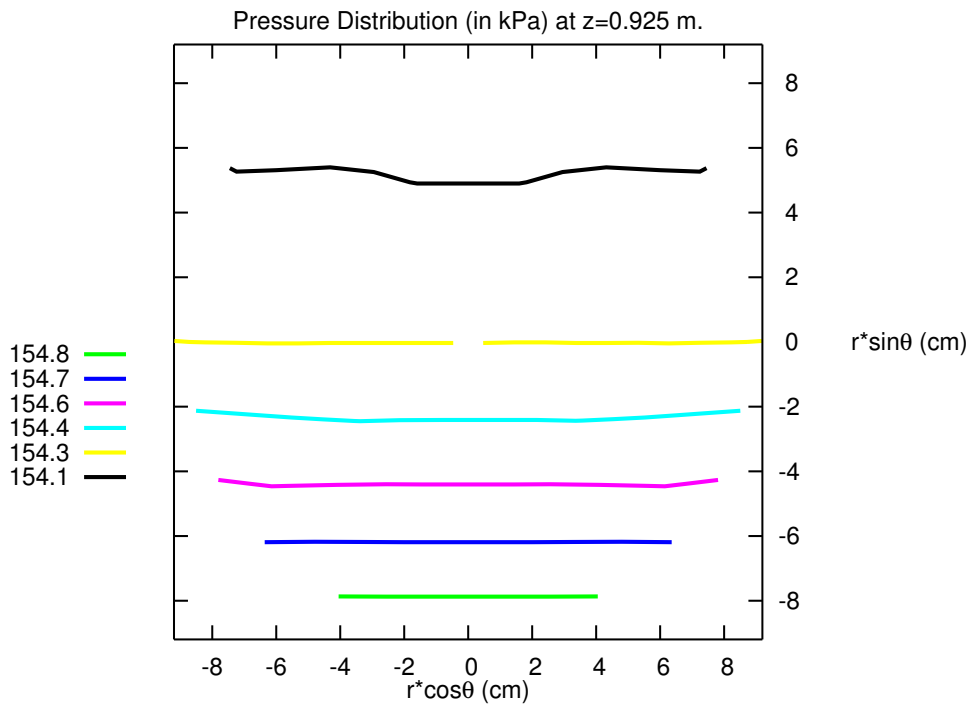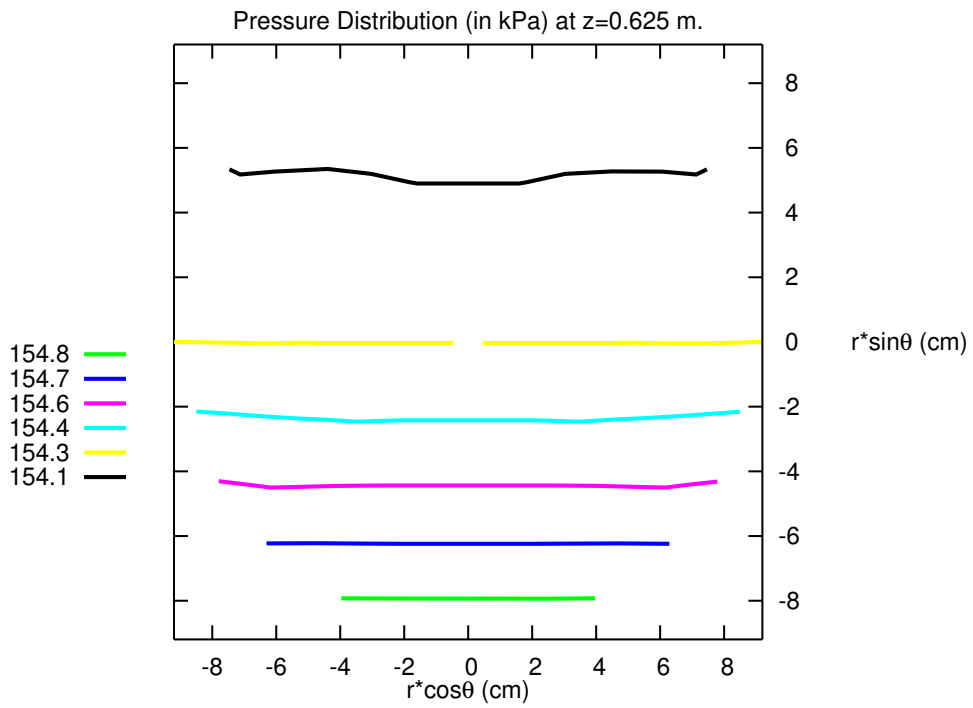Figure 7.34: Void Distribution-III, Test Matrix-J2

Figure 7.35: Pressure Distribution-III, Test Matrix-J2

7.1.2.4 Test Matrix-K1 (K001, K002)

Feeders 3 and 4 are selected to form Test Matrix-K1 by taking the data obtained from Test-K001 and Test-K002. Test-K001 is used to obtain initial pressure profile inside the drum. Single-phase Test-K001 conditions are applied until the code is reached to steady solutions at t=10 s. for inlet mass flow rate of 2.111 kg/s. Then, by changing void fraction from 0.001 to 0.146 and mass flow rate from 2.111 to 2.078 kg/s, two-phase transient starts.

Figure 7.36 shows the steady-state convergence of the variables. Resulting mass flow rates at the inlet and at the two outlets (F-3, F-4) and total outflow are shown in Figure 7.37. Mass residual goes to zero at about 120 seconds after injection of two-phase mixture at t=10 s. (See Figure 7.38).

The curves in Figure 7.37 gives a convergent mass flow rates of 1.243 kg/s and 0.837 kg/s for feeder-3 and feeder-4 respectively. Flow split ratio is found to be about 1.485. It increased from initial value of 1.339. Experimental results also showed similar behaviour by reaching to 1.487. It can be said that the code's prediction gives a very close results to the test's results in Test-Matrix-K1. Table 7.5 summarises the comparison between the experimentally measured data and numerically predicted data.

Table 7.5: Flow Distribution Through Feeder-3 and Feeder-4, Test Matrix K1

TEST MATRIX K1							
	Single Phase (K001)						
	θ_{in}	$\dot{m}_{in}$ (kg/s)	θ_3	θ_4	$\dot{m}_3$ (kg/s)	$\dot{m}_4$ (kg/s)	FSR
Experimental	0.000	2.111	0.000	0.000	1.209	0.903	1.339
Numerical	0.001	2.111	0.000	0.000	1.209	0.903	1.339
	Two Phase (K002)						
	θ_{in}	$\dot{m}_{in}$ (kg/s)	θ_3	θ_4	$\dot{m}_3$ (kg/s)	$\dot{m}_4$ (kg/s)	FSR
Experimental	0.146	2.078	0.000	0.151	1.307	0.879	1.487
Numerical	0.146	2.078	0.066	0.194	1.243	0.837	1.485

Void fraction is calculated as 0.066 for nozzle-3 and 0.194 for nozzle-4, which are somewhat higher values than that of measured ones (0.000 and 0.151 respectively). The code predicted higher void fraction and lower flow rate in the feeder-4 as expected, possibly due to its location closer to the inlet nozzle and the smaller flow area than feeder-3.

The void distribution contours are predicted as represented by Figure 7.39 for the points at z=0.075 m. and at z=0.175 m. planes. Since feeder-3 and feeder-4 are at different locations but having angles between 270° and 360°. The distortions at the pressure contours are observed in the right-lower parts of the Figure 7.40 at z=0.175 m and of the Figure 7.42 at z=0.375 m. Beyond z=0.525 m almost similar contours are found for void and pressure distributions (Figures 7.41, 7.42, 7.43, 7.44).
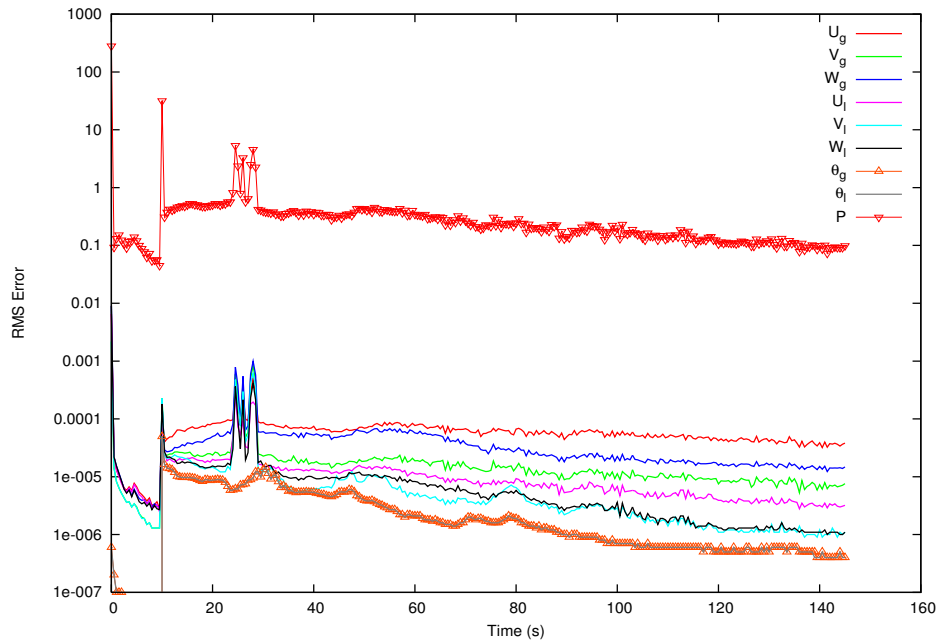

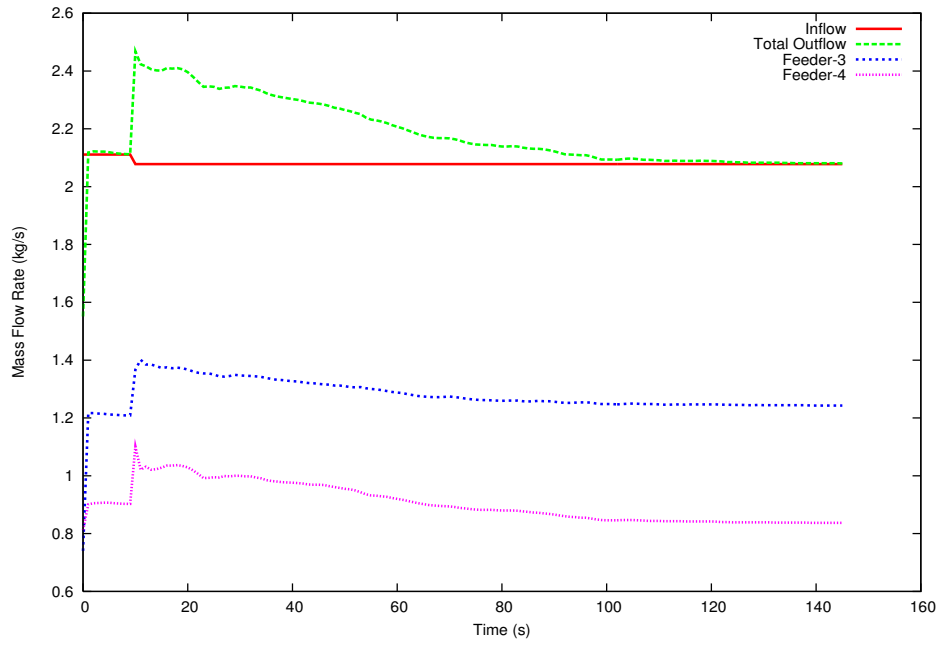Figure 7.36: Root-Mean-Square Error, Test Matrix-K1

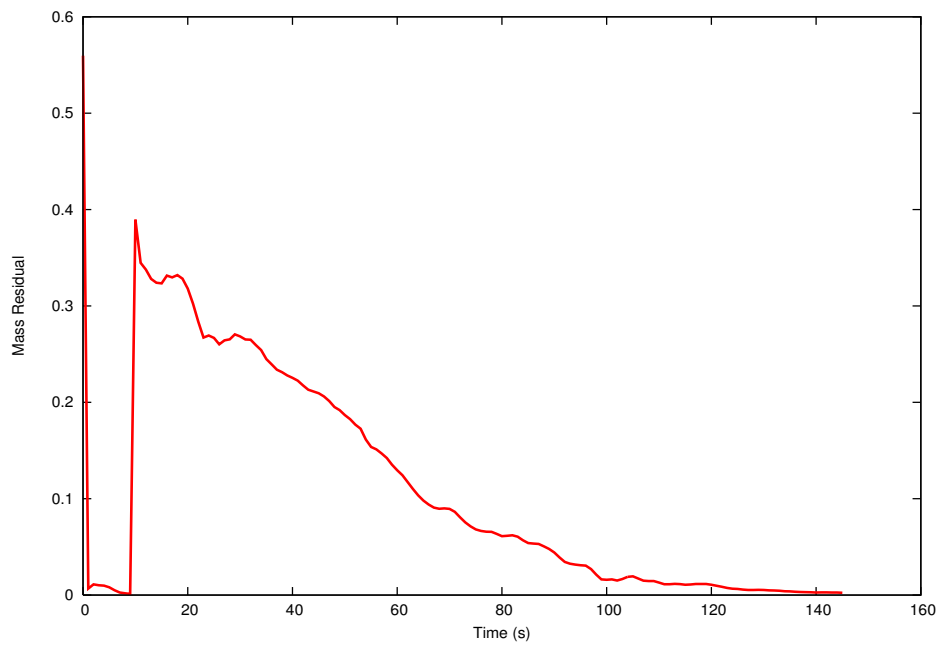Figure 7.37: Mass Flow Rates, Test Matrix-K1
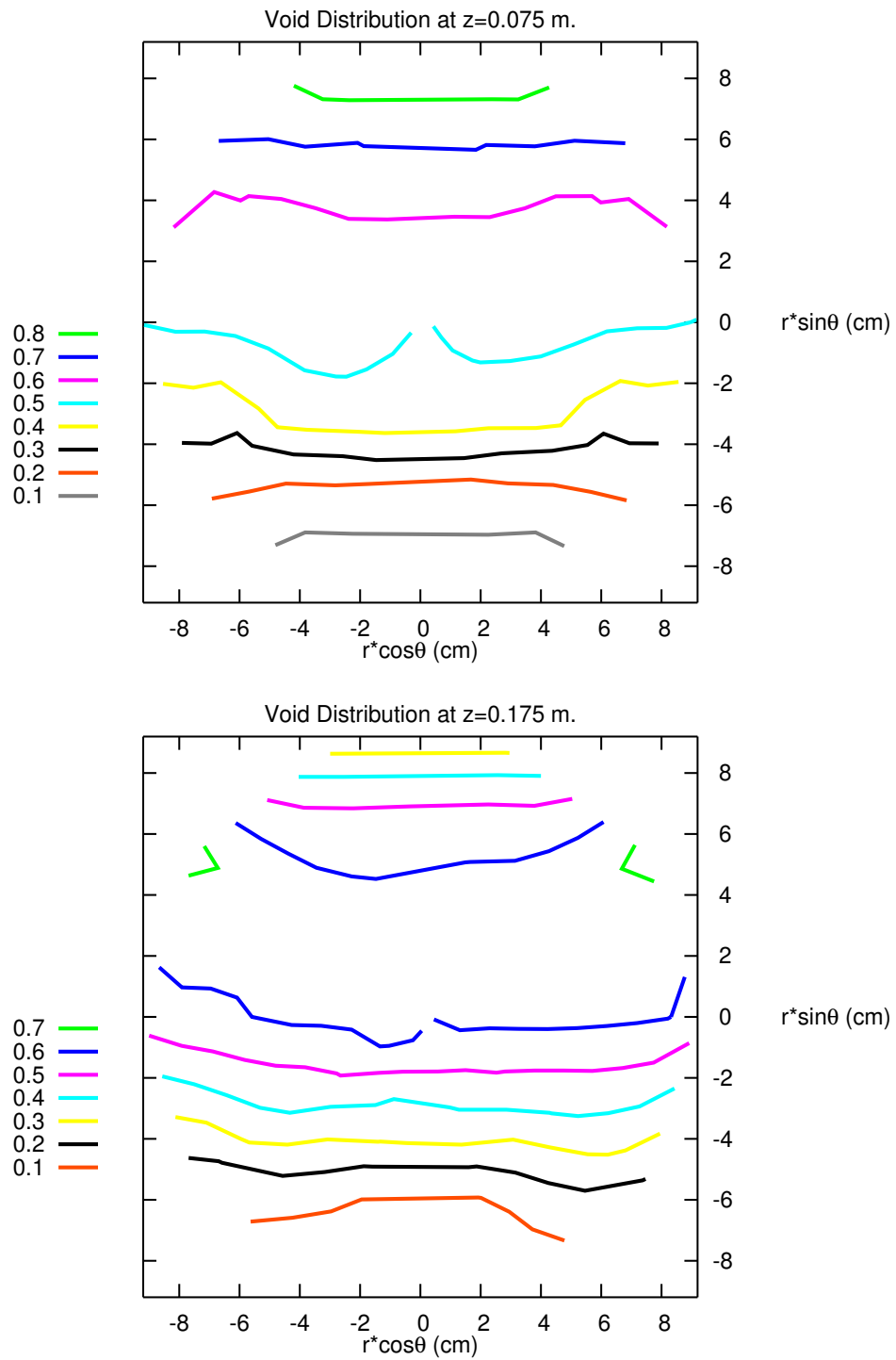

Figure 7.38: Mass Residual, Test Matrix-K1

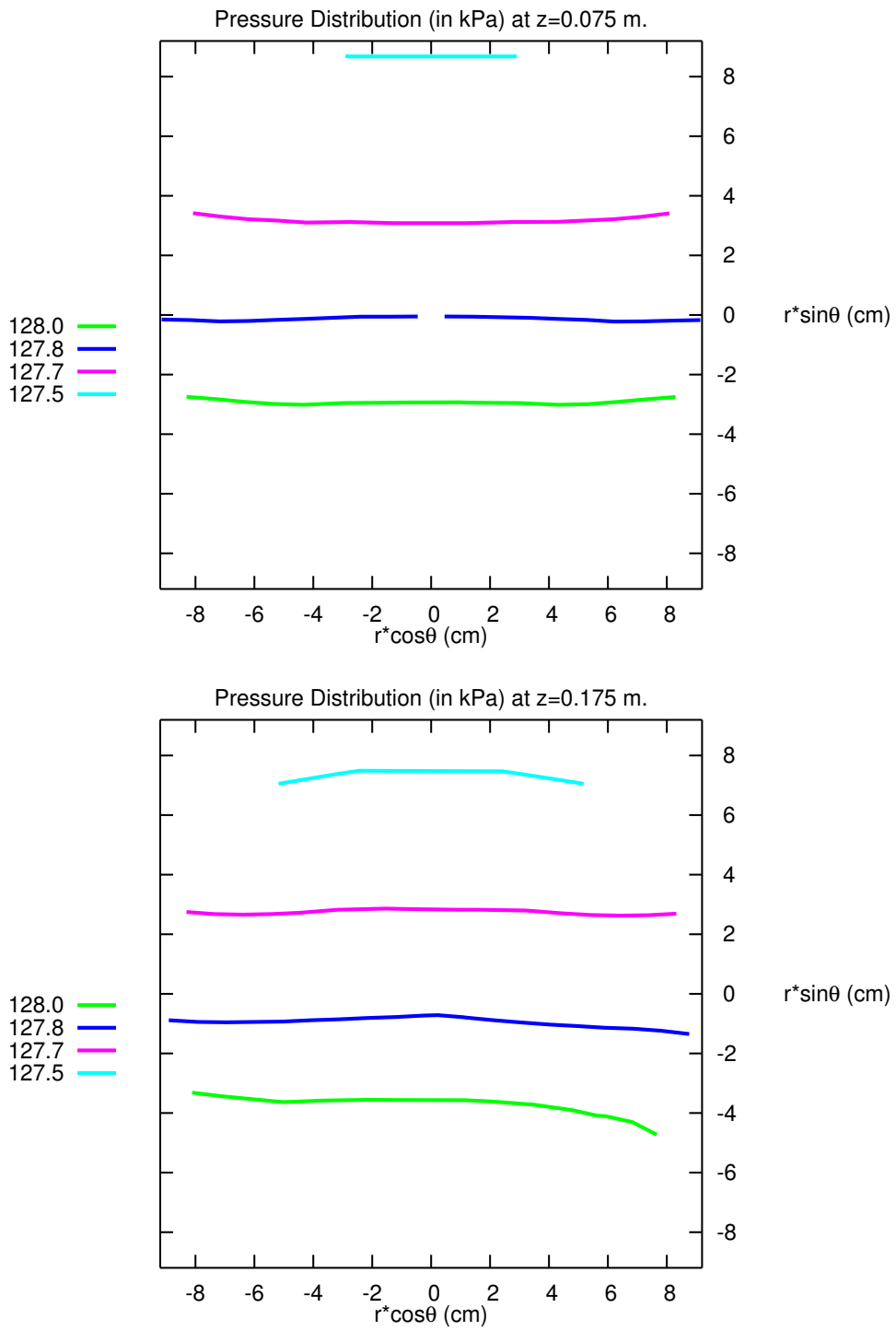Figure 7.39: Void Distribution-I, Test Matrix-K1

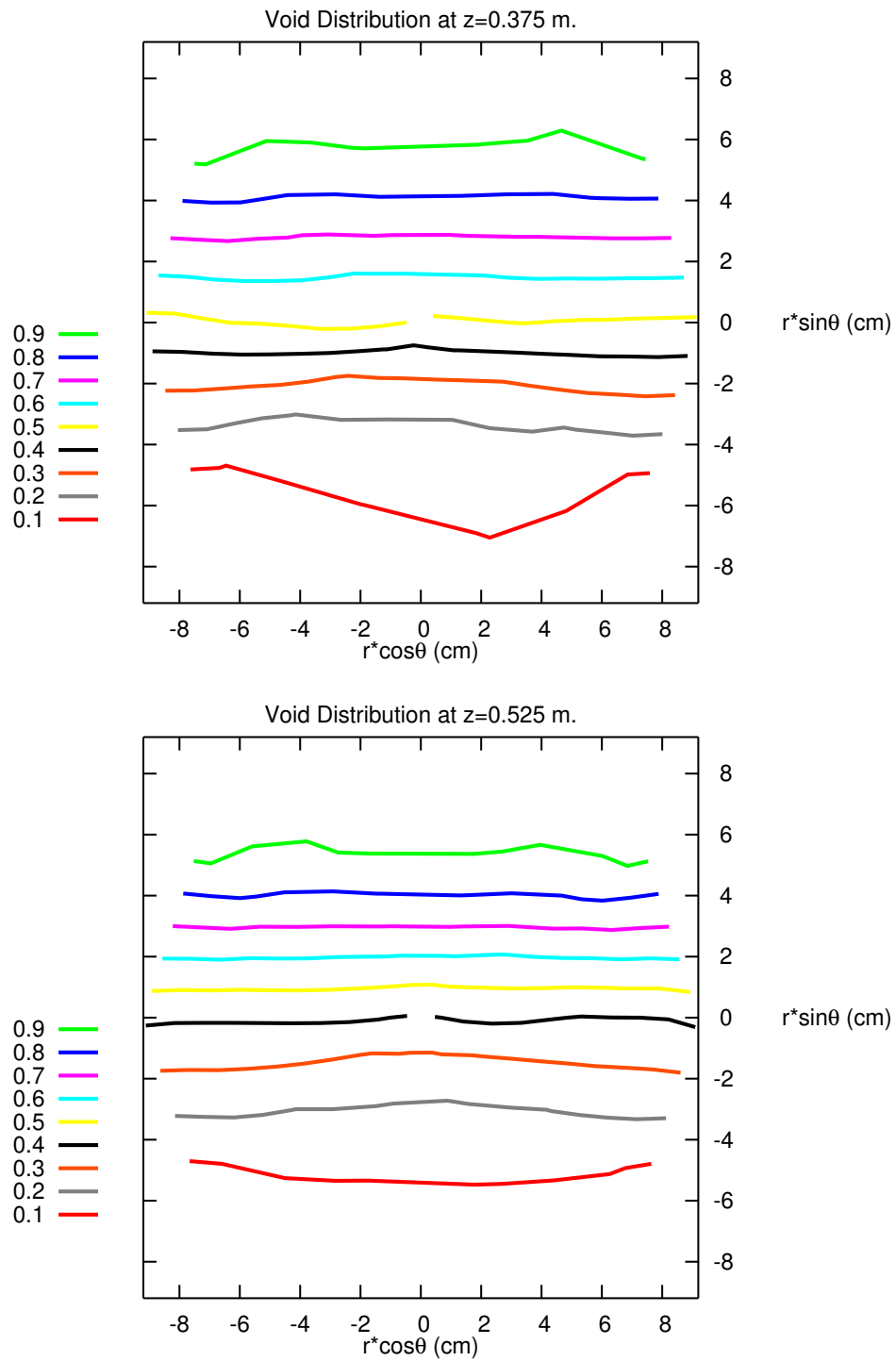Figure 7.40: Pressure Distribution-I, Test Matrix-K1
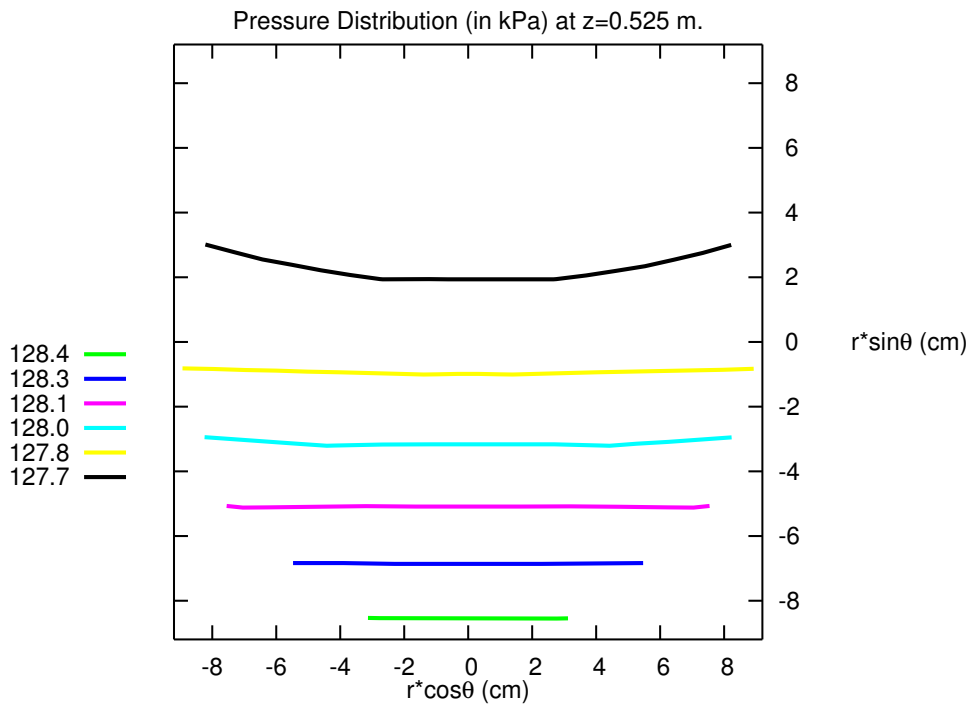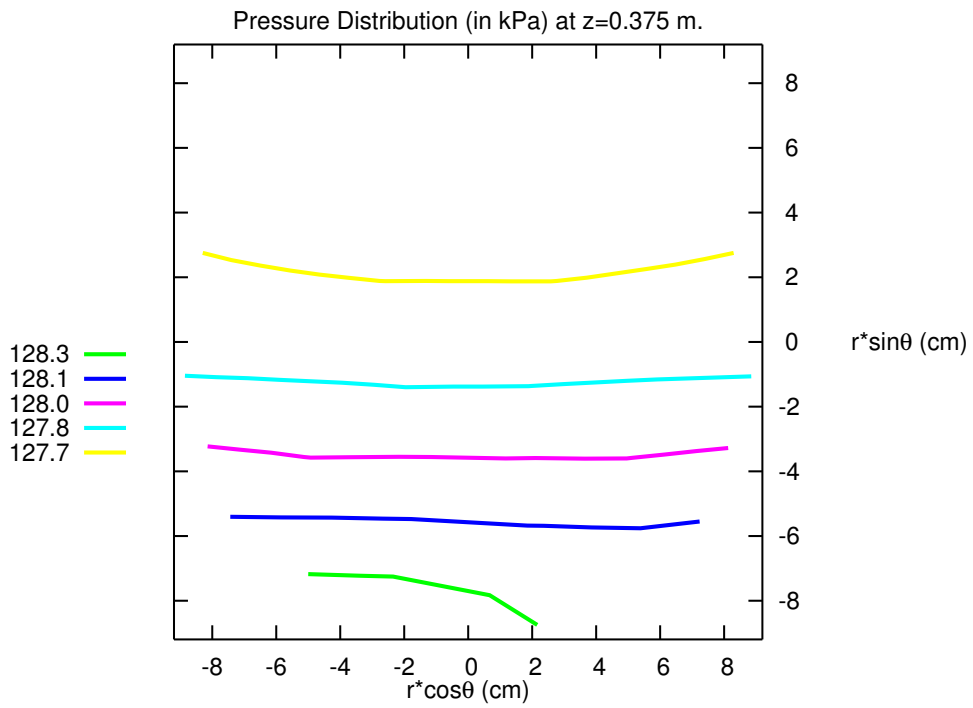
Figure 7.41: Void Distribution-II, Test Matrix-K1

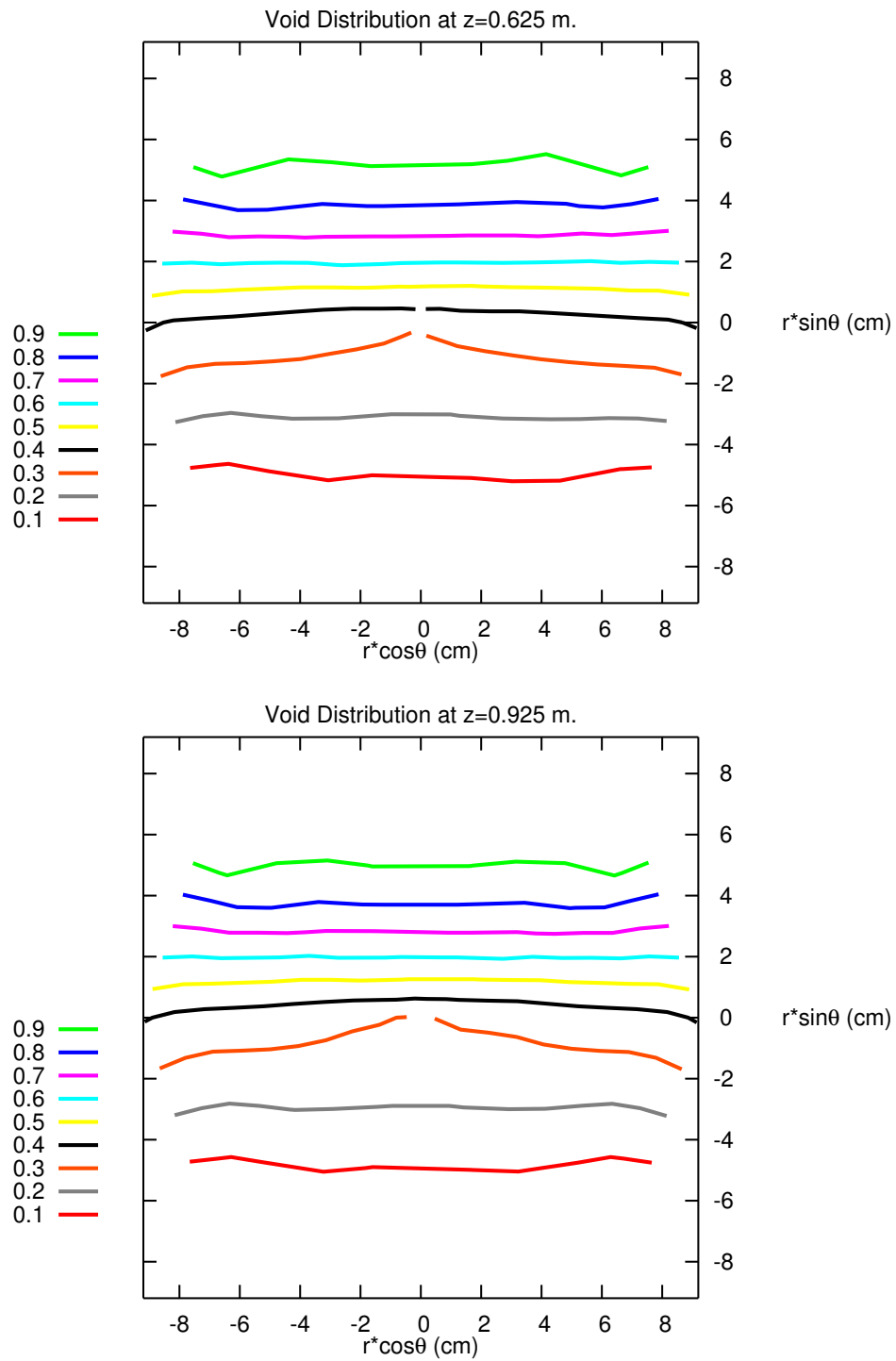Figure 7.42: Pressure Distribution-II, Test Matrix-K1

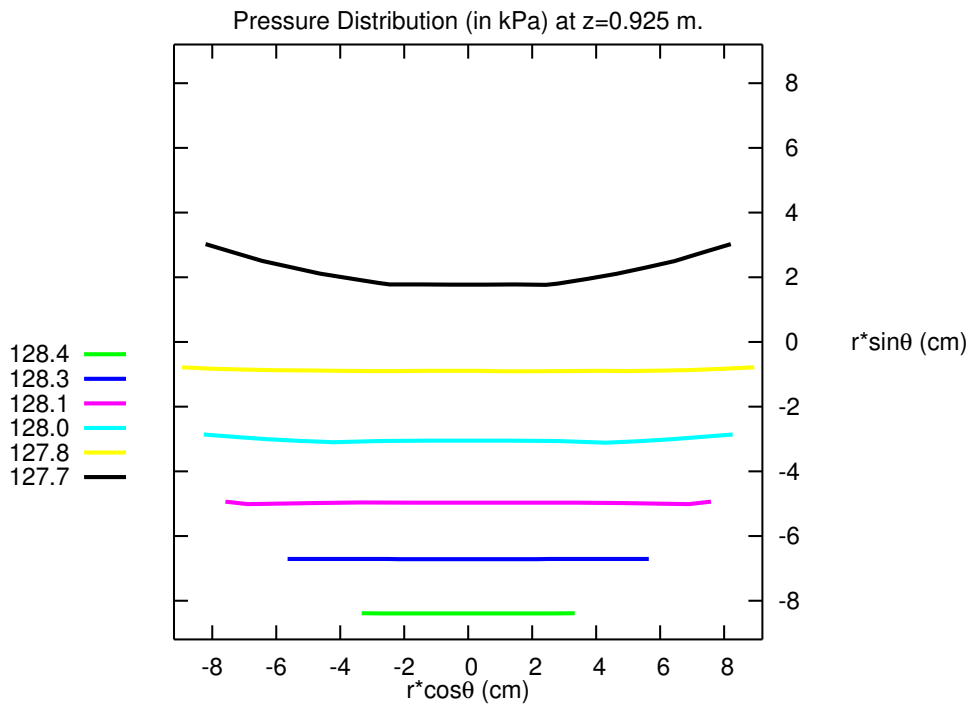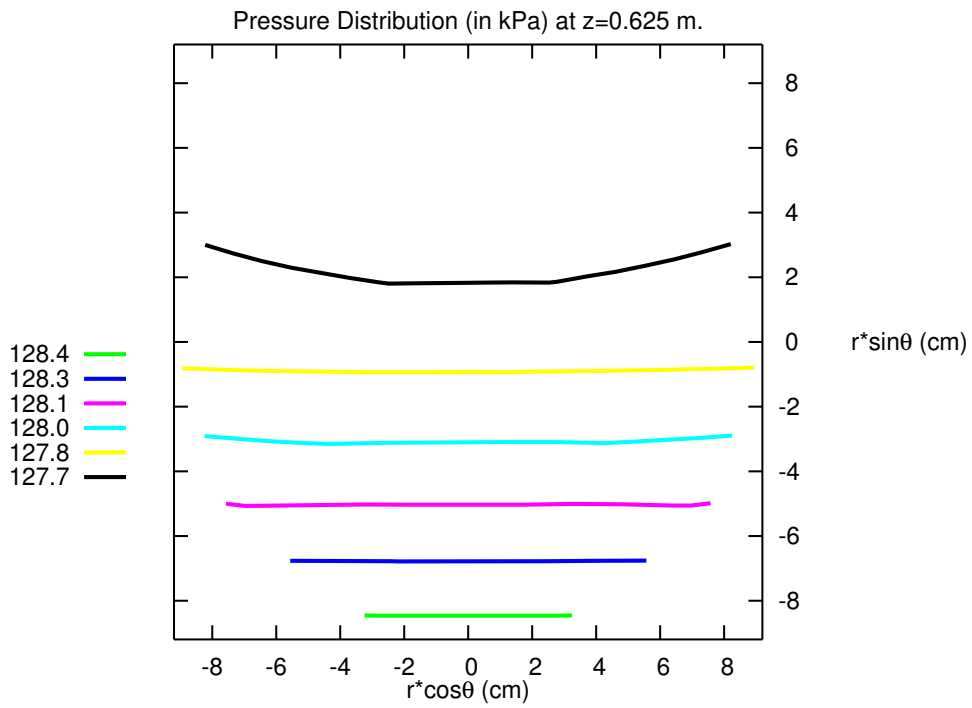**Figure 7.43:** Void Distribution-III, Test Matrix-K1

Figure 7.44: Pressure Distribution-III, Test Matrix-K1

7.1.2.5   Test Matrix-K2 (K001, K003)

Two-phase flow through Feeders 3 and 4 is further investigated in this section, with almost the same inlet mass flow rate but with higher inlet void fraction. After obtaining the single-phase converged solution (Test-K001) for inlet mass flow rate of 2.111 kg/s, transient is started at t=10 s. by imposing void fraction of 0.171 and mass flow rate of 2.167 kg/s to the inflow boundary conditions. Figure 7.45 shows the steady-state convergence of the variables. Figure 7.46 shows the mass flow rates of two-phase flow at the inlet and at the outlets (F-3, F-4) and the total outflow. The convergence history for the mass residual is reflected by Figure 7.47. It approaches to zero after about 90 seconds of the transient.

Table 7.6 summarises the comparison between the experimentally measured data and numerically predicted data. Code predicts mass flow rates of 1.303 kg/s and 0.865 kg/s for feeder-3 and feeder-4 respectively. Flow split ratio is found to be about 1.506. It increased from the initial value of 1.338. Experimental results also showed similar trend by reaching to 1.556. As in Test Matrix-K1, it can be said that the code's prediction is very close to the test's results.

Table 7.6: Flow Distribution Through Feeder-3 and Feeder-4, Test Matrix K2

TEST MATRIX K2							
	Single Phase (K002)						
	θ_{in}	$\dot{m}_{in}$ (kg/s)	θ_3	θ_4	$\dot{m}_3$ (kg/s)	$\dot{m}_4$ (kg/s)	FSR
Experimental	0.000	2.111	0.000	0.000	1.209	0.903	1.339
Numerical	0.001	2.111	0.000	0.000	1.211	0.905	1.338
	Two Phase (K003)						
	θ_{in}	$\dot{m}_{in}$ (kg/s)	θ_3	θ_4	$\dot{m}_3$ (kg/s)	$\dot{m}_4$ (kg/s)	FSR
Experimental	0.171	2.167	0.052	0.176	1.414	0.909	1.556
Numerical	0.171	2.167	0.067	0.227	1.303	0.865	1.506

Void fraction is calculated as 0.067 for nozzle-3 and 0.227 for nozzle-4, which are somewhat higher values than those of measured ones (0.052 and 0.176 respectively). Increase in inlet void fraction compared with Test Matrix-K1, resulted an increase in the void fraction prediction for feeder-4. The code predicted higher void fraction and lower flow rate in the feeder-4 as expected due to the same reasons stated in the previous Section 7.1.2.4.

Introduction of more voids into the domain resulted the void distribution profile as presented by Figure 7.48 at z=0.075 m and at z=0.175 m planes. At the other sections of the header beyond z=0.325 m (Figures 7.50 and 7.52) similar formations are predicted. Pressure distribution contours are presented in Figures 7.49, 7.51 and 7.53. These figures shows constant isobars near the bottom sections as predicted in the previous section.
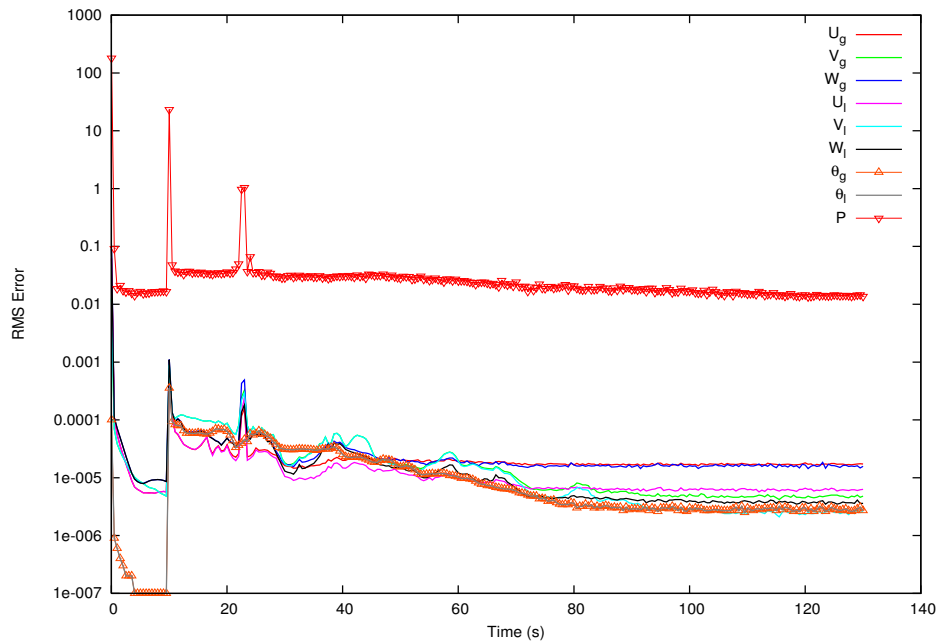
Figure 7.45: Root-Mean-Square Error, Test Matrix-K2

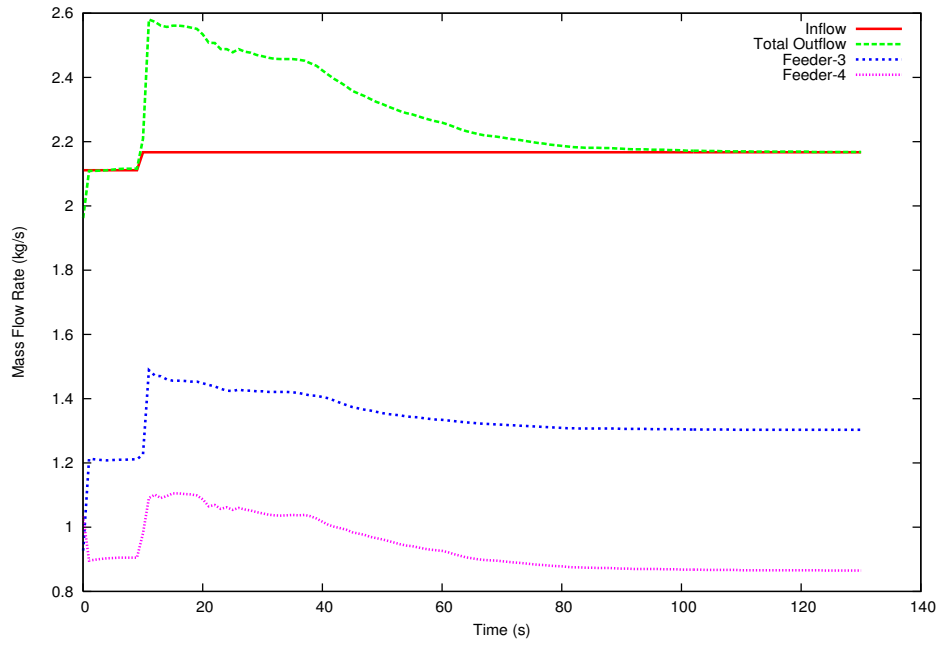Figure 7.46: Mass Flow Rates, Test Matrix-K2
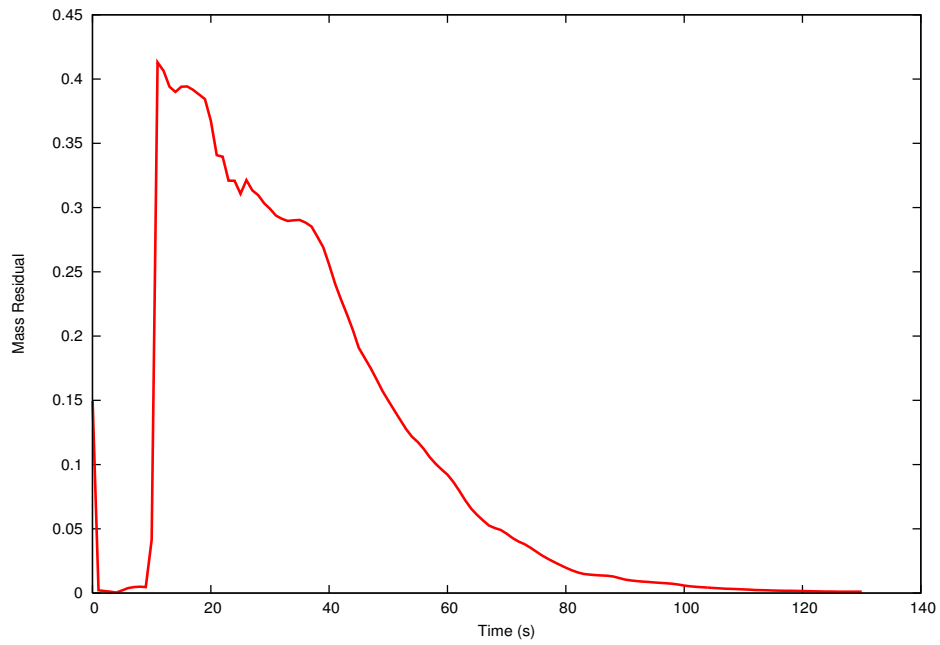
Figure 7.47: Mass Residual, Test Matrix-K2
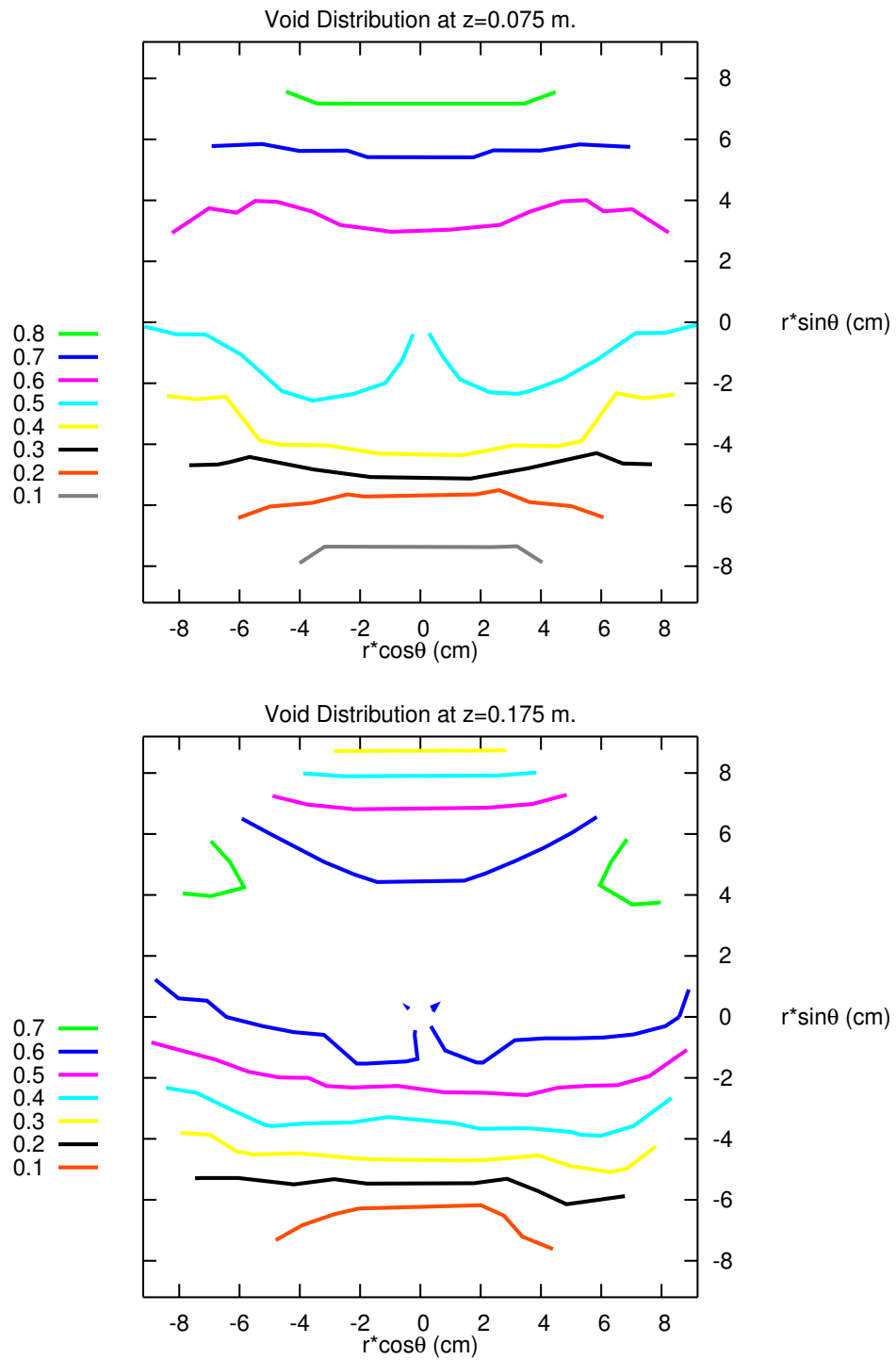
Figure 7.48: Void Distribution-I, Test Matrix-K2
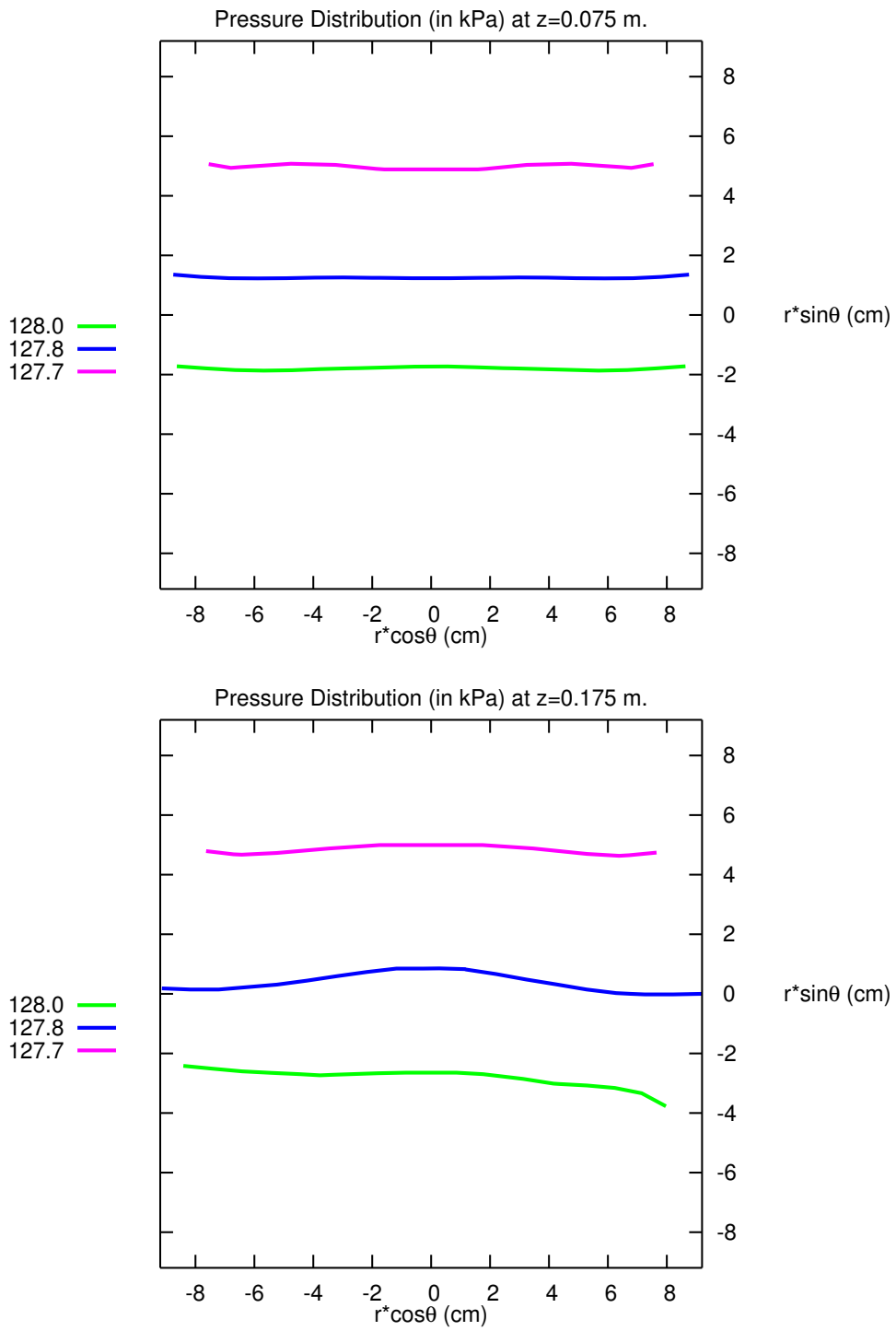
Figure 7.49: Pressure Distribution-I, Test Matrix-K2
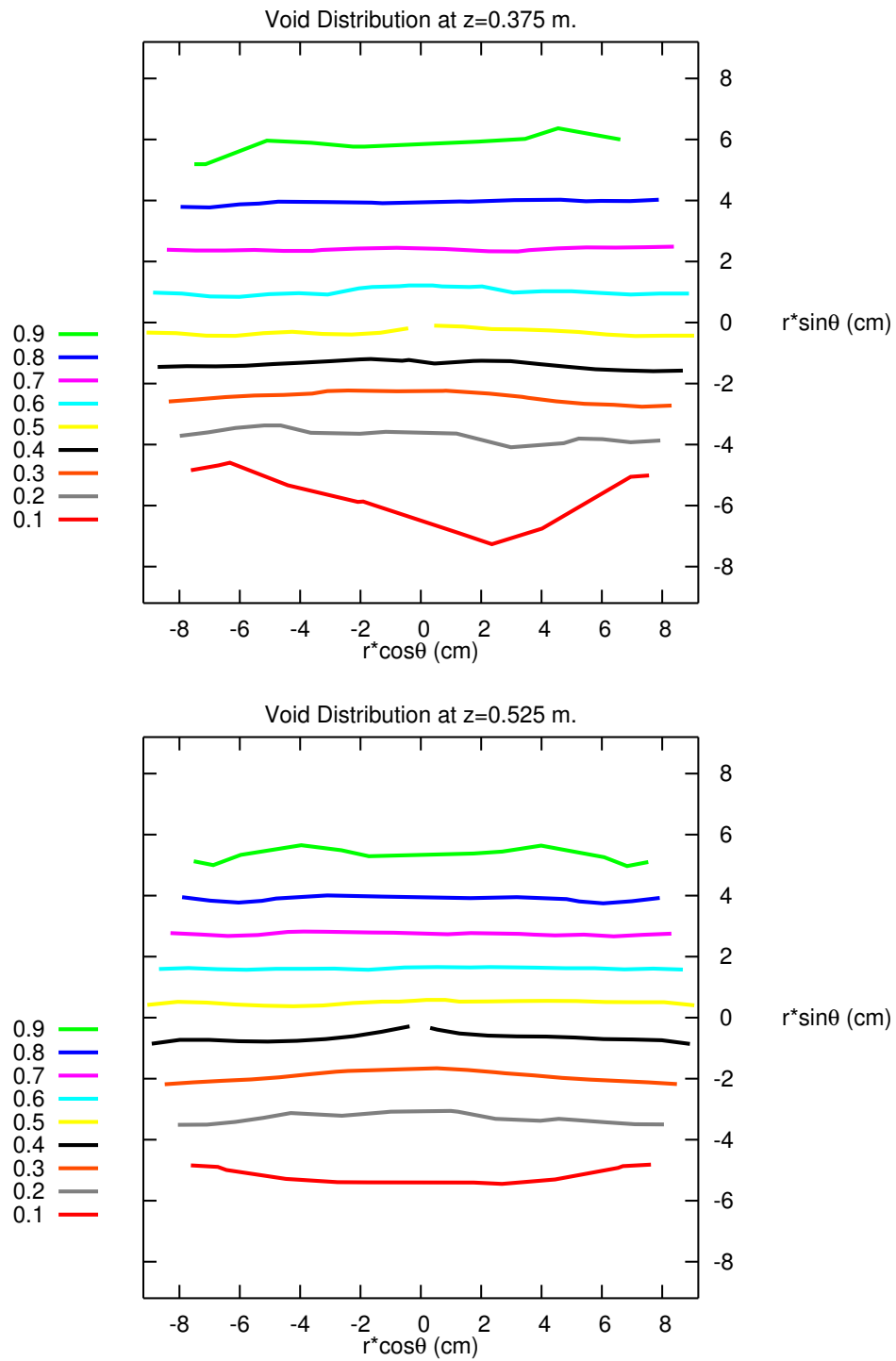
Figure 7.50: Void Distribution-II, Test Matrix-K2
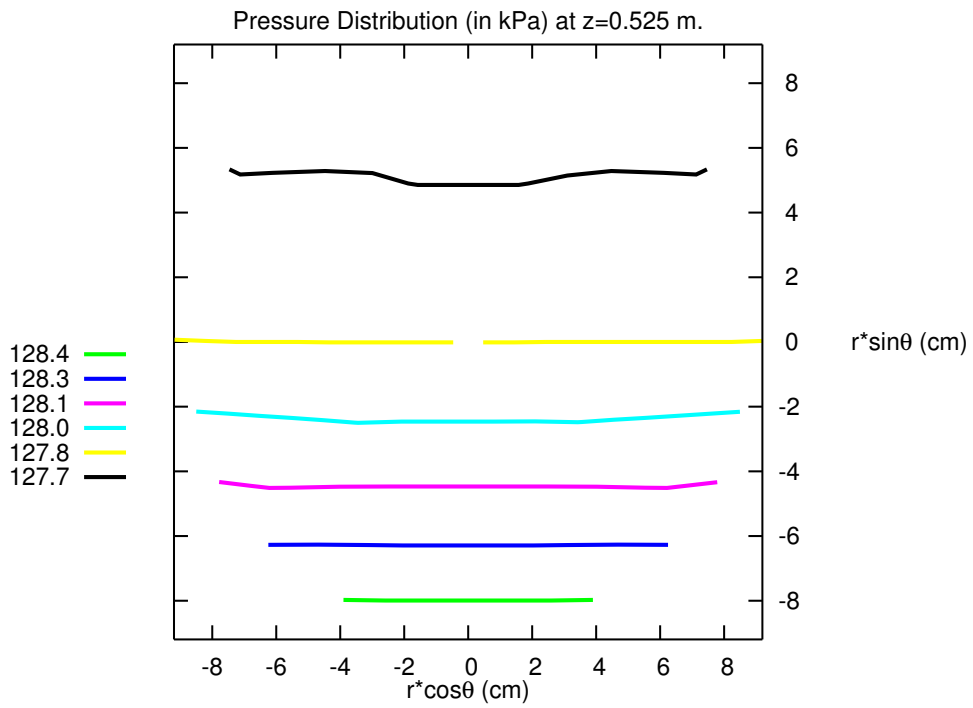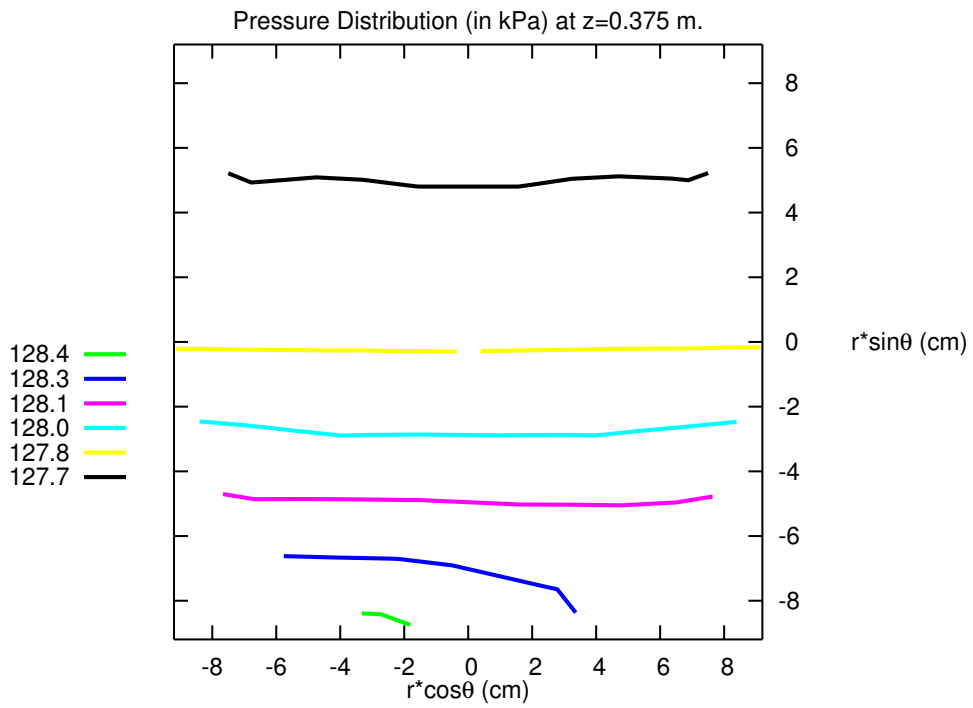
Figure 7.51: Pressure Distribution-II, Test Matrix-K2
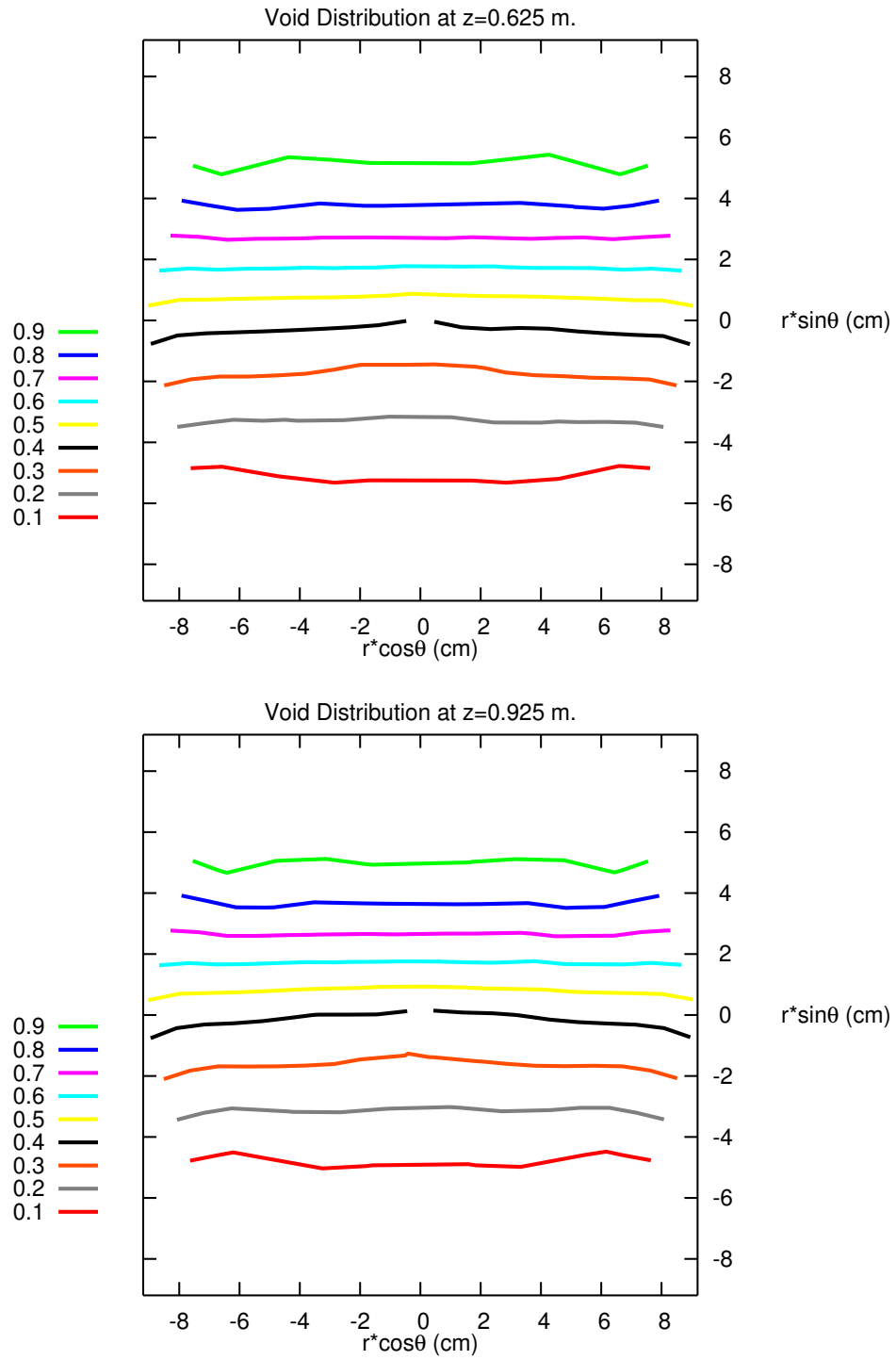
Figure 7.52: Void Distribution-III, Test Matrix-K2
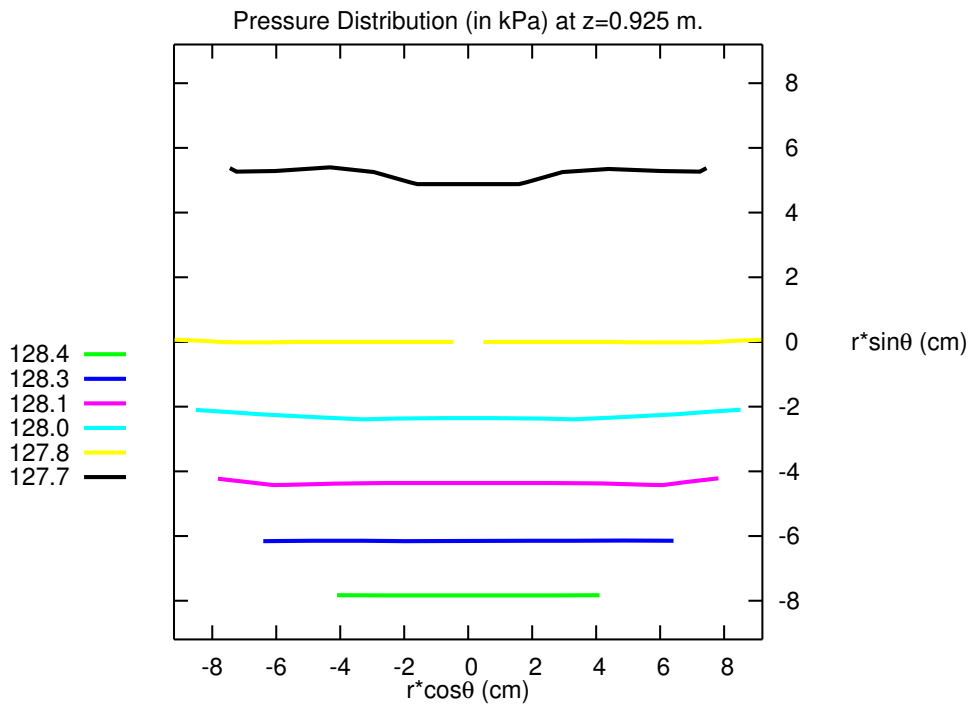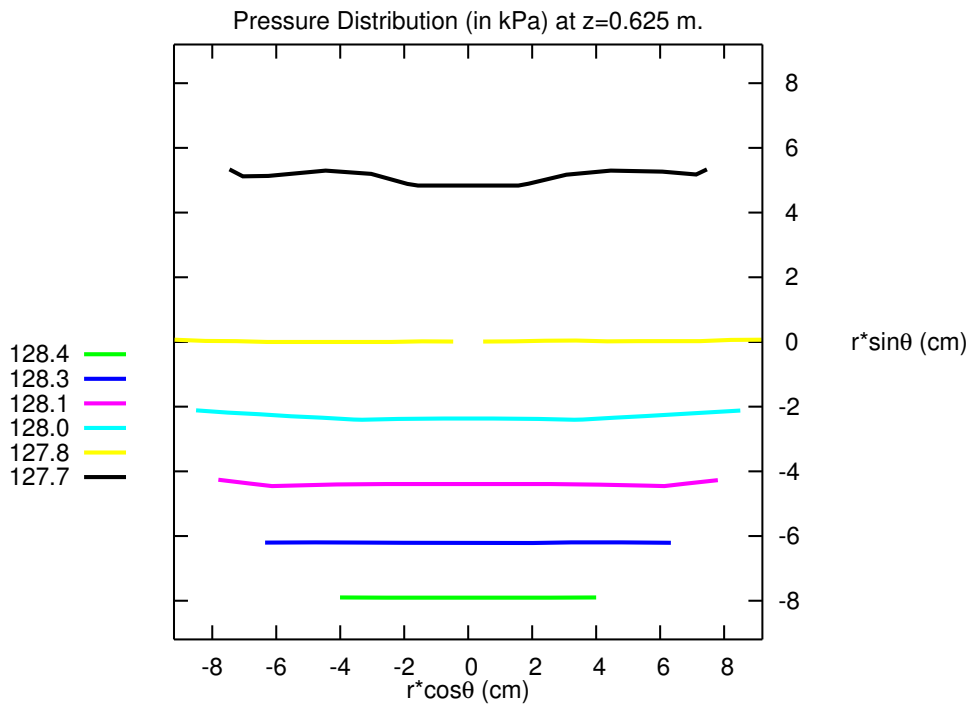
Figure 7.53: Pressure Distribution-III, Test Matrix-K2

164

CHAPTER 8

CONCLUSIONS

The aim of this study is to investigate two-phase (air and water) flow distribution through the outlets from the horizontal cylindrical header component of the Middle East Technical University Two-Phase Flow Test Facility (METU-TPFTF) both numerically and experimentally.

First of all, three-dimensional incompressible finite-difference equations in cylindrical dimensions were derived by using two-fluid model. Then a numerical solution algorithm was established by using the principles of Implicit Multifield Model(IMF) of Harlow and Amsden [41]. After that, a computer code was written to solve those derived governing equations using the boundary conditions.

The solution algorithm was tested by three benchmark problems. First one was a one-dimensional problem, "Water Faucet Problem", solved in z-direction and the numerical results obtained in simulating this problem demonstrated the capability of the code to accurately predict the void wave propogation. Very similar transient simulation results were obtained as compared with the studies found in the literature. Decreasing time step size and mesh refinement gave more satisfactory results. No numerical instability problems have been encountered.

The second one was "Pure Radial Symmetric Flow Problem" defined in r-direction only. A one-dimensional version of the code was generated and the simulation of this problem gave very close results to analytical ones. Radial momentum equations were tested in the numerical algorithm.

The third one was "R-ϕ Symmetric Flow Problem" in r and ϕ directions. A two-dimensional version of the code was generated to simulate this problem. Both radial and azimuthal momentum equations were tested and the results were found to be in agreement with that of exact solution. Periodic boundary condition implementation in angular direction resulted in overcoming the code running problems very well.

After making calibration tests for all of the instrumentation of the Test Facility, a number of tests covering single and two phase flow distibution through different combinations of outlet pairs from the header were performed. A multi-layered neural network system was developed to process the calibration and experimental data in this study. The results obtained from the neural network system trained by calibration data were in good agreement with the test results. This methodology has provided a useful tool to calculate the two-phase flow rate in each of the feeders under consideration without measuring it directly or without developing complicated emprical relations.

The specific header's three-dimensional geometry was then imposed to the code in order to give a possibility to model the single/dual/multiple discharges from the header region. A sensitivity analysis was performed for the drag function and, Lee and Shah's [81] formulation was found to be better suited for the present study and it was selected for use in all simulations.

After that, the code results were compared with the results of six experimental test matrices. Some simulation results, especially performed with the nozzles 3 and 4, showed very similar behaviours with the experimental results. Some of them are, especially performed with the symmetrically located nozzles 4 and 5, somehow deviated from the measurements. Some physical

phonemon like the occurance of stratified flow and formation of chaotic distribution of void at/near the inlet section in the experimental tests are also predicted numerically in this study.

This study provided a three-dimensional computational tool for two-phase analysis of the header in the METU-TPFTF. This code, however, can also be used to simulate other problems in cylindrical geometry in various dimensions. IMF model of Harlow and Amsden [41] was tested successively with three benchmark studies for incompressible flow.

In this study also some data were obtained for the single and two phase flow experiments which were performed in METU-TPFTF. The Code predicted the void fraction and pressure distibution in any section of the header.

With the help of brilliant ideas of Çamlıkaya [15], some improvements were made especially in the data acquisition system of the test facility which provided more reliable measurements. This study also provided an experimental data processing system which was developed by using neural network approach.

8.1 Suggestions for Future Work

This study would be extended for the following studies;

- Experimental tests might be done to cover a large range of tests having different combinations of dual/multiple discharges.

- The code might be simplified and optimized to make the computations faster.

- Modelling of all five feeder lines might be coupled to the Code in order to simulate the whole system in METU-TPFTF which is essential to analyze combined effects of the discharging nozzles.

- Studies might be done to find a more reliable drag function applicable for stratified flow occuring in the header.

- The design of the impedance probes might be updated or a new design might be developed to provide more reliable void fraction measurements.

- Neural Network Toolbox and Data Acquisition Toolbox of MATLAB [17] can be combined with the Data Acquisition System for gathering data from the instruments faster in future experimental tests.

- Code results might be compared with the CATHENA [40] or other CFD codes e.g. FLUENT, CFX.

REFERENCES

[1] Amsden A. A., "KIVA-3: A KIVA Program with Block-Structured Mesh for Complex Geometries", *LA-12503-MS UC-361*, March-1993.

[2] Amsden A.A., Daly B., Dienes J., Travis J., "Detailed Studies of Reactor Components", *Los Alamos Science, 2, 2, 54*, 1981.

[3] Amsden A.A., Harlow F.H., "KACHINA: An Eulerian Computer Program for Multifield Fluid Flows", *Tecnical Report, LA-5680, LASL*, December-1974.

[4] Amsden A.A., Harlow F.H., "K-TIF: A Two-Fluid Computer Program for Downcomer Flow Dynamics", *Technical Report, LA-6994, LASL*, January-1978.

[5] Amsden A.A., Harlow F.H., "The SMAC Method, A Numerical Technique for Calculating Incompressible Fluid Flows", *Technical Report, LA-4370, LASL*, May-1970.

[6] Andrianov N., "Analytical and Numerical Investigation of Two-Phase Flows", *Ph.D thesis, Otto-von-Guericke Universitat, Magdeburg*, June-2003.

[7] van Baten J.M., Krishna R., "Comparison of Hydrodynamics and Mass Transfer in Airlift and Bubble Column Reactors Using CFD", *Chemical Engineering & Technology, 26, pp.1074-1079*, 2003.

[8] Bestion D., "The Phase Appearance and Disappearance in the CATHARE Code", *Trends in Numerical and Physical Modeling for Industrial Multiphase Flows, Cargese, (Corse), France*, 27-29 September 2000.

[9] Bird R.B., Stewart W.E., Lightfoot E.N., "Transport Phenomena", *John Wiley & Sons*, 1960.

[10] Broadus C.R., Doyle R.J., James S.W., Lime J.F., Mings W.J., Ramsthaler J.A., Sahota M.S., "BEACON/MOD3: A Computer Program for Thermal-Hydraulic Analysis of Nuclear Reactor Containments-User's Manual", *NUREG/CR-1148, EGG-2008*, April-1980.

[11] Cerne G., Petelin S., Tiselj I., "Coupling of Interface Tracking and the Two-Fluid Models for the Simulation of Incompressible Two-Phase Flow", *Journal of Computational Physics, 171, pp.776-804*, 2001.

[12] Chandraker D.K., Maheshwari N.K., Saha D., Raj V.V., "Experimental and Analytical Investigations On Core Flow Distribution and Pressure Dsitribution in the Outlet Header of a PHWR", *Experimental Thermal and Fluid Science, 27, pp.11-24*, 2002.

[13] Coquel F., El Amine K., Godlewski E., Perthame B., Rascle P., "A Numerical Method Using Upwind Schemes for the Resolution of Two-Phase Flows", *Journal of Computational Physics, 136, pp.272-288*, 1997.

[14] Cortes J., "On the Construction of Upwind Schemes for Non-Equilibrium Transient Two-Phase Flows", *Computers & Fluids, pp.159-182*, 2002.

[15] Çamlıkaya T., Personal Communications.

[16] Davidson M., "Numerical Calculations of Two-Phase Flow In a Liquid Bath with Bottom Gas Injection: The Central Plume", *Appl. Math. Modelling, 14, pp.67-76*, 1990.

[17] Demuth H., Beale M., "Neural Network Toolbox For Use With MATLAB, User's Guide, Version-4", *The Mathworks, http://www.mathworks.com/access/helpdesk/help/toolbox/nnet*, March 2005.

[18] Devia F., Fossa M., "Design and Optimisation of Impedance Probes for Void Fraction Measurements", *Flow Measurement and Instrumentation, 14, pp139-149*, 2003.

[19] Dinh T.N., Nourgaliev R.R. and Theofanous T.G., "Understanding the Illposed Two-fluid Model", *The 10th International Topical Meeting on Nuclear Reactor Thermal Hydraulics, NURETH10, Seoul, Korea*, October 2003.

[20] Dong F., Jiang Z.X., Qiao X.T., Xu L.A., "Application of Electrical Resistance Tomography to Two-Phase Pipe Flow Parameters Measurement", *Flow Measurement and Instrumentation, 14, pp.183-192*, 2003.

[21] Durran D.R., "Numerical Methods for Wave Equations in Geophysical Fluid Dynamics", *Springer-Verlag, New York, pp.20-26*, 1999.

[22] Elkow K.J., Rezkallah K.S., "Void Fraction Measurements In Gas-Liquid Flows Under 1-g and μ-g Conditions Using Capacitance Sensors", *International Journal of Multiphase Flow, 23(5), pp.815-829*, 1997.

[23] Enwald H., Peirano E., "Gemini: A Cartesian Multiblock Finite Difference Code for Simulation of Gas Particle Flows", *Department of Thermo and Fluid Dynamics, Chalmer's University of Technology, Gothenburg, 97/4*, 1997.

[24] Enwald H., Peirano E., Almstedt A.E., Leckner B., "Simulation of the Fluid Dynamics of a Bubbling Fluidized Bed. Experimental Validation of the Two-fluid Model and Evaluation of a Parallel Multiblock Solver", *Chemical Engineering Science 54, pp.311-328*, 1999.

[25] Evje S., Flatten T., "Hybrid-Flux Splitting Schemes For a Common Two-Fluid Model", *Journal of Computational Physics, 192, pp.175-210*, 2003.

[26] Fieno T.E., Mi Y., Ishii M., Tsoukala L.H., "Direct 3-D Visualization of Multi-Component Vertical Flow Using Electrical Impedance Signals and Neural Networks", *http://helios.ecn.purdue.edu/~ aisl/projects/scivis/draft/draft.html*, March 2006.

[27] Flatten T., Evje S., "Comparison of Various AUSM Type Schemes for the Two Fluid Model", *http://basilo.kaist.ac.kr/preprint/ Conse/070.pdf*, March 2006.

[28] Fossa M., "Design and Performance of a Conductance Probe for Measuring The Liquid Fration in Two-Phase Gas-Liquid Flows", *Flow Measurement and Instrumentation, 9, pp.103-109*, 1998.

[29] Fossa M., Guglielmini G., Marchitto A., "Intermittent Flow Parameters from Void Fraction Analysis", *Flow Measurement and Instrumentation, 14, pp.161-168*, 2003.

[30] Friberg, "Three-Dimensional Modelling and simulation of Gas/Liquid Flow Processes in Bioreactors", *Ph.D Thesis, Telemark University College, Telemark*, 1998.

[31] Gallouet T., Herard J.M., Seguin N., "Numerical Modeling of Two-phase Flows Using the Two-Fluid Two-Pressure Approach", *Mathematical Models and Methods in Applied Sciences, 14(5), pp.663-700*, 2004.

[32] Gamwo I.K., Soong Y., Lyczkowski R.W., "Numerical Simulation and Experimental Validation of Solids Flows in a Bubbling Fluidized Bed", *Powder Technology, 103(2), pp.117-129*, 1999.

[33] Gavage S.B., Coulombel J.F., Aubert S., "Boundary Conditions for Euler Equations", *AIAA Journal, 41, pp.56-63*, 2003.

[34] Ghidaglia J.M., "An Overview of the VFFC-Methods and Tools for the Simulation of Two-Phase Flows", *Report, EDF, HT-33/99/005/A*, 1999.

[35] Ghidaglia J.M., Kumbaro A., Le Coq G., "On the Numerical Solution to Two-Fluid Models via a Cell Centered Finite Volume Method", *Europ. Journal Mech. B/Fluids, 20, pp.841-867*, June-2001.

[36] Gomez L.C., Milioli F.E., Eduardo F., "Gas-solid Two-Phase Flow in the Riser of Circulating Fluidized Beds: Mathematical Modeling and Numerical Simulation", *J.Brazilian Soc. Mech.Sci., Vol 23-2, pp.179-200*, 2001.

[37] Gudmundsson R.L., "On Stability of Solutions to the Two-fluid Models for Dispersed Two-phase Flow", *Licentiate's Thesis, Royal Institute of Technology Department of Numerical Analysis and Computing Science,Stockholm*, November-2002.

[38] Gustavsson M., Almstedt A.E., "Numerical Simulation of Fluid Dynamics in Fluidized Beds with Horizontal Heat Exchanger Tubes", *Chemical Engineering Science, 55, pp.857-866*, 2000.

[39] Gustavsson K., Oppelstrup J., "Consolidation of Concentrated Suspensions - Numerical Simulations Using a Two-Phase Fluid Model", *Computing and Visualization in Science, 3, pp.39-45*, 2000.

[40] Hanna B.N., "CATHENA Abstract MOD-3.5c/Rev 0", *AECL, COG-99-6*, 1999.

[41] Harlow F.H., Amsden A.A., "Numerical Calculation of Multiphase Fluid Flow", *Journal of Computational Physics, 17, pp.19-52*, 1975.

[42] Harlow F.H., Amsden A.A., "Flow of Interpenetrating Material Phases", *Journal of Computational Physics, 18, pp.440-464*, 1975.

[43] Harlow F.H., Amsden A.A., "Numerical Fluid Dynamics Calculation Method for All Flow Speeds", *Journal of Computational Physics, 8(2), 197*, 1971.

[44] Harlow F.H., Welch, "Numerical Calculation of Time-Dependent Viscous Incompressible Flow of Fluid With Free Surface", *Physics Fluids, 8, pp.2181-2189*, 1965.

[45] Hassan I.G., Soliman H.M., Sims G.E., Kowalski J.E., "Single and Multiple Discharge from a Stratified Two-Phase Region Through Small Branches", *Nuclear Engineering and Design, 176, pp.233-245*, 1997.

172

[46] Hibiki T., Goda H., Kim S., Ishii M., Uhle J., "Structure of Vertical Downward Flow", *International Journal of Heat and Mass Transfer, 47, pp.1842-1862*, 2004.

[47] Hibiki T., Goda H., Kim S., Ishii M., Uhle J., "Axial Development of Interfacial Structure of Vertical Downward Bubbly Flow", *International Journal of Heat and Mass Transfer, 48, pp.749-764*, 2005.

[48] Hirt C.W., "Flow-3D Users Manual", *Flow Sciences Inc, Santa Fe, NM*, 1988.

[49] Hirt C.W., Nichols, "Volume of Fluid (VOF) Method for the Dynamics of Free Boundaries", *Journal of Computational Physics, 39, 201*, 1981.

[50] Hong R., Li H., Li H., Wang Y., "Studies on Inclined Jet Penetration Lenght in a Gas-Solid Fluidized Bed", *Powder Technology, 92, pp.205-212*, 1997.

[51] Horiki S., Nakamura T., Osakabe M., "Thin Flow Header To Distribute Feed Water for Compact Heat Exchanger", *Experimental Thermal and Fluid Science, 28, 201-207*, 2004.

[52] Hosanoğlu, T., "Void Fraction Measurement in a Two-Phase Flow System With Impedance Probe Technique", *M.Sc. Thesis, METU*, January-2002.

[53] Huilin L., Wentie L., Guangbo Z., Yurong H., "Eulerian Simulations of Bubble Behaviour in a Two-Dimensional Gas-Solid Bubbling Fluidized Bed", *International Journal of Energy Research, 26, pp.1285-1293*, 2002.

[54] Idaho National Engineering and Environmental Laboratory, "RELAP5-3D Code Manual Volume I: Code Structure, System Models and Solution Methods", *INEEL-EXT-98-00834 Revision 1.3a*, February-2001.

[55] Idaho National Engineering and Environmental Laboratory, "RELAP5-3D Code Manual Volume I: Code Structure, System Models and Solution Methods", *INEEL-EXT-98-00834 Revision 2.2*, October-2003.

[56] Idaho National Laboratory, "RELAP5-3D", *Technical Report, http://www.inl.gov/relap5doc/relap5doept1.htm*, March 06, 2006.

[57] Ingham P.J., Luxat J.C., Melnyk A.J., Sanderson T.V., "Natural Circulation in an Integral CANDU Test Facility", *IAEA T/C Mtg. Experimental Tests and Qualification of Analytical Methods to Address Thermalhydraulic Phenomena in Advanced Water Reactors, Switzerland*, September 14-17, 1998.

[58] Ishii M., "Thermo-Fluid Dynamic Theory of Two-Phase Flow", *Eyrolles, Paris*, 1975.

[59] Ishii M., Kim S., Uhle J., "Interfacial Area Transport Equation: Model Development and Benchmark Experiments", *International Journal of Heat and Mass Transfer, 45, pp.3111-3123*, 2002.

[60] Ishii M., Mishima K., "Two-fluid Model and Hydrodynamic Constitutive Relations", *Nuclear Engineering and Design, 82, pp.107-126*, 1984.

[61] Ishii M., Zuber N., "Drag Coefficient and Relative Velocity in Bubbly, Droplet or Particulate Flows", *AIChE Journal, Vol.25, No.5, pp.843-855*, September 1979.

[62] Ishimoto J., Kamijo K., "Numerical Study of Cavitating Flow Characteristics of Liquid Helium in a Pipe", *International Journal of Heat and Mass Transfer, 47, pp.149-163*, 2004.

[63] Jaworek A., Krupa A., "Gas/Liquid Ratio Measurements by RF Resonance Capacitance Sensor", *Sensors and Actuators A, 113, pp.133-139*, 2004.

[64] Jaworek A., Krupa A., Trela M., "Capacitance Sensor for Void Fraction Measurement in Water/Steam Flows", *Flow Measurement and Instrumentation, 15, pp.317-324*, 2004.

[65] Karni S., Kirr E., Kurganov A., Petrova G., "Compressible Two-Phase Flows by Central and Upwind Schemes", *ESAIM:Mathematical Modelling And Numerical Analysis, 38, pp.477-493*, 2004.

[66] Kawaguchi T., Sakamoto M., Tanaka T., Tsuji Y., "Quasi-Three-Dimensional Numerical Simulation of Spouted Beds in Cylinder", *Powder Technology 109, pp.3-12*, 2000.

[67] Kaya, M.B., "Flow Rate Measurements in a Two-Phase Flow System" *M.Sc. Thesis, METU*, September-2001.

[68] Kothe D.B., "Perspective on Eulerian Finite Volume Methods for Incompressible Interfacial Flow", *In H.Kuhmann and H.Rath editors, Free Surface Flows, Springer-Verlag, NewYork, pp.267-331*, 1994.

[69] Kumbaro A., Seignole V., Ghidaglia J.M., "Flux Scehemes for the Two-Fluid Models of the TRIO-U Code", *Computing Methods for Two-Fluid Models of the TRIO-U Code, Aussois, France*, 2000.

[70] Kunz R.F., Cope W.K., Venkateswaran S., "Development of an Implicit Method for Multi-Fluid Flow Simulations", *J. Computational Physics, 152, pp.78-101*, 1999.

174

[71] Kurosaki Y., Spalding D.B., "One-Dimensional Unsteady Two-Phase Flows with Interphase Slip: A Numerical Study", *Second Multi-phase Flow and Heat Transfer Symposium-Workshop, Miami Beach*, April 1979.

[72] Lahey R.T., Drew D.A., "The Analysis of Phase Distribution in Fully Developed Two-Phase Flows", *Proceedings of the Second Multi-phase Flow and Heat Transfer Symposium-Workshop, Miami*, April 1979.

[73] Lahey Jr.R.T., Drew D.A., "The Three-Dimensonal Time and Volume Averaged Conservation Equations of Two-Phase Flow", *Adv. Nuclear Science Tech., 20, pp.1-69*, 1988.

[74] Lakehal D., Meier M., Fulgosi M., "Interface Tracking Towards the Direct Simulation of Heat and Mass Transfer in Multiphase Flows", *International Journal of Heat and Fluid Flow, 23, pp.242-257*, 2002.

[75] Lamarre E., Melville W.K., "Instrumentation for the Measurement of Void Fraction in Breaking Waves: Laboratory and Field Results", *IEEE Journal of Oceanic Engineering, 17(2), pp.204-215*, April 1992.

[76] Latsa M., Assimacopoulos D., Stamou A., Markatos N., "Two-phase Modeling of Batch Sedimentation", *Applied Mathematical Modelling, 23, pp.881-897*, 1999.

[77] Laurien E., Becker S., Saptoadi D., Giese T., "Multidimensional Modeling of Bubbly Flows for Nuclear Reactor Passive Decay Heat Removal", *Eurotherm Seminar No.63 : Single and Two-phase Natural Circulation, Genoa, Italy*, 6-8 September 1999.

[78] Lee W.H., "A Pressure Iteration Scheme for Two-phase Flow Modeling", *Multiphase Transport Fundamentals, Reactor Safety Applications, Vol.1, Hemisphere Publishing, Washington D.C., pp.407-431*, 1980.

[79] Lee J.K., Lee S.Y., "Distribution of Two-Phase Annular Flow at Header-Channel Junctions", *Experimental and Thermal Fluid Science, 28, pp.217-222*, 2004.

[80] Lee W.H., Lyczkowski R.W., "Basic Character of Five Two-Phase Flow Model Equation Sets", *International Journal for Numerical Methods in Fluids, 33, pp.1075-1098*, 2000.

[81] Lee, W.H., Shah, V.L., "Numerical Simulation for Two-Phase Jet Problem", *Numerical Methods in Laminar and Turbulent Flows, Proceedings of the 2nd International Conference, Venice, pp.841-852*, 1981.

[82] Lezeau P., Thompson C.P., "Numerical Simulation of One Dimensional Transient Multiphase Flow", *http://www.cranfield.ac.uk/sme/amac/tmf/implicit.pdf*, March 2006.

[83] Liles D., "Two-phase Flow", *Los Alamos Science, pp.26-35.*

[84] Lyczkowski R.W., Bouillard J.X., "State-of-the-Art Review of Erosion Modeling in Fluid/Solids Systems", *Progress in Energy and Combustion Science, 28, pp.543-602*, 2002.

[85] Maier R.M., Soliman H.M., Sims G.E., "Onsets of Entrainment During Dual Discharge from a Stratified Two-Phase Region Through Horizontal Branches with Centreline Falling in an Inclined Plane: Part 2 - Experiments on Gas and Liquid Entrainment", *International Journal of Multiphase Flow, 27, pp.1029-1049*, 2001.

[86] Maier R.M., Soliman H.M., Sims G.E., Armstrong K.F., "Onsets of Entrainment During Dual Discharge from a Stratified Two-Phase Region Through Horizontal Branches with Centreline Falling in an Inclined Plane: Part 1 - Analysis of Liquid Entrainment", *International Journal of Multiphase Flow, 27, pp.1011-1028*, 2001.

[87] Malayeri M.R., Steinhagenier H.M., Smith J.M., "Neural Network Analysis of Void Fraction in Air/Water Two-Phase Flows At Elevated Temperatures", *Chemical Engineering and Processing, 42, pp.587-597*, 2003.

[88] Meier M., "Numerical and Experimental Study of Large Steam-Air Bubbles Injected In a Water Pool", *Doctor of Technical Sciences thesis, Swiss Federal Institute of Technology, Zurich*, 1999.

[89] Mi Y., Ishii M., Tsoukalas L.H., "Vertical Two-Phase Flow Identification Using Advanced Instrumentation and Neural Networks", *Nuclear Engineering and Design, 184, pp.409-420*, 1998.

[90] Minato, A., Nagayoshi, T., Takamori K., Harada I., Mase, M., Otani, K., "Numerical Simulation of Gas-Liquid Two-Phase Flow in Siphon Outlets of Pumping Plants", *http://www.hitachi-hic.com/technical/pdf/pump004.pdf*, February 2006.

[91] Moukalled F., Darwish M., "A Comparative Assessment of the Performance of Mass Conservation Based Algorithms For Incompressible Multi-Phase flows", *Numerical Heat Transfer Part B:Fundamentals, 42(3), pp.259-283*, September 2002.

[92] Munkejord S.T., M.J. Molnvik, J.A. Melheim, Gran I.R., Olsen R., "Development of a 2D Multiphase Simulator and Validation for High-Pressure Pipe Flows", *http://www.pw.org/~stm/dring/pipeflow-p.pdf*, March 2006.

[93] Nae C., Pricop V., Wang B., Rehm W., "Overview of Models for Multifluid/Multiphase Flows Based on CFD Codes D3UNS, CFX-5, IFSAS

with Test Cases for Complex Flows (Part-2)", *EC-EXPRO Project, 15 Month Report, Forschungrzentrum, Julich, Germany*, 15 February 2003.

[94] Nagayoshi T., Minato A., Misawa M., Suzuki A., Kuroda M., Ichikawa N., "Simulation of Multi-dimensional Heterogeneous and Intermittent Two-Phase Flow by Using an Extended Two-Fluid Model", *Journal of Nuclear Science and Technology, 40(10), pp.827-833*, October-2003.

[95] Nichols B.D., Hirt C.W., Hotchkiss R.S., "SOLA-VOF: A Solution Algorithm for Transient Fluid Flow with Multiple Free Boundaries", *Los Alamos Scientific Laboratory Report, LA-8355*, 1988.

[96] Nourgaliev R.R., Dinh T.N., Theofanous T.G., "A Pseudo-Compressibility Method for the Simulation of Multiphase Incompressible Flows", *International Journal of Multiphase Flow, 30(7-8), pp.901-937*, 2004.

[97] Nourgaliev R., Dinh N., Theofanous T., "A Characteristics-Based Approach to the Numerical Solution of the Two-Fluid Model", *Proceedings of FEDSM03 4TH ASME/JSME Joint Fluids Engineering Conference, Honolulu, Hawaii, USA*, 6-11 July 2003.

[98] Oliveira M.S.A., Sousa A.C.M., "Neural Network Analysis of Experimental Data for Air/Water Spray Cooling", *Journal of Materials Processing Technology, 113, pp.439-445*, 2001.

[99] Oliveira P.J, Issa R.I., "Numerical Aspects of an Algorithm for the Eulerian Simulation of Two-Phase Flow", *International Journal for Numerical Methods in Fluids, 43, pp.1177-1198*, 2003.

[100] Osakabe M., Hamada T., Horiki S., "Water Flow Distribution in Horizontal Header Contaminated With Bubbles", *International Journal of Multiphase Flow, 25, pp.827-840*, 1999.

[101] Osher S., Sethian J.A., "Front Propogating with Curvature-Dependent Speed: Algorithms Based on Hamilton-Jacobi Formulations", *Journal of Computational Physics Multiphase Flow, 79(1), pp.1-49*, 1988.

[102] Paillere H., "Benchmarks Physico-Numeriques Calcules avec La Methode AUSM+", *CEA-SYSCO*, 9 November 1999.

[103] Paillere H., Kumbaro A., Viozat C., Clerc S., "Development of an AUSM++ type Scheme for the Homogeneous Equilibrium Two-Phase Flow Model", *Seminaire Schemas de Flux pour la Simulation Numerique des Ecoulements Diphasiques, Reunion du Groupe de Travail CEA-EDF-CMLA, Cargese*, 22-24 September 1999.

[104] Pain C.C., Mansoorzadeh S., de Oliveira C.R.E., Goddard A.J.H., "Numerical Modelling of Gas Solid Fluidized Beds Using the Two-Fluid Approach", *International Journal for Numerical Methods in Fluids, 36, pp.91-124*, 2001.

[105] Parrott, S.D., "Experimental Characterization of Flow and Phase Distribution in an RD-14M Inlet Header Under Steam-Water Flow Conditions", *AECL, WPIR 1503, Draft Report*, March 1999.

[106] Patankar S.V., Spalding D.B., "Calculation Procedure for Heat, Mass and Momentum Transfer in 3-Dimensional Parabolic Flows", *International Journal of Heat and Mass Transfer, 15(10), 1797*, 1972.

[107] Pokharna H., Mori M., Ransom V.H., "Regularization of Two-Phase Flow Models: A Comparison of Numerical and Differential Approaches", *Journal of Computational Physics, 134, pp.282-295*, 1997.

[108] Ramos D., "Quelques Resultats Mathematiques et Simulations Numeriques D'ecoulements Regis par des Modeles Bidluides", *Ph.D Thesis, Ecole Normale Superieure de Cachan*, 15 December 2000.

[109] Ransom, V.H., "Faucet Flow", *Multiphase Science and Technology, Hemisphere Publishing Corp. and Springer, 3, pp.495-497*, 1987.

[110] Rivard W.C., Torrey M.D., "K-FIX: A Computer Program for Transient Two-Dimensional, Two-Fluid Flow", *Technical Report, LA-NUREG-6623, LASL*, April-1977.

[111] Rivard W.C., Torrey M.D., "Numerical Calculation of Flashing from Long Pipes Using a Two-Field Model", *LA-6104-MS*, November-1975.

[112] Rivard W.C., Torrey M.D., "K-FIX: A Computer Program for Transient Two-Dimensional, Two-Fluid Flow, THREED:An Extention of the K-FIX Code for Three-Dimensional Calculations", *Technical Report, LA-NUREG-6623, Suppl. II-R4, LASL*, January-1979.

[113] Saurel R., Abgrall R., "A Simple Method for Compressible Multifluid Flows", *SIAM J. Sci. Comput., 21(8), pp.1115-1145*, 1999.

[114] Scannapieco E., Harlow F.H., "Introduction to Finite Difference Methods for Numerical Fluid Dynamics", *Technical Report, LA-12984, Los Alamos National Laboratory*, 1995.

[115] Shieh A.S., Ransom V.H., Krishnamurthy R., "RELAP5-Mod3 Code Manual Volume 6: Validation of Numerical Techniques in RELAP5/MOD3.0", *NUREG/CR-5535/Rev 1-Vol VI*, October-1994.

[116] Silva M.W., "A Computational Study of Highly Viscous Impinging Jets", *ANRCP-1998*, 18 November 1998.

[117] Snider D.M., "An Incompressible Three-Dimensional Multiphase Particle-In-Cell Model for Dense Particle Flows", *Journal of Computational Physics, 170, pp.523-549*, 2001.

[118] Song C.H., Chung M.K., No H.C., "Measurements of Void Fraction by An Improved Multi-Channel Conductance Void Meter", *Nuclear Engineering and Design, 184, pp.269-285*, 1998.

[119] Song J.H., Ishii M., "The Well-Posedness of Incompressible One-Dimensional Two-Fluid Model", *International Journal of Heat and Mass Transfer, 43, pp.2221-2231*, 2000.

[120] Stadtke H., "Advanced Modelling and Numerical Strategies in Nuclear Thermal-Hydraulics", *International Conference, Nuclear Energy in Central Europe*, 2001.

[121] Stadtke H., de Cachard F., Cascales J.R.G., Deconinck H., Franchello G., Graf U., Kumbaro A., Mimouni S., Paillere H., Ricchiuto M., Romenski E., Romstedt P., Smith B., Toro E.F., Worth B., "The ASTAR Project - Status and Perspective", *The 10th. International Topical Meeting on Nuclear Reactor Thermal-Hydraulics (NURETH-10), Seoul-Korea*, 5-9 October 2003.

[122] Syamlal M., "MFIX Documentation Numerical Technique", *U.S. Department of Energy, DOE/MC31346-5824*, January-1998.

[123] Syamlal M., Rogers W., O'Brien T.J., "MFIX Documentation Theory Guide", *U.S. Department of Energy, DOE/METC-94/1004*, December-1993.

[124] Syamlal M., "MFIX Documentation User's Manual", *U.S. Department of Energy, DOE-METC-95/1013*, November-1994.

[125] Teclemariam Z., Soliman H.M., Sims G.E., Kowalski J.E., "Experimental Investigation of Two-Phase Flow Distribution in the Outlets of a Horizontal Multi-Branch Header", *Nuclear Engineering and Design, 222, pp.29-39*, 2003.

[126] Toumi I., Kumbaro A., Seignole V., Pailliere H., "Towards Multi-Dimensional Simulation of Two-Phase Flow Using an Approximate Riemann Solver", *http://www.cmla.ens-cachen.fr/ utilisateurs/performans/aussois00 article/paper14.ps*, March 2006.

[127] Uchiyama T., "Petrov-Galerkin Finite Element MEthod for Gas-Liquid Two Phase Flow Based on an Incompressible Two-Fluid Model", *Nuclear Engineering and Design, 193, pp.145-157*, 1999.

[128] Uchiyama T., "ALE Finite Element Method for Gas-Liquid Two-Phase Flow Including Moving Boundary Based on an Incompressible Two-Fluid Model", *Nuclear Engineering and Design, 205, pp.69-82*, 2001.

[129] Unverdi S.O., Tryggvason G., "A Front Tracking Method for Viscous, Incompressible, Multi-Fluid Flows", *Journal of Computational Physics, 100, 25*, 1992.

[130] Welter K.B., Wu Q., You Y., Abel K., McCreary D., Bajorek S.M., Reyes J.N., "Experimental Investigation and Theoretical Modeling of Liquid Entrainment in a Horizontal Tee with a Vertical-up Branch", *International Journal of Multiphase Flow, 30, pp.1451-1484*, 2004.

[131] Youngs D.L., "Sedimentation", *Multiphase Science and Technology, Hemisphere Publishing Corp. and Springer, 3, pp.474-476*, 1987.

APPENDIX A

A.1 Convection Terms In The Liquid Phase Continuity Equation

$$
< \theta_l U_l r >_{i,j,k} = U_{l i+\frac{1}{2},j,k} r_{i+\frac{1}{2}} \begin{cases} \theta_{l i,j,k} & \text{if} \quad U_{l i+\frac{1}{2},j,k} \geq 0 \\ \theta_{l i+1,j,k} & \text{if} \quad U_{l i+\frac{1}{2},j,k} < 0 \end{cases}
$$

$$
- U_{l i-\frac{1}{2},j,k} r_{i-\frac{1}{2}} \begin{cases} \theta_{l i-1,j,k} & \text{if} \quad U_{l i-\frac{1}{2},j,k} \geq 0 \\ \theta_{l i,j,k} & \text{if} \quad U_{l i-\frac{1}{2},j,k} < 0 \end{cases} \tag{A.1}
$$

$$
< \theta_l V_l >_{i,j,k} = V_{l i,j+\frac{1}{2},k} \begin{cases} \theta_{l i,j,k} & \text{if} \quad V_{l i,j+\frac{1}{2},k} \geq 0 \\ \theta_{l i,j+1,k} & \text{if} \quad V_{l i,j+\frac{1}{2},k} < 0 \end{cases}
$$

$$
- V_{l i,j-\frac{1}{2},k} \begin{cases} \theta_{l i,j-1,k} & \text{if} \quad V_{l i,j-\frac{1}{2},k} \geq 0 \\ \theta_{l i,j,k} & \text{if} \quad V_{l i,j-\frac{1}{2},k} < 0 \end{cases} \tag{A.2}
$$

$$
< \theta_l W_l >_{i,j,k} = W_{l i,j,k+\frac{1}{2}} \begin{cases} \theta_{l i,j,k} & \text{if} \quad W_{l i,j,k+\frac{1}{2}} \geq 0 \\ \theta_{l i,j,k+1} & \text{if} \quad W_{l i,j,k+\frac{1}{2}} < 0 \end{cases}
$$

$$
- W_{l i,j,k-\frac{1}{2}} \begin{cases} \theta_{l i,j,k-1} & \text{if} \quad W_{l i,j,k-\frac{1}{2}} \geq 0 \\ \theta_{l i,j,k} & \text{if} \quad W_{l i,j,k-\frac{1}{2}} < 0 \end{cases} \tag{A.3}
$$

A.2 Convection Terms In The Momentum Equations

A.2.1 Z-Direction Equations For Gas Phase

$$
< \theta_g V_g U_g r >_{i,j+\frac{1}{2},k} \;=\; U_{g_{i+\frac{1}{2},j+\frac{1}{2},k}} r_{i+\frac{1}{2}}
\begin{cases}
(\theta_g V_g)_{i,j+\frac{1}{2},k} & \text{if } U_{g_{i+\frac{1}{2},j+\frac{1}{2},k}} \geq 0 \\[2mm]
(\theta_g V_g)_{i+1,j+\frac{1}{2},k} & \text{if } U_{g_{i+\frac{1}{2},j+\frac{1}{2},k}} < 0
\end{cases}
$$

$$
- U_{g_{i-\frac{1}{2},j+\frac{1}{2},k}} r_{i-\frac{1}{2}}
\begin{cases}
(\theta_g V_g)_{i-1,j+\frac{1}{2},k} & \text{if } U_{g_{i-\frac{1}{2},j+\frac{1}{2},k}} \geq 0 \\[2mm]
(\theta_g V_g)_{i,j+\frac{1}{2},k} & \text{if } U_{g_{i-\frac{1}{2},j+\frac{1}{2},k}} < 0
\end{cases}
\tag{A.4}
$$

$$
< \theta_g V_g V_g >_{i,j+\frac{1}{2},k} \;=\; V_{g_{i,j+1,k}}
\begin{cases}
(\theta_g V_g)_{i,j+\frac{1}{2},k} & \text{if } V_{g_{i,j+1,k}} \geq 0 \\[2mm]
(\theta_g V_g)_{i,j+\frac{3}{2},k} & \text{if } V_{g_{i,j+1,k}} < 0
\end{cases}
$$

$$
- V_{g_{i,j,k}}
\begin{cases}
(\theta_g V_g)_{i,j-\frac{1}{2},k} & \text{if } V_{g_{i,j,k}} \geq 0 \\[2mm]
(\theta_g V_g)_{i,j+\frac{1}{2},k} & \text{if } V_{g_{i,j,k}} < 0
\end{cases}
\tag{A.5}
$$

$$
< \theta_g V_g W_g >_{i,j+\frac{1}{2},k} \;=\; W_{g_{i,j+\frac{1}{2},k+\frac{1}{2}}}
\begin{cases}
(\theta_g V_g)_{i,j+\frac{1}{2},k} & \text{if } W_{g_{i,j+\frac{1}{2},k+\frac{1}{2}}} \geq 0 \\[2mm]
(\theta_g V_g)_{i,j+\frac{1}{2},k+1} & \text{if } W_{g_{i,j+\frac{1}{2},k+\frac{1}{2}}} < 0
\end{cases}
$$

$$
- W_{g_{i,j+\frac{1}{2},k-\frac{1}{2}}}
\begin{cases}
(\theta_g V_g)_{i,j+\frac{1}{2},k-1} & \text{if } W_{g_{i,j+\frac{1}{2},k-\frac{1}{2}}} \geq 0 \\[2mm]
(\theta_g V_g)_{i,j+\frac{1}{2},k} & \text{if } W_{g_{i,j+\frac{1}{2},k-\frac{1}{2}}} < 0
\end{cases}
\tag{A.6}
$$

A.2.2 ϕ Direction Equations For Gas Phase

$$
< \theta_g W_g U_g r >_{i,j,k+\frac{1}{2}} \;=\; U_{g_{i+\frac{1}{2},j,k+\frac{1}{2}}} r_{i+\frac{1}{2}}
\begin{cases}
(\theta_g W_g)_{i,j,k+\frac{1}{2}} & \text{if } U_{g_{i+\frac{1}{2},j,k+\frac{1}{2}}} \geq 0 \\[2mm]
(\theta_g W_g)_{i+1,j,k+\frac{1}{2}} & \text{if } U_{g_{i+\frac{1}{2},j,k+\frac{1}{2}}} < 0
\end{cases}
$$

$$
- U_{g_{i-\frac{1}{2},j,k+\frac{1}{2}}} r_{i-\frac{1}{2}}
\begin{cases}
(\theta_g W_g)_{i-1,j,k+\frac{1}{2}} & \text{if } U_{g_{i-\frac{1}{2},j,k-\frac{1}{2}}} \geq 0 \\[2mm]
(\theta_g W_g)_{i,j,k+\frac{1}{2}} & \text{if } U_{g_{i-\frac{1}{2},j,k+\frac{1}{2}}} < 0
\end{cases}
\tag{A.7}
$$

$$
< \theta_g W_g V_g >_{i,j,k+\frac{1}{2}} \;=\; V_{g_{i,j+\frac{1}{2},k+1/2}}
\begin{cases}
(\theta_g W_g)_{i,j,k+\frac{1}{2}} & \text{if } V_{g_{i,j+\frac{1}{2},k+\frac{1}{2}}} \geq 0 \\[2mm]
(\theta_g W_g)_{i,j+1,k+\frac{1}{2}} & \text{if } V_{g_{i,j+\frac{1}{2},k+\frac{1}{2}}} < 0
\end{cases}
$$

$$
-V_{g_{i,j-\frac{1}{2},k+\frac{1}{2}}} \begin{cases} (\theta_g W_g)_{i,j-1,k+\frac{1}{2}} & \text{if} \quad V_{g_{i,j-\frac{1}{2},k+\frac{1}{2}}} \geq 0 \\ (\theta_g W_g)_{i,j,k+\frac{1}{2}} & \text{if} \quad V_{g_{i,j-\frac{1}{2},k+\frac{1}{2}}} < 0 \end{cases} \tag{A.8}
$$

$$
< \theta_g W_g W_g >_{i,j,k+\frac{1}{2}} = W_{g_{i,j,k+1}} \begin{cases} (\theta_g W_g)_{i,j,k+\frac{1}{2}} & \text{if} \quad W_{g_{i,j,k+1}} \geq 0 \\ (\theta_g W_g)_{i,j,k+\frac{3}{2}} & \text{if} \quad W_{g_{i,j,k+1}} < 0 \end{cases}
$$

$$
-W_{g_{i,j,k}} \begin{cases} (\theta_g W_g)_{i,j,k-\frac{1}{2}} & \text{if} \quad W_{g_{i,j,k}} \geq 0 \\ (\theta_g W_g)_{i,j,k+\frac{1}{2}} & \text{if} \quad W_{g_{i,j,k}} < 0 \end{cases} \tag{A.9}
$$

A.2.3   R-Direction Equations For Liquid Phase

$$
< \theta_l U_l U_l r >_{i+\frac{1}{2},j,k} = U_{l_{i+1,j,k}} r_{i+1} \begin{cases} (\theta_l U_l)_{i+\frac{1}{2},j,k} & \text{if} \quad U_{l_{i+1,j,k}} \geq 0 \\ (\theta_l U_l)_{i+\frac{3}{2},j,k} & \text{if} \quad U_{l_{i+1,j,k}} < 0 \end{cases}
$$

$$
-U_{l_{i,j,k}} r_i \begin{cases} (\theta_l U_l)_{i-\frac{1}{2},j,k} & \text{if} \quad U_{l_{i,j,k}} \geq 0 \\ (\theta_l U_l)_{i+\frac{1}{2},j,k} & \text{if} \quad U_{l_{i,j,k}} < 0 \end{cases} \tag{A.10}
$$

$$
< \theta_l U_l V_l >_{i+\frac{1}{2},j,k} = V_{l_{i+\frac{1}{2},j+\frac{1}{2},k}} \begin{cases} (\theta_l U_l)_{i+\frac{1}{2},j,k} & \text{if} \quad V_{l_{i+\frac{1}{2},j+\frac{1}{2},k}} \geq 0 \\ (\theta_l U_l)_{i+\frac{1}{2},j+1,k} & \text{if} \quad V_{l_{i+\frac{1}{2},j+\frac{1}{2},k}} < 0 \end{cases}
$$

$$
-V_{l_{i+\frac{1}{2},j-\frac{1}{2},k}} \begin{cases} (\theta_l U_l)_{i+\frac{1}{2},j-1,k} & \text{if} \quad V_{l_{i+\frac{1}{2},j-\frac{1}{2},k}} \geq 0 \\ (\theta_l U_l)_{i+\frac{1}{2},j,k} & \text{if} \quad V_{l_{i+\frac{1}{2},j-\frac{1}{2},k}} < 0 \end{cases} \tag{A.11}
$$

$$
< \theta_l U_l W_l >_{i+\frac{1}{2},j,k} = W_{l_{i+\frac{1}{2},j,k+\frac{1}{2}}} \begin{cases} (\theta_l U_l)_{i+\frac{1}{2},j,k} & \text{if} \quad W_{l_{i+\frac{1}{2},j,k+\frac{1}{2}}} \geq 0 \\ (\theta_l U_l)_{i+\frac{1}{2},j,k+1} & \text{if} \quad W_{l_{i+\frac{1}{2},j,k+\frac{1}{2}}} < 0 \end{cases}
$$

$$
-W_{l_{i+\frac{1}{2},j,k-\frac{1}{2}}} \begin{cases} (\theta_l U_l)_{i+\frac{1}{2},j,k-1} & \text{if} \quad W_{l_{i+\frac{1}{2},j,k-\frac{1}{2}}} \geq 0 \\ (\theta_l U_l)_{i+\frac{1}{2},j,k} & \text{if} \quad W_{l_{i+\frac{1}{2},j,k-\frac{1}{2}}} < 0 \end{cases} \tag{A.12}
$$

A.2.4   Z-Direction Equations For Liquid Phase

$$< \theta_l V_l U_l r >_{i,j+\frac{1}{2},k} \;=\; U_{l i+\frac{1}{2},j+\frac{1}{2},k} r_{i+\frac{1}{2}} \begin{cases} (\theta_l V_l)_{i,j+\frac{1}{2},k} & \text{if}\;\; U_{l i+\frac{1}{2},j+\frac{1}{2},k} \geq 0 \\[2mm] (\theta_l V_l)_{i+1,j+\frac{1}{2},k} & \text{if}\;\; U_{l i+\frac{1}{2},j+\frac{1}{2},k} < 0 \end{cases}$$

$$-U_{l i-\frac{1}{2},j+\frac{1}{2},k} r_{i-\frac{1}{2}} \begin{cases} (\theta_l V_l)_{i-1,j+\frac{1}{2},k} & \text{if}\;\; U_{l i-\frac{1}{2},j+\frac{1}{2},k} \geq 0 \\[2mm] (\theta_l V_l)_{i,j+\frac{1}{2},k} & \text{if}\;\; U_{l i-\frac{1}{2},j+\frac{1}{2},k} < 0 \end{cases} \tag{A.13}$$

$$< \theta_l V_l V_l >_{i,j+\frac{1}{2},k} \;=\; V_{l i,j+1,k} \begin{cases} (\theta_l V_l)_{i,j+\frac{1}{2},k} & \text{if}\;\; V_{l i,j+1,k} \geq 0 \\[2mm] (\theta_l V_l)_{i,j+\frac{3}{2},k} & \text{if}\;\; V_{l i,j+1,k} < 0 \end{cases}$$

$$-V_{l i,j,k} \begin{cases} (\theta_l V_l)_{i,j-\frac{1}{2},k} & \text{if}\;\; V_{l i,j,k} \geq 0 \\[2mm] (\theta_l V_l)_{i,j+\frac{1}{2},k} & \text{if}\;\; V_{l i,j,k} < 0 \end{cases} \tag{A.14}$$

$$< \theta_l V_l W_l >_{i,j+\frac{1}{2},k} \;=\; W_{l i,j+\frac{1}{2},k+\frac{1}{2}} \begin{cases} (\theta_l V_l)_{i,j+\frac{1}{2},k} & \text{if}\;\; W_{l i,j+\frac{1}{2},k+\frac{1}{2}} \geq 0 \\[2mm] (\theta_l V_l)_{i,j+\frac{1}{2},k+1} & \text{if}\;\; W_{l i,j+\frac{1}{2},k+\frac{1}{2}} < 0 \end{cases}$$

$$-W_{l i,j+\frac{1}{2},k-\frac{1}{2}} \begin{cases} (\theta_l V_l)_{i,j+\frac{1}{2},k-1} & \text{if}\;\; W_{l i,j+\frac{1}{2},k-\frac{1}{2}} \geq 0 \\[2mm] (\theta_l V_l)_{i,j+\frac{1}{2},k} & \text{if}\;\; W_{l i,j+\frac{1}{2},k-\frac{1}{2}} < 0 \end{cases} \tag{A.15}$$

A.2.5 ϕ-Direction Equations For Liquid Phase

$$< \theta_l W_l U_l r >_{i,j,k+\frac{1}{2}} \;=\; U_{l i+\frac{1}{2},j,k+\frac{1}{2}} r_{i+\frac{1}{2}} \begin{cases} (\theta_l W_l)_{i,j,k+\frac{1}{2}} & \text{if}\;\; U_{l i+\frac{1}{2},j,k+\frac{1}{2}} \geq 0 \\[2mm] (\theta_l W_l)_{i+1,j,k+\frac{1}{2}} & \text{if}\;\; U_{l i+\frac{1}{2},j,k+\frac{1}{2}} < 0 \end{cases}$$

$$-U_{l i-\frac{1}{2},j,k+\frac{1}{2}} r_{i-\frac{1}{2}} \begin{cases} (\theta_l W_l)_{i-1,j,k+\frac{1}{2}} & \text{if}\;\; U_{l i-\frac{1}{2},j,k-\frac{1}{2}} \geq 0 \\[2mm] (\theta_l W_l)_{i,j,k+\frac{1}{2}} & \text{if}\;\; U_{l i-\frac{1}{2},j,k+\frac{1}{2}} < 0 \end{cases} \tag{A.16}$$

$$< \theta_l W_l V_l >_{i,j,k+\frac{1}{2}} \;=\; V_{l i,j+\frac{1}{2},k+\frac{1}{2}} \begin{cases} (\theta_l W_l)_{i,j,k+\frac{1}{2}} & \text{if}\;\; V_{l i,j+\frac{1}{2},k+\frac{1}{2}} \geq 0 \\[2mm] (\theta_l W_l)_{i,j+1,k+\frac{1}{2}} & \text{if}\;\; V_{l i,j+\frac{1}{2},k+\frac{1}{2}} < 0 \end{cases}$$

$$-V_{l\,i,j-\frac{1}{2},k+\frac{1}{2}} \begin{cases} (\theta_l W_l)_{i,j-1,k+\frac{1}{2}} & \text{if} \quad V_{l\,i,j-\frac{1}{2},k+\frac{1}{2}} \geq 0 \\ (\theta_l W_l)_{i,j,k+\frac{1}{2}} & \text{if} \quad V_{l\,i,j-\frac{1}{2},k+\frac{1}{2}} < 0 \end{cases} \tag{A.17}$$

$$< \theta_l W_l W_l >_{i,j,k+\frac{1}{2}} = W_{l\,i,j,k+1} \begin{cases} (\theta_l W_l)_{i,j,k+\frac{1}{2}} & \text{if} \quad W_{l\,i,j,k+1} \geq 0 \\ (\theta_l W_l)_{i,j,k+\frac{3}{2}} & \text{if} \quad W_{l\,i,j,k+1} < 0 \end{cases}$$

$$-W_{l\,i,j,k} \begin{cases} (\theta_l W_l)_{i,j,k-\frac{1}{2}} & \text{if} \quad W_{l\,i,j,k} \geq 0 \\ (\theta_l W_l)_{i,j,k+\frac{1}{2}} & \text{if} \quad W_{l\,i,j,k} < 0 \end{cases} \tag{A.18}$$

A.3   Viscous Terms in the Momentum Equations

$$(\tau_{qrr})_{i,j,k}^n = \mu_q \Bigg\{ 2\Big(\frac{U_{q_{i+\frac{1}{2},j,k}}^n - U_{q_{i-\frac{1}{2},j,k}}^n}{\delta r}\Big)$$
$$-\frac{2}{3}\Big(\frac{U_{q_{i+\frac{1}{2},j,k}}^n r_{i+\frac{1}{2}} - U_{q_{i-\frac{1}{2},j,k}}^n r_{i-\frac{1}{2}}}{r_i \delta r}$$
$$+\frac{V_{q_{i,j+\frac{1}{2},k}}^n - V_{q_{i,j-\frac{1}{2},k}}^n}{\delta z} + \frac{W_{q_{i,j,k+\frac{1}{2}}}^n - W_{q_{i,j,k-\frac{1}{2}}}^n}{r_i \delta \phi}\Big)\Bigg\} \tag{A.19}$$

$$(\tau_{qr\phi})_{i-\frac{1}{2},j,k+\frac{1}{2}}^n = \mu_q \Bigg\{ \frac{U_{q_{i-\frac{1}{2},j,k+1}}^n - U_{q_{i-\frac{1}{2},j,k}}^n}{r_{i-\frac{1}{2}} \delta \phi}$$
$$+\frac{r_{i-\frac{1}{2}}\Big(\frac{W_{q_{i,j,k+\frac{1}{2}}}^n}{r_i} - \frac{W_{q_{i-1,j,k+\frac{1}{2}}}^n}{r_{i-1}}\Big)}{\delta r} \Bigg\} \tag{A.20}$$

$$(\tau_{qr\phi})_{i+\frac{1}{2},j,k-\frac{1}{2}}^n = \mu_q \Bigg\{ \frac{U_{q_{i+\frac{1}{2},j,k}}^n - U_{q_{i+\frac{1}{2},j,k-1}}^n}{r_{i+\frac{1}{2}} \delta \phi}$$
$$+\frac{r_{i+\frac{1}{2}}\Big(\frac{W_{q_{i+1,j,k-\frac{1}{2}}}^n}{r_{i+1}} - \frac{W_{q_{i,j,k-\frac{1}{2}}}^n}{r_i}\Big)}{\delta r} \Bigg\} \tag{A.21}$$

$$(\tau_{q\phi z})_{i,j+\frac{1}{2},k-\frac{1}{2}}^n = \mu_q \Bigg\{ \frac{V_{q_{i,j+\frac{1}{2},k}}^n - V_{q_{i,j+\frac{1}{2},k-1}}^n}{r_i \delta \phi}$$
$$+\frac{W_{q_{i,j+1,k-\frac{1}{2}}}^n - W_{q_{i,j,k-\frac{1}{2}}}^n}{\delta z} \Bigg\} \tag{A.22}$$

$$
(\tau_{q\phi z})^n_{i,j-\frac{1}{2},k+\frac{1}{2}} \;=\; \mu_q\bigg\{ \frac{V^{\,n}_{q_{i,j-\frac{1}{2},k+1}} - V^{\,n}_{q_{i,j-\frac{1}{2},k}}}{r_i\delta\phi}
$$
$$
+\frac{W^{\,n}_{q_{i,j,k+\frac{1}{2}}} - W^{\,n}_{q_{i,j-1,k+\frac{1}{2}}}}{\delta z}\bigg\} \qquad\qquad (A.23)
$$

$$
(\tau_{q\phi\phi})^n_{i,j,k+1} \;=\; \mu_q\bigg\{ 2\Big(\frac{U^{\,n}_{q_{i,j,k+1}}}{r_i} + \frac{W^{\,n}_{q_{i,j,k+\frac{3}{2}}} - W^{\,n}_{q_{i,j,k+\frac{1}{2}}}}{r_i\delta\phi}\Big)
$$
$$
-\;\frac{2}{3}\Big(\frac{r_{i+\frac{1}{2}}U^{\,n}_{q_{i+\frac{1}{2},j,k+1}} - r_{i-\frac{1}{2}}U^{\,n}_{q_{i-\frac{1}{2},j,k+1}}}{r_i\delta r}
$$
$$
+\;\frac{V^{\,n}_{q_{i,j+\frac{1}{2},k+1}} - V^{\,n}_{q_{i,j-\frac{1}{2},k+1}}}{\delta z}
$$
$$
+\;\frac{W^{\,n}_{q_{i,j,k+\frac{3}{2}}} - W^{\,n}_{q_{i,j,k+\frac{1}{2}}}}{r_i\delta\phi}\Big)\bigg\} \qquad\qquad (A.24)
$$

$$
(\tau_{q\phi\phi})^n_{i,j,k} \;=\; \mu_q\bigg\{ 2\Big(\frac{U^{\,n}_{q_{i,j,k}}}{r_i} + \frac{W^{\,n}_{q_{i,j,k+\frac{1}{2}}} - W^{\,n}_{q_{i,j,k-\frac{1}{2}}}}{r_i\delta\phi}\Big)
$$
$$
-\frac{2}{3}\Big(\frac{r_{i+\frac{1}{2}}U^{\,n}_{q_{i+\frac{1}{2},j,k}} - r_{i-\frac{1}{2}}U^{\,n}_{q_{i-\frac{1}{2},j,k}}}{r_i\delta r}
$$
$$
+\frac{V^{\,n}_{q_{i,j+\frac{1}{2},k}} - V^{\,n}_{q_{i,j-\frac{1}{2},k}}}{\delta z}\,\frac{W^{\,n}_{q_{i,j,k+\frac{1}{2}}} - W^{\,n}_{q_{i,j,k-\frac{1}{2}}}}{r_i\delta\phi}\Big)\bigg\} \quad (A.25)
$$

$$
(\tau_{qzz})^n_{i,j,k} \;=\; \mu_q\bigg\{ 2\Big(\frac{V^{\,n}_{q_{i,j+\frac{1}{2},k}} - V^{\,n}_{q_{i,j-\frac{1}{2},k}}}{\delta z}\Big)
$$
$$
-\frac{2}{3}\Big(\frac{r_{i+\frac{1}{2}}U^{\,n}_{q_{i+\frac{1}{2},j,k}} - r_{i-\frac{1}{2}}U^{\,n}_{q_{i-\frac{1}{2},j,k}}}{r_i\delta r}
$$
$$
+\frac{V^{\,n}_{q_{i,j+\frac{1}{2},k}} - V^{\,n}_{q_{i,j-\frac{1}{2},k}}}{\delta z} + \frac{W^{\,n}_{q_{i,j,k+\frac{1}{2}}} - W^{\,n}_{q_{i,j,k-\frac{1}{2}}}}{r_i\delta\phi}\Big)\bigg\} \; (A.26)
$$

$$
(\tau_{qrz})^n_{i+\frac{1}{2},j-\frac{1}{2},k} = \mu_q\bigg\{ \frac{V^{\,n}_{q_{i+1,j-\frac{1}{2},k}} - V^{\,n}_{q_{i,j-\frac{1}{2},k}}}{\delta r} + \frac{U^{\,n}_{q_{i+\frac{1}{2},j,k}} - U^{\,n}_{q_{i+\frac{1}{2},j-1,k}}}{\delta z}\bigg\}(A.27)
$$

$$
(\tau_{qrz})^n_{i-\frac{1}{2},j+\frac{1}{2},k} = \mu_q\bigg\{ \frac{V^{\,n}_{q_{i,j+\frac{1}{2},k}} - V^{\,n}_{q_{i-1,j+\frac{1}{2},k}}}{\delta r} + \frac{U^{\,n}_{q_{i-\frac{1}{2},j+1,k}} - U^{\,n}_{q_{i-\frac{1}{2},j,k}}}{\delta z}\bigg\}(A.28)
$$

VITA

Enis Pezek was born in Ankara on August 27, 1973. He was graduated in June 1990 from Sivas Lisesi. The following September he entered Hacettepe University and in July 1995 received the degree of Bachelor of Science in Nuclear Engineering. He reentered Hacettepe University in September 1995 and in January 1999 received a Master of Science degree in Nuclear Engineering. He worked as a Research Assistant in the same department from 1995 to 1997. He had worked for the Nuclear Power Plants Department of the former Turkish Electricity Generation and Transmission Corporation during the period of 1997-2001. He took part in the bid evaluation team for the Akkuyu Nuclear Power Plant Project with special focus on the nuclear steam supply system. He has been working for the Electricity Generation Corporation as a chief engineer since 2001. His main areas of interests are quality management systems and project management.